High-speed slotless permanent magnet machines:

modeling and design frameworks

Sultan Jumayev

High-speed slotless permanent magnet machines: modeling and design frameworks

door

Sultan Jumayev

geboren te Seydi, Turkmenistan

Dit proefschrift is goedgekeurd door de promotoren en de samenstelling van de promotiecommissie is als volgt:

voorzitter:	prof.dr.ir. A.B. Smolders
1e promotor:	prof.dr. E.A. Lomonova MSc
2e promotor:	prof.dr. J. Pyrhönen MSc (Lappeenranta University of Technology)
copromotor:	dr. K.O. Boynov MSc
leden:	prof.dr. C. Gerada (The University of Nottingham)
	prof.dr.ir. L. Dupré (Ghent University)
	dr.ir. J.W. Jansen
adviseur:	dr. R. Keller (Dr. Fritz Faulhaber GMBH & Co. KG)
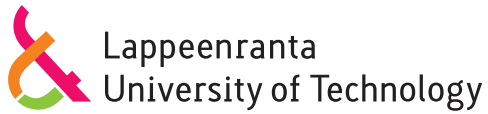
Lappeenrannan teknillinen yliopisto
Lappeenranta University of Technology

Technische Universiteit Eindhoven
Eindhoven University of Technology

Sultan Jumayev

HIGH-SPEED SLOTLESS PERMANENT MAGNET MACHINES: MODELING AND DESIGN FRAMEWORKS

Thesis for the degree of Doctor of Science (Technology) to be presented with due permission for public examination and criticism in the Auditorium 4 at Eindhoven University of Technology, Eindhoven, the Netherlands on the 1st of June, 2017, at 16.00.

The thesis was written under a double doctoral degree agreement between Lappeenranta University of Technology, Finland and Eindhoven University of Technology, the Netherlands and jointly supervised by supervisors from both universities.

Summary

High-speed slotless permanent magnet machines: modeling and design frameworks

The number of applications driven by high-speed electrical machines has drastically increased during the recent decades. Some applications require high speeds to operate effectively, e.g. turbocompressors, spindles and turbomolecular pumps. In other applications, for instance in space or transport, these machines are vital due to their high power density. Among these machines, high-speed slotless permanent magnet (PM) machines are attractive at very high speeds (>100 000 rpm) and low-power applications because of the absence of cogging torque and losses caused by slotting.

Slotless winding configurations with skewed conductors require 3D field modeling. In this case, traditionally, the finite element method (FEM) modeling is applied. However, often it requires a significant calculation time, which is unsatisfactory in optimization of machine designs. On the other hand, (semi-) analytical approaches are much faster alternatives compared with FEM. Nevertheless, no (semi-) analytical electromagnetic modeling approaches that are able to model various complex slotless winding configurations can be found in the literature.

In this thesis, the semi-analytical harmonic modeling technique is extended to be able to model 3D electromagnetic fields in cylindrical coordinates. This extended harmonic modeling technique is obtained by incorporating the 2D harmonic modeling, formulated by the magnetic vector potential, and the 3D harmonic modeling, formulated by the second order magnetic vector potential. The spatial distribution of the magnetic field source, given by a linear current density, is described by 2D Fourier series, which includes current density components with single or double coordinate dependencies. This electromagnetic modeling technique can be applied to model high-speed slotless PM machines with a wide range of slotless winding configurations. Moreover, it is able to model eddy currents induced in conducting

regions, such as permanent magnet material and rotor retaining sleeve. Prediction of the rotor eddy currents is essential for high-speed machines, because it facilitates assessing the rotor eddy-current losses.

Based on the armature and PM magnetic field distributions, obtained by the harmonic modeling, expressions to calculate the machine electromagnetic quantities, such as electromagnetic torque, electromotive force (emf) induced by the PM field, and synchronous inductance, are derived. A generalized expression to calculate the electromagnetic torque is obtained using the armature and PM field solutions in the air gap for 2D and 3D electromagnetic problems using Maxwell's stress tensor. The torque expression can be employed to calculate the time and position dependent torque profiles. The emf induced by the PM field is calculated by integrating the magnetic field over the winding's spatial distribution. The calculation of the synchronous inductance using the field obtained by the harmonic modeling takes into account the reaction field of the rotor eddy currents.

Following, using the electromagnetic field distribution, a research on calculation of the electromagnetic losses occurring in high-speed slotless PM machines is conducted. Precise assessment of losses in electrical machines is of primary importance, as it facilitates an accurate prediction of the machine efficiency, thermal stresses on vulnerable machine parts, and accounting for the material property change caused by the temperature variation. Rotor eddy-current losses produced by the armature reaction field are calculated using the Poynting vector. Expressions for the calculation of skin and proximity losses in winding conductors caused by the changing PM field are introduced for straight and skewed conductors. Calculation of other electromagnetic losses, such as DC Joule and iron, is also considered in the thesis.

Since all high-speed machines are supplied by power converters, the investigation of the influence of the current ripple produced by the PWM on rotor eddy-current losses is performed. An analytical approach to predict the current ripple caused by the PWM is presented. This approach is based on the solution of the electrical circuit of the slotless PM machines with frequency-dependent circuit parameters, where the PWM is defined as a Fourier series over the frequency domain.

Further, a design framework for high-speed slotless PM machines is developed based on the described electromagnetic modeling framework. This framework is applied to design a slotless high-speed PM machine for a benchmark application, which is a mobile medical ventilation system. In this application the high-speed slotless PM machine drives a miniature centrifugal blower in highly dynamic motion profile within wide speed and torque ranges. Therefore, the optimization of the machine is performed considering a highly dynamic operation for the extreme neonatal and adult ventilation cases. The mechanical stability of the rotor is ensured by limiting the mechanical stresses in the rotor parts originated from centrifugal forces as well as considering the rotor-dynamic stability. The thermal behavior of the machines is predicted by using the thermal equivalent circuit model,

and temperature conditions of the wire insulation and PMs are kept below their fatigue points. During the design procedure three different machines with various slotless windings, namely toroidal, concentrated, and Faulhaber, have been analyzed. The optimization is done towards minimization of the power consumption of the machine. A prototype of the high-speed PM machine with Faulhaber winding has been manufactured, and measurements have been conducted to validate the developed electromagnetic modeling and design frameworks.

Contents

Nomenclature

Notation

Symbol	Description
A	scalar
$\vec{A}$	vector
$\boldsymbol{A}$	matrix
$\bar{A}$	complex number
$\hat{A}$	peak value

Operators

Symbol	Description
$\cdot$	Dot product
$\times$	Cross product
∇	Gradient
$\nabla\cdot$	Divergence
$\nabla\times$	Curl
$\dfrac{\partial}{\partial t}$	Time derivative

Parameters with Roman Symbols

Symbol	Units	Description
$\vec{A}$	Wb/m	magnetic vector potential
a	-	number of parallel strands
$\vec{B}$	T	magnetic flux density
$\vec{B}_{\mathrm{rem}}$	T	remanent flux density
$\vec{D}$	C/m^2	electric flux density
d_{m}	m	PM diameter
$\vec{E}$	V/m	electric field strength
$\vec{e}$	-	unit vector
e	V	electromotive force
f	Hz	frequency
f_{sw}	Hz	switching frequency
f_{w}	-	distribution function
$\vec{H}$	A/m	magnetic field strength
$\vec{H}_c$	A/m	coercivity
h_{w}	m	winding thickness
i	A	current
$\vec{J}$	A/m^2	electric current density
J_{im}	kgm^2	impeller inertia
J_{m}	kgm^2	rotor inertia
$\vec{K}$	A/m	electric linear current density
k	-	time harmonic order
k_{e}	V/s	emf constant
k_{sCu}	-	space factor
k_{T}	Nm/A	torque constant
k_{t}	W/m/K	thermal conductivity
L	-	integer number
L_{s}	H	synchronous inductance
l	m	machine active length
l_{c}	m	conductor length
$\vec{M}$	A/m	magnetization
M	-	amplitude modulation ratio
$\vec{M}_0$	A/m	internal magnetization

Symbol	Units	Description
$\vec{M}_\mathrm{e}$	A/m	external magnetization
m	-	space harmonic order in axial direction
m_f	-	frequency modulation ratio
N	-	number of turns per coil
n	rpm	rotational speed
$\vec{P}$	C/m^2 or W/m^2	polarization or Poynting vector
P_Cu	W	Joule losses in winding caused by applied current
P_Fe	W	iron losses
P_b	W	bearing losses
P_in	W	input electrical power
P_loss	W	power losses
P_out	W	shaft power
P_p	W	proximity effect losses
P_r	W	rotor eddy-current losses
P_w	W	windage losses
q	W	heat source
R	Ω	DC resistance
r	m	radial coordinate
r_c	m	conductor radius
r_m	m	PM radius
S	m^2	surface
s	rad	phase spread in circumference
$\vec{T}$	Nm	torque vector
T	°C	temperature
T	Nm or s	torque or period
T_m	Nm	electromagnetic torque
$\mathbb{T}$	N/m^2	Maxwell's stress tensor
t	s	time
u	V	voltage
V	m^3	volume
$\vec{W}$	Wb	second-order vector potential
W_1	Wb	scalar potential function
W_2	Wbm	scalar potential function
x	m	coordinate

Symbol	Units	Description
y	m	coordinate
z	m	axial coordinate

Parameters with Greek Symbols

Symbol	Units	Description
δ	m	air gap
ψ	Wb (Vs)	flux linkage
Φ	Wb (Vs)	magnetic flux
ϵ_0	F/m	permittivity of free space
η	%	efficiency
λ	m	electromagnetic field wavelength
μ	H/m	magnetic permeability
μ_0	H/m	magnetic permeability of free space
μ_r	-	relative magnetic permeability
ν	-	space harmonic order in circumferential direction
Ω	rad/s	mechanical angular velocity
ω	rad/s	angular velocity
ω_r	rad/s	relative angular velocity
ϕ	A	magnetic scalar potential
ρ	Ωm	electric resistivity
ρ_e	C/m^3	free electric volume charge density
σ	S/m	electrical conductivity
θ	rad	circumferential coordinate
θ_r	rad	circumferential coordinate in rotor reference frame
θ_0	rad	initial rotor position
φ	A	magnetic scalar potential
χ_m	-	magnetic susceptibility

Symbol	Description
AR	armature reaction
a	armature or axial
c	cosine component
n	normal component
PM	permanent magnet
ph	phase
r	radial
s	stator, sine component
si	stator inner (radius)
so	stator outer (radius)
wc	winding center (radius)
wo	winding outer (radius)
wi	winding inner (radius)
z	axial
θ	circumferential

Subscripts

Acronyms

Abbreviation	Description
1D	one-dimensional
2D	two-dimensional
3D	three-dimensional
AC	alternating current
AR	armature reaction
BEM	boundary element method
DC	direct current
emf	electromotive force
FEM	finite element method
HM	harmonic modeling
mmf	magnetomotive force

Abbreviation	Description
PAM	pulse-amplitude modulation
PM	permanent magnet
PMSM	permanent magnet synchronous machine
PPU	power processing unit
PWM	pulse-width modulation
SAN	semianalytical
SOVP	second order vector potential
TEC	thermal equivalent circuit
VSI	voltage source inverter

1

Introduction

This introductory chapter gives the background and actual status of the research and defines the thesis objectives.

1.1   Small-sized high-speed applications

High-speed machine technology (10–1000 krpm) has been researched and developed for various applications, such as gas compressors, turbomolecular pumps, flywheel energy storage systems, microturbines, aerospace, and nuclear centrifuges for several decades. Some of these applications require high speeds to operate more efficiently, while others aim to decrease the volume and mass of the electrical drive system by increasing the power density. The emergence of new high-speed applications, such as compact power generation systems, machining and drilling spindles, and optical applications, directs the research and production trends towards small-sized high-speed machines.

Medical application

Small-sized high-speed machines are widely used for medical purposes. An example of such an application can be electric surgical systems manufactured by Medtronic and Nouvag. Their systems contain high-speed drilling devices. These drilling devices are driven by small-sized high-speed machines, which are capable of rotating at 80 krpm. Besides, the majority of the modern dental drilling devices are driven by small-sized high-speed machines. An example is special small-sized high-speed machines for dental tools made by Sirona; the power of these machines ranges from 40 W up to 80 W with the maximum speed of 40 krpm.

Another medical application of small-sized high-speed machines is a portable medical ventilator, which provides breathing assistance for people suffering from a respiratory system malfunction. Nowadays, there is a high interest in portable medical ventilators for stationary and autonomous operation. Current medical ventilators, which are usually based on closed systems with an external pressurized air or oxygen source, are not suitable for these purposes. Moreover, they are usually energy inefficient and heavy, and require extensive maintenance. The general objective is development of a compact, energy-efficient, low life-cycle cost, and reliable breathing support system for innovative medical ventilators, which can be universally employed for stationary use (both adults and neonates), during emergency transportation and independent of medical gases. The portable medical ventilator solution can be achieved by employing a centrifugal blower driven by a small-sized high-speed electric motor drive system, which can provide the energy-efficient and lightweight solutions needed. An example of such a system is shown in Figure 1.1. To replicate human breathing patterns, this high-speed electric motor drive system should operate at high-dynamic motion profile. The small-sized high-speed motor for the blower module shown in Figure 1.1 delivers about 50 W of shaft power with a maximum speed of 100 krpm.

Centrifugal   Machine   PPU
blower
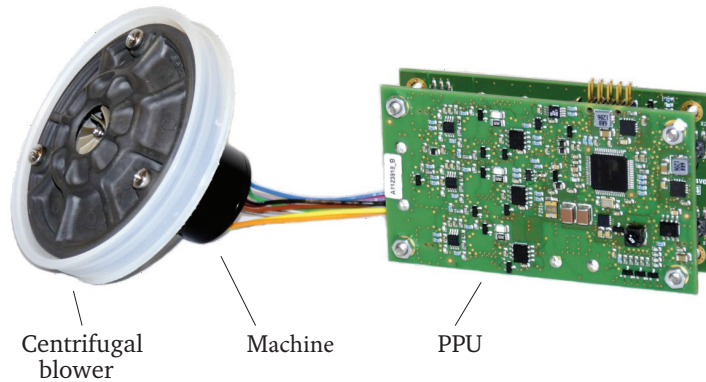
Figure 1.1: OEM blower module containing a centrifugal blower, a high-speed machine, and a power processing unit (PPU) developed by DEMCON Medical Devices.

Other applications

An example of a compact power generation system based on an axial impulse turbine, which uses compressed air to generate electrical energy, is described in [64]. As a generator in this system, a high-speed PM machine with an output power of 60 W and a rotating speed of 350 krpm is employed. Another example of a power generation system is presented in [116], which introduces a portable (mobile) power unit for a gas turbine. This unit, working on fuel, uses a 100 W high-speed PM generator rotating at 500 krpm. The manufacturing of compact printed circuit boards (PCBs) requires high precision, which is facilitated by high-speed drilling and routing spindles. An example of a high-speed drilling spindle is the drilling spindle D1795 manufactured by Westwind, which is capable of drilling holes of 75 μm on PCBs. The high-speed PM machine assembled on this spindle is able to exceed 370 krpm with an output power of several. Optical systems require small-sized high-speed machines in laser scanning systems (LIDARs), where the rotation speed of the mirror set defines the scanning resolution of the system. Currently available laser scanning spindles, for instance produced by General Dynamics or Westwind, rotate at speeds up to 100 krpm. To significantly increase the resolution of such a system, the research on a small-sized ultra high-speed PM machine with a self-bearing system has been conducted in [4] and [5]. The proposed machine solution is able to reach a speed of 500 krpm and provide an output power of 300 W.

1.2   Small-sized high-speed machines

1.2.1   Machine topology

Various machine topologies can be used in small-sized high-speed machines; however, the only feasible solution is a permanent magnet (PM) synchronous machine or a brushless DC machine, when a high efficiency is needed [33], [11]. The permanent magnet excitation enables, in principle, lossless excitation of the machine, which is the key to a high efficiency. Other machine topologies, such as induction and reluctance machines, require the magnetizing current to excite the machine, which leads to higher losses. Moreover, PM machines demonstrate a higher power density and a higher power factor [117]. In this thesis, the permanent magnet synchronous machine is the subject of the research.

1.2.2   Winding configurations of small-sized high-speed permanent magnet synchronous machines

In general, for the high-speed PM machine design, two stator configurations can be considered, viz. slotted or slotless ones, as it is shown in Figure 1.2. The advantages of the slotted structure are a higher magnetic loading and better cooling capabilities of the winding [9]. However, in slotted PM machines there are cogging torque [81], [26] and rotor eddy-current losses, induced by the PM excitation and circumferential permeance variation [60]. Slotless PM machines do not suffer from these disadvantages [20], [60], [63], and furthermore, they are less exposed to the PM demagnetization [9], and have less radial magnetic pull caused by possible rotor eccentricity [60], and lower noise levels. Nevertheless, slotless machines usually reach lower magnetic loading values because of the increased effective air gap, which also includes the winding, as the copper relative permeability is close to one. The conductors of the slotless (air-cored) winding are directly penetrated by the time-changing PM field, which causes eddy currents in these conductors. The consideration of the benefits and drawbacks of slotted and slotless PM machines should also cover the manufacturing aspects; however, it depends on the manufacturing capabilities of a certain machine producer. Based on the aforementioned advantages and disadvantages, the slotless winding configuration is considered to be more feasible for small-sized high-speed PM machines.

Various types of slotless (air-cored) windings are used in high-speed PM machines; for example, the toroidal winding type, shown in Figure 1.3(a), is advantageous for machines with a short active length [14]. The winding distribution in the active part is similar to a distributed winding, which yields a high winding factor value. This winding type has the flank and outer parts, which may induce eddy currents in other machine parts [13].
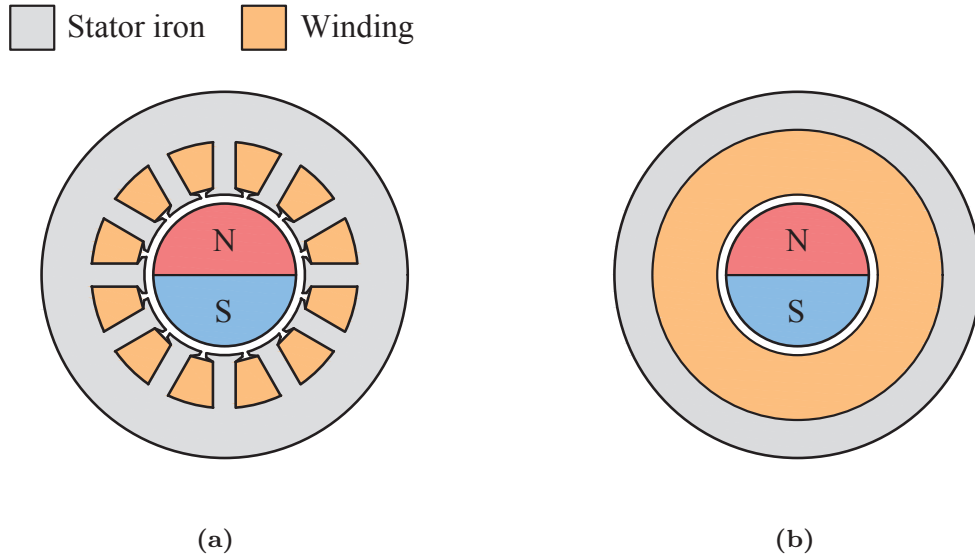
Figure 1.2: General layout of slotted and slotless PM machine configurations.

Another slotless winding type is the concentrated winding (3 coil/2 pole combination), one winding coil of which is illustrated in Figure 1.3(b). These windings are mainly used because of the manufacturing simplicity [86]. This winding type has short end windings compared with the toroidal one, but the winding factor is lower. This winding has a spatial second-order harmonic value, which is larger than the fundamental one.

The third winding type, which actually represents a set of windings, is the self-supporting winding type. Examples of the self-supporting windings, viz. Faulhaber, rhombic, and diamond windings, are illustrated in Figure 1.4. The term 'self-supporting' originates from the fact that these windings have a robust structure and do not need a frame, for instance stator iron, to be supported. These windings types are mainly introduced and used by producers that manufacture large volumes of small-sized high-speed PM machines. The windings are wound in an automated process and then molded into a robust structure using epoxy resin. Another method to produce these windings is using a flexible printed circuit board (PCB) [23], [24]. In this case, the pattern of the winding geometry is printed on a flexible PCB and then wrapped into a cylindrical shape. This technology enables complex winding geometries, which can improve the winding factor, and offer a higher copper space factor according to [22], [25]. The authors, however, faced some difficulties with the alignment of the coils during the wrapping process.

Usually, the radial thickness of classical self-supporting windings is small (two wire diameters), owing to limitations in the automated winding process. Therefore, main machine producers, such as Faulhaber and Maxon, have introduced thick self-
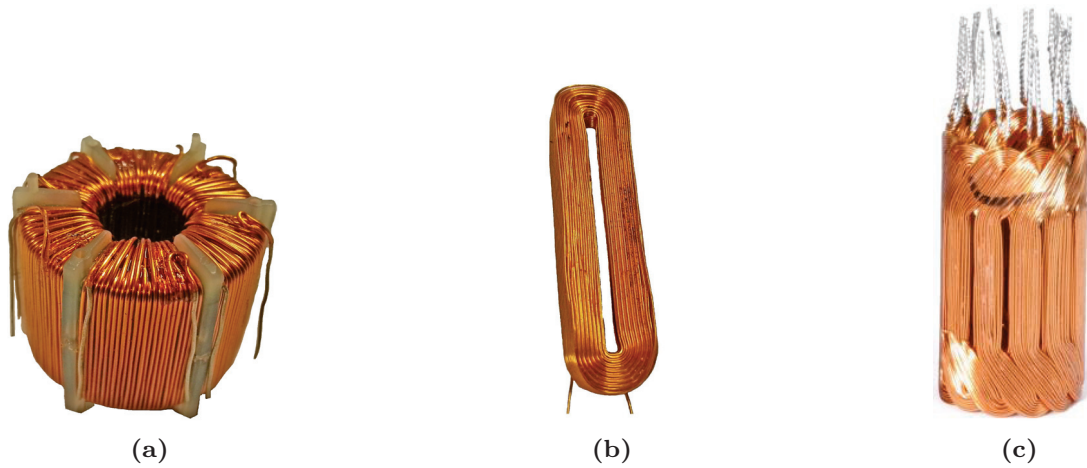
Figure 1.3: Examples of slotless windings: a) AC toroidal winding, b) coil of an AC concentrated winding, and c) knitted winding for a DC motor [75].
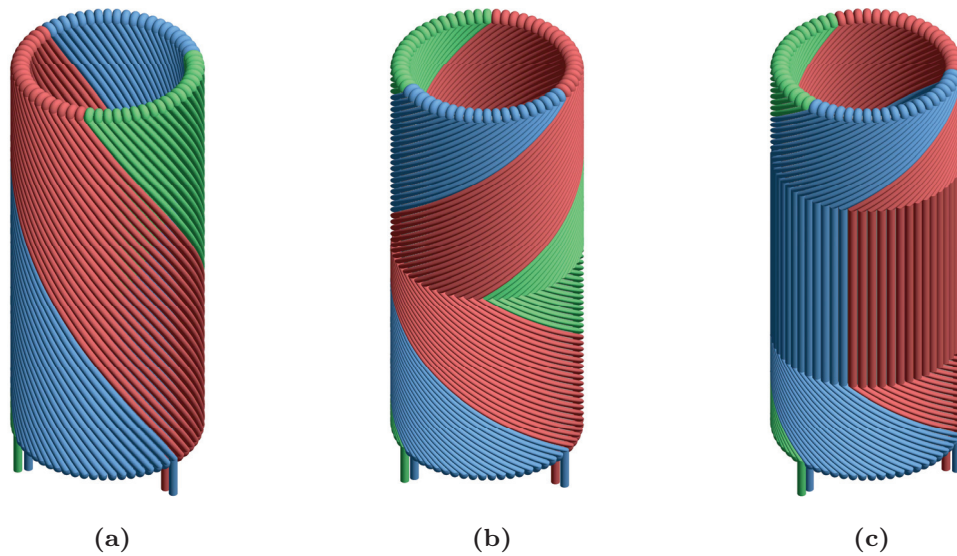
Figure 1.4: Examples of slotless (air-cored) self-supporting windings: a) Faulhaber, b) rhombic, and c) diamond types.

supporting slotless windings, also called knitted windings [75], which is illustrated in Figure 1.3(c). The coils of the winding are wound separately and then stacked together, for example by using a self-bonding layer of the wires. The knitted windings usually have a higher copper space factor.

It is challenging to select the most suitable slotless winding type based on a preliminary consideration, as the selection is highly dependent on the winding manufacturing facilities available.

1.2.3 Electromagnetic modeling of small-sized high-speed slotless permanent magnet machines

The slotless winding configuration allows manufacturing windings with complex shapes including skewing of the conductors. In practice, the complex configuration facilitates the improvement of the machine performance. From the theoretical point of view, it requires complex electromagnetic modeling approaches to derive the machine parameters, such as delivered electromagnetic torque, electromotive force, and electromagnetic losses to be dissipated. As the machine under consideration is a high-speed machine, the high-frequency-related phenomena, such as rotor eddy-current losses caused by the armature field and skin and proximity losses in the winding conductors, have to be taken into account. Moreover, all high-speed machines are supplied by frequency converters, which cause extra losses in the machines as a result of pulse-width modulation (PWM).

Electromagnetic modeling of electrical machines is often performed by finite element modeling (FEM). In spite of its accuracy and ability to model complex geometries, simultaneously taking nonlinear electromagnetic behavior of materials into account, the required simulation time is typically longer than in (semi-) analytical models. This holds especially for three-dimensional (3D) electromagnetic FEM models. Depending on the model properties, solving the problem can take hours or even days [58]. In the design optimization of an electrical machine, the machine electromagnetic modeling is often performed over multiple machine parameter sets. Therefore, (semi-) analytical models are the best candidates to be used for design optimization purposes, as they require significantly less simulation time, yet provide satisfactory modeling accuracy.

There are a few studies on analytical modeling of slotless machines with complex skewed windings. In [92] and [53], the magnetic field of machines with slotless windings has been modeled by applying the Biot-Savart law. The obtained magnetic field solution is further used to determine the self and mutual inductance values of the phases. The authors of [72] and [52] have employed the Lorentz force method to calculate the forces and torque in machines with Faulhaber and rhombic slotless windings. The approach presented in [3] and [74] is capable of predicting the armature field in a slotless machine with the Faulhaber winding using a harmonic modeling approach. However, it is obvious that high-speed slotless PM machines lack generally applicable (semi-) analytical modeling tools, which are also able to take the rotor eddy-current losses into account.

1.3   Research objectives

The preliminary analysis has identified gaps in the established high-speed electrical machine theory. This missing knowledge defines the essence of the research objectives of the thesis, which can be formulated as:

- **Extend the (semi-) analytical modeling approach to predict the electromagnetic field including the induced rotor eddy currents in slotless PM machines for a wide range of slotless winding types**
  Discussed in Chapter 2
  Because physical quantities, for instance electromagnetic torque, emf, and electromagnetic losses of an electrical machine can be derived from the electromagnetic field distribution in the machine, it is essential to develop a (semi-)analytical model to obtain this field. Furthermore, the electromagnetic modeling should include rotor eddy currents, as they cause partial or full PM demagnetization in high-speed PM machines. Generally, (semi-) analytical models are fast compared with other models (e.g. FEM), which facilitates a reduction in the time required for the design optimization process.

- **Predict the electromagnetic quantities of slotless PM machines based on the magnetic field distribution**
  Discussed in Chapter 3
  By using the electromagnetic field distribution obtained in Chapter 2, a general approach to calculate the generated electromagnetic torque, the emf induced in the winding coils, and the synchronous inductance should be developed.

- **Investigate the influence of a PWM voltage on the rotor-eddy current losses**
  Discussed in Chapters 4
  The main origin of the rotor eddy-current losses in high-speed slotless PM machines is the current ripple caused by the supply voltage [54]. As high-speed slotless PM machines are mainly supplied by voltage source inverters with the pulse-width modulation (PWM) technique, it is necessary to investigate the influence of the PWM on the rotor eddy-current losses.

- **Design procedure of slotless high-speed PM machines**
  Discussed in Chapter 5
  Using the developed (semi-) analytical electromagnetic model, given in Chapters 2, 3, and 4, an approach should be developed to design high-speed slotless PM machines. The design framework should also include consideration of thermal and mechanical aspects, as their significance grows with an increase in the machine speed.

- **Implement a prototype and experimental verification of the proposed models**
  Discussed in Chapter 6
  It is essential to build and test a prototype of the designed high-speed PM machine to validate the proposed modeling and design frameworks. Furthermore, the prototype allows estimating the manufacturing limitations, which are often only roughly estimated or even neglected in the modeling and design of high-speed PM machines.

1.4   Outline of the thesis

Part 1: Electromagnetic modeling framework

In electrical machines, the energy is converted from electrical to mechanical form or vice versa by means of an electromagnetic field. Having the electromagnetic field distribution in the machine, electromagnetic quantities and losses can be determined. Therefore, the first part of this thesis continues with derivation of the electromagnetic field modeling techniques. In **Chapter 2**, the harmonic modeling (HM) technique, which directly solves quasi-static Maxwell's equations, is extended to be able to model the armature field of slotless PM machines with a wide range of winding types. This approach can take into account the induced eddy currents in the conducting parts of the machine and their reaction field. The extended model is validated by a transient 3D FEM.

Derivation of the electromagnetic quantities in slotless PM machines, namely the developed electromagnetic torque, the emf induced by the PM flux linkage, and the synchronous inductance, by using the electromagnetic field distribution is presented in **Chapter 3**.

Chapter 4 focuses on the analysis of electromagnetic losses in high-speed slotless PM machines. This chapter begins with modeling of the Joule losses caused by the applied current and the skin and proximity effects in the slotless windings. Further, calculation of the rotor eddy-current losses and their reduction mechanisms are explained. The iron losses are treated by using the classical loss separation model. Finally, the assessment of the losses caused by the PWM is analyzed.

Part 2: Design framework

The design optimization framework of high-speed slotless PM machines intended for dynamic operation is the topic of **Chapter 5**. Initially, the machine design requirements and limitations are determined, and the selection of the slotless PM machine configuration is discussed. Three slotless PM machines with distinct winding configurations, namely toroidal, concentrated, and Faulhaber windings, are selected to be considered in the design optimization process. Further, the design optimization routine, including considerations of the mechanical and thermal conditions, is introduced. This routine allows to find the machine design with minimum power consumption, which is, especially, desired for the specified application. The results of the optimal designs of the three high-speed slotless PM machines are presented and discussed.

Prototype implementation of the designed high-speed PM machines with a Faulhaber winding is addressed in **Chapter 6**. To validate the proposed electromagnetic modeling framework, measurements are conducted on the prototype. These measurements include verification of the electrical circuit parameters (resistance and synchronous inductance), torque and emf constants, rotor eddy-current losses, and no-load losses.

Part 3: Closing

Finally, in **Chapter 7**, conclusions on the defined research objectives are drawn. Recommendations for further research directions and improvements are given.

Part I

Electromagnetic modeling framework

2

Electromagnetic field modeling

This chapter provides the background theory, practical implementation, and validation of the three-dimensional quasi-static electromagnetic field modeling of a slotless PM machine with complex winding geometries.

2.1   General electromagnetic theory

2.1.1   Maxwell's equations

The behavior of electromagnetic fields is governed by Maxwell's equations, which are given in the differential form by

$$\nabla \times \vec{H} = \vec{J} + \frac{\partial \vec{D}}{\partial t}, \qquad\qquad \text{Ampère's law} \qquad\qquad (2.1)$$

$$\nabla \times \vec{E} = -\frac{\partial \vec{B}}{\partial t}, \qquad\qquad \text{Faraday's law} \qquad\qquad (2.2)$$

$$\nabla \cdot \vec{B} = 0, \qquad\qquad \text{Gauss's law for magnetic field} \qquad (2.3)$$

$$\nabla \cdot \vec{D} = \rho_{\mathrm{e}}, \qquad\qquad \text{Gauss's law for electric field} \qquad (2.4)$$

where $\vec{H}$ is the magnetic field strength [A/m], $\vec{J}$ is the electric current density [A/m^2], $\vec{D}$ is the electric flux density [C/m^2], t is the time [s], $\vec{E}$ is the electric field strength [V/m], $\vec{B}$ is the magnetic flux density [T], and ρ_{e} is the free electric volume charge density [C/m^3]. To complete the electromagnetic field description, Maxwell's equations should be supplemented by constitutive material relations, which are given as

$$\vec{B} = \mu_0 \left(\vec{H} + \vec{M} \right), \qquad\qquad (2.5)$$

$$\vec{D} = \varepsilon_0 \vec{E} + \vec{P}, \qquad\qquad (2.6)$$

$$\vec{J} = \sigma \vec{E}, \qquad\qquad (2.7)$$

where μ_0 is the permeability of free space [H/m], ε_0 is the permittivity of free space [F/m], $\vec{M}$ is the magnetization of the material [A/m], and $\vec{P}$ is the polarization of the material [C/m^2]. The magnetization is a sum of internal, $\vec{M}_0$, and external, $\vec{M}_{\mathrm{e}}$, magnetizations. $\vec{M}_0$ is linked with the remanent flux density, $\vec{B}_{\mathrm{rem}}$, as

$$\vec{M}_0 = \frac{\vec{B}_{\mathrm{rem}}}{\mu_0}. \qquad\qquad (2.8)$$

The second magnetization term, $\vec{M}_{\mathrm{e}}$, represents magnetization caused by an external magnetic field source. The external magnetic field causes a change in the material magnetization and is written as

$$\vec{M}_{\mathrm{e}} = \chi_{\mathrm{m}} \vec{H}, \qquad\qquad (2.9)$$

where χ_{m} is the magnetic susceptibility. The constitutive relation (2.5) can be rewritten as

$$\vec{B} = \mu_0(1 + \chi_{\mathrm{m}})\vec{H} + \mu_0 \vec{M}_0 = \mu_0 \mu_{\mathrm{r}} \vec{H} + \vec{B}_{\mathrm{rem}}, \qquad\qquad (2.10)$$

where $\mu_{\mathrm{r}} = (1 + \chi_{\mathrm{m}})$ is the relative permeability. Maxwell's equations (2.1)–(2.4) together with the constitutive relations (2.5)–(2.7) describe the electromagnetic behavior of a system. Typically, electromechanical systems operate at frequencies $f < 1$ MHz, which results in an electromagnetic field wavelength of $\lambda > 300$ m. If the electromagnetic system dimensions under consideration are relatively small compared with the electromagnetic field wavelength, which is the case for electromechanical actuators, the quasistatic field theory can be applied [30]. In this case, the magnetic field change can be assumed simultaneous at any point of the system, which neglects the propagation speed of the electromagnetic field. Therefore, the term in Maxwell's equations that represents the displacement current $(\partial D / \partial t)$ can be neglected, and Maxwell's equations reduce to

$$\nabla \times \vec{H} = \vec{J}, \tag{2.11}$$

$$\nabla \times \vec{E} = -\frac{\partial \vec{B}}{\partial t}, \tag{2.12}$$

$$\nabla \cdot \vec{B} = 0, \tag{2.13}$$

$$\nabla \cdot \vec{D} = \rho_{\mathrm{e}}, \tag{2.14}$$

The quasistatic Maxwell's equations cover a wide range of applications, such as power electrical circuits and electromechanical devices, including induced eddy currents in the conducting media. For the quasistatic Maxwell's equations, by taking a divergence of (2.11), the continuity equation is expressed as

$$\nabla \cdot \vec{J} = 0, \tag{2.15}$$

which assumes no free-charge conservation in the system.

The quasistatic Maxwell's equations can be directly used to calculate electromagnetic fields; however, this process can be simplified by using the concept of magnetic potentials. In this case, the system of first-order differential equations (2.11)–(2.14) can be reduced to one second-order differential equation.

2.1.2 Magnetic scalar potential

Considering Ampère's law, (2.11), in a current-free region $(\vec{J} = 0)$, we obtain

$$\nabla \times \vec{H} = 0. \tag{2.16}$$

Using this expression and keeping in mind the vector calculus identity $\nabla \times (\nabla \varphi) = 0$, the magnetic scalar potential is introduced as

$$\vec{H} = -\nabla \varphi, \tag{2.17}$$

where φ is the magnetic scalar potential [A]. Substituting (2.17) and (2.10) into (2.13) gives the Poisson equation for the magnetic scalar potential

$$\nabla^2 \varphi = \frac{1}{\mu_{\mathrm{r}}} \nabla \cdot \vec{M}_0. \tag{2.18}$$

This equation describes the behavior of the magnetic scalar potential in a region with internal magnetization, that is, a PM region. For the air region, where the internal magnetization is zero, the equation reduces to the Laplace equation

$$\nabla^2 \varphi = 0. \tag{2.19}$$

It should be explicitly specified that the concept of magnetic scalar potential is valid only in current-free regions.

2.1.3   Magnetic vector potential

Having Gauss's law for magnetism, (2.13), and the vector calculus identity - $\nabla \cdot (\nabla \times \vec{A}) = 0$, the magnetic vector potential is introduced as [39]

$$\vec{B} = \nabla \times \vec{A}, \tag{2.20}$$

where $\vec{A}$ is the vector potential [Wb/m]. Combining the quasistatic Maxwell's equations, (2.11)–(2.13), and the constitutive equation (2.5), under the Coulomb gauge condition ($\nabla \cdot \vec{A} = 0$) results in the Poisson equation for the magnetic vector potential

$$\nabla^2 \vec{A} = -\mu \vec{J} - \mu_0 \nabla \times \vec{M}_0. \tag{2.21}$$

where μ is the permeability [H/m], calculated as $\mu = \mu_{\mathrm{r}} \mu_0$. The Poisson equation describes the behavior of the magnetic vector potential in a region with magnetic field sources. In a source-free region, this equation reduces to the Laplace equation

$$\nabla^2 \vec{A} = 0. \tag{2.22}$$

The current density in (2.21) represents an externally imposed current, which can be exemplified by a winding with current flowing in it.

In an electrically conducting region, the current is caused by the changing magnetic flux penetrating the region. The electric field in this region is expressed by the magnetic vector potential, using (2.12), as

$$\vec{E} = -\frac{\partial \vec{A}}{\partial t}. \tag{2.23}$$

The induced current is introduced by substituting (2.23) into (2.7), which results in

$$\vec{J} = -\sigma \frac{\partial \vec{A}}{\partial t}. \tag{2.24}$$

Then, the Poisson equation can be transformed into a more general governing equation by combining (2.21) and (2.24)

$$\nabla^2 \vec{A} = \mu\sigma \frac{\partial \vec{A}}{\partial t} - \mu\vec{J} - \mu_0 \nabla \times \vec{M_0}. \tag{2.25}$$

When a conducting region, which does not consist of any internal magnetization or external current, is placed in a changing magnetic field, then (2.25) is reduced to the Helmholtz equation

$$\nabla^2 \vec{A} = \mu\sigma \frac{\partial \vec{A}}{\partial t}. \tag{2.26}$$

2.1.4 Second-order vector potential

Three-dimensional electromagnetic problem consideration by means of the magnetic vector potential, $\vec{A}$, in the rectangular coordinate system results in a three-dimensional scalar field, where each of the scalars can be solved separately. Consideration of a similar problem in curvilinear coordinates (e.g. cylindrical or spherical) poses an additional difficulty as the scalar field equations are mutually coupled and cannot be separated [102].

For the Helmholtz and Laplace equations, this inconvenience is overcome by introducing the second-order vector potential (SOVP). Similarly to the magnetic vector potential, the SOVP can be introduced using the Coulomb gauge ($\nabla \cdot \vec{A} = 0$) and the identity - $\nabla \cdot (\nabla \times \vec{W}) = 0$ as

$$\vec{A} = \nabla \times \vec{W}, \tag{2.27}$$

where $\vec{W}$ is the SOVP [Wb]. It is possible to represent $\vec{W}$ by two orthogonal scalar functions as [102]

$$\vec{W} = W_1 \vec{e} + \nabla \times W_2 \vec{e}, \tag{2.28}$$

where W_1 and W_2 are the scalar potential functions, [Wb] and [Wb·m], respectively, and $\vec{e}$ is a unit vector. In the cylindrical coordinate system, $\vec{e}$ is assumed to have an axial component only, which, after combining (2.26), (2.27), and (2.28) results in

$$\nabla^2(\nabla \times (W_1 \vec{e_z} + \nabla \times W_2 \vec{e_z})) = \mu\sigma \frac{\partial}{\partial t} (\nabla \times (W_1 \vec{e_z} + \nabla \times W_2 \vec{e_z})). \tag{2.29}$$

The SOVP, W, consists of two orthogonal scalars, and therefore, separate expressions for these scalars, satisfying the Helmholtz equation, can be written as

$$\nabla^2 W_1 = \mu\sigma \frac{\partial W_1}{\partial t},$$ (2.30)

$$\nabla^2 W_2 = \mu\sigma \frac{\partial W_2}{\partial t}.$$

The obtained equations are the governing equations in conducting regions. For a nonconducting region, the right part of (2.30) is zero, and thus, the governing equations are as follows

$$\nabla^2 W_1 = 0,$$ (2.31)

$$\nabla^2 W_2 = 0.$$

By expressing the flux density by means of the SOVP as

$$\vec{B} = \nabla \times \nabla \times (W_1 \vec{e}_z + \nabla \times W_2 \vec{e}_z) =$$

$$\nabla \times \nabla \times W_1 \vec{e}_z + \nabla \times \nabla(\nabla \cdot W_2 \vec{e}_z) + \nabla \times \nabla^2 W_2 \vec{e}_z,$$ (2.32)

it can be found that W_2 has no contribution to the magnetic flux density in nonconducting regions, because $\nabla^2 W_2 = 0$ and $\nabla \times \nabla(\text{scalar}) = 0$. Thus, (2.31) can be simplified to

$$\nabla^2 W_1 = 0.$$ (2.33)

The magnetic flux density in a vacuum depends only on one scalar, which is also the case with the magnetic scalar potential φ. Using (2.17), (2.27), and (2.20), it is possible to link φ and W_1 as

$$W_1 = -\mu_0 \int \varphi \, \mathrm{d}z.$$ (2.34)

The concept of SOVP is a powerful concept to solve three-dimensional electromagnetic problems in curvilinear coordinate systems. This concept considers modeling of electromagnetic fields in a isotropic material and conducting regions.

2.2   Harmonic modeling

The concept of magnetic potentials allows Maxwell's equations to be transformed into linear second-order partial differential equations (2.21), (2.22), (2.26), (2.30), and (2.31). These equations describe the electromagnetic field behavior in media with distinct electromagnetic properties. Although there are many suitable mathematical techniques to solve these equations, this thesis applies the harmonic
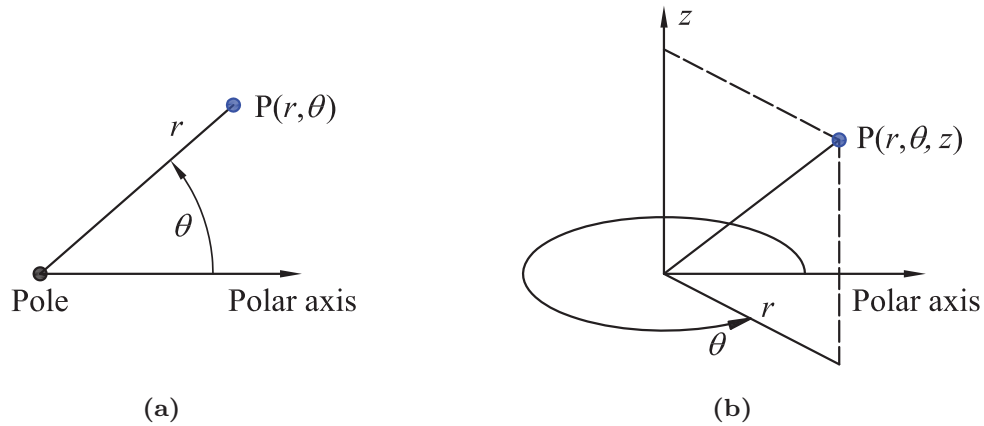
Figure 2.1: General representation of a) polar and b) cylindrical coordinate system.

modeling (HM) technique to derive a solution. This HM is widely used to model electromagnetic fields in electromechanical systems, where the application under consideration is divided into domains with distinct electromagnetic properties. Examples of this are a winding region with imposed current, governed by the Poisson equation, and an air-gap region, governed by the Laplace equation. More specifically, separation of variables is applied in [45]. The solution of a governing equation is defined for each spatial harmonic and contains unknown coefficients. In order to obtain these unknown coefficients, initial and boundary conditions between domains have to be defined. For the regions with magnetic field sources, to comply with the periodic part of the solution, these sources are represented by a Fourier series. With certain assumptions, as discussed further in this chapter, this method is very suitable to derive an application-specific solution of Maxwell's equations.

The application of a rotating slotless machine, as considered in this thesis, required the HM to be performed in either a polar (see Figure 2.1(a)) or a cylindrical (see Figure 2.1(b)) coordinate system. Its specific use depends on the machine properties. The modeled domain of a rotating slotless machine is assumed to be homogeneous and periodical in the circumferential and axial directions, which makes the HM unbound in these directions. In the radial direction, the domain under study is divided into regions, and specific boundary conditions are determined on the interface between the regions. A further important aspect of the HM is the assumed linearity of the problem, meaning that all the electromagnetic properties are assumed to be linear and isotropic. Specifically within slotless PM machines, this justifies the use of superposition and separate modeling of the armature and permanent magnet (PM) fields to accurately describe its electromagnetic behavior.

2.2.1   2D electromagnetic problem

The electromagnetic field modeling of some slotless machines, for instance with toroidal, concentrated, and distributed windings, can be reduced to a two-dimensional (2D) problem. This is explained by the fact that the main magnetic field in the machine can be assumed to contain only two components, namely radial and circumferential ones. Table 2.1 provides the general properties of the armature and PM field modeling in a 2D problem. As it is indicated, the field modeling is carried out by means of the 2D HM in the polar coordinate system. Modeling of

Table 2.1: Modeling framework arrangement of armature and PM field modeling in 2D and 3D problems

	2D problem	**3D problem**
Armature field		
Modeling approach	2D HM	2D and 3D HM
Coordinate system	Polar (r, θ)	Cylindrical (r, θ, z)
Space current components	$\vec{I}_z$	$\vec{I}_z$ and $\vec{I}_\theta$
Source description	1D Fourier series	2D Fourier series
Potential formulation	$\vec{A}$	$\vec{A}$ and $\vec{W}$
Periodicity	θ-direction	θ- and z-directions
PM field		
Modeling approach	2D HM	
Coordinate system	Polar (r, θ)	
Magnetization direction	$\vec{M}_r$ and $\vec{M}_\theta$	
Source description	1D Fourier series	
Potential formulation	$\vec{A}$	
Periodicity	θ-direction	

the electromagnetic field in rotating PM machines by using the 2D HM has been thoroughly considered by numerous researchers, for instance in [38], [46], [85], [114]. The 2D HM has been implemented for slotless PM machines with various winding configurations taking into account the induced eddy currents in the rotor. An overview of the 2D HM in the polar coordinate system is presented in Table 2.2, whereas a more thorough explanation is provided in the following sections of this chapter as indicated in this table.

As stated above, for the sake of convenience, the armature and PM fields are modeled separately. The armature field harmonics caused by a nonsinusoidal winding distribution and nonsinusoidal phase currents induce eddy currents in the rotor of slotless PM machines. However, the PM field in slotless machines, because of the

Table 2.2: Overview of 2D harmonic modeling

Governing equations		Described in
Air (vacuum) region	$\nabla^2 \vec{A}_z = 0$	Section 2.3.1
Winding region	$\nabla^2 \vec{A}_z = -\mu \vec{J}$	Section 2.3.2
PM region	$\nabla^2 \vec{A}_z = -\mu_0 \nabla \times \vec{M}_0$	Section 2.3.3
Conducting region	$\nabla^2 \vec{A}_z = \mu \sigma \dfrac{\partial \vec{A}_z}{\partial t}$	Section 2.3.4
Boundary conditions		
Continuous	$\bar{B}_{r,1} - \bar{B}_{r,2} = 0,$ $\bar{H}_{\theta,1} - \bar{H}_{\theta,2} = 0$	Section 2.5.1
Dirichlet	$\bar{A}_z\|_{r=0}\|_{r\to\infty} = 0$	Section 2.5.2
Magnetic field source		
Current density	$\vec{J} = \bar{J}_z(\theta,t) \cdot \vec{e}_z$	Section 2.6.2
Magnetization	$\vec{M}_0 = \bar{M}_r(\theta) \cdot \vec{e}_r + \bar{M}_\theta(\theta) \cdot \vec{e}_\theta$	Section 2.6.1

absence of permeance variation in the stator over the circumference, induces no eddy currents in the rotor. Hence, while modeling the PM field with the 2D HM, no conducting region is included in the model.

As any other modeling approach, the HM has its limitations on considering certain phenomena, and therefore, some simplifications are introduced. For the 2D HM, the following assumptions are accepted

- Materials are considered isotropic, i.e., the relative permeability and conductivity remain the same in all directions;

- Materials have linear properties, i.e., no saturation is considered;

- Soft-magnetic material (iron) parts are infinitely permeable. Even though it is possible to model the iron parts as regions with constant permeability, in order to reduce the calculation time, iron parts are neglected;

- Only balanced 3-phase currents in the windings are considered;

- The reaction fields of skin and proximity effects in conductors and eddy currents in iron are not taken into account.

2.2.2 3D electromagnetic problem

Further complexity is introduced in some types of slotless PM machines, where the conductors within the windings are skewed. These are commonly defined as Faulhaber, rhombic, and diamond windings. Owing to the presence of circumferential space current components, such windings should be treated as 3D electromagnetic problems. These current components, together with the axial ones, produce all three field components, namely the radial, circumferential, and axial ones. In Table 2.1, a description of 3D field modeling in rotating slotless PM machines is presented. It demonstrates that to model the armature field, a combination of the 2D and 3D HM in the cylindrical coordinate system is proposed.

As described, the 2D HM obtains the electromagnetic field solution by means of the vector potential, $\vec{A}$. The separation of variables for a 3D problem in the cylindrical coordinate system poses a difficulty for the governing equations describing the vector potential (see section 2.1.4), and therefore, in the 3D HM, the governing equations are described by means of the second order vector potential (SOVP), $\vec{W}$. The concept of the SOVP to model 3D electromagnetic problems including the induced eddy currents has previously been implemented by a few researchers, in particular in [107], [73], [110], [87], and [58]. However, the proposed models do not provide an option to implement the 3D HM for a wide range of winding geometries. Application of the 2D Fourier series allows to describe the space distribution of the current in windings with complex geometries, and thereby, extends the implementation of the HM. The space current distribution, which is obtained by the 2D Fourier series, contains current components with 1D ($f(z)$) and 2D ($f(\theta, z)$) dependences. Therefore, the 2D HM is employed to model the armature field produced by a 1D Fourier series of current distribution, whereas the 3D HM is used for a 2D Fourier series of current distribution. Considering the modeling of the PM field, it is assumed to be solely a 2D problem with magnetization vector components in the radial and circumferential directions.

An overview of the 3D HM is provided in Table 2.3, whereas a detailed explanation of the governing equation solutions, boundary conditions, and description of the linear current density are given as stated in the table. Similarly to any other modeling techniques, the 3D HM has assumptions of its own. These assumptions include those of the 2D HM and additionally, the following ones:

- The winding current is modeled by linear current density, which assumes an infinitely thin winding, placed on a boundary;

- The model has periodicity in both axial and circumferential directions;

- The stator iron and rotor lengths are equal to the axial periodicity.

Table 2.3: Overview of 3D harmonic modeling

Governing equations		Described in
Air region	$\nabla^2 \bar{W} = 0$	Section 2.4.2
Conducting region	$\nabla^2 \bar{W}_1 = \mu\sigma \dfrac{\partial \bar{W}_1}{\partial t},$ $\nabla^2 \bar{W}_2 = \mu\sigma \dfrac{\partial \bar{W}_2}{\partial t}$	Section 2.4.1
Boundary conditions		
Continuous	$\bar{B}_{r,1} - \bar{B}_{r,2} = 0,$ $\bar{H}_{\theta,1} - \bar{H}_{\theta,2} = \bar{K}_\theta,$ $\bar{H}_{z,1} - \bar{H}_{z,2} = \bar{K}_z,$ $\bar{E}_{z,1} - \bar{E}_{z,2} = 0 \text{ or } \bar{E}_{\theta,1} - \bar{E}_{\theta,2} = 0$	Section 2.5.1
Dirichlet	$\bar{W}_1\vert_{r=0}\vert_{r\to\infty} = 0,$ $\bar{W}_2\vert_{r=0}\vert_{r\to\infty} = 0$	Section 2.5.2
Source description		
Linear current density	$\vec{\bar{K}} = \bar{K}_z \vec{e}_z + \bar{K}_\theta \vec{e}_\theta$	Section 2.6.3

2.3 Solution of magnetic vector potential in polar coordinates

This section presents the solution of the vector potential in the polar coordinate system (r, θ) for different governing equations. In the polar coordinates, the magnetic field has only radial and circumferential components, and thus, according to its definition, the vector potential has only the axial component. Additionally, it should be mentioned that for modeling of the eddy-current phenomenon, the complex representation of the vector potential is beneficial, as it facilitates the solution of the Helmholtz equation.

2.3.1 Magnetic vector potential in a vacuum

The governing equation for an air-gap (vacuum) region by means of vector potential is given by the Laplace equations (2.22). In terms of complex vector potential, it is written as

$$\nabla^2 \bar{A}_z \vec{e}_z = 0, \tag{2.35}$$

where $\bar{A}_z$ is the complex axial component of the vector potential [Wb/m]. By separation of variables, the solution of the Laplace equation for any harmonic

order takes the form [38]

$$\bar{A}_z(r, \theta, t, \nu) = (\bar{C}(\nu)r^{-\nu} + \bar{D}(\nu)r^\nu)e^{j(\nu\theta + \omega_r t)}, \tag{2.36}$$

where $\bar{C}$ and $\bar{D}$ are complex unknown coefficients, ν is the space harmonic order, and ω_r is the relative angular velocity between the medium under consideration and magnetic field [rad/s]. The solution consists of a periodic part containing the exponential function. Using (2.20), the magnetic flux density for the case of axial vector potential can be found by

$$\vec{B} = \frac{1}{r}\frac{\partial \bar{A}_z}{\partial \theta}\vec{e}_r - \frac{\partial \bar{A}_z}{\partial r}\vec{e}_\theta. \tag{2.37}$$

2.3.2 Magnetic vector potential in a region with imposed current

The equation that describes the behavior of the vector potential in a region with imposed current is given by the Poisson equation, which is expressed in the complex form as

$$\nabla^2 \bar{A}_z \vec{e}_z = -\mu \bar{J}\vec{e}_z. \tag{2.38}$$

The solution of any Poisson's equation consists of two parts: a homogeneous solution and a particular solution. The homogeneous solution is the solution of the Laplace equation (2.36). The periodic part of the particular solution is the same as that of the Laplace equation, and therefore, the solution of the governing equation in the winding region can be written as [38]

$$\bar{A}_z(r, \theta, t, \nu) = \left(\bar{C}(\nu)r^{-\nu} + \bar{D}(\nu)r^\nu + \hat{A}_{\text{part}}(\nu)\right)e^{j(\nu\theta + \omega_r t)}, \tag{2.39}$$

where

$$\hat{A}_{\text{part}}(\nu) = \begin{cases} -\dfrac{\mu\hat{J}_z}{2\nu}r^2\ln(r), & \text{for } \nu^2 = 4, \\ \dfrac{\mu\hat{J}_z}{\nu^2 - 4}r^2, & \text{else}, \end{cases} \tag{2.40}$$

in which $\hat{J}_z$ is the amplitude of the current density [A/m^2]. In this case the axial current density component is defined as

$$J_z(\theta, t, \nu) = \hat{J}_z e^{j(\nu\theta + \omega_r t)}. \tag{2.41}$$

2.3.3 Magnetic vector potential in a region with internal magnetization

A region with internal magnetization assumes Poisson's type of equation for the magnetic vector potential. For the 2D case, the equation is given in the complex form by

$$\nabla^2 \bar{A}_z \vec{e}_z = -\mu_0 \nabla \times \vec{\bar{M}}_0(\theta). \tag{2.42}$$

The solution of (2.42) consists of homogeneous and particular solutions and can be written as

$$\bar{A}_z(r, \theta, t, \nu) = \left(\bar{C} r^{-\nu} + \bar{D} r^{\nu} + \bar{A}_{\text{part}}(r, \nu) \right) e^{j(\nu\theta + \omega_r t)}. \tag{2.43}$$

According to (2.42), it is evident that the internal magnetization contains only radial, M_{0r}, and circumferential, $M_{0\theta}$, magnetization components, which are represented as

$$\vec{\bar{M}}_0(\theta, t, \nu) = \bar{M}_{0r}(\theta)\vec{e}_r + \bar{M}_{0\theta}(\theta)\vec{e}_\theta = (\bar{M}_{ra}\vec{e}_r + \bar{M}_{\theta a}\vec{e}_\theta)e^{j(\nu\theta + \omega_r t)}, \tag{2.44}$$

where $\bar{M}_{ra}$ and $\bar{M}_{\theta a}$ are the aperiodic parts of the radial and circumferential magnetization distributions [A/m], respectively. Taking into account (2.44), the aperiodic part of the particular solution can be derived as [85]

$$\bar{A}_{\text{part}}(r, \nu) = \begin{cases} \dfrac{\mu_0 \left(j\nu \bar{M}_{ra} - \bar{M}_{\theta a} \right)}{2} r \ln(r), & \text{for } \nu = \pm 1, \\ \dfrac{\mu_0 \left(j\nu \bar{M}_{ra} - \bar{M}_{\theta a} \right)}{1 - \nu^2} r, & \text{else.} \end{cases} \tag{2.45}$$

2.3.4 Magnetic vector potential in a conducting medium

In a conducting medium, the governing equation in terms of vector potential is defined by the Helmholtz equation, (2.26). For the mechanically moving conducting media this equation is incomplete and should be updated with the motional emf. An example of this can be a mechanically rotating rotor in a magnetic field. Then, the governing equation for the moving conducting region in the cylindrical coordinates in terms of vector potential is given as

$$\nabla^2 \bar{A}_z \vec{e}_z = \mu\sigma \left(\frac{\partial \bar{A}_z \vec{e}_z}{\partial t} + \vec{V} \times \nabla \times \bar{A}_z \vec{e}_z \right) = \mu\sigma \left(\frac{\partial \bar{A}_z \vec{e}_z}{\partial t} + \Omega \frac{\partial \bar{A}_z \vec{e}_z}{\partial \theta} \right), \tag{2.46}$$

where V is the linear speed [m/s], and Ω is the mechanical angular velocity [rad/s]. However, there is a more convenient approach to take account of the motional emf.

The approach is based on representing the magnetic vector potential in a reference frame of the conducting region as it is shown in Section 2.6.4, which makes the conducting region mechanically stationary. This helps to avoid consideration of the motional emf in the governing equation.

The resulting governing equation in the conducting region takes into account the induced eddy currents caused by the time-varying magnetic field and the reaction field produced by the induced eddy currents, and is written in the complex form as [46]

$$\nabla^2 \bar{A}_{\mathrm{z}} \vec{e}_{\mathrm{z}} = \mu\sigma \frac{\partial \bar{A}_{\mathrm{z}} \vec{e}_{\mathrm{z}}}{\partial t}. \tag{2.47}$$

The solution of this equation can be found as

$$\bar{A}_{\mathrm{z}}(r,\theta,t,\nu) = \begin{cases} (\bar{C} I_\nu(\beta r) + \bar{D} K_\nu(\beta r)) \mathrm{e}^{\mathrm{j}(\nu\theta + \omega_{\mathrm{r}} t)}, & \text{for } \beta \neq 0, \\ (\bar{C} r^{-\nu} + \bar{D} r^\nu) \mathrm{e}^{\mathrm{j}(\nu\theta + \omega_{\mathrm{r}} t)}, & \text{for } \beta = 0, \end{cases} \tag{2.48}$$

$$\beta^2 = \mathrm{j}\mu_{\mathrm{r}}\mu_0 \sigma \omega_{\mathrm{r}},$$

where I and K are the modified Bessel functions of the first and second kind.

2.4 Solution of magnetic second-order vector potential in cylindrical coordinates

To model the 3D electromagnetic field in the cylindrical coordinate system (r, θ, z) (see Figure 2.1(b)), the concept of the SOVP is applied. This section presents the solutions of the SOVP for the Laplace and Helmholtz equations, which are found by the separation of variables. In analogy to the vector potential, to facilitate the solution of the Helmholtz equation, the part of the solution of the SOVP that contains time dependence is represented using exponential functions.

2.4.1 Second-order vector potential in a conducting medium

As it was previously explained, the second-order vector potential (SOVP) is expressed by two orthogonal scalars, W_1 and W_2. Owing to this representation, the governing equations in a conducting region result in two Helmholtz equations of these two scalars, which are given in the complex form as

$$\nabla^2 \bar{W}_1 = \mu\sigma \frac{\partial \bar{W}_1}{\partial t}, \tag{2.49}$$

$$\nabla^2 \bar{W}_2 = \mu\sigma \frac{\partial \bar{W}_2}{\partial t}.$$

The solutions of these equations can be obtained independently. In a general form, the solution of these scalars for any ν is given as [110]

$$
\begin{aligned}
\bar{W}_1 =& [(\bar{C}_1 I_\nu(\xi_1 r) + \bar{D}_1 K_\nu(\xi_1 r))(\bar{F}_1 \cos(\lambda_1 z) + \bar{G}_1 \sin(\lambda_1 z)) + \\
& (\bar{S}_1 J_\nu(\xi_1 r) + \bar{T}_1 Y_\nu(\xi_1 r)) \cdot (\bar{V}_1 \cosh(\lambda_2 z) + \bar{X}_1 \sinh(\lambda_2 z))]e^{j(\nu\theta + \omega_r t)},
\end{aligned}
$$
(2.50)

$$
\begin{aligned}
\lambda_1^2 &= \xi_1^2 - \beta^2, \\
\lambda_2^2 &= \xi_1^2 + \beta^2, \\
\beta^2 &= j\mu_r \mu_0 \sigma \omega_r,
\end{aligned}
$$

$$
\begin{aligned}
\bar{W}_2 =& [(\bar{C}_2 I_\nu(\xi_2 r) + \bar{D}_2 K_\nu(\xi_2 r))(\bar{F}_2 \cos(\eta_1 z) + \bar{G}_2 \sin(\eta_1 z)) + \\
& (\bar{S}_2 J_\nu(\xi_2 r) + \bar{T}_2 Y_\nu(\xi_2 r)) \cdot (\bar{V}_2 \cosh(\eta_2 z) + \bar{X}_2 \sinh(\eta_2 z))]e^{j(\nu\theta + \omega_r t)},
\end{aligned}
$$
(2.51)

$$
\begin{aligned}
\eta_1^2 &= \xi_2^2 - \beta^2, \\
\eta_2^2 &= \xi_2^2 + \beta^2,
\end{aligned}
$$

where λ and η are spatial frequencies in the axial direction [m^{-1}], J and Y are Bessel functions of the first and second kind, and C, D, F, G, S, T, V, and X are unknown constants. Using (2.27) and (2.28), the vector potential in the conducting region can be written as

$$
\vec{A} = \left(\frac{1}{r} \frac{\partial \bar{W}_1}{\partial \theta} + \frac{\partial^2 \bar{W}_2}{\partial r \partial z} \right) \vec{e}_r + \left(\frac{1}{r} \frac{\partial^2 \bar{W}_2}{\partial \theta \partial z} - \frac{\bar{W}_1}{\partial r} \right) \vec{e}_\theta + \left(\frac{\partial^2 \bar{W}_2}{\partial z^2} - \beta^2 \bar{W}_2 \right) \vec{e}_z.
$$
(2.52)

Substituting the expression of the vector potential into (2.20) results in an expression of the flux density inside the conducting region, which is written as

$$
\vec{B} = \left(\frac{\partial^2 \bar{W}_1}{\partial r \partial z} - \frac{\beta^2}{r} \frac{\partial \bar{W}_2}{\partial \theta} \right) \vec{e}_r + \left(\frac{1}{r} \frac{\partial^2 \bar{W}_1}{\partial \theta \partial z} + \beta^2 \frac{\bar{W}_2}{\partial r} \right) \vec{e}_\theta + \left(\frac{\partial^2 \bar{W}_1}{\partial z^2} - \beta^2 \bar{W}_1 \right) \vec{e}_z.
$$
(2.53)

2.4.2 Second-order vector potential in air

In an air region, the SOVP is given only by one scalar because the other scalar does not contribute to the flux density. Therefore, the governing equation in an air region is given in the complex form as

$$
\nabla^2 \bar{W} = 0.
$$
(2.54)

The solution of the scalar is written as [110]

$$
\begin{aligned}
\bar{W} =& [(\bar{C}I_\nu(\zeta r) + \bar{D}K_\nu(\zeta r))(\bar{F}\cos(\zeta z) + \bar{G}\sin(\zeta z)) + \\
& (\bar{S}J_\nu(\zeta r) + \bar{T}Y_\nu(\zeta r))(\bar{V}\cosh(\zeta z) + \bar{X}\sinh(\zeta z))]e^{j(\nu\theta + \omega_r t)}.
\end{aligned}
\tag{2.55}
$$

The expression for the flux density in the air region can be derived from (2.53) by setting $\bar{W}_2$ to zero, and is given by

$$
\vec{B} = \frac{\partial^2 W}{\partial r \partial z}\vec{e}_r + \frac{1}{r}\frac{\partial^2 W}{\partial\theta\partial z}\vec{e}_\theta + \frac{\partial^2 W}{\partial z^2}\vec{e}_z.
\tag{2.56}
$$

2.5 Boundary conditions

The solutions of the governing equations (2.36), (2.39), (2.43), (2.48), (2.50), (2.51), and (2.55) contain unknown coefficients. These unknown coefficients are calculated by setting boundary conditions between the regions under consideration and solving the system of linear equations, as stated in [30].

2.5.1 Continuous boundary conditions

The first continuous boundary condition is determined by Gauss's law for magnetism. This implies that the normal components of the magnetic flux densities of different regions on the boundary are equal. Mathematically, this is expressed as

$$
\vec{n} \cdot (\vec{B}_1 - \vec{B}_2) = 0,
\tag{2.57}
$$

where $\vec{n}$ is surface normal and $\vec{B}_1$ and $\vec{B}_2$ are flux densities of two interfacing regions. The following boundary condition results from Ampère's law, which states that on the boundary of two regions, the tangential components of magnetic field strength are continuous and written as

$$
\vec{n} \times (\vec{H}_1 - \vec{H}_2) = \vec{K},
\tag{2.58}
$$

where $\vec{K}$ is the linear current density [A/m], and $\vec{H}_1$ and $\vec{H}_2$ are magnetic field strengths in two regions on the boundary obtained by (2.10). The third boundary condition results from Faraday's law. This condition states that on the boundary of two conducting regions, the tangential components of the electrical field strength of each region are equal and expressed as

$$
\vec{n} \times (\vec{E}_1 - \vec{E}_2) = 0,
\tag{2.59}
$$

where $\vec{E}_1$ and $\vec{E}_2$ are the electric field strengths of two regions on the boundary. It must be noted, however, that on the boundary of two conducting regions, it suffices

to apply this boundary condition only for one component of the electrical field. The boundary condition of the other electrical field component is met automatically. This statement results from the continuity equation (2.15), keeping in mind the conservation absence of free charge in the system. This statement can also be proven by Gauss's law. Therefore, on the boundary of two conducting regions, the field is defined by three conditions for the magnetic field and one for the electrical field.

2.5.2 Dirichlet boundary condition

The Dirichlet boundary condition specifies the solution of a differential equation along the boundary. This value can be given by a known function or a constant. For the regions that are not enclosed by another region from the outer boundary, the solution of the governing equation should be zero when r is approaching infinity as the magnetic field should also be zero. Additionally, the solution is zero when r is zero. Mathematically, for the 2D HM this can be summarized as

$$\bar{A}_z|_{r=0}|_{r\to\infty} = 0, \tag{2.60}$$

and for the 3D HM as

$$\bar{W}_1|_{r=0}|_{r\to\infty} = 0,$$
$$\bar{W}_2|_{r=0}|_{r\to\infty} = 0. \tag{2.61}$$

2.6 Magnetic field source description

The definition of the magnetic field sources in the harmonic modeling (HM), for the sake of convenience, should comply with the solutions of the magnetic field in the modeled regions. The periodical part of the solutions is represented by an exponential function, and therefore, it is logical also to express the magnet field sources by complex exponential functions. This can be perfectly achieved by using a Fourier series to describe the magnetic field source. The Fourier series is able to express any periodic function as a summation of sinusoidal or exponential functions with the corresponding amplitudes and frequencies [29]. This approach results in an approximation of the original function, the accuracy of which is dependent on the summation limits. However, the original signal can never be obtained because of Gibb's phenomenon, which causes oscillation near the rapid edges of the signal [34].

In the case of 2D HM, the one-dimensional (1D) Fourier series is applied to describe the PM magnetization and the winding current density distributions. 2D Fourier series is used to express the linear current density distribution, which is

then applied to the 3D HM. It should be noted that only sources without DC components are considered. This assumption is valid for the majority of the HM models of AC machines.

2.6.1   Magnetization distribution

Because this thesis deals only with rotating electrical PM machines, it is assumed that the magnetization of the magnet is constant along the axial direction. Therefore, a 2D approximation of the PM magnetic field can be used without introducing a large error. As it was mentioned previously, for the 2D and 3D cases, the magnetization is assumed to contain only the radial and circumferential components (see (2.44)). The radial and circumferential magnetization components obtained by the complex Fourier series are given by the following expressions

$$\bar{M}_{0r} = \sum_{\nu=-\infty}^{\infty} \bar{M}_{ra} e^{j\nu\theta}, \tag{2.62}$$

$$\bar{M}_{0\theta} = \sum_{\nu=-\infty}^{\infty} \bar{M}_{\theta a} e^{j\nu\theta},$$

where

$$\bar{M}_{ra} = \frac{1}{2\pi} \int_{-\pi}^{\pi} \bar{M}_{0r} e^{-j\nu\theta} d\theta, \tag{2.63}$$

$$\bar{M}_{\theta a} = \frac{1}{2\pi} \int_{-\pi}^{\pi} \bar{M}_{0\theta} e^{-j\nu\theta} d\theta.$$

To translate the series into the real number domain, the real part of the expressions should be extracted to obtain the sine term, and the imaginary part to obtain the cosine term.

2.6.2   Current density distribution for a 2D problem

To complete the solution of the vector potential in a region with imposed current, or in the case of electrical machines in the winding region, an expression of the current density distribution has to be derived. The winding current density distribution can be derived by superimposing the current density distributions of all three phases. A phase current density distribution of a winding can be obtained as

$$J_{z,ph}(\theta, t) = \frac{N i_{ph}(t)}{s(r_{wo}^2 - r_{wi}^2)/2} f_w(\theta), \tag{2.64}$$
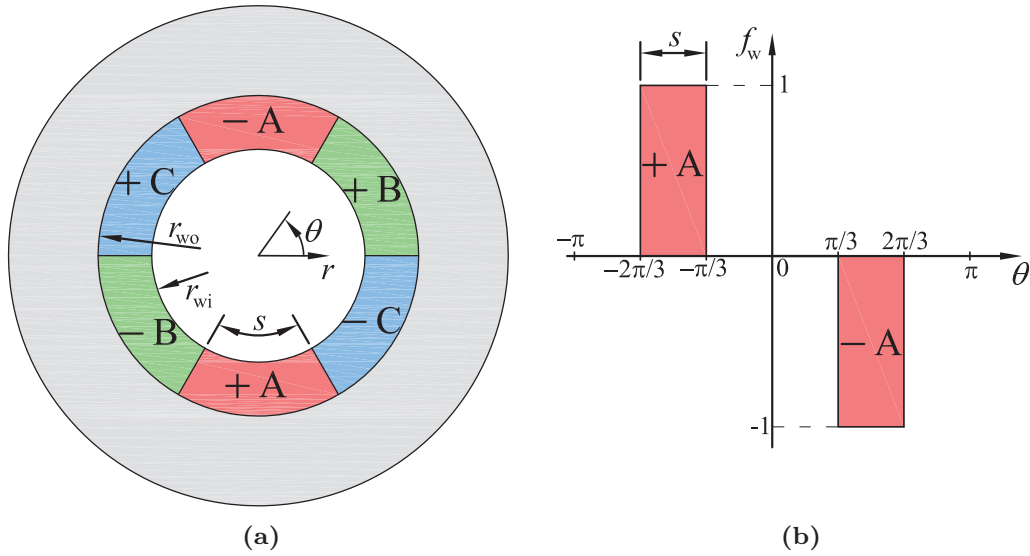
Figure 2.2: a) General representation of an iron core and inserted distributed winding, b) distribution function of phase A.

where N is the number of turns in series per stator phase winding, i_{ph} is the phase current [A], s is the phase spread in circumference [rad], r_{wi} and r_{wo} are the inner and outer winding radii [m], respectively, and f_{w} is the distribution function, the amplitude of which is 1. An example of a phase distribution function of the slotless stator with a distributed winding is given in Fig. 2.2. The distribution function of a phase coil can be derived using the Fourier series as

$$f_{\mathrm{w}}(\theta) = \sum_{\nu=1}^{\infty} \left(c_{\mathrm{s}}(\nu) \sin(\nu\theta) + c_{\mathrm{c}}(\nu) \cos(\nu\theta) \right), \tag{2.65}$$

$$c_{\mathrm{s}}(\nu) = \frac{1}{\pi} \int_{-\pi}^{\pi} f_{\mathrm{w}}(\theta) \sin(\nu\theta) \, d\theta,$$

$$c_{\mathrm{c}}(\nu) = \frac{1}{\pi} \int_{-\pi}^{\pi} f_{\mathrm{w}}(\theta) \cos(\nu\theta) \, d\theta.$$

Because the focus of this study is on three-phase rotating machines only, the phase coils are mutually shifted in space by an electrical angle of $2\pi/3$, and the phase

currents are given as

$$i_{\mathrm{ph}}(t) = \sum_{k=1}^{\infty} \hat{I}(k) \cos(k(\omega t + x)), \tag{2.66}$$

$$x = \left(0, \frac{2\pi}{3}, \frac{4\pi}{3}\right),$$

where k is the time harmonic order. Using (2.64) and (2.66) and taking into account the spatial distribution of the phases, the current density distribution for a three-phase system can be written as

$$J_{\mathrm{z}}(\theta, t) = \sum_{\substack{k=1 \\ \nu=1}}^{\infty} \frac{N}{s(r_{\mathrm{wo}}^2 - r_{\mathrm{wi}}^2)/2} \left[\hat{I}(k) \cos(k\omega t)\, (c_{\mathrm{s}}(\nu) \sin(\nu\theta) + c_{\mathrm{c}}(\nu) \cos(\nu\theta)) + \right.$$

$$\hat{I}(k) \cos(k(\omega t + \frac{2\pi}{3}))(c_{\mathrm{s}}(\nu) \sin(\nu(\theta + \frac{2\pi}{3})) + c_{\mathrm{c}}(\nu) \cos(\nu(\theta + \frac{2\pi}{3}))) +$$

$$\left. \hat{I}(k) \cos(k(\omega t + \frac{4\pi}{3}))(c_{\mathrm{s}}(\nu) \sin(\nu(\theta + \frac{4\pi}{3})) + c_{\mathrm{c}}(\nu) \cos(\nu(\theta + \frac{4\pi}{3}))) \right]. \tag{2.67}$$

The above equation can be simplified to

$$J_{\mathrm{z}}(\theta, t) = \sum_{\substack{k=1 \\ L=-\infty}}^{\infty} \frac{3}{2} \frac{N\hat{I}(k)}{s(r_{\mathrm{wo}}^2 - r_{\mathrm{wi}}^2)/2} \cdot$$

$$(c_{\mathrm{s}}(L, k) \sin((3L - k)\theta + k\omega t) + c_{\mathrm{c}}(L, k) \cos((3L - k)\theta + k\omega t)), \tag{2.68}$$

where L represents the set of all integer numbers and in c_{s} and c_{c} all ν should be replaced by $(3L - k)$. In order for the current density distribution to comply with the solution of vector potential in the winding regions, (2.39) and (2.68) should be rewritten in the complex form as

$$\bar{J}_{\mathrm{z}}(\theta, t) = \sum_{\substack{k=1 \\ L=-\infty}}^{\infty} \frac{3}{2} \frac{N\hat{I}(k)}{s(r_{\mathrm{wo}}^2 - r_{\mathrm{wi}}^2)/2} \cdot$$

$$\left(c_{\mathrm{s}}(L, k) \mathrm{e}^{\mathrm{j}((3L-k)\theta + k\omega t)} + c_{\mathrm{c}}(L, k) \mathrm{e}^{\mathrm{j}((3L-k)\theta + k\omega t)} \right). \tag{2.69}$$

The complex form of the current density can be translated back to the real number domain using Euler's equation, which is given as

$$\mathrm{e}^{\mathrm{j}x} = \cos(x) + \mathrm{j}\sin(x), \tag{2.70}$$

and thus, the trigonometric functions can be written as

$$\cos(x) = \mathrm{Re}(\mathrm{e}^{\mathrm{j}x}), \tag{2.71}$$

$$\sin(x) = \mathrm{Im}(\mathrm{e}^{\mathrm{j}x}).$$

2.6.3 Linear current density distribution for a 3D problem

Modeling of regions with imposed currents in the 3D HM does not seem feasible by means of the second-order vector potential [107]. Therefore, the winding region is replaced by an air region, and the current density is replaced by the linear current density, which is included in a boundary condition as shown in (2.58). A slotless PM machine requires a 3D consideration if the winding current distribution contains two space vector components. In the case of radial field rotating machines, these two components are usually the axial and circumferential ones. The additional, circumferential, component in slotless machines is introduced by skewing of the winding conductors, as it can be clearly distinguished in the example of the Faulhaber winding shown in Figure 2.3. In this case, the linear current density can be written as

$$\vec{K} = K_z\vec{e}_z + K_\theta\vec{e}_\theta, \tag{2.72}$$

where K_z and K_θ are the axial and circumferential linear current density components, respectively, [A/m].
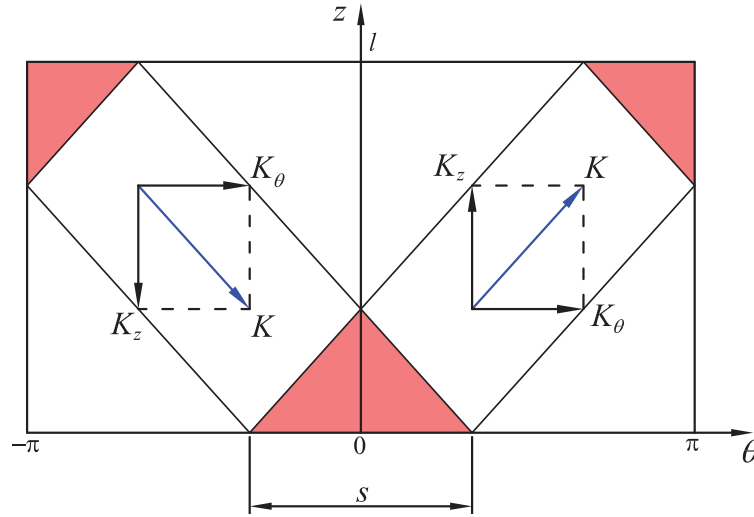
Figure 2.3: Phase coil of a Faulhaber winding represented by means of two current-carrying strips. K indicates the linear current density of each strip, and K_z and K_θ indicate the axial and circumferential components, respectively.

Axial component of linear current density

The axial component of the linear current density in a single phase can be obtained as

$$K_z(\theta, z, t) = \frac{Ni(t)}{sr} f_{wz}(\theta, z), \tag{2.73}$$

where r is the radius at which the linear current density is defined [m], and f_{wz} is the axial distribution function dependent on the geometry of the winding. This axial distribution function can be generally expressed by a 2D Fourier series as

$$
\begin{aligned}
f_{wz}(\theta, z) = \sum_{\substack{\nu=0 \\ m=0}}^{\infty} \Big[& c_{ssz}(\nu, m) \sin(\omega_\theta \theta) \sin(\omega_z z) + \\
& c_{scz}(\nu, m) \sin(\omega_\theta \theta) \cos(\omega_z z) + \\
& c_{csz}(\nu, m) \cos(\omega_\theta \theta) \sin(\omega_z z) + \\
& c_{ccz}(\nu, m) \cos(\omega_\theta \theta) \cos(\omega_z z) \Big], \\
\omega_\theta =& \frac{\nu 2\pi}{\tau_\theta}, \\
\omega_z =& \frac{m 2\pi}{\tau_z},
\end{aligned}
\tag{2.74}
$$

where ω_θ and ω_z are the spatial frequencies in the θ- and z-directions, m is the axial harmonic order, and τ_θ and τ_z the periodicities in the θ- and z-directions. The minimum value of the τ_z equals to the winding length, l. In some cases, to take into account end effects caused by unequal geometrical and physical properties the value of τ_z can be increased. The example of such a case is shown in Section 2.7.2, where the value of τ_z is set to $2l$ in order to take into consideration the magnetic field caused by the return path of the rotor eddy-currents. The coefficients c_{ssz}, c_{scz}, c_{csz}, and c_{ccz} are derived by the following integrals

$$c_{ssz}(\nu, m) = \frac{\kappa}{4\tau_\theta\tau_z} \int_0^{\tau_z} \int_0^{\tau_\theta} f_{wz}(\theta, z) \sin(\omega_\theta \theta) \sin(\omega_z z) \, d\theta dz,$$

$$c_{scz}(\nu, m) = \frac{\kappa}{4\tau_\theta\tau_z} \int_0^{\tau_z} \int_0^{\tau_\theta} f_{wz}(\theta, z) \sin(\omega_\theta \theta) \cos(\omega_z z) \, d\theta dz,$$

$$c_{csz}(\nu, m) = \frac{\kappa}{4\tau_\theta\tau_z} \int_0^{\tau_z} \int_0^{\tau_\theta} f_{wz}(\theta, z) \cos(\omega_\theta \theta) \sin(\omega_z z) \, d\theta dz,$$

$$c_{ccz}(\nu, m) = \frac{\kappa}{4\tau_\theta\tau_z} \int_0^{\tau_z} \int_0^{\tau_\theta} f_{wz}(\theta, z) \cos(\omega_\theta \theta) \cos(\omega_z z) \, d\theta dz, \tag{2.75}$$

where

$$
\kappa = \begin{cases}
4, & \text{for } \nu > 0, \ m > 0 \\
2, & \text{for } \nu = 0, \ m > 0 \\
2, & \text{for } \nu > 0, \ m = 0 \\
1, & \text{for } \nu = 0, \ m = 0
\end{cases}.
\tag{2.76}
$$

The integral limits in (2.75) can be set by linear equations to describe winding skewing [88].

Assuming three-phase windings, meaning that the phase currents and coils are shifted by $2\pi/3$, and substituting (2.66) and (2.74) into (2.73) results in a 2D Fourier series representation of the axial linear current density

$$
\begin{aligned}
K_z(\theta, z, t) = \sum_{\substack{m=0 \\ k=1 \\ L=-\infty}}^{\infty} \Big[& \hat{K}_{ssz}(m, k, L) \sin((3L-k)\theta + k\omega t) \sin(\omega_z z) + \\
& \hat{K}_{scz}(m, k, L) \sin((3L-k)\theta + k\omega t) \cos(\omega_z z) + \\
& \hat{K}_{csz}(m, k, L) \cos((3L-k)\theta + k\omega t) \sin(\omega_z z) + \\
& \hat{K}_{ccz}(m, k, L) \cos((3L-k)\theta + k\omega t) \cos(\omega_z z) \Big],
\end{aligned}
\tag{2.77}
$$

where $\hat{K}_{ssz}$, $\hat{K}_{scz}$, $\hat{K}_{csz}$, and $\hat{K}_{ccz}$ are the amplitudes of the Fourier series components [A/m], which are determined as

$$
\hat{K}_z(m, k, L) = \frac{N\hat{I}(k)}{sr} c_z(\nu, m).
$$

Since the solutions of the governing equations (2.50), (2.51), and (2.55) are in the complex form, the linear current density expression (2.77), for simplicity, is also transformed into the complex form as

$$
\begin{aligned}
\bar{K}_z(\theta, z, t) = \sum_{\substack{m=0 \\ k=1 \\ L=-\infty}}^{\infty} \Big[& \hat{K}_{ssz}(m, k, L) e^{j((3L-k)\theta + k\omega t)} \sin(\omega_z z) + \\
& \hat{K}_{scz}(m, k, L) e^{j((3L-k)\theta + k\omega t)} \cos(\omega_z z) + \\
& \hat{K}_{csz}(m, k, L) e^{j((3L-k)\theta + k\omega t)} \sin(\omega_z z) + \\
& \hat{K}_{ccz}(m, k, L) e^{j((3L-k)\theta + k\omega t)} \cos(\omega_z z) \Big].
\end{aligned}
\tag{2.78}
$$

This complex linear current density can be transformed from the complex domain back into (2.77) using (2.71).

Circumferential component of linear current density

The circumferential component of the linear current density can be derived using the same procedure, or alternatively from the continuity equation, (2.15), as

$$\frac{\partial K_z}{\partial z} = -\frac{1}{r}\frac{\partial K_\theta}{\partial \theta}. \tag{2.79}$$

However, there is no need to derive the circumferential component of the linear current density for the field calculation. On the boundary with linear current density, the transition conditions for the normal and single tangential (axial or circumferential) magnetic field components are satisfied, and the second tangential component is also satisfied [42]. This statement results from the continuity equation (2.15) and Ampère's law.

2.6.4   Rotor reference frame

Current density (2.69) and linear current density (2.78) are given in the stator reference frame, where the field angular velocity is defined by the angular frequency of the phase current. To take account of the motion emf, which causes rotor eddy currents caused by the mechanical movement of the rotor, these sources should be represented in the rotor reference frame. In this case, only magnetic field harmonics traveling with respect to the rotor will cause rotor eddy currents.

The angular position of the rotor can be linked to the angular position of the stator through the angular velocity of the rotor as

$$\theta = \theta_r + \omega t, \tag{2.80}$$

where θ_r is the angular position in the rotor reference frame [rad]. This equation is valid for all pole pair combinations. Then, substituting (2.80) into (2.69) results in the expression of current density in the rotor reference frame:

$$\bar{J}_z(\theta_r, t) = \sum_{\substack{k=1 \\ L=-\infty}}^{\infty} \frac{N\hat{I}}{s(r_{wo}^2 - r_{wi}^2)/2}.$$
$$\left(c_s(L,k)e^{j((3L-k)\theta_r + 3L\omega t)} + c_c(L,k)e^{j((3L-k)\theta_r + 3L\omega t)} \right). \tag{2.81}$$

In the same manner, the expression for the linear current density in the rotor

reference frame can be obtained as

$$
\bar{K}_z(\theta_r, z, t) = \sum_{\substack{m=0 \\ k=1 \\ L=-\infty}}^{\infty} \Big[\hat{K}_{ss}(m, k, L) e^{j((3L-k)\theta_r + 3L\omega t)} \sin(\omega_z z) +
$$
$$
\hat{K}_{sc}(m, k, L) e^{j((3L-k)\theta_r + 3L\omega t)} \cos(\omega_z z) +
$$
$$
\hat{K}_{cs}(m, k, L) e^{j((3L-k)\theta_r + 3L\omega t)} \sin(\omega_z z) +
$$
$$
\hat{K}_{cc}(m, k, L) e^{j((3L-k)\theta_r + 3L\omega t)} \cos(\omega_z z) \Big].
$$

(2.82)

2.7 Model implementation and validation

2.7.1 Geometry and physics of the benchmark machines

To validate the HM discussed in the previous sections, it is implemented for benchmark slotless PM machines. A schematic of the benchmark machines is shown in Figure 2.4. The rotor of the benchmark machine consists solely of a radially magnetized PM. The stator back iron (or iron yoke) represents a hollow cylinder made of a soft-magnetic material (magnetic steel). The geometrical and physical parameters of the benchmark motors are provided in Table 2.4. The only difference between the benchmark machines lies in the winding configuration. The winding configurations modeled by the 2D HM, that is, toroidal, concentrated, and distributed windings, have previously been studied by numerous researchers, for instance [15], [85], and [46], and therefore, modeling of PM slotless machines with self-supporting windings, where the skewing of the conductors is present, is of primary interest in this study. Faulhaber, rhombic, and diamond winding topologies, shown in Figure 2.5, are chosen to be modeled by the 3D modeling approach and verified with a 3D finite-element method (FEM) model. It should be explicitly noted that the rotor in the benchmark machines overhangs the stator, which is also usually the case in practice. Additionally, the implementation and verification of the PM field model using the 2D HM is presented in Appendix B.

(a)

(b)
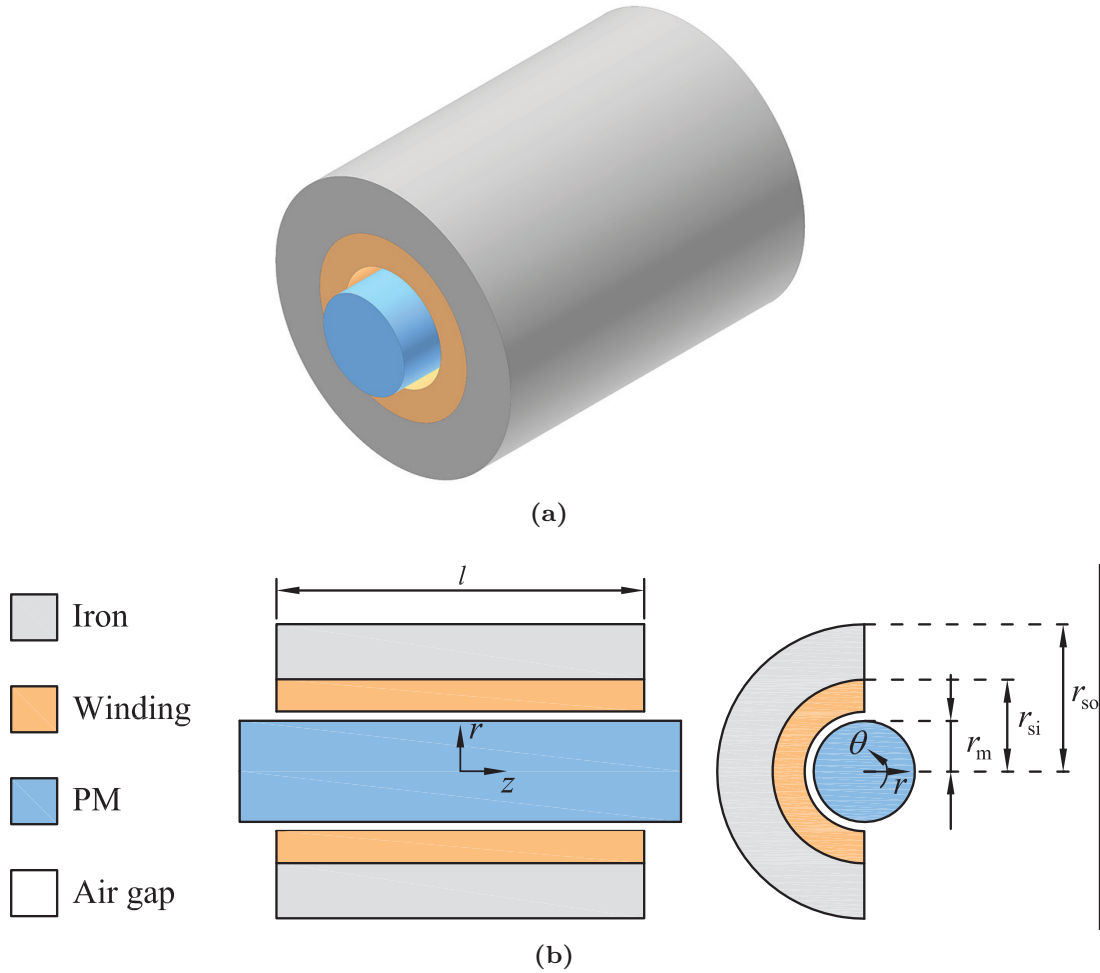
Figure 2.4: a) 3D appearance of the benchmark machines, b) cross-sections of the benchmark machines.

2.7.2   Modeling of armature field

Modeling of the armature field for the benchmark machines necessitates implementation of the 3D model because the current in the windings includes two spatial components: axial and circumferential. The stator iron is assumed to be infinitely permeable, and therefore, it is replaced by a boundary. As the copper permeability is close to 1, the winding is merged with the air gap and modeled as an air region as shown in Figure 2.6. Thus, the model contains two regions, namely PM and air. The winding current is modeled as linear current density placed on the inner surface of the stator iron bore $(r = r_{\mathrm{si}})$.

An important model detail is the axial periodicity, which is assumed to be $\tau_{\mathrm{z}} = 2l$ in this case, as shown in Figure 2.6. This is explained by the fact that the rotor of the benchmark machines overhangs the stator from both flank sides. There-

Table 2.4: Material and geometrical properties of the benchmark PM machines

Parameter	Symbol	Value	Unit
Rotational speed	n	10^5	rpm
Relative magnetic permeability of PM	μ_{rPM}	1.05	
Electrical conductivity of PM	σ_{PM}	5.9 10^5	S/m
PM remanent flux density	B_{rem}	1.2	T
Number of turns per coil	N	16	-
Winding spread	s	$2\pi/3$	rad
Machine active length	l	20	mm
PM radius	r_{m}	2.75	mm
Stator inner radius	r_{si}	5	mm
Stator outer radius	r_{so}	8	mm
Air-gap length	δ	0.5	mm
-	L	-11÷11	-
Axial harmonic order	m	1÷21	-

fore, accepting the model axial periodicity to be l introduces an error to the rotor eddy-current distribution by confining the return path of the rotor eddy currents. Ideally, the axial periodicity should be equal to the rotor length; however, in order to simplify derivation of the linear current density distribution, it is accepted to be $2l$. Additionally, the 3D model implementation of only the rhombic winding benchmark machine will be discussed further as the implementation of the benchmark machines with Faulhaber and diamond windings is identical.

The 3D model implementation starts with the derivation of the linear current density as explained in section 2.6. The linear current density for the rhombic winding is derived as

$$\bar{K}_{\mathrm{z}}(\theta_{\mathrm{r}}, z, t) = \bar{K}_{\mathrm{z1}} + \bar{K}_{\mathrm{z2}}, \tag{2.83}$$

$$\bar{K}_{\mathrm{z1}} = \sum_{\substack{m=1 \\ k=1 \\ L=-\infty}}^{\infty} \hat{K}_{\mathrm{sc1}}(m,k,L)\cos(\omega_{\mathrm{z1}}z)\mathrm{e}^{\mathrm{j}((3L-k)\theta_{\mathrm{r}}+3L\omega t)},$$

$$\bar{K}_{\mathrm{z2}} = \sum_{\substack{m=1 \\ k=1 \\ L=-\infty}}^{\infty} \hat{K}_{\mathrm{sc2}}(m,k,L)\cos(\omega_{\mathrm{z2}}z)\mathrm{e}^{\mathrm{j}((3L-k)\theta_{\mathrm{r}}+3L\omega t)},$$
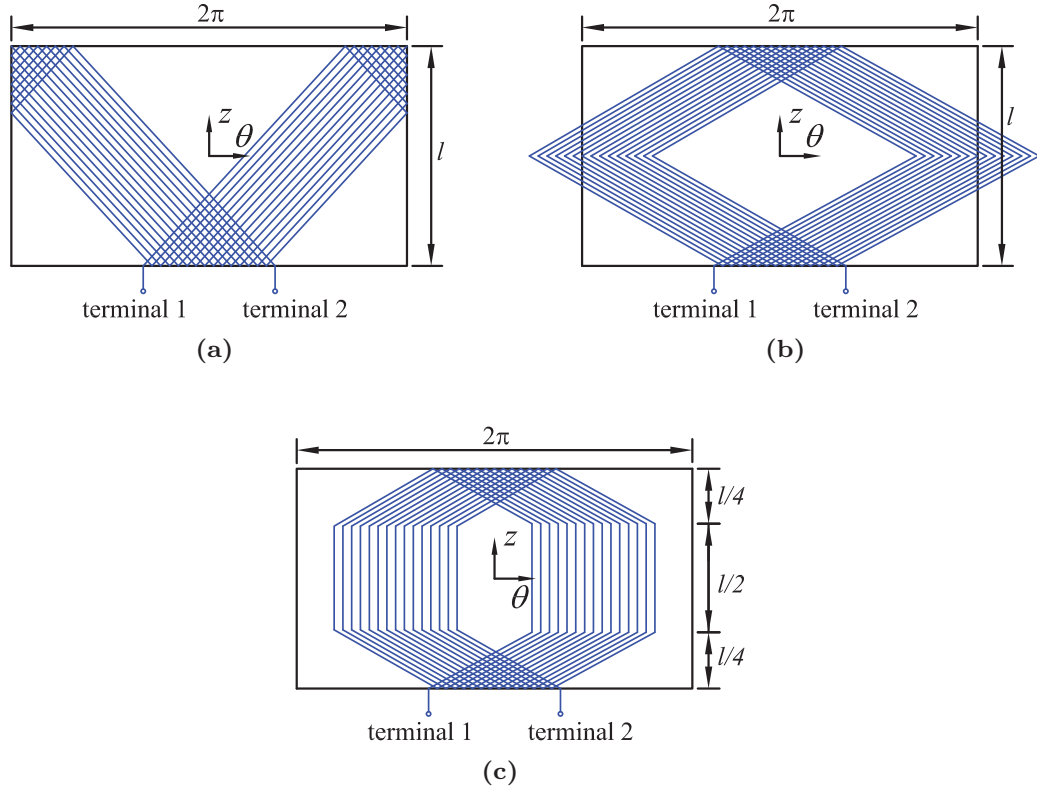
Figure 2.5: Phase coil views of a) Faulhaber, b) rhombic, and c) diamond winding types.
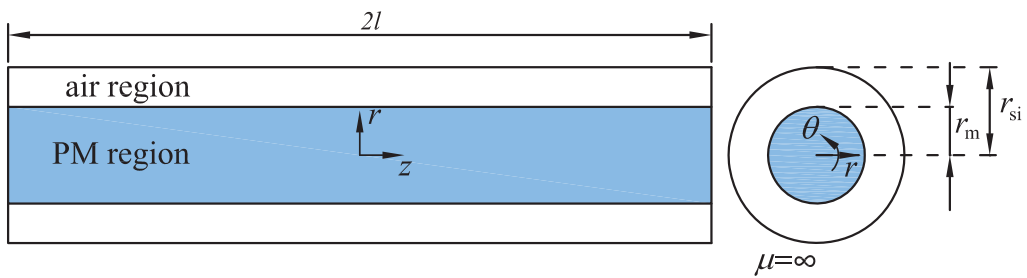
Figure 2.6: Representation of regions in the 3D semianalytical model (iron is assumed to be infinitely permeable).

$$\omega_{z1} = \frac{\left(3L - k - \dfrac{m}{2}\right)\pi}{l},$$

$$\omega_{z2} = \frac{\left(3L - k + \dfrac{m}{2}\right)\pi}{l},$$

where $\hat{K}_{sc1}$ and $\hat{K}_{sc2}$ are amplitudes [A/m] of the linear current density compo-

nents. These amplitude expressions and the derivation of linear current density for the rhombic winding , as well as the expressions for the linear current density distributions for Faulhaber and diamond windings are given in Appendix A. The linear current density expression of the rhombic winding consists of two components, and thus, the field is calculated for each component separately and superimposed in order to obtain the total field.

The electromagnetic field behavior, expressed by means of the SOVP, is governed in the air region by the Laplace equation (2.54), and in the PM region, modeled as conducting region, by the Helmholtz equation (2.49).The solution of the Laplace (2.55) and Helmholtz (2.50), (2.51) equations has to comply with the expression of the linear current density. As the linear current density expression contains two components, the SOVP should also contain two components.

Taking into account the Dirichlet boundary (2.61), the first component of the SOVP solution in the PM region can be written as

$$
\bar{W}_{1\mathrm{PM}1}(r,\theta_\mathrm{r},z,t) =
$$
$$
\sum_{\substack{m=1\\k=1\\L=-\infty}}^{\infty} \bar{C}_{1\mathrm{PM}1}(m,k,L)I_{3L-k}(\xi_{\mathrm{PM}1}r)\sin(\omega_{\mathrm{z}1}z)\mathrm{e}^{\mathrm{j}((3L-k)\theta_\mathrm{r}+3L\omega t)},
$$
$$
\bar{W}_{2\mathrm{PM}1}(r,\theta_\mathrm{r},z,t) =
$$
$$
\sum_{\substack{m=1\\k=1\\L=-\infty}}^{\infty} \bar{C}_{2\mathrm{PM}1}(m,k,L)I_{3L-k}(\xi_{\mathrm{PM}1}r)\cos(\omega_{\mathrm{z}1}z)\mathrm{e}^{\mathrm{j}((3L-k)\theta_\mathrm{r}+3L\omega t)},
$$

$$(2.84)$$

$$
\beta_{\mathrm{PM}}^2 = \mathrm{j}3L\omega\sigma_{\mathrm{PM}}\mu_{\mathrm{PM}},
$$
$$
\xi_{\mathrm{PM}1}^2 = \omega_{\mathrm{z}1}^2 + \beta_{\mathrm{PM}}^2,
$$

and the second component as

$$
\bar{W}_{1\mathrm{PM}2}(r,\theta_\mathrm{r},z,t) =
$$
$$
\sum_{\substack{m=1\\k=1\\L=-\infty}}^{\infty} \bar{C}_{1\mathrm{PM}2}(m,k,L)I_{3L-k}(\xi_{\mathrm{PM}2}r)\sin(\omega_{\mathrm{z}2}z)\mathrm{e}^{\mathrm{j}((3L-k)\theta_\mathrm{r}+3L\omega t)},
$$

$$\bar{W}_{2\text{PM2}}(r, \theta_\text{r}, z, t) =$$
$$\sum_{\substack{m=1 \\ k=1 \\ L=-\infty}}^{\infty} \bar{C}_{2\text{PM2}}(m, k, L) I_{3L-k}(\xi_{\text{PM2}} r) \cos(\omega_{\text{z2}} z) e^{\text{j}((3L-k)\theta_\text{r} + 3L\omega t)},$$

$$(2.85)$$

$$\beta_{\text{PM}}^2 = \text{j} 3L\omega \sigma_{\text{PM}} \mu_{\text{PM}},$$
$$\xi_{\text{PM2}}^2 = \omega_{\text{z2}}^2 + \beta_{\text{PM}}^2.$$

The Dirichlet boundary condition sets the unknown constant in front of the modified Bessel function of the second kind to zero, because the modified Bessel function of the second kind is not zero at $r = 0$. Therefore, (2.84) and (2.85) contain only components dependent on the modified Bessel function of the first kind.

For the air region, the solution has also two components, where the first component is given as

$$\bar{W}_{\text{a1}}(r, \theta_\text{r}, z, t) = \sum_{\substack{m=1 \\ k=1 \\ L=-\infty}}^{\infty} (\bar{C}_{\text{a1}}(m, k, L) I_{3L-k}(\omega_{\text{z1}} r) +$$
$$\bar{D}_{\text{a1}}(m, k, L) K_{3L-k}(\omega_{\text{z1}} r)) \sin(\omega_{\text{z1}} z) e^{\text{j}((3L-k)\theta_\text{r} + 3L\omega t)}, \qquad (2.86)$$

and the second component as

$$\bar{W}_{\text{a2}}(r, \theta_\text{r}, z, t) = \sum_{\substack{m=1 \\ k=1 \\ L=-\infty}}^{\infty} (\bar{C}_{\text{a2}}(m, k, L) I_{3L-k}(\omega_{\text{z2}} r) +$$
$$\bar{D}_{\text{a2}}(m, k, L) K_{3L-k}(\omega_{\text{z2}} r)) \sin(\omega_{\text{z2}} z) e^{\text{j}((3L-k)\theta_\text{r} + 3L\omega t)}. \qquad (2.87)$$

For the cases when $\omega_\text{z} = 0$, the 2D HM should be implemented, as the linear current density becomes z-independent. The 2D HM should also be applied for the cases
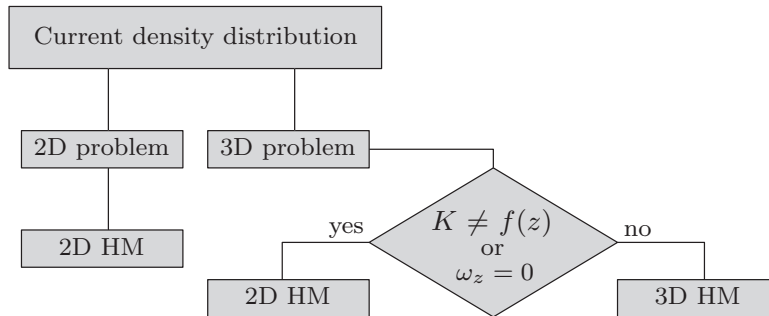
Figure 2.7: Selection algorithm for the 2D or 3D HM implementation.

when the linear current density inherently contains an z-independent component, for instance, one component of the linear current density of a diamond winding (see Appendix B). Figure 2.7 presents a diagram that, depending on the current distribution, shows the cases to implement either the 2D HM or the 3D HM in a 3D problem case.

If $\omega_z = 0$, the field behavior is obtained using the vector potential. Similarly to the 3D HM, taking into account (2.48) and (2.83), the solution in the PM region for both linear current density components can be written as

$$\bar{A}_z(r, \theta_r, t) = \sum_{\substack{k=1 \\ L=-\infty}}^{\infty} \begin{cases} \bar{C}_{PM}(k, L) I_{3L-k}(\beta_{PM}r) e^{j((3L-k)\theta_r + 3L\omega t)} & \text{if } L \neq 0, \\ \bar{C}_{PM}(k, L) r^{|3L-k|} e^{j((3L-k)\theta_r + 3L\omega t)} & \text{if } L = 0, \end{cases}$$
(2.88)

$$\beta_{PM}^2 = j\omega_r \mu_{PM}\sigma_{PM} = j3L\omega\mu_{PM}\sigma_{PM}.$$

Identically to the 3D solutions, by applying the Dirichlet condition (2.60), one of the unknown constants of the solution is set to zero. For the air region, the solution is expressed as

$$\bar{A}_z(r, \theta_r, t) = \sum_{\substack{k=1 \\ L=-\infty}}^{\infty} (\bar{C}_a(k, L) r^{-(3L-k)} + \bar{D}_a(k, L) r^{3L-k}) e^{j((3L-k)\theta_r + 3L\omega t)}.$$
(2.89)

To determine the unknown coefficients C and D in (2.84)–(2.89), a system of equations based on the boundary condition information should be composed. For the 3D HM, the system is determined as follows

$$\begin{cases} \bar{B}_{rPM} - \bar{B}_{ra} = 0, & \text{for } r = r_m \\ \bar{H}_{\theta PM} - \bar{H}_{\theta a} = 0, & \text{for } r = r_m \\ \bar{H}_{zPM} - \bar{H}_{za} = 0, & \text{for } r = r_m \\ \bar{H}_{\theta a} = \bar{K}_z, & \text{for } r = r_{si} \end{cases}.$$
(2.90)

The system of equations consists of four equations, which equals to the number of unknowns in the PM and air regions in the 3D HM, meaning that the system is defined. The system of equations for the 2D HM is given as

$$\begin{cases} \bar{B}_{rPM} - \bar{B}_{ra} = 0, & \text{for } r = r_m \\ \bar{H}_{\theta PM} - \bar{H}_{\theta a} = 0, & \text{for } r = r_m \\ \bar{H}_{\theta a} = \bar{K}_z, & \text{for } r = r_{si} \end{cases}.$$
(2.91)

Here as well, the number of equations satisfies the number of unknowns. Consequently, solving these systems of equations for both components of the linear current density, the unknown coefficients can be calculated.

2.7.3   Validation by the linear 3D finite element method

At this stage, the validation of the developed 3D semianalytical model is performed by a comparison with the transient 3D finite element method (FEM) implemented in FLUX3D (by Cedrat). The material and geometrical properties used in the 3D FEM models are the same as specified for the benchmark machines (see Table 2.4). The rotor overhang from the stator is set to be 3 mm from each side, and the stator iron is modeled as a nonconducting material with $\mu_\mathrm{r} = 10^5$. No axial periodicity has been implemented in the 3D FEM model. The windings in the 3D FEM models are implemented as infinitely thin nonmeshed coils placed at $r = 4.5$ mm. Hence, no induced currents can be modeled in the conductors. The FEM model consists of approximately half a million second-order volume elements.

The results of the radial flux densities of the benchmark machines obtained by the HM at $r = r_\mathrm{m}$ and their difference from the 3D FEM model are shown in Figure 2.8. These flux densities are extracted for the first time harmonic order (ω_1=80 krpm) with the phase current amplitude of 1A, and the difference between them is calculated as $\Delta B_\mathrm{r} = B_\mathrm{r,FEM} - B_\mathrm{r,HM}$. The small difference indicates a good agreement between the HM and FEM models, where the maximum relative difference, which is calculated as $\Delta B_\mathrm{r}/\hat{B}_\mathrm{r,FEM}$, is less than 10%. The weighted mean value difference over the physical part of the rotor is about 3%. It is observed that the obtained difference is close to the difference demonstrated by the 3D HM in Cartesian coordinates [88], [101].

The axial component of the electric field strengths for the benchmark machines calculated using the 3D semianalytical model and their difference with the 3D FEM is shown in Figure 2.9. The electric field strength distribution in the 3D FEM is obtained from the current density distribution using the relation (2.7). In the case of the electric field strength, the peaks of the differences may even reach 20% of the maximum value of the axial component of the electric field strength. However, the mean weighted value of the difference over the rotor does not exceed 10%.

Considering the calculation time of both methods, it can be stated that the 3D FEM requires several (2–3) days to perform the simulation, whereas the semianalytical method implemented in Matlab (by Mathworks) requires less than a minute on the same personal computer (PC).
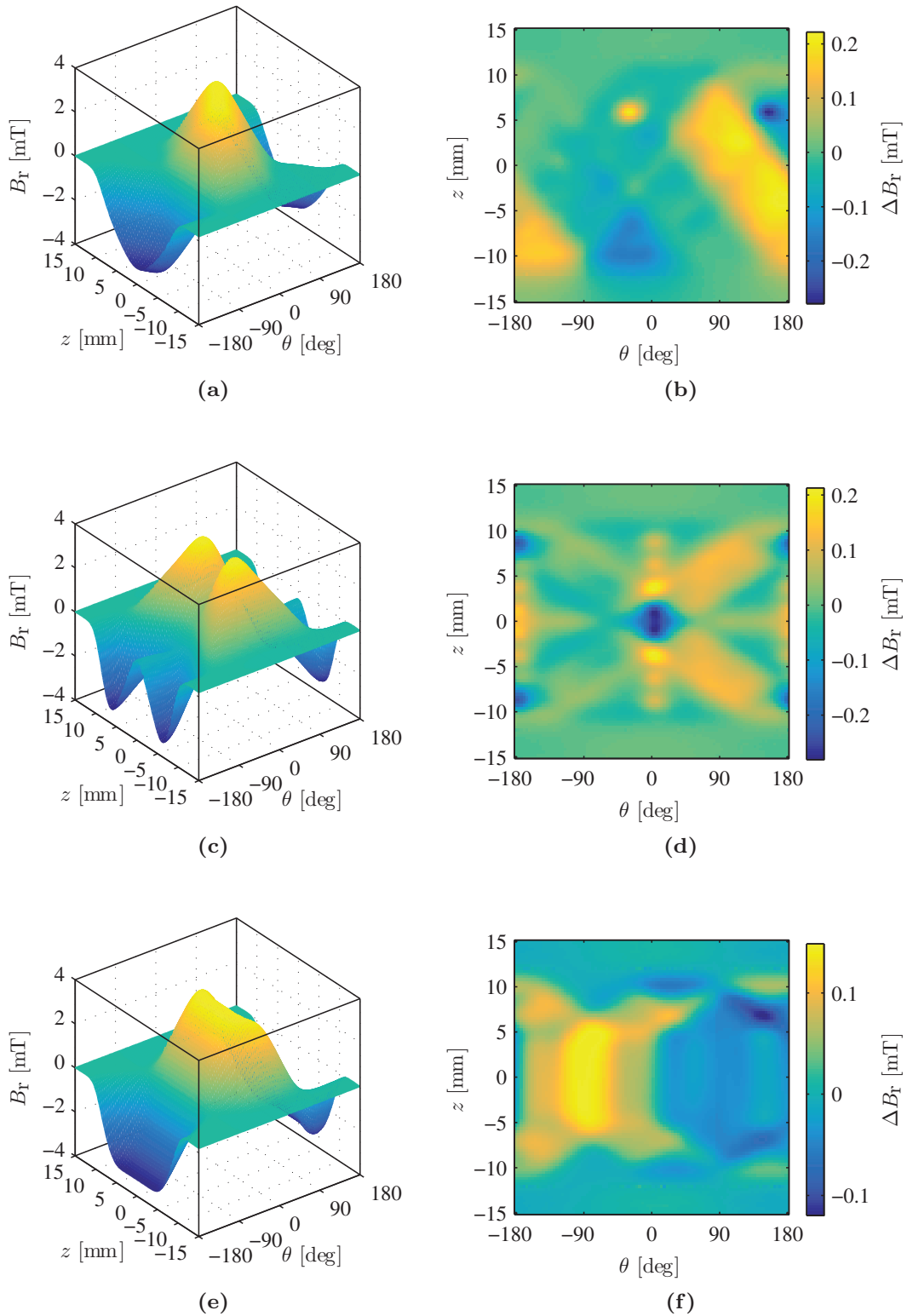
Figure 2.8: Radial component of the armature reaction magnetic flux densities calculated with HM and their difference from the 3D FEM of the benchmark PM machines with a), b) Faulhaber, c), d) rhombic, and e), f) diamond slotless winding types, respectively, at $r = r_{\mathrm{m}}$.
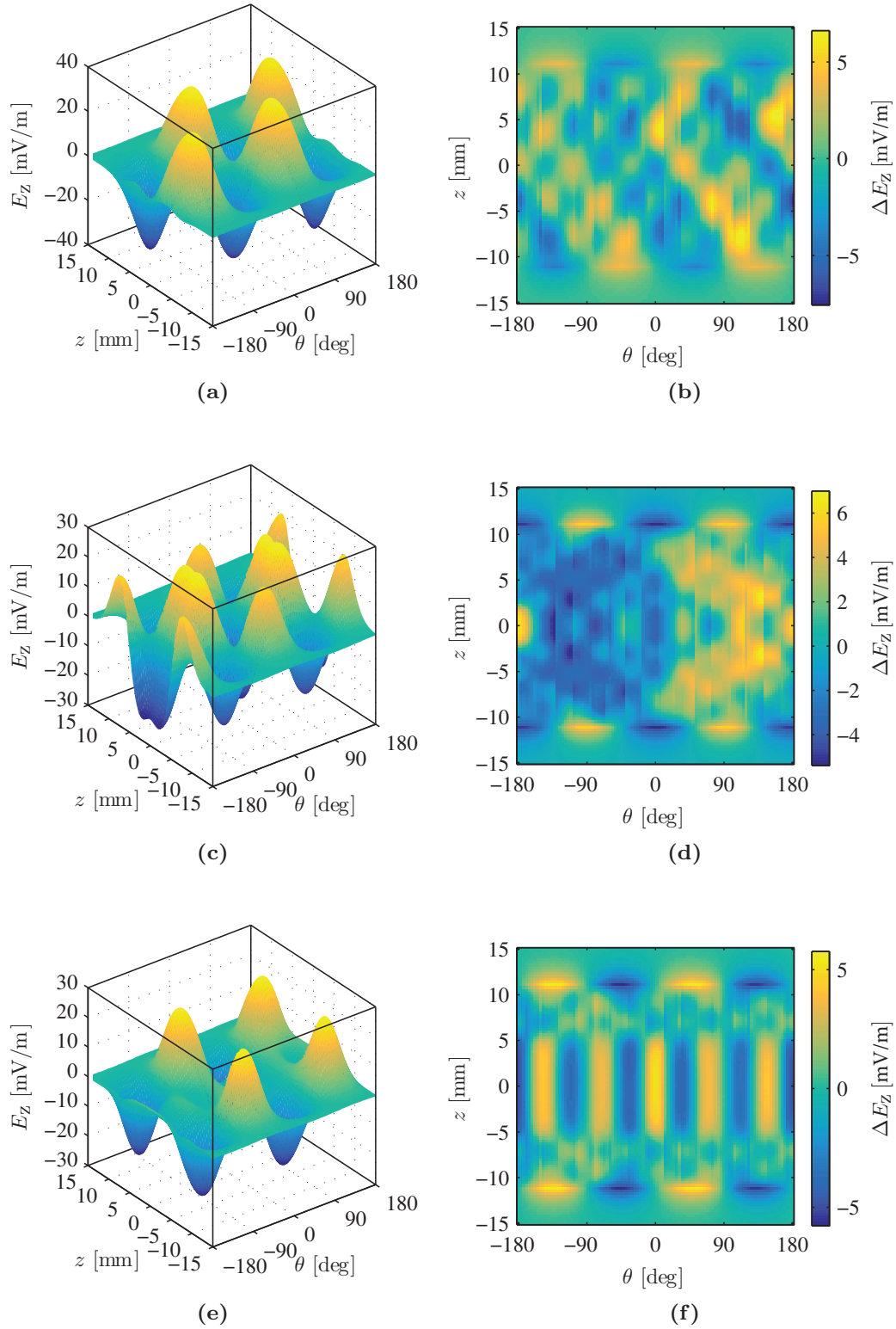
Figure 2.9: Axial component of the electric field strengths calculated with HM and their difference with the 3D FEM of the benchmark PM machines with a), b) Faulhaber, c), d) rhombic, and e), f) diamond slotless winding types, respectively, at $r = r_{\mathrm{m}}$.

2.7.4   Influence of iron permeability and saturation

One of the assumptions set on the HM is the infinitely permeable stator iron. This assumption was made in order to simplify the model by excluding the iron region, which results in a faster model. To evaluate the influence of this assumption on the magnetic field calculation accuracy, a HM model with the stator iron region is built. This model allows to take into account the relative permeability of the stator iron. The relative difference of the armature magnetic flux density, obtained by the HM in the middle of the air gap, over the relative permeability of the benchmark machine is shown in Figure 2.10, where the reference value of the flux density is given at $\mu_\mathrm{r} = 10^5$. The figure shows that for $\mu_\mathrm{r} = 10^2$, the calculation error is less than 1%. Such a small error can be explained by a relatively high effective air gap value, which in the slotless PM machine case is defined by the thickness of the PM, winding, and air gap itself. Certainly, the dependence will change if the geometry differs; however, it can be stated for slotless PM machines that if the stator iron is not saturated, the field modeling with the HM gives a satisfactory accuracy.

An important feature of soft-magnetic materials is their nonlinear behavior, which is defined by a hysteresis curve (also called *B-H* curve). This curve gives information about the dependence of relative permeability over the magnetic flux density. The *H-B* curve for M270-35A electrical steel as well as the μ_r dependence are given in Figure 2.11. It should explicitly stated, that this μ_r represents relative
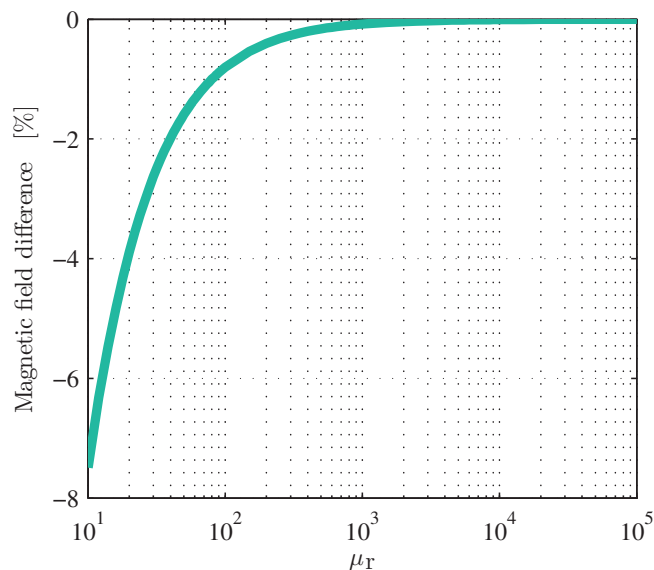
Figure 2.10: Relative difference of magnetic flux density calculation versus the stator iron relative permeability of benchmark machines, where the reference magnetic density is obtained for $\mu_\mathrm{r} = 10^5$.
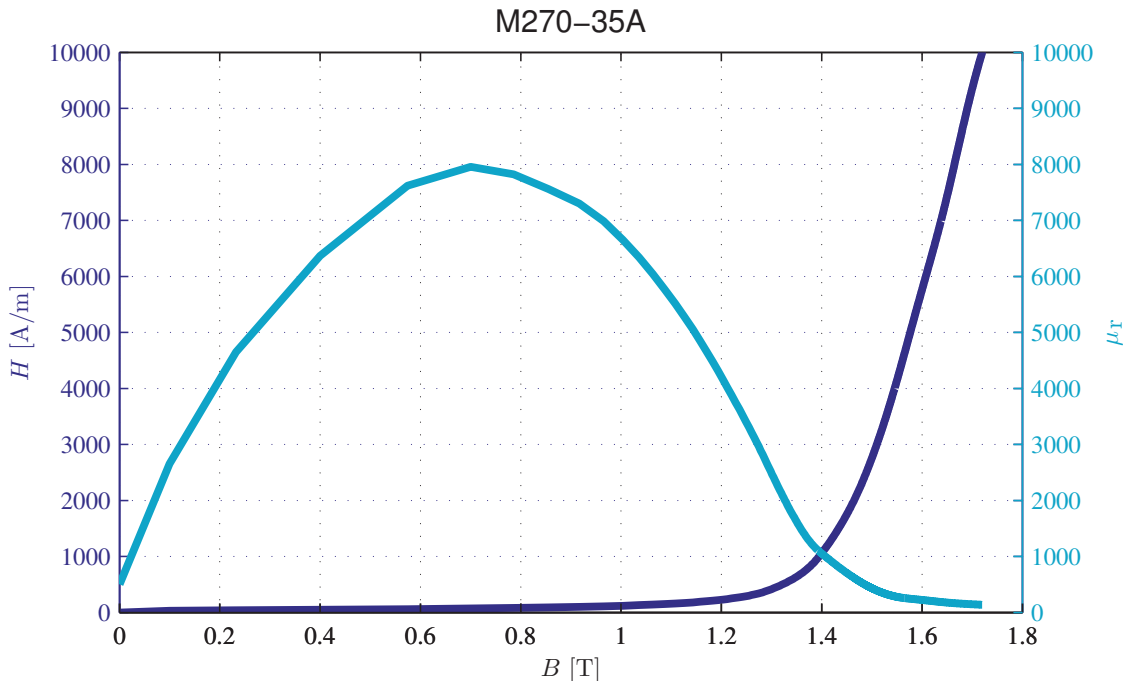
Figure 2.11: H-B and μ_r-B curves of M270-35A electrical steel [91].

permeability linearized to the operation point. From the H-B curve it is clear that at high flux density values the material starts to saturate. Based on Figure 2.10, it can be concluded that if the iron parts are not highly saturated, the error introduced to the HM calculation by the iron nonlinearity is insignificant.

2.8　Summary

This chapter discusses the 2D and 3D models based on the harmonic modeling (HM) technique, which is applied to model the electromagnetic behavior of high-speed slotless PM machines, but not limited to it. The HM employs the concept of magnetic potentials to describe the field behavior in machine regions with different electromagnetic properties. The expression of a magnetic potential is the solution of a differential equation resulting directly from Maxwell's equations. These expressions for each region contain unknown coefficients, which are determined by solving a system of linear equations derived from the boundary conditions.

The magnetic field source terms used in the HM, such as spatial current and PM magnetization distributions, are given by means of 1D and 2D Fourier series. This source representation is well suited to describe the spatial current distribution of complex winding geometries, for instance Faulhaber, rhombic, and diamond windings.

To reduce the complexity of the model, the iron parts of the machine are assumed infinitely permeable. Nevertheless, it should be mentioned that for machines with large effective air gaps, such as slotless PM machines, this assumption does not have a significant influence unless the iron parts are highly saturated.

The obtained results of the magnetic flux density and the electric field strength for the benchmark machines with Faulhaber, rhombic, and diamond windings are in good agreement with those produced by the 3D FEM. The maximum relative difference between the flux density distributions obtained by the HM and 3D FEM is less than 10%, whereas the maximum relative difference in the case of the electric field strengths can reach 20%.

The calculation time of the HM is significantly shorter than that of the FEM, which makes it very effective for parametric search in the machine design.

3

Calculation of electromagnetic quantities

This chapter presents calculation of the developed electromagnetic torque, the emf induced by the permanent-magnet field, and the synchronous inductance in slotless PM machines. These electromagnetic quantities are obtained using the electromagnetic field solution introduced in Chapter 2.

3.1   Electromagnetic force and torque

3.1.1   Introduction

One of the most important quantities for rotating electromechanical devices is electromagnetic torque; therefore, it is of primary importance to be able to predict it accurately. Electromagnetic torque, which is the result of the electromagnetic interaction between the stator and the rotor, can be calculated using various approaches. Most commonly, the torque and force calculation in electrical machines is performed by the following approaches: applying the Lorentz force, virtual work, a method based on the Poynting vector, or the Maxwell stress tensor. Usually, the choice of the torque and force calculation method depends on the electromagnetic application and the field-obtaining approach. The advantages and disadvantages of alternative methods are discussed in detail in [18], [82], [96].

The Lorentz force calculation in the volume integral form requires the current density distribution in a coil and the distribution of external flux density penetrating this coil [30]. This method is best suited for the force calculation in slotless structures, because it is not able to take into account either cogging or reluctance force components. To accurately calculate torque and forces in high-speed machines, this external flux density should also contain the field component originating from the rotor eddy currents.

The method of virtual work calculates forces acting on an object from the change of electromagnetic energy caused by a virtual displacement of the mover (rotor) [21][62]. Calculation of the force applying the method of virtual work requires calculation of the electromagnetic energy in two rotor positions, which results in two volume integrals over the energy. Therefore, application of this method for the force calculation inherently requires two calculations. This method is often used in numerical modeling approaches, for instance the FEM or the boundary element method (BEM).

Integration of the Poynting vector over the rotor surface results in the total power crossing the air gap from the stator to the rotor in the motor operation mode [46]. By subtracting the electromagnetic losses on the rotor side from this total power and dividing the result by the angular velocity, the generated electromagnetic torque can be calculated. To obtain the Poynting vector, the electrical field distribution is required [90].

The Maxwell stress tensor is a generic method that enables to calculate forces acting on an object. The necessary applicability condition of the method is that the object should be surrounded by a vacuum (air). To be able to calculate the electromagnetic force, the distribution of the magnetic field components around the object should be known.

The Lorentz force, the Maxwell stress tensor, and the Poynting vector approaches are convenient tools to calculate forces acting on the rotor in slotless PM machines. The Maxwell stress tensor approach has been chosen to assess the torque production of these machines. Analytical expressions for 2D and 3D cases are derived using the electromagnetic field distribution, which was defined in the general form in the previous chapter.

3.1.2 Maxwell stress tensor in cylindrical coordinates

To calculate the electromagnetic force acting on a body, surface integration of the Maxwell stress tensor around the body should be performed as

$$\vec{F} = \oint_S \mathbb{T} \cdot \vec{n} \mathrm{d}S, \tag{3.1}$$

where $\vec{n}$ is the unit vector normal to the surface. In the cylindrical coordinate system, the Maxwell stress tensor, $\mathbb{T}$, can be defined as [76]

$$\mathbb{T} = \begin{bmatrix} \tau_{\mathrm{rr}} & \tau_{\mathrm{r\theta}} & \tau_{\mathrm{rz}} \\ \tau_{\theta\mathrm{r}} & \tau_{\theta\theta} & \tau_{\theta\mathrm{z}} \\ \tau_{\mathrm{zr}} & \tau_{\mathrm{z\theta}} & \tau_{\mathrm{zz}} \end{bmatrix} = $$
$$\frac{1}{\mu_0} \begin{bmatrix} \dfrac{B_{\mathrm{r}}^2 - B_{\theta}^2 - B_{\mathrm{z}}^2}{2} & B_{\mathrm{r}}B_{\theta} & B_{\mathrm{r}}B_{\mathrm{z}} \\ B_{\theta}B_{\mathrm{r}} & \dfrac{B_{\theta}^2 - B_{\mathrm{r}}^2 - B_{\mathrm{z}}^2}{2} & B_{\theta}B_{\mathrm{z}} \\ B_{\mathrm{z}}B_{\mathrm{r}} & B_{\mathrm{z}}B_{\theta} & \dfrac{B_{\mathrm{z}}^2 - B_{\mathrm{r}}^2 - B_{\theta}^2}{2} \end{bmatrix}, \tag{3.2}$$

where τ represents the components of the Maxwell stress tensor [N/m^2]. The first index of τ indicates the direction of the stress tensor component, and the second index of τ indicates the direction of $\vec{n}$. This normal unit vector is always directed outwards from the body in question. Representing the rotor of an electrical machine as a cylinder, $\vec{n}$ exists only in axial and radial directions as shown in Figure 3.1.

The unit vectors $\vec{n}$ normal to the surfaces S_2 and S_3 are aligned with the axial axis but have opposite directions. Considering the assumption that the electromagnetic field distribution is periodic in the axial direction in the 3D HM, it can be stated that the integration of the Maxwell stress tensor over S_2 and S_3 will result in a zero net force. Therefore, the force exerted to the rotor can be calculated on the surface S_1. The unit vector to the surface S_1 has a radial direction, and consequently, the
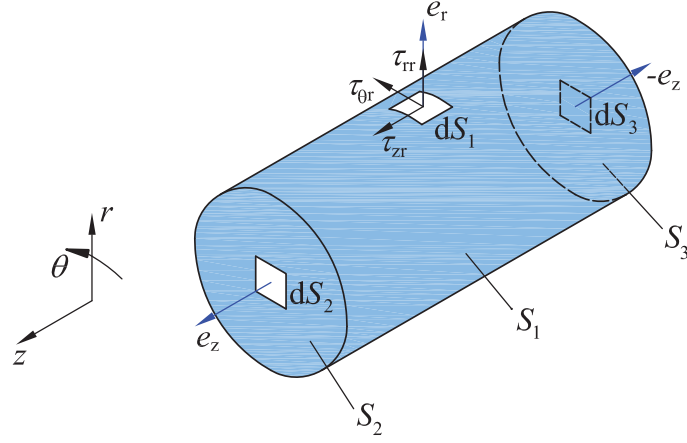
Figure 3.1: Cylindrical rotor with normal vectors on surfaces and stress tensor components.

forces acting on the rotor in this case are defined as

$$F_{\mathrm{r}} = \frac{1}{\mu_0} \oint_{S_1} \frac{B_{\mathrm{r}}^2 - B_{\theta}^2 - B_{\mathrm{z}}^2}{2} \mathrm{d}S_1, \tag{3.3}$$

$$F_{\theta} = \frac{1}{\mu_0} \oint_{S_1} B_{\theta} B_{\mathrm{r}} \mathrm{d}S_1, \tag{3.4}$$

$$F_{\mathrm{z}} = \frac{1}{\mu_0} \oint_{S_1} B_{\mathrm{z}} B_{\mathrm{r}} \mathrm{d}S_1. \tag{3.5}$$

Since the main interest is the torque directed along the axial axis, only the circumferential force is considered further. It should be, however, mentioned that some self-supporting slotless windings produce transversal torque and axial force [72].

The tangential force expression can further be used to obtain the axial torque as

$$T_{\mathrm{z}} = F_{\theta} r, \tag{3.6}$$

where r is the radius of the Maxwell tensor integration surface [m].

3.1.3   Force calculation based on the 2D harmonic modeling

For some slotless machines, for instance with toroidal or concentrated windings, the 2D field modeling is sufficient to predict the electromagnetic behavior of these machines. In this case, the electromagnetic field in the machines has only radial and circumferential components, meaning that no axial force is present.

To obtain the general expression of force calculation for the 2D case, the following

vector potential of the PM field given in the stator reference frame is assumed

$$A_{z,\mathrm{PM}} = \sum_{\nu=1}^{\infty} (C_{\mathrm{PM}} r^{-\nu} + D_{\mathrm{PM}} r^{\nu}) \sin(\nu(\theta - \omega t) + \theta_0), \tag{3.7}$$

where θ_0 is the initial rotor position [rad]. The expression of the vector potential is given in the real number domain in order to simplify the derivation of the force calculation expression. Additionally, it is assumed that the vector potential contains only sine terms, which can be obtained by choosing a proper origin of the coordinate system while deriving the PM magnetization distribution. Using (2.20), the radial and circumferential components of the PM flux density are written as

$$B_{\mathrm{r,PM}} = \frac{1}{r} \sum_{\nu=1}^{\infty} \Lambda_{\mathrm{PM,r}} \cos(\nu(\theta - \omega t) + \theta_0), \tag{3.8}$$

$$B_{\theta,\mathrm{PM}} = \sum_{\nu=1}^{\infty} \Lambda_{\mathrm{PM,\theta}} \sin(\nu(\theta - \omega t) + \theta_0), \tag{3.9}$$

where $\Lambda_{\mathrm{PM,r}}$ and $\Lambda_{\mathrm{PM,\theta}}$ are defined by (C.1) in Appendix C.

Similarly to the PM field, the general expression for the armature reaction vector potential in the stator reference frame can be given as

$$\bar{A}_{z,\mathrm{AR}} = \sum_{\substack{k=1 \\ L=-\infty}}^{\infty} \left[\left(\bar{C}_{\mathrm{s,AR}} r^{-(3L-k)} + \bar{D}_{\mathrm{s,AR}} r^{(3L-k)} \right) \mathrm{e}^{\mathrm{j}((3L-k)\theta + k\omega t)} + \right.$$
$$\left. \left(\bar{C}_{\mathrm{c,AR}} r^{-(3L-k)} + \bar{D}_{\mathrm{c,AR}} r^{(3L-k)} \right) \mathrm{e}^{\mathrm{j}((3L-k)\theta + k\omega t)} \right]. \tag{3.10}$$

where $\bar{C}_{\mathrm{s,AR}}$ and $\bar{D}_{\mathrm{s,AR}}$ are complex unknown constants related to the sine term of the vector potential, and $\bar{C}_{\mathrm{c,AR}}$ and $\bar{D}_{\mathrm{c,AR}}$ are complex unknown constants related to the cosine term of the vector potential. After applying (2.20) to (3.10), the radial and circumferential components of the armature reaction flux density are found as

$$B_{\mathrm{r,AR}} = \frac{1}{r} \sum_{\substack{k=1 \\ L=-\infty}}^{\infty} \left[\mathrm{Im}(\bar{\Lambda}_{\mathrm{s,r}} \mathrm{e}^{\mathrm{j}((3L-k)\theta + k\omega t)}) + \mathrm{Re}(\bar{\Lambda}_{\mathrm{c,r}} \mathrm{e}^{\mathrm{j}((3L-k)\theta + k\omega t)}) \right],$$

$$B_{\theta,\mathrm{AR}} = \sum_{\substack{k=1 \\ L=-\infty}}^{\infty} \left[\mathrm{Im}(\bar{\Lambda}_{\mathrm{s,\theta}} \mathrm{e}^{\mathrm{j}((3L-k)\theta + k\omega t)}) + \mathrm{Re}(\bar{\Lambda}_{\mathrm{c,\theta}} \mathrm{e}^{\mathrm{j}((3L-k)\theta + k\omega t)}) \right], \quad (3.11)$$

where $\bar{\Lambda}_{\mathrm{s,r}}$, $\bar{\Lambda}_{\mathrm{c,r}}$, $\bar{\Lambda}_{\mathrm{s,\theta}}$, and $\bar{\Lambda}_{\mathrm{c,\theta}}$ are defined by (C.2) in Appendix C. The circumferential force expression (3.4) contains the radial and circumferential flux densities of the total field, including PM and armature fields, which are obtained as

$$B_{\mathrm{r}} = B_{\mathrm{r,PM}} + B_{\mathrm{r,AR}},$$
$$B_{\theta} = B_{\theta,\mathrm{PM}} + B_{\theta,\mathrm{AR}}. \tag{3.12}$$

In this case, the armature field also contains the reaction of the rotor eddy currents. By substituting (3.12) into (3.4), the tangential force expression can be rewritten as

$$F_\theta = \frac{lr}{\mu_0} \int\limits_{-\pi}^{\pi} (B_{r,PM}B_{\theta,AR} + B_{\theta,PM}B_{r,AR} + B_{r,AR}B_{\theta,AR} + B_{r,PM}B_{\theta,PM})d\theta.$$

(3.13)

It should be noted here that the radial and tangential PM field components are always shifted by $\pi/2$, because no circumferential permeance variation in the stator is present. This means slotless PM machines do not produce any cogging torque. Whereas the phase shift of the radial and tangential field components of the armature field might not be $\pi/2$ because of the influence of the rotor eddy-current reaction. Taking into account (3.8), (3.9) and (3.11), the above integral results in

$$F_\theta = \frac{l}{\mu_0} \sum_{\substack{\nu=1 \\ k=1 \\ L=-\infty \\ \nu=|3L-k|}}^{\infty} \left[\mathrm{Im}(\pi\Lambda_{PM,r}\bar{\Lambda}_{s,\theta}e^{j\theta_T}) + \mathrm{Re}(\pi\Lambda_{PM,r}\bar{\Lambda}_{c,\theta}e^{j\theta_T}) + \right.$$

$$\mathrm{Im}(\pi\frac{(k-3L)}{\nu}\Lambda_{PM,\theta}\bar{\Lambda}_{s,r}e^{j\theta_T}) +$$

$$\left. \mathrm{Re}(\pi\frac{(k-3L)}{\nu}\Lambda_{PM,\theta}\bar{\Lambda}_{c,r}e^{j\theta_T}) \right] + F_{\theta,eddy2D},$$

(3.14)

where

$$\theta_T = 3L\omega t - \frac{(3L-k)}{\nu}\theta_0.$$

(3.15)

This expression is only valid for the case when $\nu = |(3L - k)|$, otherwise the tangential force integral results in zero. This means that only the PM and armature field components of the same spatial harmonic order produce tangential force. The first part of the expression considers the force produced by the interaction of the armature and PM fields. The force generated by the armature and rotor eddy-current fields is represented by $F_{\theta,eddy2D}$, where the expression is given by (C.4) in Appendix C. Integrals in this expression should be calculated numerically. The derived tangential force expression for the 2D case takes into account the time dependence, and thus, makes it possible to model the force ripples caused by the time and spatial harmonics.

3.1.4 Force calculation based on the 3D harmonic modeling

The calculation of the force and torque in a 3D electromagnetic problem is similar to the 2D one. To derive the tangential force for the 3D case, the armature field in the air gap in terms of second-order vector potential can be generally assumed as

$$
\bar{W}_{\mathrm{AR}} = \sum_{\substack{m=0 \\ k=1 \\ L=-\infty}}^{\infty}
$$

$$
\big[(\bar{C}_{\mathrm{ss}}I_{(3L-k)}(\omega_{\mathrm{z}}r) + \bar{D}_{\mathrm{ss}}K_{(3L-k)}(\omega_{\mathrm{z}}r))\mathrm{e}^{\mathrm{j}((3L-k)\theta+k\omega t)}\sin(\omega_{\mathrm{z}}z + \theta_{\mathrm{z}}) +
$$
$$
(\bar{C}_{\mathrm{sc}}I_{(3L-k)}(\omega_{\mathrm{z}}r) + \bar{D}_{\mathrm{sc}}K_{(3L-k)}(\omega_{\mathrm{z}}r))\mathrm{e}^{\mathrm{j}((3L-k)\theta+k\omega t)}\cos(\omega_{\mathrm{z}}z + \theta_{\mathrm{z}}) +
$$
$$
(\bar{C}_{\mathrm{cs}}I_{(3L-k)}(\omega_{\mathrm{z}}r) + \bar{D}_{\mathrm{cs}}K_{(3L-k)}(\omega_{\mathrm{z}}r))\mathrm{e}^{\mathrm{j}((3L-k)\theta+k\omega t)}\sin(\omega_{\mathrm{z}}z + \theta_{\mathrm{z}}) +
$$
$$
(\bar{C}_{\mathrm{cc}}I_{(3L-k)}(\omega_{\mathrm{z}}r) + \bar{D}_{\mathrm{cc}}K_{(3L-k)}(\omega_{\mathrm{z}}r))\mathrm{e}^{\mathrm{j}((3L-k)\theta+k\omega t)}\cos(\omega_{\mathrm{z}}z + \theta_{\mathrm{z}})\big], \quad (3.16)
$$

where the first letter in the subscript of the unknown coefficient relates to the sine or cosine terms of circumferential spatial distribution, and the second letter in the subscript of the unknown coefficient relates to the sine or cosine terms of axial spatial distribution. Using (2.56), the real-number representation of the radial and circumferential components of the flux density can be derived as

$$
B_{\mathrm{r,AR}} = \sum_{\substack{m=0 \\ k=1 \\ L=-\infty}}^{\infty} \big[\mathrm{Re}(\bar{A}_{\mathrm{ss,r}}\mathrm{e}^{\mathrm{j}((3L-k)\theta+k\omega t)}\cos(\omega_{\mathrm{z}}z + \theta_{\mathrm{z}})) +
$$
$$
\mathrm{Re}(\bar{A}_{\mathrm{sc,r}}\mathrm{e}^{\mathrm{j}((3L-k)\theta+k\omega t)}\sin(\omega_{\mathrm{z}}z + \theta_{\mathrm{z}})) +
$$
$$
\mathrm{Im}(\bar{A}_{\mathrm{cs,r}}\mathrm{e}^{\mathrm{j}((3L-k)\theta+k\omega t)}\cos(\omega_{\mathrm{z}}z + \theta_{\mathrm{z}})) +
$$
$$
\mathrm{Im}(\bar{A}_{\mathrm{cc,r}}\mathrm{e}^{\mathrm{j}((3L-k)\theta+k\omega t)}\sin(\omega_{\mathrm{z}}z + \theta_{\mathrm{z}}))\big], \quad (3.17)
$$

$$
B_{\theta,\mathrm{AR}} = \sum_{\substack{m=0 \\ k=1 \\ L=-\infty}}^{\infty} \frac{1}{r}\big[\mathrm{Re}(\bar{A}_{\mathrm{ss,\theta}}\mathrm{e}^{\mathrm{j}((3L-k)\theta+k\omega t)}\cos(\omega_{\mathrm{z}}z + \theta_{\mathrm{z}})) +
$$
$$
\mathrm{Re}(\bar{A}_{\mathrm{sc,\theta}}\mathrm{e}^{\mathrm{j}((3L-k)\theta+k\omega t)}\sin(\omega_{\mathrm{z}}z + \theta_{\mathrm{z}})) +
$$
$$
\mathrm{Im}(\bar{A}_{\mathrm{cs,\theta}}\mathrm{e}^{\mathrm{j}((3L-k)\theta+k\omega t)}\cos(\omega_{\mathrm{z}}z + \theta_{\mathrm{z}})) +
$$
$$
\mathrm{Im}(\bar{A}_{\mathrm{cc,\theta}}\mathrm{e}^{\mathrm{j}((3L-k)\theta+k\omega t)}\sin(\omega_{\mathrm{z}}z + \theta_{\mathrm{z}}))\big], \quad (3.18)
$$

where $\bar{A}_{\mathrm{ss,r}}$, $\bar{A}_{\mathrm{sc,r}}$, $\bar{A}_{\mathrm{cs,r}}$, $\bar{A}_{\mathrm{cc,r}}$, $\bar{A}_{\mathrm{ss,\theta}}$, $\bar{A}_{\mathrm{sc,\theta}}$, $\bar{A}_{\mathrm{cs,\theta}}$, and $\bar{A}_{\mathrm{cc,\theta}}$ are given by (C.3) in Appendix C. The equation for the circumferential force calculation, (3.4), for a 3D

case can be rewritten as

$$F_\theta = \frac{r}{\mu_0} \int\limits_{-\pi}^{\pi} \int\limits_{-l/2}^{l/2} (B_{\mathrm{r,PM}}B_{\theta,\mathrm{AR}} + B_{\theta,\mathrm{PM}}B_{\mathrm{r,AR}} + B_{\mathrm{r,AR}}B_{\theta,\mathrm{AR}}+$$

$$B_{\mathrm{r,PM}}B_{\theta,\mathrm{PM}})\mathrm{d}\theta\mathrm{d}l. \tag{3.19}$$

As mentioned previously, the last component of this expression for slotless PM machine cases results in zero. After substituting (3.8), (3.9), (3.17) and (3.18) into (3.19), the circumferential force component can be written as

$$F_\theta = \frac{2\pi r}{\mu_0 \omega_{\mathrm{z}}} \sum_{\substack{\nu=1 \\ k=1 \\ L=-\infty \\ \nu=|3L-k|}}^{\infty} \Big[\mathrm{Re}(r^{-2}\varLambda_{\mathrm{PM,r}}\bar{\varLambda}_{\mathrm{ss},\theta}\mathrm{e}^{\mathrm{j}\theta_{\mathrm{T}}}\cos(\theta_{\mathrm{z}})\sin(l\omega_{\mathrm{z}}/2))+$$

$$\mathrm{Re}(r^{-2}\varLambda_{\mathrm{PM,r}}\bar{\varLambda}_{\mathrm{sc},\theta}\mathrm{e}^{\mathrm{j}\theta_{\mathrm{T}}}\sin(\theta_{\mathrm{z}})\sin(l\omega_{\mathrm{z}}/2))+$$

$$\mathrm{Im}(r^{-2}\varLambda_{\mathrm{PM,r}}\bar{\varLambda}_{\mathrm{cs},\theta}\mathrm{e}^{\mathrm{j}\theta_{\mathrm{T}}}\cos(\theta_{\mathrm{z}})\sin(l\omega_{\mathrm{z}}/2))+$$

$$\mathrm{Im}(r^{-2}\varLambda_{\mathrm{PM,r}}\bar{\varLambda}_{\mathrm{cc},\theta}\mathrm{e}^{\mathrm{j}\theta_{\mathrm{T}}}\sin(\theta_{\mathrm{z}})\sin(l\omega_{\mathrm{z}}/2))+$$

$$\mathrm{Re}(\mathrm{j}(3L-k)\nu^{-1}\varLambda_{\mathrm{PM},\theta}\bar{\varLambda}_{\mathrm{ss,r}}\mathrm{e}^{\mathrm{j}\theta_{\mathrm{T}}}\cos(\theta_{\mathrm{z}})\sin(l\omega_{\mathrm{z}}/2))+$$

$$\mathrm{Re}(\mathrm{j}(3L-k)\nu^{-1}\varLambda_{\mathrm{PM},\theta}\bar{\varLambda}_{\mathrm{sc,r}}\mathrm{e}^{\mathrm{j}\theta_{\mathrm{T}}}\sin(\theta_{\mathrm{z}})\sin(l\omega_{\mathrm{z}}/2))+$$

$$\mathrm{Im}(\mathrm{j}(3L-k)\nu^{-1}\varLambda_{\mathrm{PM},\theta}\bar{\varLambda}_{\mathrm{cs,r}}\mathrm{e}^{\mathrm{j}\theta_{\mathrm{T}}}\cos(\theta_{\mathrm{z}})\sin(l\omega_{\mathrm{z}}/2))+$$

$$\mathrm{Im}(\mathrm{j}(3L-k)\nu^{-1}\varLambda_{\mathrm{PM},\theta}\bar{\varLambda}_{\mathrm{cc,r}}\mathrm{e}^{\mathrm{j}\theta_{\mathrm{T}}}\sin(\theta_{\mathrm{z}})\sin(l\omega_{\mathrm{z}}/2))\Big] +$$

$$F_{\theta,\mathrm{eddy3D}}, \tag{3.20}$$

where θ_{T} is given by (3.15). In this expression, the term under the summation refers to the force component produced by the interaction between the armature and PM fields, and $F_{\theta,\mathrm{eddy3D}}$ is the force component generated by the interaction between the armature and rotor eddy-current fields and given by (C.6) in Appendix C.

3.1.5   Comparison of the modeling results

The derived expressions (3.14) and (3.20) are implemented to calculate the axial torque of the benchmark machine with the Faulhaber winding, the properties of which are given in Table 2.4. The PM magnetization of the benchmark model is assumed radial (see Appendix B). The results of the torque calculation are compared with those obtained by the transient 3D FEM. The properties of the transient 3D FEM model include a stator iron with $\mu_{\mathrm{r}} = 10^5$ [-], nonmeshed coils (placed at $r = 4.5$ mm), and no periodicity in the axial direction (see Section 2.7.3).

It should be noted that the 3D electromagnetic modeling of the benchmark machine assumes combination of the 2D and 3D harmonic models, which is explained by the presence of the 1D and 2D Fourier series in the spatial linear current density distribution of the Faulhaber winding. Therefore, both expressions (3.14) and (3.20) are necessary for the torque calculation of the benchmark machine.

Figure 3.2 shows the torque profiles of the benchmark machine produced by changing the initial rotor angular position, θ_0, generated by means of semianalytical and FEM models. In this case, the relative error of the peak values is less than -4%. This difference can be explained by the fact that the linear current density in the 3D semianalytical model is placed on the stator iron bore, whereas the nonmeshed coils in the 3D FEM model are located at $r = 4.5$ mm.
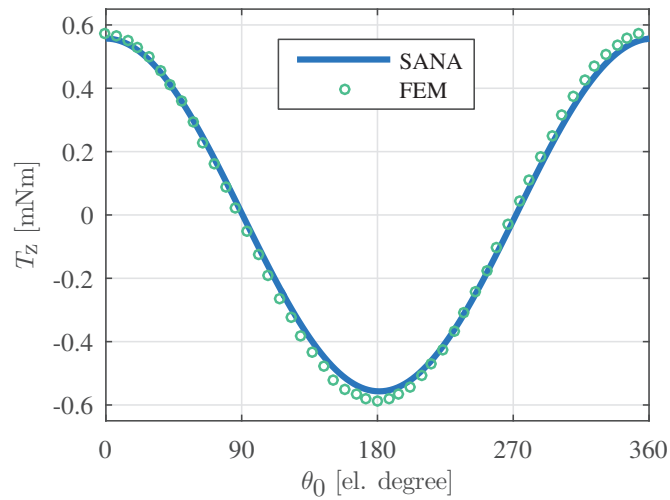
Figure 3.2: Torque profile of the benchmark machine with the Faulhaber winding over the initial rotor position with constant current in the phases ($\hat{I} = 1$ A) which correspond to $t = 0$ s, obtained by the 3D semianalytical model (SAN) and the 3D FEM.

The torque profile of the benchmark machine over one electrical period obtained by the semianalytical and FEM models is shown in Figure 3.3. The initial rotor position for this simulation is set to achieve maximum torque per ampere ($I_d = 0$ control), which is equivalent to $\theta_0 = 0$. The torque profile demonstrates the presence of the torque ripple with six periods per one rotation. This ripple results from the interaction of the 5th and 7th spatial harmonics of the PM and armature fields. The torque ripple can be explained by the fact that all spatial harmonics of the PM field have the same angular velocity, whereas the angular velocity of the armature field harmonics depends on the time and spatial harmonic orders. This results in the slip between the armature and PM spatial harmonics of the same time and spatial orders.

Additionally, it should mentioned that the torque profile in Figure 3.2 is not purely
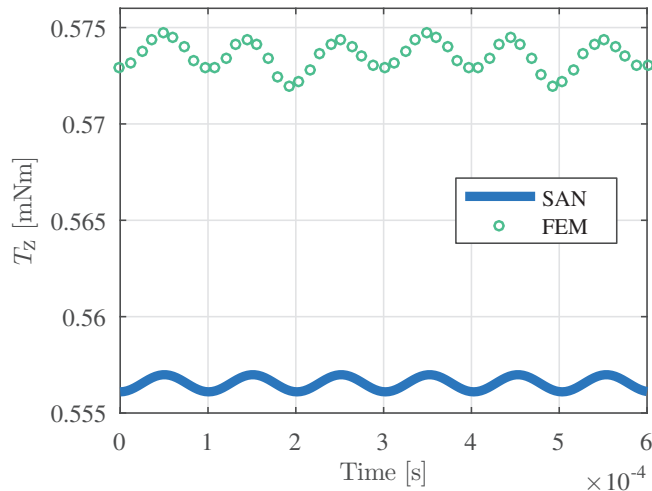
Figure 3.3: Torque profile of the benchmark machine with the Faulhaber winding over one electrical period at $\theta_0 = 0$, obtained by the 3D semianalytical model (SAN) and the 3D FEM.

sinusoidal and contains harmonic components of the higher order; however, because of the low value of these harmonics, they are not visible in the graph.

3.2   Permanent magnet electromotive force

Another important quantity of an electrical machine is the electromotive force (emf). The instantaneous value of the phase voltage in a PM machine can be defined by the following expression

$$u_{\mathrm{ph}}(t) = i_{\mathrm{ph}}(t)R + \frac{\mathrm{d}\psi_{\mathrm{ph}}(t)}{\mathrm{d}t}, \tag{3.21}$$

where i_{ph} is the instantaneous value of the phase current [A], R is the phase resistance [Ω], and ψ_{ph} is the instantaneous phase flux linkage [Vs]. The latter part of the equation is the emf, which is induced by the changing magnetic flux in the phase coil. This flux linkage of the coil includes flux originating from the PM, armature field, and the field of eddy currents. In this section, an approach to calculate the PM emf based on field solutions obtained from the 2D and 3D harmonic modeling is discussed.

3.2.1 Permanent magnet emf calculation for the 2D case

The PM flux penetrating a turn of a coil can be calculated as

$$\Phi_{\mathrm{PM}} = \int_{S_{\mathrm{turn}}} \vec{B}_{\mathrm{PM}} \mathrm{d}\vec{S}, \tag{3.22}$$

where $\vec{S}$ is the area enclosed by the coil turn [m^2]. The formulation of the magnetic field in the 2D HM is performed by means of vector potential. Taking into account Stoke's theorem, (3.22) for a 2D problem can be rewritten as

$$\Phi_{\mathrm{PM}}(t) = \oint_C \vec{A}_{\mathrm{PM}}(r,\theta,t) \mathrm{d}\vec{l}, \tag{3.23}$$

where $\vec{l}$ is the contour of the coil turn [m]. The PM flux linkage of a coil is defined as a summation of fluxes through each coil turn. Using the winding distribution function, f_{w}, the equation for the flux linkage of the PM field through a coil can be defined as in [15], [58]

$$\psi_{\mathrm{PM}}(t) = \frac{lN}{s} \int_{-\pi}^{\pi} f_{\mathrm{w}}(\theta) A_{z,\mathrm{PM}}(r = r_{\mathrm{wc}}, \theta, t) \mathrm{d}\theta, \tag{3.24}$$

where s is the phase spread in the circumference [rad], and r_{wc} is the radial coordinate of the winding center [m], which is calculated as

$$r_{\mathrm{wc}} = \frac{r_{\mathrm{wo}} + r_{\mathrm{wi}}}{2}. \tag{3.25}$$

Substituting (2.65) and (3.7) into (3.24) and taking the time derivative results in the expression of the PM emf of a phase coil

$$e_{\mathrm{PM}}(t) = \frac{lN}{s} \sum_{\nu=1}^{\infty} (C_{\mathrm{PM}}(\nu) r_{\mathrm{wc}}^{-\nu} + D_{\mathrm{PM}}(\nu) r_{\mathrm{wc}}^{\nu}) \Big(c_{\mathrm{s}}(\nu) \frac{\omega(2\pi\nu - \sin(2\pi\nu))}{2} .$$

$$\sin(\theta_0 - \nu\omega t) - c_{\mathrm{c}}(\nu) \frac{\omega(2\pi\nu + \sin(2\pi\nu))}{2} \cos(\theta_0 - \nu\omega t) \Big). \tag{3.26}$$

It should be noted that the PM field contains all odd harmonics, and these harmonics induce the phase emf harmonics of the same order.

3.2.2   PM emf calculation for the 3D case

The PM emf calculation for a 3D electromagnetic problem using (3.23) seems inconvenient, because the winding distribution contains a 2D Fourier series. In this case, it is thus more suitable to calculate the PM flux linking a phase coil by employing (3.22), which can be written as

$$\psi_{\mathrm{PM}}(t) = \sum_{w=1}^{N} \int_{S_w} B_{\mathrm{r,PM}}(r, \theta, t) \mathrm{d}S_w, \tag{3.27}$$

where w indicates a turn in the phase coil.

3.2.3   Comparison of the modeling results

To compare the PM emf calculation results given by the FEM and the semianalytical models, the benchmark machine with the Faulhaber winding is taken as an example. The calculation of the PM flux linkage of the machine with the Faulhaber winding represents a 3D problem, and therefore, (3.27) has to be implemented. Figure 3.4 shows one phase coil of the Faulhaber winding type, where the red area indicates the area of the PM flux density integration for the calculation of the flux penetrating the turn indicated by blue. Thus, using (3.8) and (3.9), the expression (3.27) for the Faulhaber winding type can be rewritten as

$$\psi_{\mathrm{PM}}(t) = \sum_{w=1}^{N} \sum_{\nu=1}^{\infty} \left(\int_{-\pi}^{0} \int_{(l\theta/\pi - l/2)}^{l/2} \Lambda_{\mathrm{PM,r}}(r = r_{\mathrm{wc}}) \cos(\nu(\theta - \omega t) + \theta_0 + \alpha) \mathrm{d}z \mathrm{d}\theta \right.$$

$$\left. + \int_{0}^{\pi} \int_{(-(\theta+\pi)l/\pi + l/2)}^{l/2} \Lambda_{\mathrm{PM,r}}(r = r_{\mathrm{wc}}) \cos(\nu(\theta - \omega t) + \theta_0 + \alpha) \mathrm{d}z \mathrm{d}\theta \right), \tag{3.28}$$

$$\alpha = -\frac{\pi}{3} + \frac{2\pi w}{3N}.$$

The eventual expression of the PM emf is obtained by performing the time derivation over (3.28), which results in

$$e_{\mathrm{PM}}(t) = \sum_{w=1}^{N} \sum_{\nu=1}^{\infty} \Lambda_{\mathrm{PM,r}}(r = r_{\mathrm{wc}}) \frac{4l\omega}{\nu\pi} \left(2\nu\pi \cot\left(\frac{\nu\pi}{2}\right) - 1 \right) \cdot$$

$$\sin\left(\frac{\nu\pi}{2}\right)^2 \sin(\theta_0 + \alpha(w) - \nu\omega t). \tag{3.29}$$
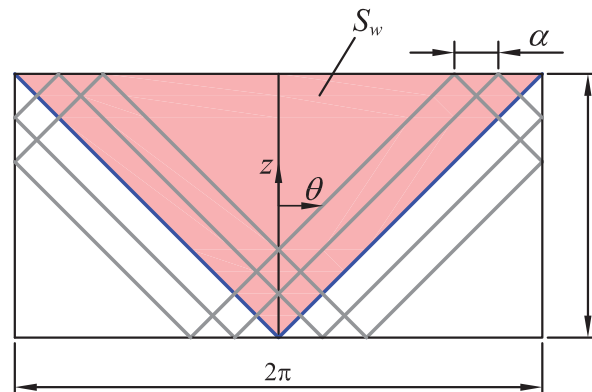
Figure 3.4: Representation of one phase of the Faulhaber coil in the $\theta - z$ plane. The red area indicates the flux density integration area, and α is the shift between the neighboring turn.

The results of the PM emf calculations are shown in Figure 3.5, where the relative discrepancy between the FEM and the semianalytical modeling results does not exceed 4%. The difference can be explained by the different radial positions of the winding in the 3D semianalytical and 3D FEM models.
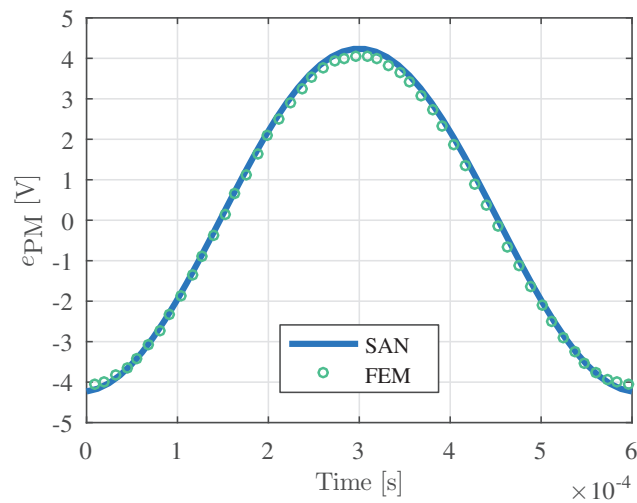
Figure 3.5: Emf profile induced in the winding as a result of the changing PM field, calculated by the 3D semianalytical model (SAN) and the 3D FEM.

3.3   Synchronous inductance

Inductance defines the ability of a coil to produce flux linkage [91], and can be calculated by dividing the flux linkage of this coil by the current in it. The term 'synchronous inductance' usually refers to polyphase systems, where a mutual influence on the flux linkage of the phase coils is present. Hence, the synchronous inductance of a phase coil in a three-phase PM machine consists of the self-inductance and two mutual inductances, where these mutual inductances are usually merged into one term. From the inductance definition it is evident that the calculation of the synchronous inductance considers only the flux linkage originating from the armature field, and it can be written mathematically as

$$L_\mathrm{s} = \frac{\psi_\mathrm{AR,ph}}{i_\mathrm{ph}}. \tag{3.30}$$

Taking into account the influence of the eddy-current reaction on the armature flux linkage, the inductance calculation using the above equation should be performed at the time instant when the phase current reaches its amplitude value.

3.3.1   Synchronous inductance in a 2D problem

Calculation of the phase flux linkage originating from the armature field for a 2D problem is performed, similarly to (3.24), as

$$\psi_\mathrm{AR,ph}(t) = \frac{lN}{s} \int\limits_{-\pi}^{\pi} f_\mathrm{w}(\theta) A_\mathrm{z,AR}(r = r_\mathrm{wc}, \theta, t)\mathrm{d}\theta. \tag{3.31}$$

Using (2.65), (3.10), and (3.31), the synchronous inductance can be derived in the general form for a 2D problem as

$$L_\mathrm{s}(k) = \sum_{L=-\infty}^{\infty} \frac{lN}{i(t,k)s} \left[\mathrm{Re}\left(\pi c_\mathrm{s}(L,k)\bar{\Lambda}_\mathrm{s}\mathrm{e}^{\mathrm{j}k\omega t} + \pi c_\mathrm{c}(L,k)\bar{\Lambda}_\mathrm{c}\mathrm{e}^{\mathrm{j}k\omega t} \right) \right], \tag{3.32}$$

where

$$\bar{\Lambda}_\mathrm{s} = \bar{C}_\mathrm{s,AR} r_\mathrm{wc}^{-(3L-k)} + \bar{D}_\mathrm{s,AR} r_\mathrm{wc}^{(3L-k)},$$
$$\bar{\Lambda}_\mathrm{c} = \bar{C}_\mathrm{c,AR} r_\mathrm{wc}^{-(3L-k)} + \bar{D}_\mathrm{c,AR} r_\mathrm{wc}^{(3L-k)}.$$

Here, it should be noted that even if the winding distribution function contains both sine and cosine components simultaneously, the flux linkage, which results from the sine components of the winding distribution function and the cosine component of the vector potential, as well as the cosine components of the winding

distribution function and the sine component of the vector potential, will be zero. The equation also takes into account the change in the synchronous inductance value caused by the induced eddy currents. This is important information in the modeling and design process of high-speed PM machines, which helps to predict the behavior of these machines under the influence of different time harmonics present in the phase current.

3.3.2   Synchronous inductance in a 3D problem

In a 3D electromagnetic problem the calculation of the phase synchronous inductance is performed by the following equation

$$L_{\mathrm{s}}(k) = \frac{1}{i(t,k)} \sum_{w=1}^{N} \int_{S_w} B_{\mathrm{AR,r}}(r = r_{\mathrm{wc}}, \theta, z, t, k) \mathrm{d}S_w. \tag{3.33}$$

3.3.3   Comparison of the inductance calculation

The benchmark machine with the Faulhaber winding (see Table 2.4) is used in order to compare the synchronous inductance calculation results produced by the 3D FEM and the method proposed earlier. Similarly to 3.28, the expression for the synchronous inductance calculation of the benchmark machine is defined as

$$\begin{aligned}
L_{\mathrm{s}}(k) = {}& \sum_{L=-\infty}^{\infty} \sum_{w=1}^{N} \frac{1}{i(t,k)} \left(\int_{-\pi}^{0} \int_{(l\theta/\pi - l/2)}^{l/2} B_{\mathrm{AR,r}}(r = r_{\mathrm{wc}}, \theta + \alpha, z, t, k) \mathrm{d}z \mathrm{d}\theta \right. \\
& \left. + \int_{0}^{\pi} \int_{(-(\theta+\pi)l/\pi + l/2)}^{l/2} B_{\mathrm{AR,r}}(r = r_{\mathrm{wc}}, \theta + \alpha, z, t, k) \mathrm{d}z \mathrm{d}\theta \right), \\
\alpha = {}& -\frac{\pi}{3} + \frac{2\pi w}{3N}.
\end{aligned} \tag{3.34}$$

Here, the expression of the radial component of the flux density for the benchmark machine contains three terms, which is explained by three terms of the linear current density distribution of a Faulhaber winding (see A.11). Although, an analytical solution of this equation may exist, the synchronous inductance value has been numerically calculated.

The results of the synchronous inductance calculation using the 3D FEM and solving (3.34) are depicted in Figure 3.6. The relative difference between these results does not exceed 5%. The decrease in the inductance over the time harmonic order can be explained by the influence of the reaction field of the induced rotor
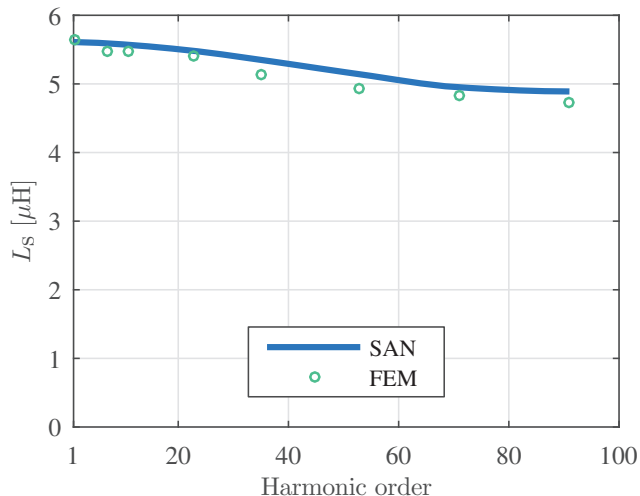
Figure 3.6: Results of the synchronous inductance over the time harmonic order, obtained by using the 3D semianalytical model (SAN) and the 3D FEM for the benchmark machine with the Faulhaber winding.

eddy currents. The change of the synchronous inductance depends on the machine geometry, material parameters, such as conductivity and magnetic permeability, and the fundamental frequency. These dependences are discussed in detail in the following chapter with the explanation of the rotor eddy-current losses.

3.4   Summary

This chapter gives insight into the calculation of the electromagnetic quantities, such as the electromagnetic torque, PM electromotive force (emf), and synchronous inductance, of slotless PM machines.

Using the general expression of the PM and armature magnetic field distributions in the air gap given by the HM, the Maxwell stress tensor is applied to derive general semianalytical expressions for the torque calculation for the 2D and 3D cases. These expressions also contain the components for the calculation of the torque component resultant from the interaction of the armature and rotor eddy-current fields. The benchmark machine with the Faulhaber winding is used to verify the semianalytical torque calculation by the 3D FEM, where the obtained relative error is about -4%. The expressions to calculate the PM emf for the 2D and 3D cases are provided in Section 3.2 of this chapter. The verification of these expressions is performed on the benchmark machine with the Faulhaber winding by comparing the results with the 3D FEM. The obtained PM emf shows good agreement with a relative error of 4%.

Section 3.3 of the chapter deals with the synchronous inductance calculation of the slotless machines by providing the calculation expressions for the 2D and 3D cases. The synchronous inductance calculation expressions contain the expression of the armature field produced by the HM and thereby take into account the inductance change caused by rotor eddy currents. This frequency-dependent synchronous inductance will be used in Chapter 4 to predict the influence of the PWM on the rotor eddy-current losses. Similarly as in the previous sections, the verification of the synchronous inductance calculation is performed for the benchmark machine with the Faulhaber winding by comparing the results with the 3D FEM. The obtained relative error does not exceed 5%.

4

Electromagnetic losses

In this chapter, an analysis and analytical assessment of electromagnetic losses induced in high-speed slotless PM machines are given.

4.1 Power losses

The electromechanical power conversion in electrical machines is not an ideal process, because power losses are present during power conversion. For motoring mode, these dissipated losses can be determined as a difference between the input (electrical) power and the output (shaft) power,

$$P_{\text{loss}} = P_{\text{in}} - P_{\text{out}}, \tag{4.1}$$

which additionally represents the power balance for the high-speed slotless PM machines. The main losses present in these machines are described by the Sankey diagram shown in Figure 4.1. The losses in this diagram are divided into two

Input (electrical) power

Losses caused by armature current P_{in} *Losses caused by rotation*

Joule losses in the winding, caused by

    applied current, P_{Cu}

    skin effect, P_{s}

    proximity effect, P_{pa}

Joule losses in the winding, caused by

PM field proximity effect, P_{pPM}

Eddy-current losses in,

    rotor, P_{r}

    housing, P_{h}

Iron losses, P_{FePM}

Iron losses, P_{Fea}

Mechanical losses

    Windage losses, P_{w}

    Bearing losses, P_{b}

P_{out}

Output (mechanical) power

Figure 4.1: Sankey diagram of the main losses present in high-speed slotless PM motors.

groups, namely losses caused by the armature current and losses caused by rotation of the rotor. Using the concept of these two groups of losses, the input and output power can be linked with the electromagnetic torque, T_{m}. The input power of the machine equals the sum of the power caused by the electromagnetic torque and

losses caused by the armature current, which is written as

$$P_{\text{in}} = T_{\text{m}}\Omega + P_{\text{Cu}} + P_{\text{s}} + P_{\text{pa}} + P_{\text{r}} + P_{\text{h}} + P_{\text{Fea}}. \tag{4.2}$$

Again, the output power equals the difference of the power caused by electromagnetic torque and losses caused by rotation, which is expressed as

$$P_{\text{out}} = T_{\text{m}}\Omega - P_{\text{pPM}} - P_{\text{FePM}} - P_{\text{w}} - P_{\text{b}}. \tag{4.3}$$

These relations are important in the machine design routine, since usually electromagnetic torque is the intermediate parameter by which the power on the shaft and the input power/voltage of the machine can be obtained. Further in this chapter, only the analysis and calculation of electromagnetic losses present in high-speed slotless PM machines are discussed.

4.2   Joule losses in the windings

In general, Joule losses (also known as ohmic losses) in an electrical conductor can be calculated as

$$P = I^2 R, \tag{4.4}$$

where I is the DC or RMS value of the current passing through the conductor [A] and R is the DC resistance of the conductor [Ω], which is calculated as

$$R = \rho \frac{l_{\text{c}}}{S_{\text{c}}}, \tag{4.5}$$

where $\rho = 1/\sigma$ is the electrical resistivity of the conductor material [Ω·m], l_{c} is the length of the conductor [m], and S_{c} is the cross-section of the conductor [m^2]. The electrical resistivity is a temperature-dependent parameter, and therefore the temperature influence on the DC resistance should be taken into consideration during the machine design. The power calculated using this DC resistance value ignores extra Joule losses caused by a changing magnetic field in the conductor.

4.2.1   Joule losses in the winding caused by the applied current

Joule losses in the machine winding caused by the three-phase currents applied through the machine terminals, considering a symmetrical three-phase system, can be determined as

$$P_{\text{Cu}} = 3I^2 R_{\text{ph}}, \tag{4.6}$$

where 3 in this equation refers to the number of phases in the winding, I is the RMS value of the phase current [A], and R_{ph} is the resistance of the phases [Ω].

In practice, Joule losses caused by the applied current are also present in the connecting wires (wires that connect the winding with the power supply). These losses can be significant, and therefore, in the machine analysis/design, it is recommended to include the resistance of the connecting wire in the resistance of the winding coil.

4.2.2 Joule losses in the winding caused by induced eddy currents

The winding conductors of any electrical machine are always penetrated by a magnetic field. For slotless PM machines, this penetrating magnetic field has two components: armature and PM fields. As the total magnetic field changes with time, according to (2.2), an electric field is produced, which causes eddy currents in these conductors. This effect is significant and requires extra attention in high-speed machines, because the frequency of the field change is relatively high [93] [94].

According to [105], the classification of the types of Joule losses present in winding conductors as a result of induced eddy currents is illustrated in Figure 4.2. Here, the induced eddy currents are addressed both at the strand and bundle levels and considering the distribution of induced eddy currents, namely skin and proximity effects. The bundle of conductors simply represents parallel conductors, which
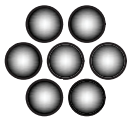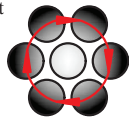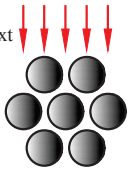

Figure 4.2: Graphical illustration of the induced eddy currents in the winding conductors caused by the skin and proximity effects; from the perspective of one strand and one bundle.

are electrically connected at the machine terminals. Usually, small-diameter conductors connected in parallel into a bundle or Litz wires are used in high-speed electrical machines in order to reduce the strand-level losses resulting from the skin or/and proximity effects. In a winding, the bundles of conductors are placed close to each other, and therefore, the bundle-level skin effect can be taken into account by the strand-level proximity effect, where the external field is the armature field.

It should be explicitly specified that all eddy currents induced in the conductors of the machines under study are assumed to be resistance limited. This means that the field produced by these eddy currents does not oppose the original field causing these eddy currents. A more detailed explanation of resistance-limited eddy currents is given in Section 4.3.

The calculation of total loss can be performed by superimposing the loss caused by each effect individually, even though these effects may occur simultaneously. The calculation of the proximity effect losses should be performed with the total field resultant from different magnetic field sources. For instance, in slotless PM machines, the proximity effect loss calculation should be done with the resultant field caused by the armature and PM fields.

Strand-level skin effect losses

The alternating current flowing inside a conductor/strand forces the current to shift towards the outer surface of this conductor; this phenomenon is known as the skin effect. The current distribution in the conductor caused by the skin effect results from the distribution of the current flowing through the conductor and the eddy currents induced by the changing magnetic field caused by this flowing current. This effect becomes significant at higher frequencies, where the losses caused by the induced eddy currents are no longer negligible. Commonly, these losses are modeled as an additional resistance and merged with the actual (DC) resistance of the conductor; this resistance is widely known as the AC resistance of a conductor.

The AC resistance of a conductor can be derived from the current density distribution inside the conductor. This current density distribution can be obtained by solving the Bessel differential equation in cylindrical coordinates within the conductor. Using the obtained current density distribution in the conductor, the impedance of the conductor can be written as [67]

$$Z_c(\omega) = R_c(\omega) + j\omega L_c(\omega) = \frac{l_c j^{\frac{3}{2}} \beta}{2\pi r_c \sigma} \frac{I_0(j^{\frac{3}{2}} \beta r_c)}{I_1(j^{\frac{3}{2}} \beta r_c)}, \tag{4.7}$$

where L_c is the internal inductance of the conductor [H], r_c is the radius of the conductor [m], I_0 and I_1 are the 0th- and 1st-order modified Bessel functions of the first kind, respectively, and $\beta = \sqrt{\omega \sigma \mu}$.

The AC resistance and internal inductance of the conductor can be expressed in terms of frequency-independent resistance, known as DC resistance, of the conductor as

$$R_{\mathrm{c}}(\omega) = R \cdot \mathrm{Re}\left(\frac{\mathrm{j}^{\frac{3}{2}}\beta}{2}\frac{I_0(\mathrm{j}^{\frac{3}{2}}\beta r_{\mathrm{c}})}{I_1(\mathrm{j}^{\frac{3}{2}}\beta r_{\mathrm{c}})}\right), \tag{4.8}$$

$$L_{\mathrm{c}}(\omega) = R \cdot \mathrm{Im}\left(\frac{\mathrm{j}^{\frac{3}{2}}\beta}{2\omega}\frac{I_0(\mathrm{j}^{\frac{3}{2}}\beta r_{\mathrm{c}})}{I_1(\mathrm{j}^{\frac{3}{2}}\beta r_{\mathrm{c}})}\right), \tag{4.9}$$

where R is calculated by using (4.5).

The skin effect is always present in conductors with AC currents; however, it can be insignificant. To quickly estimate the importance of the skin effect, the concept of skin depth, which is given by the following equation, can be used

$$\delta = \sqrt{\frac{2}{\omega\sigma\mu}}. \tag{4.10}$$

Physically, skin depth represents the depth from the conductor surface at which the current density has a value of $1/e \approx 0.37$ of the current density value at the surface of the conductor. It can be assumed that if the skin depth is larger than the conductor radius, the skin effect in the conductors can be neglected.

Strand-level proximity effect losses

In slotless PM machines, the winding conductors are penetrated by an external field resulting from two sources, namely the armature and PM fields. This field causes eddy currents within each conductor, and correspondingly, generates Joule losses [27], [83]. These losses can be assessed analytically by assuming that the induced eddy currents are resistance limited [106].

For the slotless PM machines where the conductors are directed axially in the active part of the machine, it can be assumed that the total field penetrating the conductors has only radial and circumferential components. In this case, the cross-section of the conductor in polar $(r$–$\theta)$ coordinates represents a circle. To simplify the proximity loss calculation, the conductor is placed in Cartesian $(x$–$y)$ coordinates (see Figure 4.3), and the field inside the conductor is assumed to be only a function of time.

Using the notation from Figure 4.3, the emf of the eddy-current loop can be defined as

$$e_{\mathrm{p}}(x,t) = \frac{\mathrm{d}\varPhi}{\mathrm{d}t} = 2xl_{\mathrm{c}}\frac{\mathrm{d}B(t)}{\mathrm{d}t}. \tag{4.11}$$
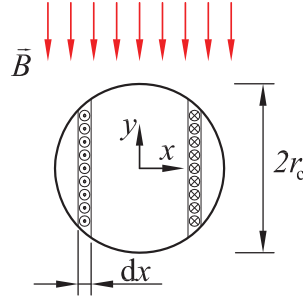
Figure 4.3: r–θ cross-section of an axially directed round conductor represented in Cartesian coordinates $(x$–$y)$. The current loop with a thickness of $\mathrm{d}x$ is the induced eddy current caused by the changing external magnetic field $\vec{B}$ [106].

The resistance of the same loop is given as

$$R_{\mathrm{p}}(x) = \frac{2l_{\mathrm{c}}\rho}{2\sqrt{r_{\mathrm{c}}^2 - x^2}\mathrm{d}x}. \tag{4.12}$$

Using the above equations, the dissipated power over the conductor can be calculated as

$$P_{\mathrm{p}}(t) = \int\limits_{0}^{r_{\mathrm{c}}} \left(2xl_{\mathrm{c}}\frac{\mathrm{d}B(t)}{\mathrm{d}t}\right)^2 \frac{\sqrt{r_{\mathrm{c}}^2 - x^2}\mathrm{d}x}{l_{\mathrm{c}}\rho} = \frac{\pi l_{\mathrm{c}} r_{\mathrm{c}}^4}{4\rho}\left(\frac{\mathrm{d}B(t)}{\mathrm{d}t}\right)^2. \tag{4.13}$$

Because the distribution of the armature and PM fields in the winding area is defined as a Fourier series, meaning that each harmonic of the field causes sinusoidal field variation, the average power over one period is given as

$$P_{\mathrm{p}} = \frac{\pi l_{\mathrm{c}} r_{\mathrm{c}}^4 \hat{B}^2 \omega^2}{8\rho}. \tag{4.14}$$

The cross-section of the conductor is symmetrical in the x- and y-directions, and therefore, (4.14) is identical for the loss calculation of the θ and r field components.

For skewed conductors, that is, conductors in Faulhaber, rhombic, and diamond windings, the cross-section of these conductors in polar $(r$–$\theta)$ coordinates represents an ellipse. As the cross-section is not symmetrical in radial and circumferential directions, the proximity loss calculation differs for the radial and circumferential field components. Similarly to the proximity loss calculation for the circular cross-section, Cartesian $(x$–$y)$ coordinates are placed in the middle of the conductor cross-section (see Figure 4.4). The values of the radial (indicated as B_{y} in the figure) and circumferential (indicated as B_{x} in the figure) magnetic field components within this conductor are assumed to be only space dependent. The
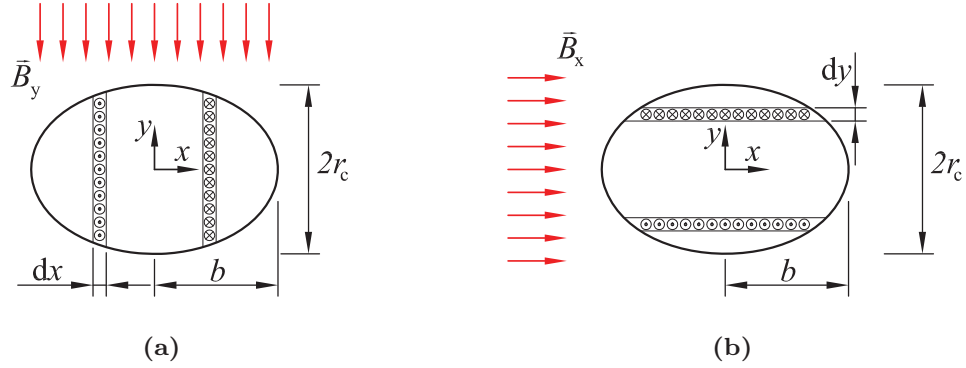
Figure 4.4: r–θ cross-section of a skewed round conductor represented in Cartesian coordinates (x–y). a) Induced current loop with a thickness of $\mathrm{d}x$ caused by the changing external $\vec{B}_\mathrm{y}$. b) Induced current loop with a thickness of $\mathrm{d}y$ caused by the changing external $\vec{B}_\mathrm{x}$.

influence of the axial field component present in the armature field of the winding with skewing on the proximity effect losses is neglected.

The calculation of the induced emf in the loop (see Figure 4.4(a)) caused by $B_\mathrm{y}(t)$ is similar to (4.11). Using the equation of an ellipse, the resistance of the loop can be obtained as

$$R_\mathrm{p}(x) = \frac{2l_\mathrm{c}\rho}{2y\mathrm{d}x} = \frac{l_\mathrm{c}\rho}{\sqrt{b^2 - x^2}\dfrac{r_\mathrm{c}}{b}\mathrm{d}x}. \tag{4.15}$$

The variable b in this equation defines the width of the ellipse, and can be calculated as

$$b = \frac{r_\mathrm{c}}{\sin(\gamma)}, \tag{4.16}$$

where γ is the skewing angle [rad], which is for instance for a Faulhaber winding defined as $\gamma = \arctan(l/(r_\mathrm{wc}\pi))$ and r_wc is given by (3.25). Using (4.11) and (4.15), the expression for power dissipated over the conductor at any time instant can be derived as

$$P_\mathrm{p}(t) = \int_0^b \left(2xl_\mathrm{c}\frac{\mathrm{d}B_\mathrm{y}(t)}{\mathrm{d}t}\right)^2 \frac{\sqrt{b^2 - x^2}\dfrac{r_\mathrm{c}}{b}\mathrm{d}x}{l_\mathrm{c}\rho} = \frac{\pi l_\mathrm{c} b^3 r_\mathrm{c}}{4\rho}\left(\frac{\mathrm{d}B_\mathrm{y}(t)}{\mathrm{d}t}\right)^2. \tag{4.17}$$

Replacing $B_\mathrm{y}(t)$ by $B_\mathrm{r}(t)$ and assuming sinusoidal field variation inside the conductor, the average power is calculated as

$$P_\mathrm{p,r} = \frac{\pi l_\mathrm{c} b^3 r_\mathrm{c} \hat{B}_\mathrm{r}^2 \omega^2}{8\rho}. \tag{4.18}$$

In a similar manner, the expression for power dissipated over the conductor in the case of Figure 4.4(b) at any time instant is derived as

$$P_\mathrm{p}(t) = \int\limits_0^{r_\mathrm{c}} \left(2yl_\mathrm{c}\frac{\mathrm{d}B_\mathrm{x}(t)}{\mathrm{d}t}\right)^2 \frac{\sqrt{r_\mathrm{c}^2 - y^2}\,\dfrac{b}{r_\mathrm{c}}\mathrm{d}y}{l_\mathrm{c}\rho} = \frac{\pi l_\mathrm{c} r_\mathrm{c}^3 b}{4\rho}\left(\frac{\mathrm{d}B_\mathrm{x}(t)}{\mathrm{d}t}\right)^2. \tag{4.19}$$

Replacing $B_\mathrm{x}(t)$ by $B_\theta(t)$ and assuming sinusoidal field variation inside the conductor, the average power dissipated because of the proximity effect caused by the circumferential field component can be obtained as

$$P_{\mathrm{p},\theta} = \frac{\pi l_\mathrm{c} b r_\mathrm{c}^3 \hat{B}_\theta^2 \omega^2}{8\rho}. \tag{4.20}$$

The expressions for the proximity loss calculations (4.14), (4.18), and (4.20) are verified by the FEM for different conductor diameters, different magnetic flux densities, and frequencies. For the round conductor cross-section, the relative error does not exceed 1%, and for the elliptic conductor cross-section, the relative error remains within 10%. The error increases when the skin depth is smaller than the conductor radius, because the induced eddy currents are not resistance limited anymore.

Bundle-level proximity effect losses

As it was explained previously, the strand-level skin and proximity losses are reduced by using conductors of a smaller diameter connected in parallel. Using parallel conductors (strands) within a bundle raises yet another issue called the bundle-level proximity effect, which considers circulating currents between these parallel conductors.

In an example shown in Figure 4.5(a), a coil consisting of one turn with two parallel strands, indicated as 1 and 2, is placed in a time-varying magnetic field. These parallel strands are electrically connected at the winding terminals, where the electrical circuit of the winding is illustrated in Figure 4.5(b). In this example, two parallel conductors are circumferentially displaced by an angle ϕ, which results in a phase shift of the induced emfs in each strand for the same angle. This phase shift in the emfs causes the circulating currents between these strands. Generally speaking, the circulating currents are a consequence of the instantaneous emf difference between each strand. This difference is explained by different fluxes linked by each strand resulting from the spatial displacement of the strands with respect to each other.

To reduce the circulating currents between parallel strands, these strands simply need to be twisted in the longitudinal direction to alternate the displacement order

(a)   (b)
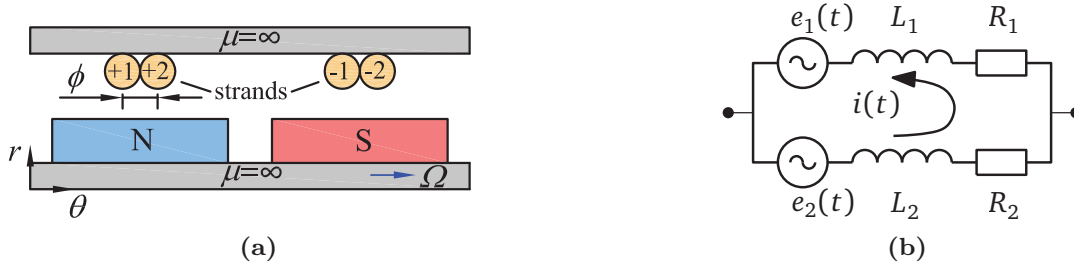
Figure 4.5: a) One-turn coil consisting of two parallel strands, which are short-circuited at the coil terminals, placed in a time-varying PM field and b) the equivalent electrical circuit of the coil, where R_1 and R_2, L_1 and L_2, and $e_1(t)$ and $e_2(t)$ are resistances, inductances, and emfs of the first and second strands, respectively.
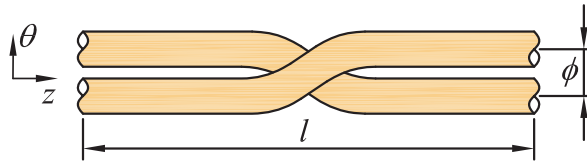
Figure 4.6: Twisting of parallel strands to reduce the bundle level proximity effect.

as shown in Figure 4.6. Only one twist in the middle part of the bundle suffices; however, for practical reasons, the bundle is usually twisted over the whole length. Litz wires are a good example of braided parallel strands, where each strand changes position in the wire cross-section within a certain distance. The use of Litz wires reduces the skin effect and proximity effect losses in high-frequency applications [1] [2]. Drawbacks of Litz wires are their high price, increased DC resistance, and lower space factor of copper compared with a bundle of non-twisted strands of the same cross-section.

Accurate assessment of the bundle-level proximity losses requires information of the exact spatial position of each strand in a bundle. The position of each strand depends on the winding process and may vary from one machine specimen to another. The bundle-level proximity losses can be estimated by analytical and FEM approaches. The authors of [8], [112] have proposed analytical methods based on an electrical circuit to calculate these losses for machines with a predetermined position of strands. Analysis of the bundle-level proximity losses for a predetermined position of strands using the FEM is presented in [61], [40], [89], [32]. Again, approaches based on an electrical circuit and the FEM for strands with random positions are reported in [70]. All these methods focus on the analysis of circulating current losses in slotted machines, where the slot geometry inherently makes it difficult to obtain the field distribution inside the slots and determine the electrical circuit parameters of each parallel strand. For slotless machines, in

the case of nontwisted strands in a bundle and having the spatial position of the strands, the bundle-level proximity losses can be assessed by using the electrical circuit of the bundle. The emfs of each strand in this circuit are obtained by using the armature and PM field distributions from the harmonic modeling (HM), given in Chapter 2. The disadvantage of this method is that it is the more complex, the higher is the number of parallel strands in the bundle.

4.3   Rotor eddy-current loss

Induced rotor eddy currents are a significant issue in high-speed PM machines as the heat generated by these currents may lead to the demagnetization of the PM. Accordingly, accurate prediction of these losses is important in the design stage to ensure safe thermal operating conditions for the PM.

Rotor eddy-current losses can be assessed using the Poynting theorem, which is expressed in the integral form for the quasi-static problem as [46]

$$-\oint_S \vec{P} \cdot \mathrm{d}\vec{S} = \frac{\partial}{\partial t} \int_V \frac{1}{2} \mu \vec{H} \cdot \vec{H} \mathrm{d}V + \int_V \vec{H} \cdot \frac{\partial \vec{B}_{\mathrm{rem}}}{\partial t} \mathrm{d}V + \int_V \vec{J} \cdot \vec{E} \mathrm{d}V, \quad (4.21)$$

where S represents the surface enclosing the volume [m^2], and $\vec{P}$ is the Poynting vector, which represents the directional energy flux density of an electromagnetic field and is given by

$$\vec{P} = \vec{E} \times \vec{H}. \tag{4.22}$$

The minus sign in front of the integral with the Poynting vector indicates that the power is transmitted to the volume, but not out of it. The expression (4.21), assuming that $\vec{J}$ belongs to the eddy currents, can be rewritten as

$$P_{\mathrm{in}} = \frac{\partial W_{\mathrm{m}}}{\partial t} + P_{\mathrm{out}} + P_{\mathrm{diss}}, \tag{4.23}$$

where P_{in} is the power that crosses the surface of the volume under consideration [W], W_{m} is the energy stored in the magnetic field [J], P_{out} is the mechanical power [W], and P_{diss} is the dissipated power resulting from the Joule losses [W]. Applying the Poynting theorem to a slotless PM machine with zero internal magnetization of the PM, (4.21) is transformed into

$$-\oint_S \vec{P} \cdot \mathrm{d}\vec{S} = \int_V \vec{J} \cdot \vec{E} \mathrm{d}V. \tag{4.24}$$

In this case, P_{out} is zero as $\vec{B}_{\mathrm{rem}} = 0$, and there is no change in the magnetic energy as there is no variation in permeance over the circumference. Therefore,

all power delivered from the stator to the rotor through the surface of the volume is dissipated in the rotor eddy-current losses. It is pointed out that this equation represents instantaneous power values. From this equation, the rotor eddy-current losses can be calculated by using integrals from both sides of the expression. Calculation of the volume integral can be problematic [113], because the expressions of both $\vec{J}$ and $\vec{E}$ obtained by the harmonic modeling (HM) contain Bessel functions. Integration of the Poynting vector over the surface is more convenient, and thus, further calculations of the rotor eddy-current losses are performed by using the Poynting vector.

Calculation of the Poynting vector requires expressions for the electrical and magnetic field strengths, which can be obtained by using the HM as a sum of sinusoidal harmonics varying at a specific frequency. Assuming that the general expression of the electrical field strength for the fundamental time harmonic is given as $\vec{E}(r,\theta,z,t) = \mathrm{Im}(\vec{E}_s(r,\theta,z)\mathrm{e}^{\mathrm{j}\omega t}) + \mathrm{Re}(\vec{E}_c(r,\theta,z)\mathrm{e}^{\mathrm{j}\omega t})$, and correspondingly for the magnetic field strength as $\vec{H}(r,\theta,z,t) = \mathrm{Im}(\vec{H}_s(r,\theta,z)\mathrm{e}^{\mathrm{j}\omega t}) + \mathrm{Re}(\vec{H}_c(r,\theta,z)\mathrm{e}^{\mathrm{j}\omega t})$, the average value of the Poynting vector at any point within the surface over one electrical period can be obtained as

$$\vec{P}_{av} = \frac{1}{2}\mathrm{Re}\left(\vec{E}_s \times \vec{H}_s^* + \vec{E}_c \times \vec{H}_c^*\right), \tag{4.25}$$

where $*$ refers to the complex conjugation, and subscripts s and c refer to the sine and cosine components of the quantities, respectively. Here it is pointed out that $\vec{E}_s(t)$ originates from $\vec{H}_s(t)$, $\vec{E}_c(t)$ from $\vec{H}_c(t)$, and the mutual circumferential shift between $\vec{H}_s(t)$ and $\vec{H}_c(t)$ is $\pi/2$. Because of this shift, the components of the Poynting vector resultant from the mutual influence of the sine and cosine terms cancel out. Further, the rotor losses over one period can be calculated by integrating the average Poynting vector over the surface around the rotor, which is written as

$$P_r = -\frac{1}{2}\oint_S \mathrm{Re}\left(\vec{E}_s \times \vec{H}_s^* + \vec{E}_c \times \vec{H}_c^*\right) \cdot \mathrm{d}\vec{S}. \tag{4.26}$$

The resultant of the eddy-current losses from all time and space harmonics calculated by using (4.26) can be summed up to calculate the average total rotor eddy-current losses dissipated in the rotor, when considering only integer time harmonics. Here, the rotor eddy-current loss fluctuation in time occurs because of the interaction between the eddy-current harmonics of the same spatial order and different time harmonic orders. However, when considering one electrical period of the fundamental harmonic, the average of the sum of the losses equals the sum of the average of the losses.

4.3.1   Calculation of rotor eddy-current losses in the 2D case

In the 2D case, the axial components of the magnetic vector potential, $\vec{A}_z$, alone define the behavior of the electric and magnetic fields in all the modeled regions of the slotless PM machines. Consequently, the magnetic field strength has only radial and circumferential components, and the electric field strength has only an axial component, as can be seen from (2.23) and (2.37). Using (4.26), which defines the power transmitted from the stator to the rotor, for the calculation of the rotor eddy-current losses, the integration surface should also be defined between the stator and the rotor. Assuming the integration surface to be a cylinder with a radius r, (4.26), regardless of the sine or cosine term, is transformed into

$$P_{\mathrm{r}} = \frac{1}{2} \int\limits_{-\pi}^{\pi} \int\limits_{-l/2}^{l/2} \mathrm{Re}\left(\hat{\bar{E}}_{\mathrm{z}}(r,\theta) \cdot \hat{\bar{H}}_{\theta}^{*}(r,\theta) \right) r \mathrm{d}\theta \mathrm{d}z, \tag{4.27}$$

where r is defined as $r_{\mathrm{ro}} \leqslant r \leqslant r_{\mathrm{wi}}$, in which r_{wi} is the inner radius of the slotless winding [m], and r_{ro} is the outer rotor radius [m]. The exact radius of the integration cylinder does not influence the power loss calculation, because there is no power dissipated in the air gap. Taking the solution of the armature magnetic vector potential in the air gap, a general expression for the rotor eddy-current loss calculation is obtained as

$$P_{\mathrm{r}} = \frac{\pi l r}{\mu} \sum_{\substack{k=1 \\ L=-\infty}}^{\infty} \frac{3L\omega}{3L - k} \mathrm{Re}\left(-\bar{\Lambda}_{\mathrm{s,r}} \bar{\Lambda}_{\mathrm{s,\theta}}^{*} - \bar{\Lambda}_{\mathrm{c,r}} \bar{\Lambda}_{\mathrm{c,\theta}}^{*} \right), \tag{4.28}$$

where $\bar{C}_{\mathrm{s,AR}}$ and $\bar{D}_{\mathrm{s,AR}}$ are complex unknown constants related to the sine term of the vector potential, $\bar{C}_{\mathrm{c,AR}}$ and $\bar{D}_{\mathrm{c,AR}}$ are complex unknown constants related to the cosine term of the vector potential, and $\bar{\Lambda}_{\mathrm{s,r}}$, $\bar{\Lambda}_{\mathrm{c,r}}$, $\bar{\Lambda}_{\mathrm{s,\theta}}$, and $\bar{\Lambda}_{\mathrm{c,\theta}}$ are defined by (C.2) in Appendix C.

4.3.2   Calculation of rotor eddy-current losses in the 3D case

As it was mentioned previously, modeling of a slotless PM machine in 3D requires implementation of both the 2D and 3D harmonic modeling approaches. Calculation of the rotor eddy-current losses using the electromagnetic field solution obtained by the 2D HM was considered earlier in this study. In the 3D HM, the magnetic vector potential has an axial component, $\vec{A}_z$, and also a circumferential one, $\vec{A}_\theta$. Assuming again an integration surface in the cylindrical form, (4.26) for

the 3D HM, regardless of the sine or cosine term, is rewritten as

$$P_\mathrm{r} = \frac{1}{2} \int\limits_{-\pi}^{\pi} \int\limits_{-l}^{l} \mathrm{Re}\left(\hat{\hat{E}}_\mathrm{z}(r,\theta,z) \cdot \hat{\hat{H}}_\theta^*(r,\theta,z) - \hat{\hat{E}}_\theta(r,\theta,z) \cdot \hat{\hat{H}}_\mathrm{z}^*(r,\theta,z)\right) r \mathrm{d}\theta \mathrm{d}z,$$

(4.29)

The integration over the z-axis is performed from $-l$ to l as it is set in the axial periodicity of the 3D HM. In the 3D HM, the electromagnetic field is solved by means of the second-order vector potential (SOVP), and $\vec{A}$ using the formulation of the SOVP is only defined within the conducting regions (see 2.1.4). Therefore, to calculate the rotor eddy-current losses, the radius of the integration surface should be placed on the outer surface of the rotor conducting region, where the $\vec{E}$ and $\vec{H}$ distributions are defined. Although it is possible to derive an analytical expression of (4.29), it has been calculated numerically in the same manner as shown in [55].

4.3.3   Verification by the 3D FEM

Verification of the rotor eddy-current loss calculation is performed on the benchmark machines (see Table 2.4). Results of rotor eddy-current losses obtained by using the HM and the 3D FEM for different time harmonics are given in Table 4.1. In both models, the amplitude value of the phase current is set to 1A. The results demonstrate good matching, where the maximum relative difference does not exceed 5%.

Table 4.1: Rotor eddy-current losses of the benchmark machines calculated for different time harmonics and the peak value of the phase current of 1A (semianalytical - SAN, 3D FEM - FEM)

P [W] $\qquad k$	1	7	13	23	35
Faulhaber					
SAN	$3.1 \cdot 10^{-5}$	$9.5 \cdot 10^{-3}$	$3.7 \cdot 10^{-2}$	0.139	0.288
FEM	$3.0 \cdot 10^{-5}$	$9.5 \cdot 10^{-3}$	$3.6 \cdot 10^{-2}$	0.132	0.289
Rhombic					
SAN	$1.6 \cdot 10^{-5}$	$8.2 \cdot 10^{-3}$	$3.2 \cdot 10^{-2}$	0.121	0.245
FEM	$1.7 \cdot 10^{-5}$	$8.3 \cdot 10^{-3}$	$3.2 \cdot 10^{-2}$	0.124	0.251
Diamond					
SAN	$9.1 \cdot 10^{-5}$	$1.4 \cdot 10^{-2}$	$5.5 \cdot 10^{-2}$	0.197	0.429
FEM	$9.5 \cdot 10^{-5}$	$1.4 \cdot 10^{-2}$	$5.5 \cdot 10^{-2}$	0.209	0.422
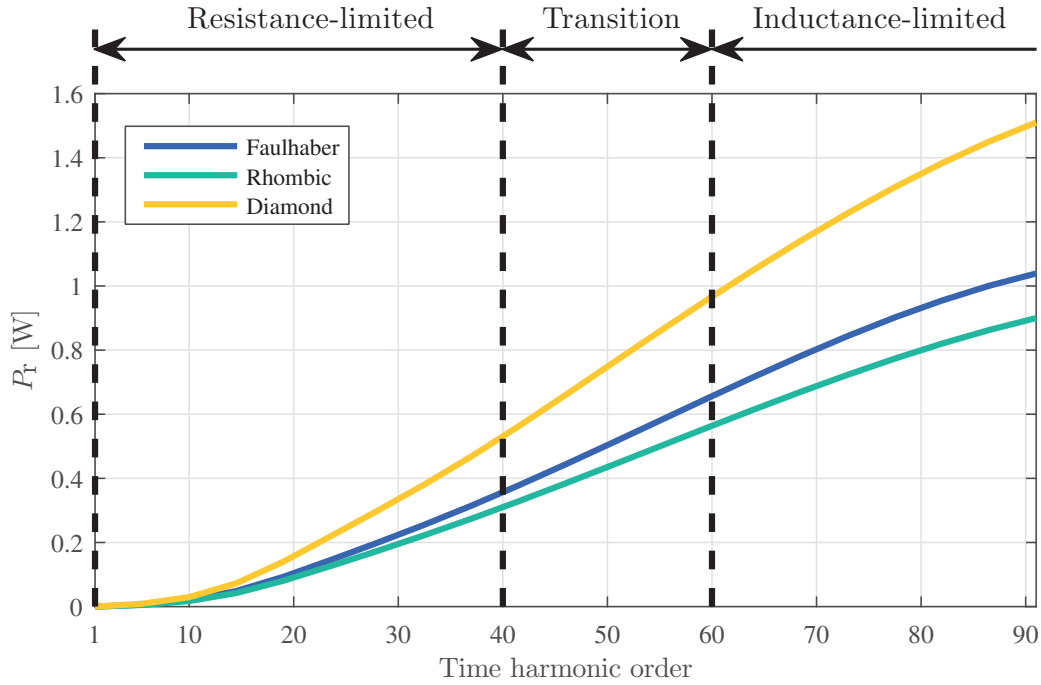
Figure 4.7: Interpolated rotor eddy-current losses of the benchmark machines versus the time harmonic order with the peak value of the phase current of 1 A.

4.3.4 Resistance- and inductance-limited eddy currents

The behavior of eddy-current losses as function of the field frequency causing them is not constant. In many cases, this behavior is assumed to be $P \propto f^2(\omega_r^2)$, which is a good assumption at "low" frequencies. However, when dealing with "high" frequencies, which can be the case for high-speed machines, this assumption is no longer valid. The rotor eddy-current losses of the benchmark machines are plotted as a function of time harmonic order in Figure 4.7. The figure shows that the dependence can be hypothetically divided into three regions, namely resistance limited, transition, and inductance limited. Further, to support the explanation of the change in the behavior of the rotor eddy-current losses, an equivalent electric circuit of the eddy-current path is introduced in Figure 4.8. In this circuit, $e_{a,ec}$ is the induced emf produced by the armature field, ψ_a, without the reaction field of the rotor eddy currents. The influence of the rotor eddy-current reaction field, ψ_r, on the equivalent electrical circuit is taken into account by the inductance L_r.

Resistance-limited eddy currents occur at low frequencies, where the impedance of the rotor equivalent circuit is mainly defined by R_r, resulting in a small phase shift between $e_{a,ec}$ and i_{ec} as shown in Figure 4.9(a). In reality, it is never possible to achieve purely resistance-limited eddy currents because L_r is never zero. In
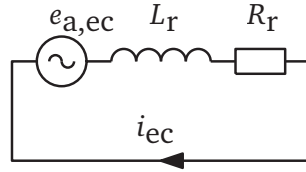
Figure 4.8: Equivalent electrical circuit of the rotor eddy currents, where $e_{a,ec}$ [V] represents the emf induced by the armature field without taking into account the rotor eddy-current field, R_r [Ω] is the resistance of the rotor eddy-current path, and L_r [H] is the inductance of the rotor eddy-current path.

the region of resistance-limited eddy currents, the influence of the rotor eddy-current field on the armature field is negligible. Thus, the current density can be considered equally distributed along the radial direction, and R_r is assumed to be constant [44]. Accordingly, the rotor eddy-current losses in the resistance-limited eddy-current region can be assumed proportional to f^2.

Inductance-limited eddy currents are generated at high frequencies, where the reaction field of the rotor eddy currents tends to oppose the armature field. According to [41], an indication of the inductance-limited eddy-current region is when i_{ec} lags from $e_{a,ec}$ for more than 45 electrical degrees. Further, according to [44], a skin effect occurs, as a result of which the eddy currents are concentrated within the skin depth. The rotor eddy-current losses in the inductance-limited eddy-current region are assumed to have a dependence of $P \propto \sqrt{f}$. A purely inductance-limited eddy-current case is illustrated in Figure 4.9(c), which corresponds to $R_r = 0$. This may happen only if the material of the rotor is superconducting. The external field does not penetrate the rotor, and the rotor eddy currents are fully concentrated on the surface of the rotor in this case [104].

The transition region, which approximately corresponds to the phase shift of 45 electrical degrees between i_{ec} and $e_{a,ec}$ as shown in Figure 4.9(b), is dependent on the geometrical parameters of the machines and their magnetic (μ) and electric

Figure 4.9: Vector diagram of the armature flux and its derivatives observed in the rotor circuit, without PM field consideration: a) for the case of purely resistance-limited eddy currents, b) for the case of a transition region, and c) for the case of purely inductance-limited eddy currents.

(σ) material properties. At the level of the equivalent rotor circuit, this practically means a change in R_r and L_r. By changing the values of these parameters, the behavior of the eddy currents over the frequency can be affected. For instance, 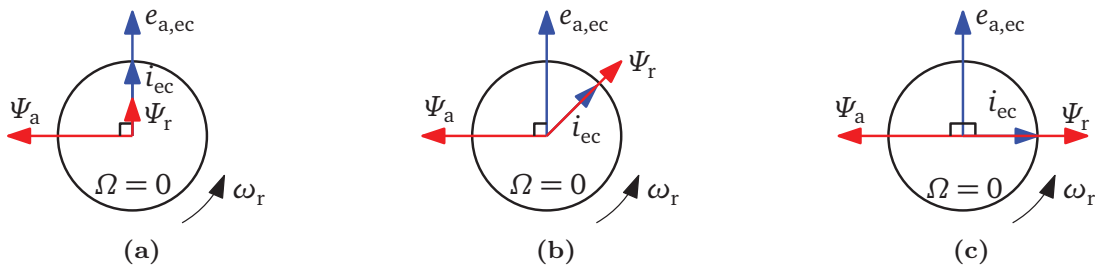by increasing the conductivity of the material it is possible to decrease losses for the time harmonics in the inductance-limited eddy-current region. However, this will simultaneously lead to an increase in losses for the time harmonics in the resistance-limited eddy-current region. This behavior of rotor eddy currents can be used to diminish the eddy-current losses for certain influential time harmonics in the supply current, for instance current harmonics resulting from pulse-width modulation switching. Similarly to rotor eddy currents, eddy currents in conductors generated by internal (skin effect) and external (proximity effect) fields can also be distinguished as resistance- and inductance-limited ones. When considering eddy currents caused by an internal field in the conductor, they are assumed to be inductance limited as these eddy currents tend to oppose the original current flowing in this conductor. This leads to the skin effect, when the current inside this conductor is "pushed" towards the walls (skin) of the conductor. In the case of the proximity effect, the field caused by the inductance-limited eddy currents, similar to the inductance-limited rotor eddy currents, tends to oppose the external field.

In practice, a fast way to distinguish the resistance- or inductance-limited behavior of the eddy currents by the external magnetic field is to apply an approximation based on the skin depth (see (4.10)). If the skin depth, δ, is larger than the thickness of the conducting material in the direction of the field penetration, the eddy currents are assumed to be resistance limited. Then again, if the skin depth is smaller, the eddy currents are inductance limited. However, this approximation is less accurate for problems considered in cylindrical coordinates [109], since the skin depth expression is derived for the Cartesian coordinate problem.

4.4 Iron losses

The history of iron loss modeling dates back to 1892, when Charles Proteus Steinmetz proposed the first approach for the analytical assessment of iron losses [103]. Even though iron loss modeling has a long history, analytical assessment of iron losses has been challenging until the present time. This is mainly related to two factors, which are the difficulty of modeling the actual physical phenomena causing iron losses, and discrepancies introduced by the manufacturing process of the machine iron parts (cutting, stacking, housing assembly) [65]. There are many of models to calculate the iron losses; however, in this study, a model based on loss separation is employed. This model adopts an empirical approach that does not describe the actual physical phenomena [95]; nevertheless, it yields reasonable accuracy with a minimum calculation effort.

The loss separation approach, proposed by [51], was originally based on dividing the iron into two components, namely hysteresis (static) losses and eddy-current (dynamic) losses. To improve the model, an additional loss component, called excess losses, was introduced. Thus, the iron losses per mass unit can be expressed as

$$p_{\text{Fe}} = p_{\text{hyst}} + p_{\text{eddy}} + p_{\text{exc}}, \tag{4.30}$$

where p_{hyst} are the hysteresis loss component [W/kg], p_{eddy} is the loss component caused by induced eddy currents [W/kg], and p_{exc} is the excess loss component [W/kg]. This expression can be rewritten as a function of the amplitude value of the flux density and its frequency

$$p_{\text{Fe}} = C_{\text{hyst}} f \hat{B}^2 + C_{\text{eddy}} f^2 \hat{B}^2 + C_{\text{exc}} f^{1.5} \hat{B}^{1.5}, \tag{4.31}$$

where C_{hyst}, C_{eddy}, and C_{exc} are hysteresis, eddy-current, and excess loss coefficients, respectively. The values of C_{eddy} and C_{exc} can be determined analytically as explained in [6], [7], whereas C_{hyst} can be determined by measurements, for instance ring core tests [65]. The loss separation approach has the following disadvantages: the losses are estimated only for sinusoidally varying magnetic flux density; the magnetic field is assumed to be alternating, but not rotating, and the eddy currents in the iron laminations are assumed to be resistance limited.

The iron losses can also be obtained for nonsinusoidal flux density variation, for example to take into account the influence of PWM switching [12], [19], [28], [35]. In this case, the PWM iron losses are dependent on the switching frequency, modulation principle, and mainly on the modulation index. In [65], the PWM influence on iron losses in slotless PM machines has been investigated, and it has been found that the iron loss rise owing to the PWM nature compared with the sinusoidal flux density can be up to 30%. However, the influence of PWM on the iron losses in slotless PM machines is not in the scope of this research, and therefore, this influence is neglected. Finally, assuming the PM field one order of magnitude higher than the armature field, only the iron losses caused by the PM field are taken into account.

4.5   PWM influence on losses

Inherently, all high-speed machines are supplied by power inverters (converters). Ideally, the current in the machine phases should have a sinusoidal waveform; however, this current contains ripple (time harmonics) because of the converter switching. Even though the values of these harmonics are low in general, because of their high-frequency nature, this current ripple may produce considerable losses caused by induced currents in the machines [31], [71]. Especially, the current

ripple can be significant in machines with a low synchronous inductance value, for instance in high-speed slotless PM machines. In these machines, high-frequency current ripple is the main cause of rotor eddy-current losses [54], [78]. Additionally, current ripple produces skin and proximity losses in the winding conductors [50]. Thus, it is important to take into account the influence of current ripple on the total losses in slotless PM machines.

Voltage source inverters (VSIs) with a three-leg topology are typically employed to supply high-speed slotless PM machines (Figure 4.10(a)). In most cases, the modulation principle of these VSIs is pulse-width modulation (PWM) or pulse-amplitude modulation (PAM) depending on the motor type, operating speed, and dynamic requirements [116], [98]. PWM VSIs have high control dynamics, but require a relatively high switching frequency. PAM VSIs with block voltage commutation have a lower switching frequency; however, these inverters require additional controllable DC link voltage [115]. Generally speaking, if the drive dynamics is not the target, the modulation principle should be selected with the aim to minimize losses in the overall drive system. Nevertheless, the aim of this study is not to find an optimal modulation principle, but the objective is to estimate the influence of the current ripple caused by the modulated voltage of the VSI on losses in slotless high-speed PM machines. As the approach of modeling the influence of PAM VSI can be implemented reciprocally, only the influence of PWM VSIs is considered in this section.

4.5.1   Modeling of the current ripple caused by PWM

Modeling of current ripple can be performed using a simplified one-phase electrical circuit of the PM machine shown in Figure 4.10(b) [79]. In this simplified circuit, the emf induced by the PM field is neglected as it is assumed that the frequency of the significant emf harmonics is lower than the switching frequency. It is well known that the higher harmonics of a three-phase VSI PWM voltage occur around the multiples of the switching frequency as shown in Figure 4.11. These harmonics are called sideband harmonics. Additionally, under some modulation schemes, lower-frequency, but higher than the fundamental, harmonics may occur. These harmonics are called baseband harmonics. Theoretically, the harmonic spectrum of any 3-phase PWM voltage can be expressed as a Fourier series. An analytical approach and examples to obtain PWM voltage harmonic spectrum are explained in detail in [47]. In a general form, this Fourier series for sideband harmonics for a three-phase system can be written as [56]

$$u_{\text{PWM}} = \sum_{m=1}^{\infty} \sum_{n=-\infty}^{\infty} \hat{U}_{\text{PWM}}(U_{\text{DC}}, M, m, n) \cos((m \cdot m_{\text{f}} + n)\omega_1 t + nx), \quad (4.32)$$

$$x = (0, \frac{2\pi}{3}, \frac{4\pi}{3}),$$

Figure 4.10: a) Three-phase voltage source inverter connected to a PM synchronous machine (PMSM). b) Simplified one-phase electrical circuit of the PMSM to model higher-order current harmonic ripple assuming the PM emf harmonics to have a much lower frequency than the switching frequency. Here, u_{PWM} [V] is the voltage harmonics (except fundamental) caused by PWM switching, L_{s} [H] is the synchronous phase inductance of the PM machine, whose value is a function of frequency, and R_{s} [Ω] is the AC resistance of the stator phase coil.
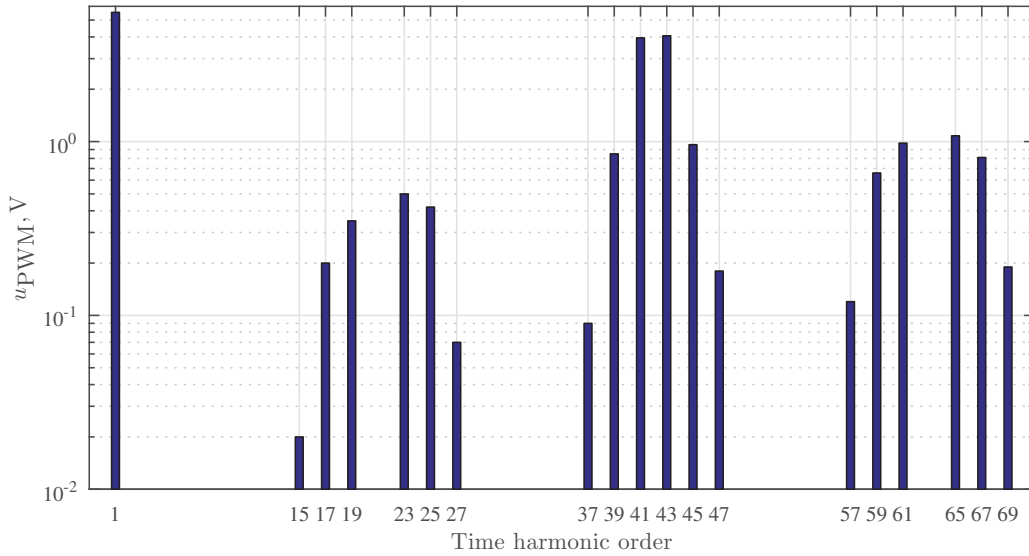
Figure 4.11: Theoretical harmonic spectrum of a three-phase voltage source inverter with the asymmetrical regular-sampled space vector modulation (amplitude modulation ratio $M = 0.4$, DC bus voltage $U_{\text{DC}} = 24$ V and frequency modulation ratio $m_{\text{f}} = 21$).

where $\hat{U}_{\text{PWM}}$ is the amplitude of a sideband harmonic [V], U_{DC} is the DC bus voltage [V], M is the amplitude modulation ratio ($0 \leq M \leq 1$), m is the sideband order, n is the position of the harmonic in the sideband, m_{f} is the frequency modulation ratio (f_{sw}/f_1), f_{sw} is the switching frequency [Hz], f_1 is the frequency of the fundamental harmonic [Hz], ω_1 is the angular frequency of the fundamental harmonic [rad/s], and x is the phase shift in a three-phase system [rad]. To relate m and n to the time harmonic order k, which is used in the electromagnetic field model, and the corresponding angular frequency, the following expression is

introduced:

$$k = m \cdot m_{\mathrm{f}} + n. \tag{4.33}$$

Expression examples of the Fourier series for the asymmetrical regular-sampled sinusoidal and asymmetrical regular-sampled space vector (SV) PWMs are given in Appendix D. Further, using the obtained PWM voltage spectrum and a simplified phase electrical circuit (see Figure 4.10(a)), the amplitude value of the phase current ripple can be calculated by [57]

$$\hat{I}(k) = \sum_{m=1}^{\infty} \sum_{n=-\infty}^{\infty} \frac{\hat{U}_{\mathrm{PWM}}(m,n)}{\sqrt{R^2(k\omega_1) + (k\omega_1 L(k\omega_1))^2}}. \tag{4.34}$$

The resultant current ripple series is further used to obtain the magnetic field and electromagnetic losses by applying the methods explained in the previous two chapters.

It should be also mentioned that sometimes passive filters are added to reduce the voltage and current ripple. The modeling of the current ripple in this case is performed in a similar manner by taking into consideration filter components.

4.5.2 Verification of the calculated current ripple

The current ripple calculation is verified by current measurements on a high-speed slotless PM machine supplied by inverters with two distinct modulation principles. The test machine represents a slotless PM machine with a three-phase toroidal winding shown in Figure 4.12(a). In these measurements, an impeller of a centrifugal blower is used as a load. As can be seen from Figure 4.12(b), the rotor of the machine has a shaftless structure with a two-pole diametrically magnetized PM, which is covered by a retaining sleeve. The stator core is made from sintered ferrite iron to reduce eddy-current losses. The machine is equipped with an aluminum housing in order to shield the high-frequency magnetic field produced by the outer part of the toroidal winding. The machine parameters are listed in Table 4.2. With these parameters, a complete 2D harmonic model of this machine is implemented, and the dependence of the phase synchronous inductance and the frequency is extracted and plotted in Figure 4.12(c). The phase resistance is assumed to be frequency independent and modeled as a DC resistance.

The test machine is tested with two three-leg inverters with sinusoidal and SV PWMs. The inverter with sinusoidal modulation has asymmetrical regular sampling with a switching frequency of 62.5 kHz and a DC bus voltage of 70 V. This inverter is equipped with filtering chokes of 60 µH at each phase output. The second inverter is based on an asymmetrical regular-sampled space vector modulation strategy. The switching frequency of the inverter is set to 60 kHz, and the

(a)

(b)

(c)
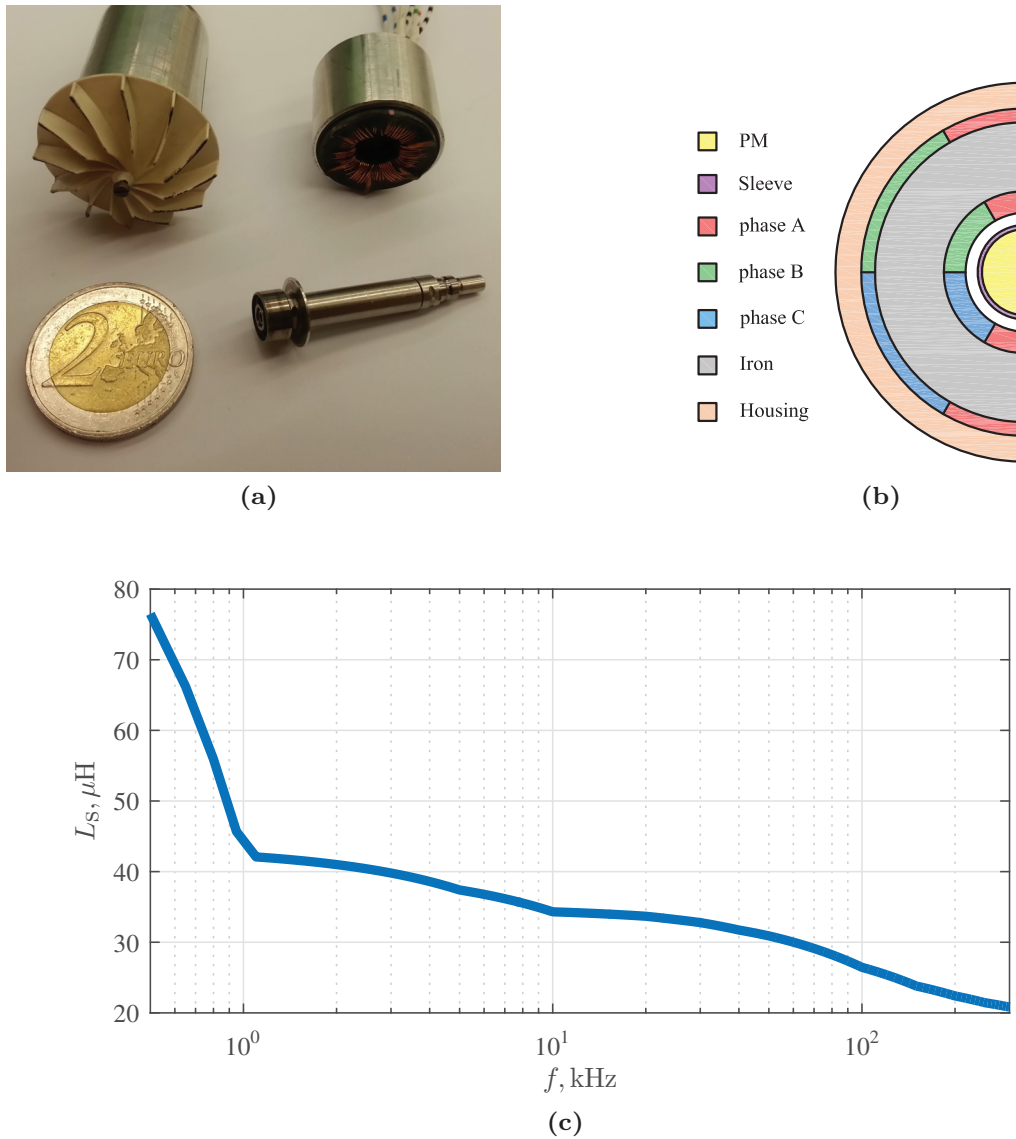
Figure 4.12: a) High-speed slotless PM machine and its parts, namely rotor and stator, with a toroidal winding configuration, which is used for current ripple measurements, b) cross-section of the test machine, and c) simulated synchronous inductance of the test machine as a function of frequency.

DC bus voltage is kept at 24 V. Inherently, the inverter has no output filtering components.

Further, by using (4.34), the peak values of PWM current harmonics for the sinusoidal and SV PWMs are calculated and given in Table 4.3. In addition, the phase currents of the test machine supplied by the two aforementioned converters are measured. The harmonics are extracted from the measured currents and represented in Table 4.3. The maximum relative error between the measured and

Table 4.2: Test machine specifications

Parameter	Value	Unit
Rated power	50	W
Rated speed	80000	rpm
Rated torque	6	mNm
DC phase resistance	0.88	Ω
Turn number	28	tuns
Active length	16	mm
PM radius	2.5	mm
Sleeve thickness	0.25	mm
Air gap	0.7	mm
Inner winding thickness	1.25	mm
Iron core thickness	4	mm
Outer winding thickness	0.8	mm
Housing thickness	1.5	mm
Sleeve material	Stainless steel	-
Housing material	Aluminum	-
PM resistivity	$1.7 \cdot 10^{-5}$	Ωm
PM permeability	$1.035 \cdot \mu_0$	Hm^{-1}

analytically obtained results is 39%. This discrepancy can be explained by the current measurement error and the parasitic impedance present in the circuit, for instance cables from the inverters to the test machine, which are not taken into account. Moreover, the Fourier series of the PWM voltage represents a purely theoretical spectrum and may vary in practice [47].

4.6 Summary

This chapter gives an introduction into main losses occurring in high-speed slotless PM machines; however, only the main electromagnetic losses are discussed in detail. The loss analysis starts with consideration of Joule losses in the winding, distinguished as losses caused by armature current conduction and losses caused by induced eddy currents. The main focus is on the analysis of winding Joule losses caused by induced currents, where the skin and proximity effect losses at the strand and bundle level are distinguished. The explanation of the physical phenomena behind each loss component, important properties, and analytical approaches to assess them are provided in Section 4.2.

Table 4.3: Harmonic comparison of the calculated and measured peak values of currents caused by the asymmetrical regular sampled sinusoidal PWM ($M = 0.23$ and $f_1 = 434$ Hz) and the asymmetrical regular-sampled space vector PWM ($M = 0.29$ and $f_1 = 507$ Hz)

Sinusoidal PWM				
m	n	Predicted current [A]	Measured current [A]	Relative error, %
1	-2	0.021	0.025	19
1	2	0.021	0.021	0
2	-1	0.113	0.11	-3
2	1	0.113	0.11	-3
3	-2	0.020	0.016	-20
3	2	0.020	0.013	-35
4	-1	0.048	0.050	4
4	1	0.048	0.051	6
5	-2	0.017	0.012	-29
5	2	0.017	0.011	-35
Space vector PWM				
m	n	Predicted current [A]	Measured current [A]	Relative error, %
1	-2	0.011	0.014	27
1	2	0.011	0.013	18
2	-1	0.085	0.090	6
2	1	0.085	0.087	2
3	-2	0.012	0.015	25
3	2	0.013	0.015	15
4	-1	0.036	0.022	-39
4	1	0.036	0.022	-39
5	-2	0.011	0.011	0
5	2	0.011	0.011	0

Section 4.3 deals with the calculation of the rotor eddy-current losses using the electromagnetic field solution obtained from the harmonic modeling. These losses are assessed by means of the Poynting vector, where a purely analytical solution of the rotor eddy-current loss calculation is derived for the 2D case. For the 3D case, a general expression is derived; however, owing to the complexity of the analytical expression it is recommended to implement it numerically. The rotor eddy-current loss approach is verified on the benchmark machines using 3D FEM models, and a good accuracy is achieved with a relative error less than 5%. Moreover, explanation of the resistance- and inductance-limited eddy currents is given.

Iron loss calculation taking a loss separation approach is discussed in brief in Section 4.4. Further, in Section 4.5, the influence of the current ripple caused by the PWM switching is analyzed. A model, based on equivalent electrical circuit calculation representing a machine phase, is proposed to predict the current ripple. The synchronous inductance of the test machine is modeled as frequency dependent, and the PWM voltage source is represented as a Fourier series. The current ripple information could later be used to predict losses in the machine caused by this ripple. The current ripple calculation is verified by measurements performed on a high-speed PM machine with toroidally wound slotless coils while supplied by three-phase inverters with sinusoidal and space vector modulations. The maximum relative error between the predicted and measured current ripple of 39% is obtained.

Part II

Design framework

5

Design of high-speed slotless permanent magnet machines

This chapter focuses on obtaining of machine specifications, a topology study, and design optimization methodology for a high-speed slotless PM machine intended for highly dynamic operations.

5.1   Design requirements

5.1.1   Application

The practical objective of this research is to design a new high-speed machine suitable for driving a centrifugal blower, which is installed to a mobile medical ventilator shown in Figure 1.1. The high-speed PM machine should be capable of responding to the dynamic needs of breathing according to Figure 5.1. This figure illustrates the two motion profiles of the high-speed machine required for the breathing support of extreme ventilation cases. The dynamic operating profile requires extra power from the machine for acceleration and deceleration of the overall system inertia. From the electrical drive system perspective, on the one hand, the drive has to satisfy the required speed profiles, and on the other hand, consume a minimum amount of energy from the battery supply to extend the autonomous operating time of the portable ventilator.
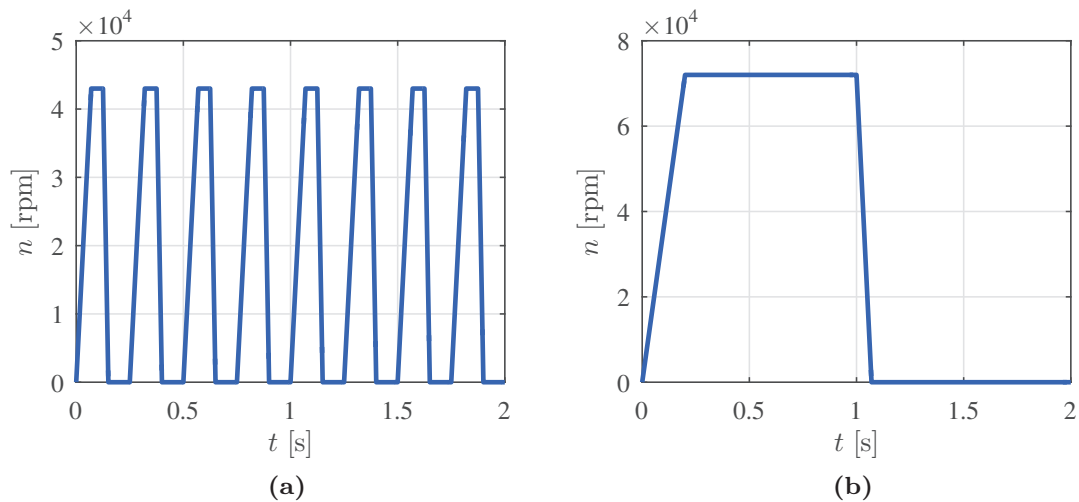
Figure 5.1: Periodic motion profiles of two extreme ventilation cases: a) extreme neonatal and b) extreme adult.

5.1.2 Machine specifications

Design of every electrical machine begins with determination of the machine specifications, which are defined by the load, ambient conditions, and electrical input. The behavior of the centrifugal blower is determined by measurements with a high-speed PM machine with known characteristics. In these measurements, the input power of the machine at different speeds and air flows of the centrifugal blower in the steady state is measured. Assuming the motor efficiency to be constant (at 90%) within the measurement range, the load power, which is consumed by the centrifugal blower, is derived and plotted as a function of speed and gas flow in Figure 5.2. However, the assumption of constant motor efficiency is inaccurate, because the efficiency usually decreases if the machine does not operate at the nominal point, which results in overestimation of the load power. Therefore, the power (torque) requirements set on the machine are higher than the actual ones, meaning that the design will result in a machine with slightly overestimated power (torque). As shown in Figure 5.2, the data for the maximum (required) and zero flows are extrapolated, and it becomes evident that the centrifugal blower requires more torque at the maximum flow. Consequently, further in the calculation, the extrapolated expression of the power required by the centrifugal blower is taken at the maximum flow ($P_{\text{load}} = P_{\text{Max}}$).
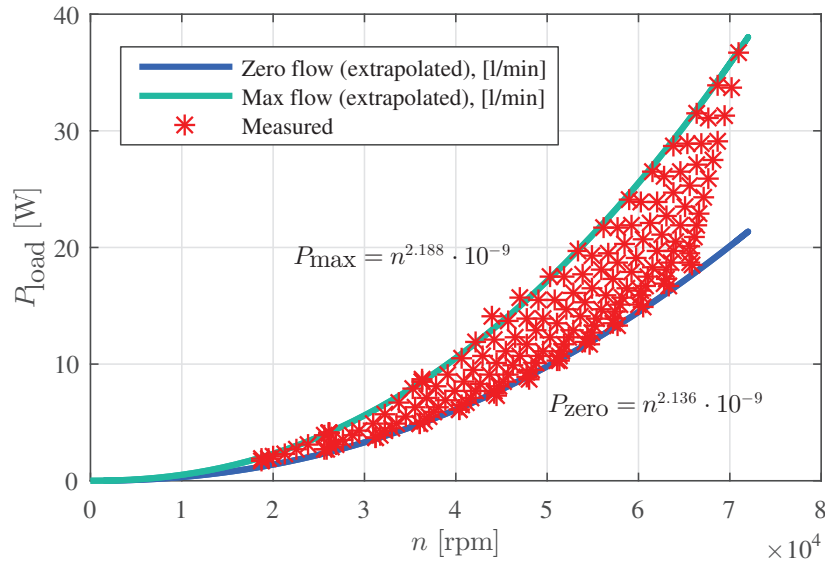
Figure 5.2: Measured steady-state power consumption of the centrifugal blower versus speed at different gas (air) flow values. Power consumption at zero and maximum (130 L/min) gas flows is extrapolated, and the dependences are shown in the figure.

Using the motor speed profile required to meet the extreme neonatal and adult ventilation cases (see Figure 5.1) and the extrapolated power-speed expression, the load torque required for both extreme cases is obtained and plotted in Figure
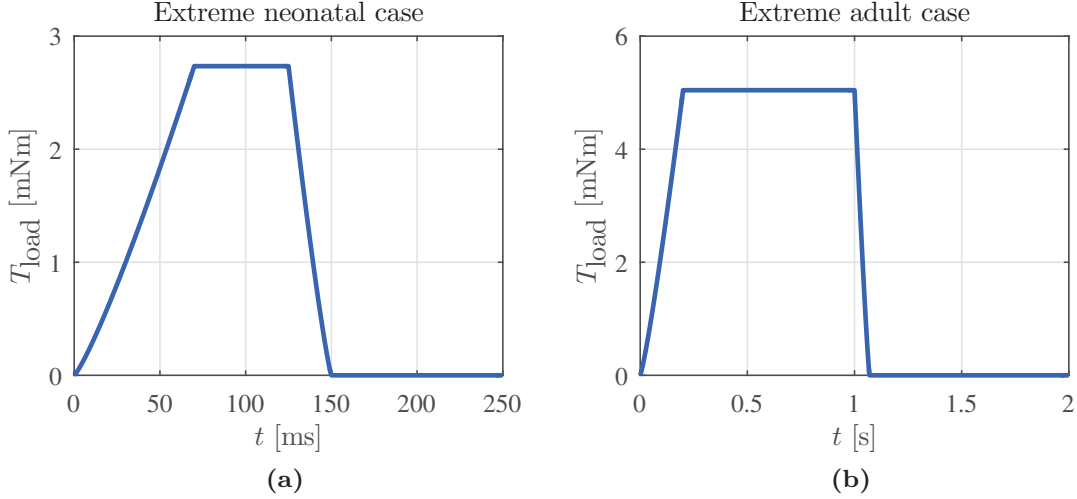
Figure 5.3: Load torque profiles of two extreme cases: a) neonatal and b) adult without taking into account the impeller inertia.

5.3. From these two torque profiles, it is clear that the extreme adult case requires a higher peak torque. However, this system continuously operates in a dynamic state, and the inertias of the motor rotor and the centrifugal blower impeller require additional "dynamic" torque to accelerate and decelerate. The instantaneous torque required from the motor is given as

$$T_{\mathrm{m}}(t) = T_{\mathrm{load}}(t) + (J_{\mathrm{m}} + J_{\mathrm{im}}) \frac{\mathrm{d}\omega(t)}{\mathrm{d}t}, \tag{5.1}$$

where J_{m} is the motor rotor inertia [kg·m²], and J_{im} is the impeller inertia [kg·m²]. The impeller inertia of the centrifugal blower is $J_{\mathrm{im}} = 2 \cdot 10^{-8}$ kg·m².

In practice, to choose an electrical machine for noncontinuous speed and torque profiles, the maximum speed and RMS torque values are usually used as rated values. The maximum theoretical required speed of the machine is 72 kprm; however, the rated speed of the machine is chosen to be 80 krpm to leave some speed reserve. The reason to employ the RMS torque value is to ensure the thermal stability of the machine by not oversizing it. Even though this approach is an assumption and depends on the thermal constant of the winding and the peak value and duration of torque, it is suitable for the load in question as the torque peaks are short compared with the thermal constant. The required RMS torque value can be assessed as

$$T_{\mathrm{req}} = \sqrt{\frac{1}{T} \int_0^T T_{\mathrm{m}}^2(t)\mathrm{d}t}, \tag{5.2}$$

where T is the period of the load torque profile [s]. By this equation, the required RMS torque values for the extreme adult and neonatal cases can be calculated.

The highest of these two values is further used as the required torque value on the shaft of the machine. However, it is not evident which value will be the highest one, as it is highly dependent on the rotor inertia. Therefore, in the optimization, the rotor size should first be defined, whereupon the required torque can be defined. Moreover, because the machine does not have a single operating point but an area of operating points, it is decided to design the machine for the maximum speed and the maximum RMS torque point required by the load. As this machine design has the highest value of total losses, ensuring the thermal stability at this point also ensures the stability at other points.

In addition to the load requirements, the ambient temperature and requirements for the machine dimensions have to be considered. The machine is supposed to operate at the maximum ambient temperature of 40°C without any forced cooling. There are no restrictions on the machine dimensions and mass.

Because the artificial ventilator is assumed to be mobile, the energy is supplied by a battery, and therefore, the input voltage of the drive is defined by the battery voltage. The battery voltage specified by the requirements is 24 V.

5.2 Machine configuration

The stator and rotor configurations of a small-size high-speed slotless PM machine do not only depend on the best machine performance for a specific application, but also on the manufacturing capabilities of a certain machine producer. This section aims to choose the stator and rotor configurations with the theoretically best performance for the load specifications under consideration.

5.2.1 Rotor configuration

Typical rotor configurations used in small-sized high-speed PM machines are illustrated in Figure 5.4. The difference between these rotors is the presence of a shaft, which facilitates manufacturing of a mechanically more balanced rotor. In the case of a shaftless rotor, the two rotor (shaft) ends are screwed and/or glued to each other after the permanent magnet has been inserted. Therefore, misalignment may occur during the rotor assembly. Comparing these rotor configurations from the viewpoint of mechanical stress, it can be noted that the mechanical stress caused by rotation in a hollow cylinder with an infinitesimally small hole is twice as high as in a full cylinder of the same size [15]. This means that the PM material in rotors with shafts experiences at least twice as high as mechanical stress than the PM material in shaftless rotors. Furthermore, a slotless PM machine with the shaftless rotor structure has higher magnetic loading because of the larger volume

(a)

(b)
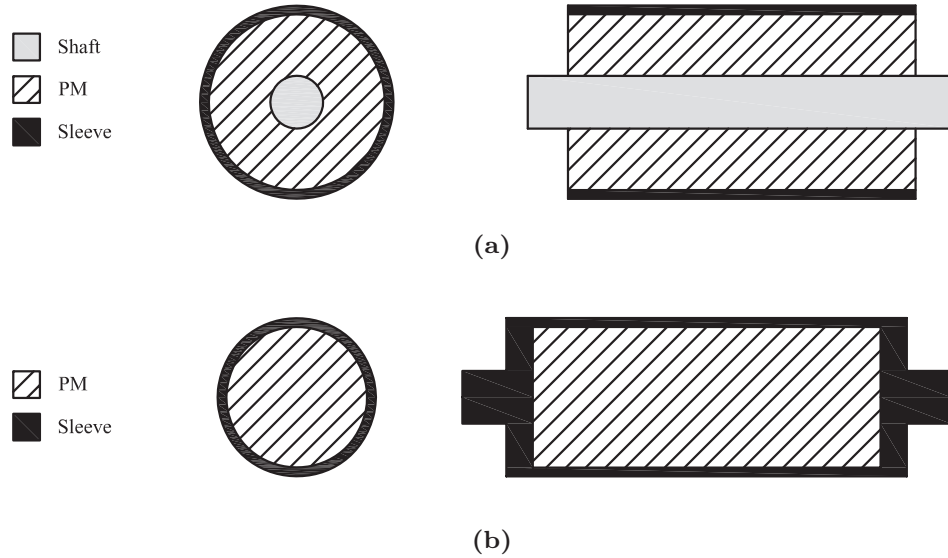
Figure 5.4: Typical rotor configurations of small-sized high-speed PM machines: a) with shaft and b) without shaft.
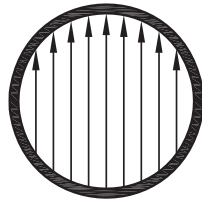
Figure 5.5: Diametrical magnet magnetization.

of the PM material. Taking into account the advantages of the shaftless rotor structure, only this rotor structure is considered further on.

PM magnetization and material

Considering the PM as a cylinder, in practice, only the diametrical magnetization can be implemented. This magnetization pattern is shown in Figure 5.5 and results in purely sinusoidal flux distribution in the air gap. When considering the PM material, NdFeB is chosen as the main candidate as it has a higher energy density and remanent flux density than the other PM types, which guarantees the highest magnetic loading.

Retaining sleeve material

The rotor of a high-speed PM machine is often covered by a retaining sleeve, whose main duty is to prevent disintegration of the PM because of the high centrifugal forces caused by fast rotation. Depending on the conditions, the retaining sleeve can be prestressed, which causes an initial opposite force to the centrifugal force. The retaining sleeve also protects the PM from corrosion by insulating it from moisture and oxygen.

There are many material types that are widely used to produce the sleeve, such as titanium and stainless steel. These materials have different electrical properties, which, as stated in Section 4.3, may influence the amount rotor eddy-current losses. In practice, the different electrical conductivities of the sleeve materials define the location of the transition region from the resistance- to inductance-limited eddy-current losses. Figure 5.6 depicts the different behaviors of the rotor eddy-current losses of the Faulhaber benchmark machine with different material types of the retaining sleeve, the thickness of which is assumed to be 0.25 mm. It can be seen that the region with the resistance-limited eddy-current losses decreases in size as the conductivity of the material increases. At the same time, the rotor eddy-current losses of the higher-conducting material are higher at lower time harmonic orders. The trend changes at higher time harmonic orders, where the rotor with an Inconel 625 sleeve, which has the highest conductivity among the materials under study, has in fact lower rotor eddy-current losses than the rotor without any sleeve. This feature can facilitate reduction of the overall rotor eddy-current losses in the machine by analyzing the losses with different sleeve materials and a specific current ripple content.

5.2.2   Slotless stator configuration

The magnetically active part of the slotless stator consists of a slotless winding and a soft-magnetic (iron) core. This iron core has a shape of a hollow cylinder, whereas the major difference between the slotless stators is the slotless winding type.

Slotless winding type

As it is stated in the introduction of the thesis, self-supporting windings are dominantly used in mass-produced small-sized high-speed machines. The reason is the ability to automate the winding manufacturing process of the self-supported windings. Disregarding the practical aspect and focusing on the theoretical performance, non-self-supporting slotless windings, such as toroidal and concentrated three-coil windings, can also be a successful solution. Obviously, it is difficult to
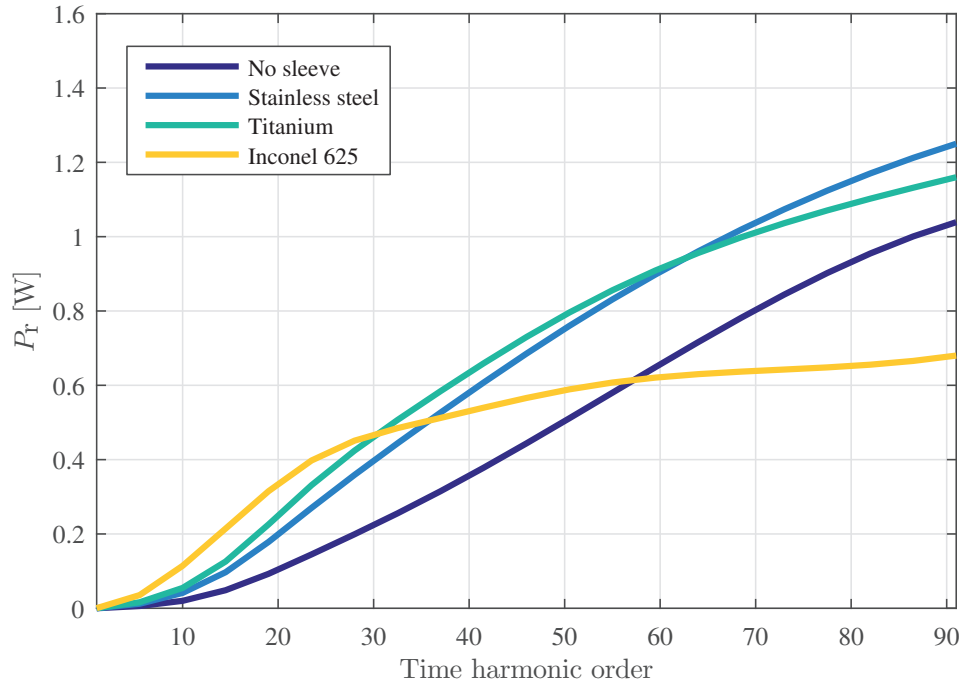
Figure 5.6: Interpolated dependence of rotor eddy-current losses of the benchmark machine with the Faulhaber winding and various sleeve options (no sleeve, stainless steel, titanium, and Inconel 625) versus the time harmonic order. The peak value of the phase current is 1 A for all time harmonic orders. The sleeve materials are listed in the legend by the increase in the electrical conductivity (from the top to the bottom).

speculate on the best winding candidate for a slotless PM machine in advance. Therefore, in the machine design optimization, it was decided to consider three slotless PM machines with toroidal, concentrated, and Faulhaber windings, shown in Figure 5.7. Then, a mutual comparison was made of the obtained designs for the application under study.

Soft-magnetic material

In conventional electrical (low frequency) machines, as soft-magnetic materials mainly alloys of iron (Fe) and silicon (Si) with a saturation flux density up to 1.8 T are used. Alloys of cobalt (Co) and iron (Fe) have higher saturation flux densities (up to 2.3 T); however, they are expensive and used mainly to reduce the size of the machine, for instance in aerospace applications. When considering the cost, alloys of nickel (Ni) and iron (Fe) are between SiFe and CoFe alloys. However, they have a higher electrical resistivity, which makes them suitable for high-speed machines [65]. The saturation flux density values of NiFe alloys may reach 1.6 T [99]. A lower-cost option used in high-speed machines is the SiFe
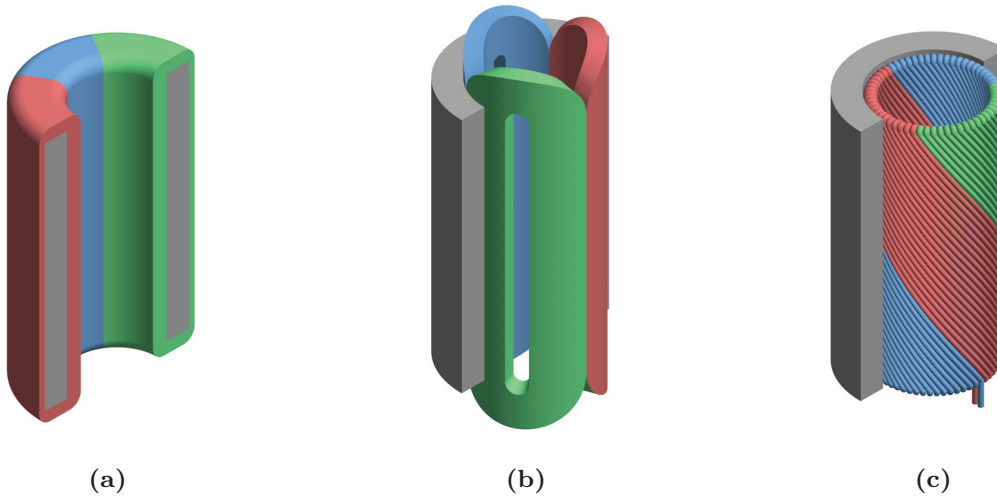
Figure 5.7: Slotless stator configurations with a) toroidal, b) concentrated, and c) Faulhaber windings considered in the optimization procedure.

alloy with up to 1% aluminum. Aluminum additive increases the resistivity of the alloy, yet it has a negative impact on the magnetic permeability and saturation point [65]. In order to reduce the induced eddy-current losses at high frequencies, the laminations are made as thin as possible (up to 0.1 mm). This makes them suitable for applications in the low and medium (up to few kHz) frequency range.

Another soft-magnetic material, which is being increasingly used in high-speed machines, is a soft magnetic composite (SMC). The SMC is made of compressed small iron particles (powder) of high purity, which are insulated from each other. This structure results in a high electric resistivity, which makes it suitable for medium- to high-frequency applications. Owing to its nature, the SMC is magnetically isotropic, which makes it advantageous in applications where a 3D magnetic field is required [66]. In addition, cores with complex shapes can be pressed from SMCs. However, because of the insulation layers between iron particles, the SMCs have a low relative permeability, which is typically less than 1000. Because of this property, SMC materials are being more used in PM machines. Moreover, at low frequencies, SMCs may have higher iron losses than the high-grade laminated Fe-based alloy, and therefore, SMCs are probably more suitable for high-speed (frequency) applications [37].

The third soft-magnetic material that deserves attention is soft-magnetic ferrites. These materials are made of Ni, zinc (Zn), and manganese (Mn), and are commonly used in high-frequency applications, such as high-frequency transformers and filtering inductors, because of their high electrical resistivity. Despite of low losses, ferrites have a low saturation flux density (up to 0.6 T), which makes them impractical in high power density applications. Moreover, ferrites are mechanically

brittle, and therefore, a thorough mechanical design is required if these materials are to be used in electrical machines.

Furthermore, amorphous steels and nanocrystallines can be mentioned as examples of materials for high-frequency magnetic field having even lower electromagnetic losses than ferrites. Their disadvantage, however, is the significantly higher price and manufacturing difficulties caused by the material brittleness, which significantly increases the core price.

Besides electromagnetic properties, the thermal properties of soft-magnetic materials should also be taken into account. Among the soft-magnetic materials under study, Fe-based alloys have the highest thermal conductivity (about 40 W/m/K), followed by SMC (about 20 W/m/K) and ferrites (about 5 W/m/K).

Housing material

In addition to the thermal conducting properties of the housing material, electrical properties are important for machines with certain winding configurations. For example, these properties are of significance in machines with toroidal windings, where the magnetic field of the outer part of the winding penetrates the housing inducing eddy-current losses in it. Therefore, to reduce the eddy-current losses and shield the magnetic field, it is recommended to use highly conducting materials, for instance aluminum. An aluminum housing, because of its high conductivity, shifts the behavior of the housing eddy-current losses to the inductance-limited region, where the reaction field of the eddy-currents opposes the winding field. It is important to shift the inductance-limited behavior to the lower frequency range, because the losses in the housing are mainly induced by the field originating from the first time harmonic because of the stationary housing. The thickness of the housing is recommended to be equal or more than the skin effect depth of the first harmonic to maximize the shielding effect [13].

5.3 Design of slotless PM machines

5.3.1 Design procedure

In an ideal case, the design procedure aims to find the optimal design for the given requirements within a design space in question. Usually, optimization algorithms are employed to reduce the time to determine the optimal design point. However, neither local optimization algorithms, that is, gradient-based methods, nor global optimization algorithms, that is, evolutionary or deterministic algorithms, can ensure convergence to the global optimum point [108]. An alternative to the optimization algorithms is optimal design determination by a parametric search.

Its advantage over optimization algorithms is evaluation of the objective function within the design space under consideration, which allows to find the global optimum point assuming sufficient discretization of the design space. However, evaluation of the designs over the entire design space requires a significantly longer time than when using optimization algorithms. Therefore, analytical and semianalytical models of the optimized functions, which are typically fast, are advantageous to keep the parametric search optimization within a rational time frame with adequate discretization of the design space. The semianalytical tools to model the electromechanical behavior of the slotless PM machines, which were discussed in the previous chapters, are favorable for the parametric search optimization. Hence, a parametric search in combination with the developed semianalytical models is used in the design procedure.

The parametric search optimization of the slotless PM machines contains variables, constants, and parameters that are dependent on certain physical or geometrical variables and should be defined in the design routine. The optimizations constants and thermal constraints for the PM and the winding temperatures are given in Table E.1 in Appendix E. The variables in the parametric search, which define the design space, are the PM radius, r_m, the active length of the machine, l, the RMS value of the current density in the conductor, J, the sleeve material, and the number of parallel strands in the conductor, a. Additionally, there are parameters that are dependent on the varying parameters, such as the required output torque, T_req, the winding thickness, h_w, the stator yoke thickness, h_y, and the outer winding thickness, h_wo (only for a slotless machine with toroidal winding), which are determined in the machine design procedure. The parametric search algorithm for determination of the slotless PM machine designs in the design space is presented in Figure 5.8. The implemented parametric search algorithm determines the machine design that meets the requirements in each point of the design space discarding designs that are infeasible. The infeasible designs are sorted out by checking the ability of the proposed geometry and the conductor current density value to achieve the required torque, the mechanical stability of the rotor, and the thermal conditions of the sensitive machine parts, such as the PM and the winding insulation. The modeling approaches for mechanical and thermal behavior are considered in more detail in this section. In addition, implementation of semianalytical modeling to determine the electromagnetic quantities and losses for each of the slotless PM machines under study is discussed.

Having the set of obtained machine designs within the design space, the optimum design for the considered application is determined as the machine design that consumes the least power from the battery. The energy-efficient solution is of primary importance, because the respiration system requires as long autonomous operation as possible.
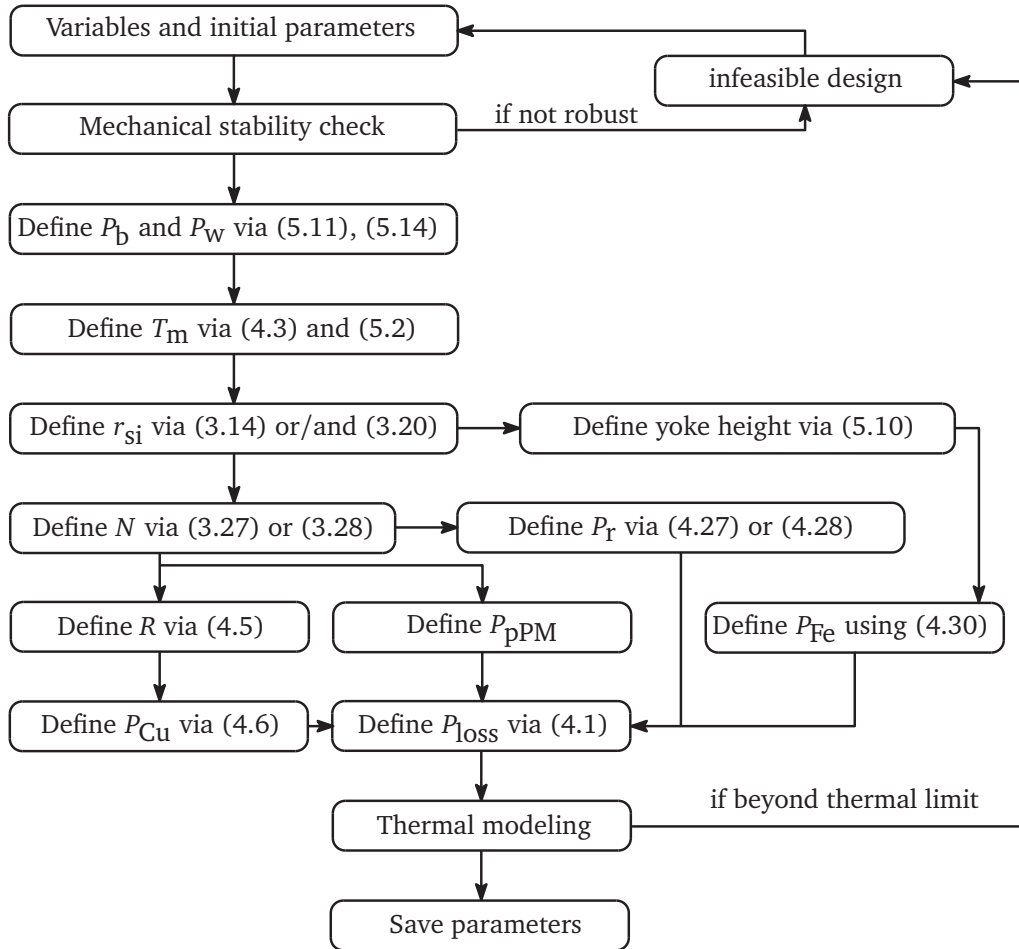
```
┌─────────────────────────────────┐
│  Variables and initial parameters │ ◄──────────────────────────────┐
└─────────────────────────────────┘                                   │
                │                            ┌──────────────────────┐  │
                ▼                            │   infeasible design   │◄─┤
┌─────────────────────────────────┐  if not robust └──────────────┘   │
│   Mechanical stability check      │──────────────►                   │
└─────────────────────────────────┘                                   │
                │                                                       │
                ▼                                                       │
┌─────────────────────────────────┐                                   │
│ Define $P_b$ and $P_w$ via (5.11), (5.14) │                          │
└─────────────────────────────────┘                                   │
                │                                                       │
                ▼                                                       │
┌─────────────────────────────────┐                                   │
│    Define $T_m$ via (4.3) and (5.2)     │                            │
└─────────────────────────────────┘                                   │
                │                                                       │
                ▼                                                       │
┌─────────────────────────────────┐   ┌──────────────────────────┐    │
│ Define $r_{si}$ via (3.14) or/and (3.20) │──►│ Define yoke height via (5.10) │   │
└─────────────────────────────────┘   └──────────────────────────┘    │
                │                                     │                 │
                ▼                                     ▼                 │
┌─────────────────────────────────┐   ┌──────────────────────────┐    │
│   Define $N$ via (3.27) or (3.28)  │──►│ Define $P_r$ via (4.27) or (4.28) │  │
└─────────────────────────────────┘   └──────────────────────────┘    │
       │            │                        │                         │
       ▼            ▼                         ▼                         │
┌──────────────┐ ┌──────────────┐  ┌──────────────────────┐           │
│ Define $R$ via (4.5) │ │ Define $P_{pPM}$ │  │ Define $P_{Fe}$ using (4.30) │          │
└──────────────┘ └──────────────┘  └──────────────────────┘           │
       │            │                                                   │
       ▼            ▼                                                   │
┌──────────────┐ ┌──────────────────────┐                             │
│ Define $P_{Cu}$ via (4.6) │ │ Define $P_{loss}$ via (4.1) │◄──────────────┐     │
└──────────────┘ └──────────────────────┘               │     │
                         │                                │     │
                         ▼          if beyond thermal limit │     │
                 ┌──────────────────┐ ─────────────────────┘     │
                 │  Thermal modeling  │─────────────────────────────┘
                 └──────────────────┘
                         │
                         ▼
                 ┌──────────────────┐
                 │  Save parameters   │
                 └──────────────────┘
```

Figure 5.8: Simplified parametric search algorithm for the optimal design determination.

5.3.2   Electromagnetic modeling

Modeling of the electromagnetic behavior of slotless PM machines was considered in general in Chapters 2, 3, and 4. In this section, these models are applied to slotless machines with toroidal, concentrated, and Faulhaber windings for the specific machine configurations discussed previously. As mentioned before, to define the electromagnetic quantities (torque, emf, synchronous inductance) and electromagnetic losses, the electromagnetic field distribution within the active magnetic parts of the machine should be derived.

PM field modeling

The machine configuration chosen for the design assumes diametrically magnetized PM with a shaftless structure, as shown in Figure 5.5. This magnetization pattern results in sinusoidal, radial, and circumferential magnetization components, obtained by (2.62), (2.63) and given as

$$\bar{M}_{0r} = -\mathrm{j}\frac{B_{\text{rem}}}{\mu_0}\mathrm{e}^{\mathrm{j}\theta}, \tag{5.3}$$

$$\bar{M}_{0\theta} = \frac{B_{\text{rem}}}{\mu_0}\mathrm{e}^{\mathrm{j}\theta}.$$

The PM field modeling process using the HM is identical to the example shown in Appendix B. Similarly to this example, winding, air gap, and sleeve regions are merged together and modeled as an air region, whereas the PM is modeled as nonconducting region with magnetization. The solution of the magnetic vector potential in these regions can be written as

$$\bar{A}_{\text{za}}(r, \theta) = (\bar{C}_{\text{a}}r^{-1} + \bar{D}_{\text{a}}r)\mathrm{e}^{\mathrm{j}\theta},$$

$$\bar{A}_{\text{zPM}}(r, \theta) = \bar{D}_{\text{PM}}r\mathrm{e}^{\mathrm{j}\theta}, \tag{5.4}$$

where $\bar{C}_{\text{a}}$, $\bar{D}_{\text{a}}$, and $\bar{D}_{\text{PM}}$ are the unknown constants in the air and PM regions, respectively. The solution of the PM regions does not contain a particular solution, because the curl of the magnetization is zero. These unknown constants are determined from a boundary condition, and unlike in the example, because of the presence of the circumferential magnetization component, the boundary conditions for the diametrically magnetized PM case are given as

$$\begin{cases} \bar{B}_{\text{rPM}} - \bar{B}_{\text{ra}} = 0, & \text{for } r = r_{\text{m}} \\ \dfrac{\bar{B}_{\theta\text{PM}}}{\mu_0\mu_{\text{r}}} - \bar{H}_{\theta\text{a}} = \dfrac{\bar{M}_{0\theta}}{\mu_{\text{r}}}, & \text{for } r = r_{\text{m}} \\ \bar{H}_{\theta\text{a}} = 0, & \text{for } r = r_{\text{si}}. \end{cases} \tag{5.5}$$

The unknown coefficients in the vector potential solutions are obtained by solving this system of linear equations.

Armature field modeling of a toroidal machine

Modeling of the armature field of the slotless PM machine with a toroidal winding is performed in the 2D HM. The inner part of the toroidal winding, which only participates in the torque production, and the outer part contain only the axial current component. Modeling of the electromagnetic field originating from the inner and outer parts of the toroidal winding is carried out in polar coordinates.
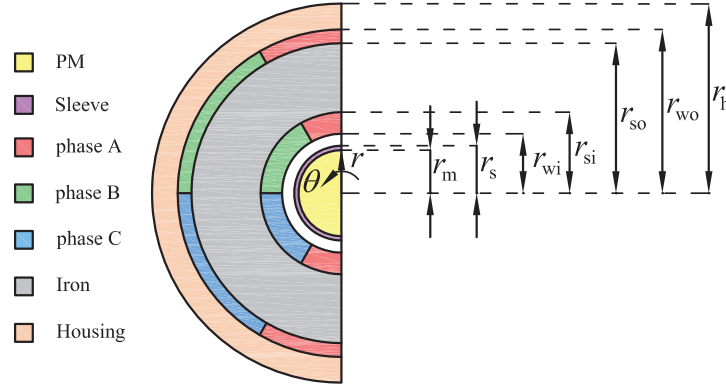
Figure 5.9: Half of the cross-section of a slotless PM machine with a toroidal winding in the polar coordinates.

Furthermore, there are two flank parts that contain only the radial current component. The field modeling in the flank parts should ideally be approached as a 3D problem. However, modeling of the flank parts can be simplified to a 2D problem and approached by the 2D HM in the θ–z plane as it is demonstrated in [59].

To simplify the process, the armature field of the inner and outer winding parts can modeled separately because of the soft-magnetic core (see Figure 5.9). This reduces the model complexity, which eventually has an effect on the calculation time. The HM of the inner part assumes division into four regions, namely the PM, sleeve, air gap, and winding. The PM and sleeve regions are considered to be conducting regions with different permeabilities and electric conductivities. The air gap is modeled as an air (vacuum) region, and the winding region is treated as a region with imposed current density. The general properties of the inner part HM are presented in Table 5.1. The solutions of the governing equations are defined by (2.36), (2.39), (2.48). In this case, the winding current density is defined by (2.69), where the Fourier series coefficient is given for the toroidal winding by (A.13). In the same manner, the HM of the outer part is implemented. The model contains three regions and the main model properties are gathered in Table 5.2.

Armature field modeling of the concentrated machine

The armature field of slotless PM machines with concentrated windings is approached with the 2D HM in the polar coordinates. As it can be seen from Figure 5.7(b), each coil of the concentrated winding has an active part, which mainly produces the electromagnetic torque, and the end windings. These end windings contribute to the torque production if the PM field penetrates them; however, this contribution is slight. Hence, the influence of the end winding on the armature field is neglected.

Table 5.1: Governing equations and boundary conditions of the inner part of the slotless PM machine with a toroidal winding

Region	Range	Governing equation	Boundary conditions
PM	$0 \leq r \leq r_\mathrm{m}$	$\nabla^2 \bar{A}_\mathrm{zPM} = \mu_\mathrm{PM} \sigma_\mathrm{PM} \dfrac{\partial \bar{A}_\mathrm{zPM}}{\partial t}$	$\bar{A}_\mathrm{zPM} = 0 \; (r = 0)$ $\bar{B}_\mathrm{rPM} = \bar{B}_\mathrm{rs} \; (r = r_\mathrm{m})$
Sleeve	$r_\mathrm{m} \leq r \leq r_\mathrm{s}$	$\nabla^2 \bar{A}_\mathrm{zs} = \mu_\mathrm{s} \sigma_\mathrm{s} \dfrac{\partial \bar{A}_\mathrm{zs}}{\partial t}$	$\bar{H}_{\theta\mathrm{PM}} = \bar{H}_{\theta\mathrm{s}} \; (r = r_\mathrm{m})$ $\bar{B}_\mathrm{rs} = \bar{B}_\mathrm{ra} \; (r = r_\mathrm{s})$
Air gap	$r_\mathrm{s} \leq r \leq r_\mathrm{wi}$	$\nabla^2 \bar{A}_\mathrm{za} = 0$	$\bar{H}_{\theta\mathrm{s}} = \bar{H}_{\theta\mathrm{a}} \; (r = r_\mathrm{s})$ $\bar{B}_\mathrm{ra} = \bar{B}_\mathrm{rwi} \; (r = r_\mathrm{wi})$
Winding	$r_\mathrm{wi} \leq r \leq r_\mathrm{si}$	$\nabla^2 \bar{A}_\mathrm{zwi} = -\mu_0 \bar{J}_\mathrm{wi}$	$\bar{H}_{\theta\mathrm{a}} = \bar{H}_{\theta\mathrm{wi}} \; (r = r_\mathrm{wi})$ $\bar{H}_{\theta\mathrm{wi}} = 0 \; (r = r_\mathrm{si})$

Table 5.2: Governing equations and boundary conditions of the outer part of the slotless PM machine with a toroidal winding

Region	Range	Governing equation	Boundary conditions
Winding	$r_\mathrm{so} \leq r \leq r_\mathrm{wo}$	$\nabla^2 \bar{A}_\mathrm{zow} = -\mu_0 \bar{J}_\mathrm{ow}$	$\bar{H}_{\theta\mathrm{ow}} = 0 \; (r = r_\mathrm{so})$ $\bar{B}_\mathrm{row} = \bar{B}_\mathrm{rh} \; (r = r_\mathrm{wo})$
Housing	$r_\mathrm{wo} \leq r \leq r_\mathrm{h}$	$\nabla^2 \bar{A}_\mathrm{zh} = \mu_\mathrm{h} \sigma_\mathrm{h} \dfrac{\partial \bar{A}_\mathrm{zh}}{\partial t}$	$\bar{H}_{\theta\mathrm{ow}} = \bar{H}_{\theta\mathrm{h}} \; (r = r_\mathrm{wo})$ $\bar{B}_\mathrm{rh} = \bar{B}_\mathrm{ram} \; (r = r_\mathrm{h})$
Ambient	$r_\mathrm{h} \leq r < \infty$	$\nabla^2 \bar{A}_\mathrm{za} = 0$	$\bar{H}_{\theta\mathrm{h}} = \bar{H}_{\theta\mathrm{am}} \; (r = r_\mathrm{h})$ $\bar{A}_\mathrm{zPM} = 0 \; (r \to \infty)$

The implementation of the HM for the slotless PM machine with a concentrated winding is identical to the one for the inner part of the slotless PM machine with a toroidal winding (see Figure 5.10), which is summarized in Table 5.1. The only difference is the winding function distribution, which is for the concentrated winding derived as (A.14). Here, the variable α is the winding opening, which is depicted in Figure 5.10. The dependence of the first and second space harmonics of the winding distribution function, f_w, over the winding opening angle is presented in Figure 5.11, whereas the value 1 on the winding function axis is the amplitude of the original distribution function. We can see that the second spatial harmonic of this winding type is larger than the fundamental one, and therefore, four-pole PM excitation would theoretically produce a higher torque. However, increasing the number of poles increases the supply frequency, which in return increases all frequency-dependent losses within the entire high-speed electrical drive system.

The winding opening angle has an optimum value, which is a trade-off between the
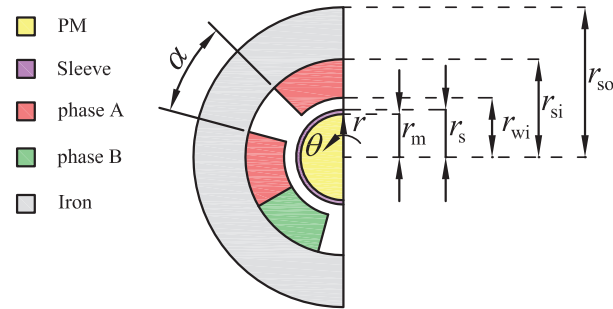
Figure 5.10: Half of the cross-section of a slotless PM machine with the concentrated winding in the polar coordinates.
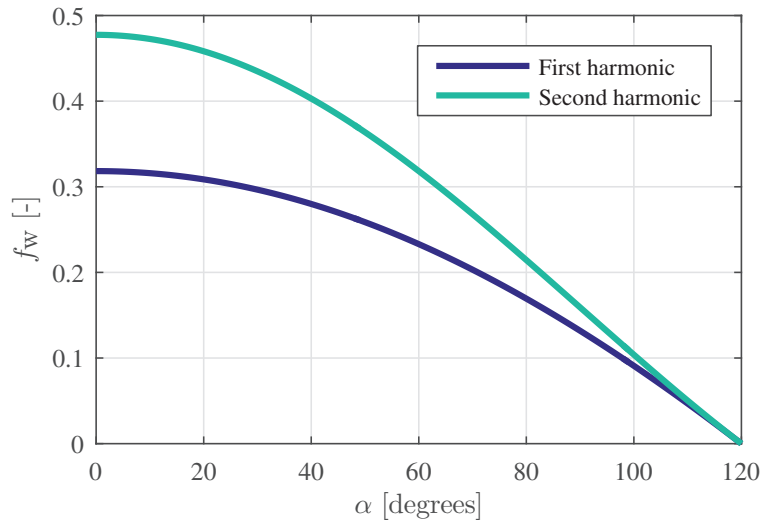

Figure 5.11: Dependence of the first and second space harmonics of the winding distribution function over the winding opening angle.

Joule losses in the winding and the torque density of the machine. Furthermore, the value of the winding opening is restricted by the manufacturing facility of a certain winding manufacturer. Certainly, this angle can be introduced as a varying parameter in the parametric search optimization. However, to reduce the time required for the parametric search, it is set to be 30 mechanical degrees.

Armature field modeling of the Faulhaber machine

The armature field calculation of the slotless PM machine with the Faulhaber winding is approached as a 3D problem, similarly as it is demonstrated in the example with the rhombic winding in Section 2.7.2. Unlike in this example, a sleeve has been added to consideration, as shown in Figure 5.12. The sleeve is modeled as a conducting region, whereas the general description of the HM of the slotless PM with the Faulhaber winding is presented in Table 5.3. Because the problem is
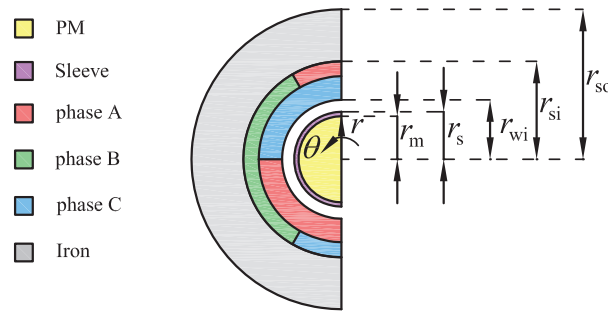

Figure 5.12: Half of the cross-section of a slotless PM machine with the Faulhaber winding in the polar coordinates at $z = 0$.

approached using the second-order vector potential formulation, which is unable to model regions with currents imposed on them, the winding and the air gap regions are merged. The winding current is formulated as a linear current density and placed on the surface of the iron bore. The expression of the linear current density for the Faulhaber winding, given by (A.11), contains four components. Consequently, the complete model should also consist of four independent models, whose superposition of field solutions results in a total armature field solution of the slotless PM machine with the Faulhaber winding. In addition, the first component of the linear current density is independent of the axial direction. Therefore, the field modeling for this component is performed only with the 2D HM.

Calculation of the stator bore radius

In the simplified flowchart of the parametric search, one of the steps is determination of the stator bore radius, r_{si}. Practically, this means adjusting the winding height to the required electromagnetic torque, as the winding inner radius is fixed. The produced electromagnetic torque can be calculated using the previously derived expressions (3.14) and (3.20), where the solutions of the armature and PM fields are required. These solutions are dependent on the stator bore radius, current in the winding conductor, and the number of phase turns, which are unknown

Table 5.3: Governing equations and boundary conditions of the slotless PM machine with the Faulhaber winding

Region	Range	Governing equation	Boundary conditions
3D HM (axial dependence of current distribution is present)			
PM	$0 \leq r \leq r_{\mathrm{m}}$	$\nabla^2 \bar{W}_{\mathrm{1PM}} = \mu_{\mathrm{PM}}\sigma_{\mathrm{PM}}\dfrac{\partial \bar{W}_{\mathrm{1PM}}}{\partial t}$ $\nabla^2 \bar{W}_{\mathrm{2PM}} = \mu_{\mathrm{PM}}\sigma_{\mathrm{PM}}\dfrac{\partial \bar{W}_{\mathrm{2PM}}}{\partial t}$	$\bar{W}_{\mathrm{1PM}} = 0 \; (r = 0)$ $\bar{W}_{\mathrm{2PM}} = 0 \; (r = 0)$ $\bar{B}_{\mathrm{rPM}} = \bar{B}_{\mathrm{rs}} \; (r = r_{\mathrm{m}})$ $\bar{H}_{\theta\mathrm{PM}} = \bar{H}_{\theta\mathrm{s}} \; (r = r_{\mathrm{m}})$
Sleeve	$r_{\mathrm{m}} \leq r \leq r_{\mathrm{s}}$	$\nabla^2 \bar{W}_{\mathrm{1s}} = \mu_{\mathrm{s}}\sigma_{\mathrm{s}}\dfrac{\partial \bar{W}_{\mathrm{1s}}}{\partial t}$ $\nabla^2 \bar{W}_{\mathrm{2s}} = \mu_{\mathrm{s}}\sigma_{\mathrm{s}}\dfrac{\partial \bar{W}_{\mathrm{2s}}}{\partial t}$	$\bar{H}_{\mathrm{zPM}} = \bar{H}_{\mathrm{zs}} \; (r = r_{\mathrm{m}})$ $\bar{E}_{\mathrm{zPM}} = \bar{E}_{\mathrm{zs}} \; (r = r_{\mathrm{m}})$ $\bar{B}_{\mathrm{rs}} = \bar{B}_{\mathrm{ra}} \; (r = r_{\mathrm{s}})$ $\bar{H}_{\theta\mathrm{s}} = \bar{H}_{\theta\mathrm{a}} \; (r = r_{\mathrm{s}})$
Air gap + Winding	$r_{\mathrm{s}} \leq r \leq r_{\mathrm{si}}$	$\nabla^2 \bar{W}_{\mathrm{a}} = 0$	$\bar{H}_{\mathrm{zs}} = \bar{H}_{\mathrm{za}} \; (r = r_{\mathrm{s}})$ $\bar{H}_{\theta\mathrm{a}} = \bar{K}_{\mathrm{z}} \; (r = r_{\mathrm{si}})$
2D HM (axial dependence of current distribution is not present)			
PM	$0 \leq r \leq r_{\mathrm{m}}$	$\nabla^2 \bar{A}_{\mathrm{zPM}} = \mu_{\mathrm{PM}}\sigma_{\mathrm{PM}}\dfrac{\partial \bar{A}_{\mathrm{zPM}}}{\partial t}$	$\bar{A}_{\mathrm{zPM}} = 0 \; (r = 0)$ $\bar{B}_{\mathrm{rPM}} = \bar{B}_{\mathrm{rs}} \; (r = r_{\mathrm{m}})$
Sleeve	$r_{\mathrm{m}} \leq r \leq r_{\mathrm{s}}$	$\nabla^2 \bar{A}_{\mathrm{zs}} = \mu_{\mathrm{s}}\sigma_{\mathrm{s}}\dfrac{\partial \bar{A}_{\mathrm{zs}}}{\partial t}$	$\bar{H}_{\theta\mathrm{PM}} = \bar{H}_{\theta\mathrm{s}} \; (r = r_{\mathrm{m}})$ $\bar{B}_{\mathrm{rs}} = \bar{B}_{\mathrm{ra}} \; (r = r_{\mathrm{s}})$
Air gap + Winding	$r_{\mathrm{s}} \leq r \leq r_{\mathrm{si}}$	$\nabla^2 \bar{A}_{\mathrm{za}} = 0$	$\bar{H}_{\theta\mathrm{s}} = \bar{H}_{\theta\mathrm{a}} \; (r = r_{\mathrm{s}})$ $\bar{H}_{\theta\mathrm{a}} = \bar{K}_{\mathrm{z}} \; (r = r_{\mathrm{si}})$

at that stage of the design algorithm. To overcome this, the current density in the winding is set at the beginning of the design algorithm, and the value of the stator bore radius is iterated within a feasible range until the developed electromagnetic torque fits the required one. For slotless PM machines approached by the 2D HM, the amplitude value of the space current density distribution (see (2.69)) is obtained as

$$\hat{J}_{\mathrm{zs}}(L, k) = \frac{3\sqrt{2}Jk_{\mathrm{sCu}}}{2}c(L, k), \tag{5.6}$$

where J is the RMS value of the current density in the conductor [A/m^2], which is varied during parametric search optimization, $c(L, k)$ is the Fourier series coefficient of the winding distribution function, and k_{sCu} is the winding space factor,

which represents the ratio of the volume of copper to the total winding volume. For a slotless PM machine with a Faulhaber winding, the amplitude of the linear current density (see (2.78)) is defined as

$$\hat{K}_{zs}(L, k) = \frac{3\sqrt{2}Jk_{sCu}\cos(\pi - \gamma)}{4r_{si}}(r_{si}^2 - r_{wi}^2)c(m, L, k), \tag{5.7}$$

where γ is the skewing angle [rad]. This skewing angle for the Faulhaber winding is defined as $\gamma = \arctan(l/(r_{wc}\pi))$, where r_{wc} is given by (3.25).

Iteration of the torque calculation would be an intensively time-consuming process if the previously developed armature field models of the slotless PM machines with the toroidal, concentrated, and Faulhaber windings were used. As it is stated in Chapter 3, the constant (useful) electromagnetic torque is only developed by the same order of the PM and armature field space harmonics at which the same-order current (time) harmonic excites the armature winding. The field of the diametrically magnetized PM contains only the fundamental space harmonic, and thus, constant torque can only be generated by the armature field fundamental harmonic excited by the fundamental harmonic of the phase current. Taking into account that the field produced by the fundamental space and time harmonics induces no eddy currents in the rotor, the armature field HM can be simplified by excluding the sleeve and the PM from the model and replacing them by air. Definitely, this introduces inaccuracy into the field calculation, because $\mu_{rPM} \neq 1$. However, the solution of the resultant model and the torque calculation can be given as simple analytical expressions, which are well suited for iterative calculations.

Phase turn number

A common practice in an electrical machine design is to initially design the magnetic circuit, after which the electrical circuit is designed. The magnetic circuit design defines the value of current linkage (mmf) that the armature winding has to produce. The current linkage generated by a winding is proportional to the number of winding turns and current in it. The turn number increment has a limit defined by the maximum voltage value provided by the inverter, as it directly increases the emf induced by the phase flux linkage.

It is assumed that the value of the phase emf induced by the PM field reaches 90% of available phase voltage (given by the inverter), $\hat{E}_{PM} = 0.9\hat{U}_{ph}$, where the rest 10% of the voltage is reserved for the voltage drop on the winding resistance, emf induced by the armature field, and control voltage reserve for the short torque overload compensation. Consequently, the phase turn number for the slotless PM machines with toroidal and concentrated windings can be derived using (3.26) and for machines with the Faulhaber winding using (3.29).

Stator yoke height

The stator yoke height is chosen to ensure operation of the soft-magnetic material before the saturation point on the $B-H$ curve. Generally speaking, the maximum flux density value in the stator yoke is decided subjectively, depending on the $B-H$ curve of a considered ferromagnetic material. Sometimes in slotless high-speed machines, to reduce the iron losses, the magnetic flux density level is kept far below the saturation level.

As the armature field of slotless PM machines is much weaker than the PM field, for the sake of simplicity, only the PM field is considered in the stator yoke height calculations. It can be stated that the maximum value of the flux in the stator yoke equals half of the maximum flux value crossing the inner surface of the yoke, which is written as

$$\hat{\Phi}_{\mathrm{y}} = \frac{\hat{\Phi}_{\mathrm{PM}}(r = r_{\mathrm{si}})}{2}. \tag{5.8}$$

Taking into account the fact that the diametrically magnetized PM produces sinusoidally distributed flux, the above expression by means of flux densities can be rewritten as

$$\hat{B}_{\mathrm{y}} h_{\mathrm{y}} k_{\mathrm{Fe}} = \hat{B}_{\mathrm{r,PM}}(r = r_{\mathrm{si}}) \cdot r_{\mathrm{si}}, \tag{5.9}$$

where h_{y} is the yoke height [m], k_{Fe} is the space (stack) factor of the iron core laminations, and $\hat{B}_{\mathrm{r,PM}}$ is the amplitude value of the PM flux density at $(r = r_{\mathrm{si}})$ [T], which can be obtained using (2.37) and (5.4). To calculate the stator yoke height, which is required to have the maximum flux density in the yoke equal to the saturation flux density of the yoke material, the following expression can be used

$$h_{\mathrm{y}} = \frac{\hat{B}_{\mathrm{r,PM}}(r = r_{\mathrm{si}})}{B_{\mathrm{max}} k_{\mathrm{Fe}}} r_{\mathrm{si}}, \tag{5.10}$$

where B_{max} is the chosen maximum flux density value of the soft-magnetic material [T].

Electromagnetic losses

To estimate the efficiency and input power of the designed machine, the electromagnetic losses have to be defined. For slotless PM machines, the most significant of these losses are discussed in Chapter 4. As shown in Figure 5.8, not all of the losses mentioned in Chapter 4 are taken into account in the machine design. For instance, strand-level skin effect and bundle-level proximity effect losses are omitted from consideration. Strand-level skin effect losses are not an issue in most

of the cases, because smaller-diameter parallel strands are used to diminish the strand-level proximity effect (see Section 4.2). The bundle-level proximity effect losses are out of consideration, because the location of parallel strands is not defined at the design stage unless the manufacturing process is known, which allows to estimate the exact location of parallel strands. Moreover, taking into account that the armature field is considerably lower than the PM field, the influence of the armature field on the iron losses is neglected. The rest of the losses discussed in Chapter 4 are included in the design optimization process. Regarding these losses, the following remarks can be made.

First, the value of magnetic field used for the strand-level proximity loss calculation is determined in the middle of the winding region. This simplification avoids calculation of the strand-level proximity losses in different radial positions.

Secondly, the housing eddy-current losses in the slotless PM machine with the toroidal winding are calculated identically to the rotor eddy-current losses by employing the Poynting vector. In this case, the integration surface of the Poynting vector is defined on the boundary between the outer winding and the housing. Finally, it is assumed that the designed machine is supplied by an inverter with the asymmetrical space vector PWM, where the amplitude modulation ratio is set to $M = 0.6$.

5.3.3 Mechanical loss modeling

Mechanical losses can be significant in high-speed machines, and therefore, these losses should be taken into account in the machine design. In agreement with the flowchat of the design process (see Figure 5.8), mechanical losses (torque) are addressed in the electromagnetic torque requirement. Practically, mechanical losses can be divided into two loss types, namely windage and bearing losses.

Windage losses

Windage losses in the machine occur in the air surrounding the rotor as a result of motion of the rotor with respect to the stator. There are many models to calculate the windage losses, such as described in [111], [10], [69], where the key difference between the models is the calculation of the friction coefficient. According to [97], the windage losses of an enclosed rotating cylinder are calculated as

$$P_{\mathrm{w}} = k_1 C_{\mathrm{f}} \rho_{\mathrm{air}} \pi \Omega^3 r_{\mathrm{r}}^4 l_{\mathrm{r}}, \tag{5.11}$$

where k_1 is the roughness coefficient (for smooth surfaces $k_1 = 1$), C_{f} is the friction coefficient, ρ_{air} is the mass density of the air surrounding the rotor [kg/m^3], r_{r} is

the radius of the rotor [m], and l_r is the length of the rotor [m]. The friction coefficient can be defined as [10]

$$C_\mathrm{f} = 0.515 \frac{\left(\dfrac{\delta}{r_\mathrm{r}}\right)^{0.3}}{Re_\delta^{0.5}}, \ (\text{for } 500 < Re_\delta < 10^4)$$

$$C_\mathrm{f} = 0.0325 \frac{\left(\dfrac{\delta}{r_\mathrm{r}}\right)^{0.3}}{Re_\delta^{0.2}}, \ (\text{for } Re_\delta > 10^4) \tag{5.12}$$

where δ is the air-gap thickness [m] and Re_δ is the Couette Reynolds number, which is derived as

$$Re_\delta = \frac{\Omega r_\mathrm{r} \delta}{\nu_\mathrm{air}}, \tag{5.13}$$

where ν_air is the air kinematic viscosity [m^2/s]. The windage losses caused by the flank parts of the rotor are not taken into account.

Bearing losses

Accurate analytical evaluation of the bearing losses is a challenging task. A few analytical models have been presented, for instance in [43], but according to [16], implementation of such models is impractical because of their complexity and uncertainties of the model parameters. Sometimes, models that are based on experimental data are preferred [85]. In this study, the bearings are selected in advance before the electromagnetic machine design is fixed. The selected bearings are SKF (637/3-2Z), and therefore, it is decided to use an empirical model of the bearing loss calculation provided by SKF [100]

$$P_\mathrm{b} = \mu_\mathrm{b} F_\mathrm{b} \Omega r_\mathrm{b}, \tag{5.14}$$

where μ_b is the friction coefficient (for deep groove bearing $\mu_\mathrm{b} = 0.0015$), r_b is the inner radius of the bearing [m], and F_b is the bearing load [N]. For normal bearing operating conditions, the bearing load can be defined as $F_\mathrm{b} = 0.1 C_\mathrm{r}$, where the C_r is the dynamic load rating [N] given in the bearing specification.

5.3.4   Rotor structural integrity

Rotor elements induce centrifugal forces during rotation, thereby causing stresses in the rotor materials. In high-speed machines, as a result of high rotational speeds, these mechanical stresses are significant and require attention in the machine design to ensure the rotor structural integrity. In general, structural integrity is

ensured if stresses in the rotor materials do not exceed their ultimate tensile stress limits. However, the dynamic motion profile of the motor presumes a cyclic stress in the rotor, which may lead to the fatigue of rotor materials. To avoid the fatigue of a material the amplitude of the periodical stress should be kept below the fatigue strength of the material [17]. In this research, the fatigue stresses for the sleeve and PM materials are assumed to be 20% of their ultimate tensile strengths, thought in reality these values are greater.

The rotor components, the PM and the sleeve, geometrically represent full and hollow cylinders. Neglecting the axial stress in the materials (planar strain assumption), the maximum reference stress occurring in the sleeve can be calculated as [68]

$$\sigma_{\text{refs,max}} = \frac{\rho_s \Omega^2}{4} \left((1 - \nu_{\text{Ps}}) r_{\text{m}}^2 + (\nu_{\text{Ps}} + 3) r_{\text{s}}^2 \right), \tag{5.15}$$

where ρ_s is the mass density of the sleeve [kg/m^3], Ω is the angular velocity [rad/s], ν_{Ps} is the Poisson's ratio of the sleeve material, r_{m} is the inner radius of the sleeve [m], and r_{s} is the outer radius of the sleeve [m]. The maximum reference stress acting on the PM material can be obtained as

$$\sigma_{\text{refm,max}} = \frac{\rho_{\text{m}} \Omega^2}{8} (\nu_{\text{Pm}} + 3) r_{\text{m}}^2, \tag{5.16}$$

where ρ_{m} is the mass density of the PM [kg/m^3], and ν_{Pm} is the Poisson's ratio of the PM material. To ensure the structural integrity of the rotor parts, the maximum reference stresses in the sleeve and the PM should not exceed the ultimate tensile stress limits of their materials (see Appendix E). Furthermore, as there is no shrink-fit between the sleeve and the PM, an adhesive connection between the sleeve and PM is provided to guarantee the contact.

Rotors of high-speed machines should also be analyzed with respect to bending modes. The bending modes of the rotor design with the highest slenderness ratio was modeled in the FEM (Solidworks). According to the modeling results the first bending frequency appears at 3.5 kHz. This frequency is notably beyond the maximum operating frequency of the design motor (1333 Hz), thereby stable rotation of the rotor is ensured within the entire operational speed range.

5.3.5 Thermal modeling

Material specifications used in manufacturing of electrical machines contain information about the operating temperature range within which the specified electromagnetic properties of the materials are guaranteed. For instance, for wire insulation they indicate the thermal classes that correlate with the operating temperature and the lifetime of the insulation. Therefore, it is important to keep the

operating temperature of the machine parts within the safety region to guarantee the machine operation over its lifetime. At the same time, operating the machine at low temperatures usually decreases the power density of the machines, which is reflected in the machine price and size. Similarly, working at higher temperatures results in poorer electromagnetic behavior of the materials, for instance, the remanence of the PM decreases. Considering these factors, it is possible to determine optimal thermal operating conditions in which the performance, mass, and dimension parameters as well as the price of the machine meet the requirements. To find this optimal point, electromagnetic and thermal modeling aspects have to be linked in order to take into account the interdependences. Furthermore, it is pointed out here that accurate prediction of the machine part temperatures allows to set a smaller safety margin, which is usually preferred in any design.

Fast models are preferred in parametric search optimization, and therefore, thermal modeling of the slotless PM machines is approached by thermal equivalent circuit (TEC) modeling, also known as the lumped parameter model. This thermal modeling technique is faster compared with others, for instance the FEM [36]. The TEC assumes modeling of the temperature distribution over the machine using thermal resistances and heat transfer rates refer to dissipated power. Thermal capacitances are used for transient thermal modeling. In general, an analogy can be drawn between a TEC model and an electrical circuit model; thermal resistance is analogous to electrical resistance, thermal capacitance to electrical capacitance, and dissipated losses to current source. Accordingly, a TEC model can be solved employing methods used for solving electrical circuits, for example as shown in [91].

There are three heat transfer mechanisms, viz. conduction, convection, and radiation. In thermal conduction, heat is transferred by molecular interaction and by means of free electrons. Conduction heat transfer is present in all states of matter (gas, liquid, and solid). Convection assumes heat transfer from a region with a higher temperature to a region with a lower temperature by means of fluid movement. Thermal radiation is electromagnetic radiation caused by movement of charges in matter. Radiation, unlike other heat transfer mechanisms, does not require a medium to transfer heat [91]. In high-speed electrical machines, heat removal by radiation from the stator and rotor surfaces in the air gap is insignificant [84], and thus, it is excluded from the consideration. Inside and between solid bodies in electrical machines, the primary mechanism of heat transfer is assumed to be conduction. Again, between the rotor and the stator through the air gap, as well as from the housing to the ambient, convection heat transfer is considered. The radiation heat removal mechanism from the motor housing to the ambient is linearized and included in the natural convection heat transfer model. Modeling and implementation of these heat transfer mechanisms in the TEC model for slotless PM machines is discussed in the following.
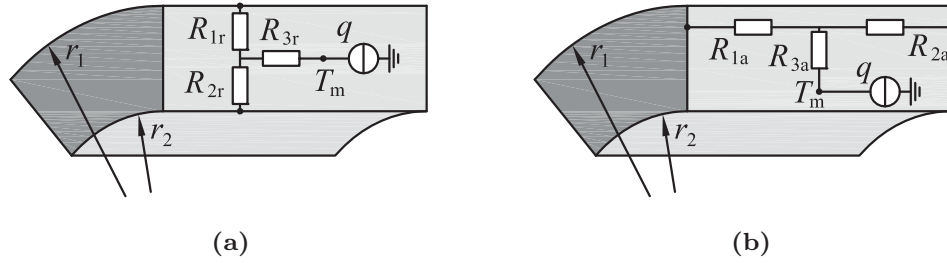
Figure 5.13: a) Radial- and b) axial-direction thermal T-equivalent models of a cylindrical component. In the figure, R represents thermal resistances [K/W] and q is the dissipated power [W].

Thermal conduction modeling

In general, parts of rotating slotless PM electrical machines, such as stator iron, winding, and sleeve, are represented by hollow cylinders. In these solid bodies, as it was mentioned above, heat transfer is modeled by thermal conduction. A thermal circuit to model a hollow cylinder used in this thesis is called T-equivalent circuit, which consists of three thermal resistances to model the heat flow in one direction. From the thermal point of view, slotless machines are assumed to be homogeneous in the circumferential direction, and therefore, the heat flow in the T-equivalent model is modeled only in the radial and axial directions as shown in Figure 5.13. The terminals of the T-equivalent model represent the temperature on the surfaces in each direction. T_{m} is the point that indicates the mean temperature over the cylinder, and if the heat flow is modeled in both directions, the common point of the two T-circuits is the T_{m} point in this case. Again, this point is the terminal for the dissipated power, which is modeled as the current source in the TEC model. The T-equivalent model has overcome the disadvantage of the classical model with two thermal resistances, that is, overestimating the mean temperature [36]. The T-equivalent model has been introduced by [77] by adding a negative thermal resistance to the classical model.

The thermal resistances for the heat flow modeling in the radial and axial directions using the T-equivalent circuit are calculated by expressions given in Table 5.4. In these equations, k_{rt} and k_{at} are the radial- and axial-direction thermal conductivities [W/m/K], respectively, l is the length of the cylinder [m], and r_1 and r_2 are the inner and outer radii of the cylinder [m], respectively. The expressions for the radial thermal resistances are not valid for the full cylinder case when $r_2 = 0$. In this case, instead of the T-equivalent model, the model represented in Figure 5.14 can be used [77] [36]. Here, the radial and axial resistances are determined

Table 5.4: Expressions for the calculation of the axial and radial thermal resistances in the T-equivalent model shown in Figure 5.13.

Radial direction	Axial direction
$R_{1\mathrm{r}} = \dfrac{1}{4\pi k_{\mathrm{rt}}l}\left(1 - \dfrac{2r_2^2\ln(r_1/r_2)}{(r_1^2 - r_2^2)}\right)$	$R_{1\mathrm{a}} = \dfrac{l}{2\pi k_{\mathrm{at}}(r_1^2 - r_2^2)}$
$R_{2\mathrm{r}} = \dfrac{1}{4\pi k_{\mathrm{rt}}l}\left(\dfrac{2r_1^2\ln(r_1/r_2)}{(r_1^2 - r_2^2)} - 1\right)$	$R_{2\mathrm{a}} = \dfrac{l}{2\pi k_{\mathrm{at}}(r_1^2 - r_2^2)}$
$R_{3\mathrm{r}} = \dfrac{-1}{8\pi(r_1^2 - r_2^2)k_{\mathrm{rt}}l}\left(r_1^2 + r_2^2 - \dfrac{4r_1^2r_2^2\ln(r_1/r_2)}{(r_1^2 - r_2^2)}\right)$	$R_{3\mathrm{a}} = -\dfrac{l}{6\pi k_{\mathrm{at}}(r_1^2 - r_2^2)}$
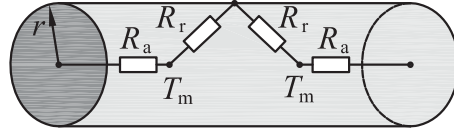
Figure 5.14: TEC model of a full cylinder.

as

$$R_{\mathrm{r}} = \frac{1}{2\pi k_{\mathrm{rt}}l}, \tag{5.17}$$

$$R_{\mathrm{a}} = \frac{l}{4\pi k_{\mathrm{at}}r^2}, \tag{5.18}$$

where l and r are the length and radius of the full cylinder [m], respectively. Modeling of the heat flow between machine parts is commonly carried out by applying contact resistances [36]. These thermal resistances are omitted in the thermal modeling of the slotless PM machines. The heat flow is also conducted from the shaft through the bearing to the housing. The thermal resistance of the bearing is taken into account by using the model proposed in [49].

It has been observed during measurements of the test machine (see Section 4.5.2) that the system thermal time constant is about one minute, which is assumed to be much greater than the machine overloading time. Therefore, the transient thermal modeling, which is performed by including thermal capacitances, is not considered in this study.

Thermal convection modeling

A thermal convection model is applied to predict the heat flow in the air gap of the machine and heat flow from the housing to the ambient. Heat flow in the air gap can be analyzed by two thermal resistances representing the thermal convection from the stator and from the rotor to the air gap [84]. These thermal resistances can be calculated as

$$R_{\text{convection}} = \frac{1}{\alpha S}, \tag{5.19}$$

where α is the heat transfer coefficient [W/m^2/K], and S is the surface area of the stator or rotor [m^2]. The derivation procedure of the air gap convection coefficient for the rotating electrical machines has been shown in [48], [84]. The heat transfer coefficient is derived through the Nusselt number as

$$\alpha = \frac{Nu\,k_{\text{t,air}}}{d_{\text{h}}}, \tag{5.20}$$

where Nu is the Nusselt number, $k_{\text{t,air}}$ is the air thermal conduction [W/m/K], and $d_{\text{h}} = \delta\sqrt{8/3}$ is the hydraulic diameter [m], and δ is the air gap length [m]. In the case where there is no axial force cooling in the air gap, the Nusselt number can be determined by the following conditional expressions

$$Nu = \begin{cases} 2, & \text{for } Ta_{\text{m}} \leqslant 1700, \\ 0.128 Ta_{\text{m}}^{0.367}, & \text{for } 1700 < Ta_{\text{m}} \leqslant 10^4, \\ 0.409 Ta_{\text{m}}^{0.241}, & \text{for } 10^4 < Ta_{\text{m}} \leqslant 10^7, \end{cases} \tag{5.21}$$

where Ta_{m} is the modified Taylor number. The modified Taylor number can be calculated as

$$Ta_{\text{m}} = \frac{1697 Ta \left(0.0056 + 0.0571 \left(\dfrac{2r_{\text{m}} - 2.304\delta}{2r_{\text{m}} - \delta}\right)^2\right)\left(1 - \dfrac{\delta}{2r_{\text{m}}}\right)}{\pi^4 \left(\dfrac{2r_{\text{m}} - 2.304\delta}{2r_{\text{m}} - \delta}\right)}, \tag{5.22}$$

where r_{m} is the mean radius between the stator and the rotor [m], and Ta is the Taylor number, which is determined as

$$Ta = \frac{\rho_{\text{air}}^2 \Omega^2 r_{\text{m}} \delta^3}{\mu_{\text{air}}^2}, \tag{5.23}$$

where μ_{air} is the dynamic viscosity of air [Pa·s].

Natural convection heat transfer occurring in the motor housing is also modeled using (5.19). The value of the natural convection heat transfer coefficient from
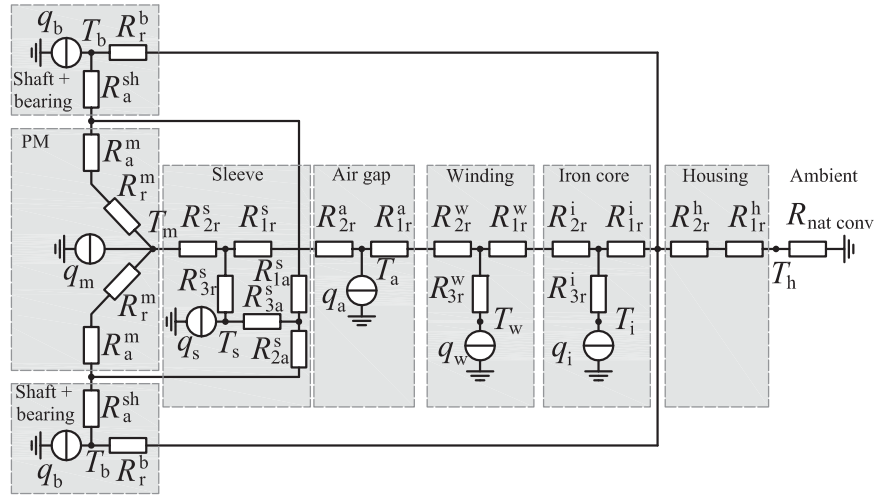
Figure 5.15: TEC model of the slotless PM machine with the Faulhaber winding.

the housing to the ambient given in Table E.1, where S is the area of the machine housing. The value of the natural convection heat transfer coefficient is obtained as the average value provided in datasheets of the manufacturers of high-speed PM machines, such as Faulhaber and Maxon, for machines with similar powers.

Dissipated power

Dissipated power in the thermal circuit, which represents the heat source, comprises the electromagnetic and mechanical losses in the machine. Calculation of these losses for high-speed slotless PM machines has been explained in Chapter 4. These losses in the thermal model should be added to the regions where they appear.

Thermal equivalent circuit model of slotless PM machines with Faulhaber windings

For the design optimization, three slotless PM machines with toroidal, concentrated, and Faulhaber windings are considered. However, for simplicity, only the TEC model example of the machine with the Faulhaber winding is presented. The TEC modeling approach explained above is implemented for the slotless PM machine with the Faulhaber winding, whose TEC model is illustrated in Figure 5.15. It is assumed that heat flows only in the radial direction in the air-gap, winding, stator iron, and housing regions. In the sleeve and PM regions, heat may also dissipate in the axial direction through the shaft, bearings, and housing to the ambient.

For the slotless PM machine with the concentrated winding, the TEC model is similar to the one in Figure 5.15, but with minor modifications. These modifications include modeling of the axial heat flow in the winding because of the end windings present in the concentrated winding. It is pointed out that the thermal conductance of the winding region in the longitudinal direction, along the conductors, is much higher that in the transverse direction, because the heat flow is mainly through the copper. In the case of the toroidal winding machine, the flank and outer parts of the windings have to be incorporated in the TEC model.

5.3.6 Optimal design evaluation

The parametric search optimization of the slotless PM machines with the chosen configurations is performed over the variable (varied parameter) ranges specified in Table 5.5. The required rated electromagnetic power of the machine for different

Table 5.5: Ranges and steps of the variables applied in the optimization procedure

Parameter, [unit]	Range	Step
PM diameter, [mm]	$4 \leq d_m \leq 6.5$	0.1
Active length, [mm]	$15 \leq l \leq 35$	1
Conductor current density, [A/mm^2]	$6 \leq J \leq 24$	2
Number of parallel strands, [-]	$1 \leq a \leq 4$	1

rotor dimensions is depicted in Figure 5.16. This plot is not made over the full PM diameter range, as specified in Table 5.5, because the machine designs obtained in the concealed region are not feasible. Figure 5.16 shows that with an increase in the rotor dimensions, also the required electromagnetic power increases. An increase in the rotor dimensions affects the inertia, and thereby, results in a higher power required during dynamic operation. The designs of slotless PM machines with toroidal, concentrated, and Faulhaber winding configurations are determined in accordance with this required power profile.

As it was already mentioned, the optimal machine design is a design with minimum required input power as the drive assumes autonomous operation. These input powers of the designed slotless PM machines over the rotor dimensions are shown in Figure 5.17.

Infeasible design configurations are sorted out by the thermal and mechanical limitations, as well as by the infeasible geometry. The empty area in Figure 5.17(c) represents the area of infeasible motor designs with the proposed geometry and current density value. The meshed areas in the graphs of the input machine power show the area of infeasible designs because of the winding and PM overheating, meaning that the temperature exceeds the maximum allowable temperature. The
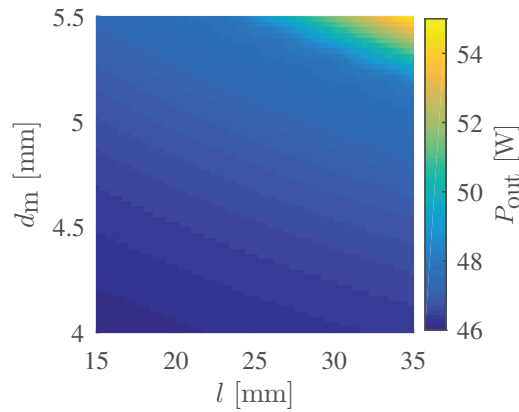
Figure 5.16: Required rated electromagnetic power of the motor over the rotor length and the PM diameter.

red dots on the figures indicate points with minimum input power in the feasible area of the machine designs. We can see that these optimal designs of the slotless machines with different winding configurations result in approximately the same input and output powers. However, in the case of the machine with the Faulhaber winding, the optimal point is on the border of the maximum allowed length. A further increase in the rotor length will result in a lower required input power, yet the decrement is negligible.

The efficiency plots are shown in Figure 5.18. The efficiency of the machine is determined as a ratio of the output (shaft) power to the input power. From the efficiency point of view, we can see that the optimal points are not at their maximum possible values in the plots, as this was not the objective of the optimization. In general, for continuous operation, higher efficiency values (over 90%) can be achieved, as the required torque value is not a function of rotor size in this case. The specifications of the machine designs with different winding topologies are given in Table 5.6. From this table it can be seen that the optimal designs of the machines result in similar input powers, sizes, and efficiencies. Even though the Faulhaber winding machine has a longer active length, it does not require extra space for the end winding. At the same time, because of the skewed conductors, it requires an extra parallel path to keep the strand-level proximity losses at the same level as with the other winding types. Furthermore, in general, the small-sized high-speed PM machines operate at higher current density values in the conductors (up to 30 A/mm^2). However, the current machine design is specially developed for high-dynamic operation, where the rotor diameter has low values. This decreases the magnetic loading of the machine, and therefore, to achieve the required torque, the electrical loading should be increased. This is done by increasing the winding thickness, which leads to poorer cooling capabilities. This, eventually, results in lower current density values.
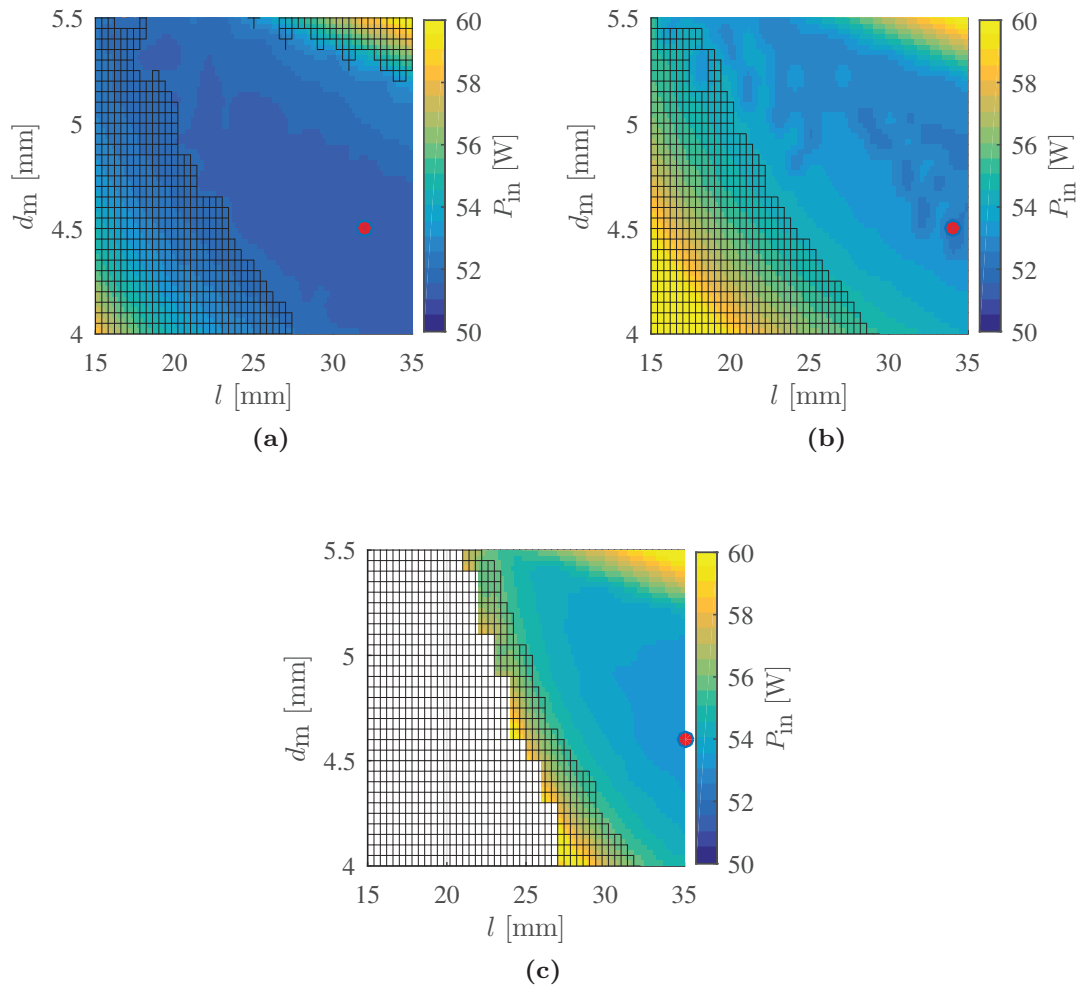
Figure 5.17: Input power of the slotless PM machine with a) toroidal, b) concentrated, and c) Faulhaber windings over the PM diameter and active length of the machine. The empty area on the third figure represents infeasible designs that are due to the inability to reach the required torque value. The meshed areas represent infeasible motor designs that are due to overheating of the winding ($T_w > 130^\circ$C) and PM ($T_{PM} > 120^\circ$C). The bold points represent the optimal designs with minimum input power, which is equal to a) $P_{in} = 51.1$ W, b) $P_{in} = 52.2$ W, and c) $P_{in} = 53.2$ W.
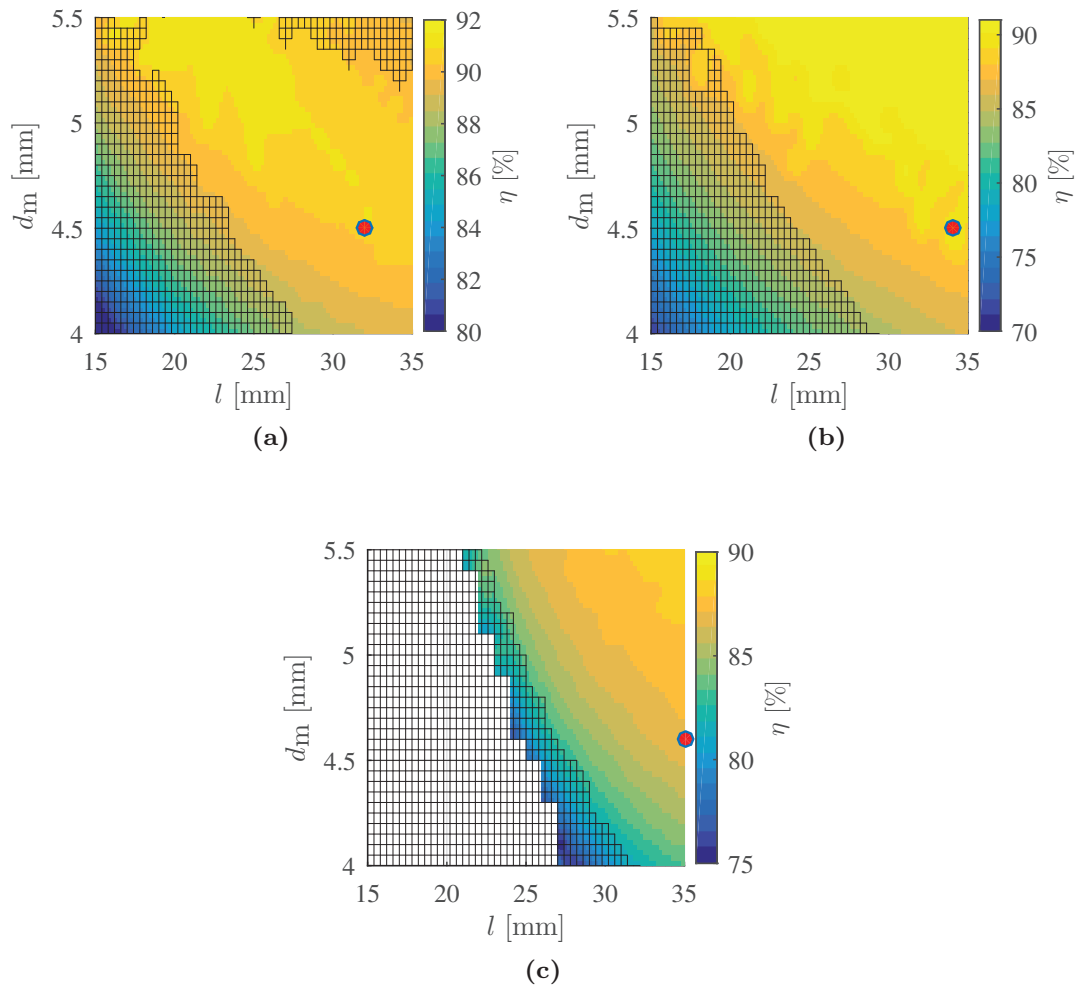
Figure 5.18: Estimated efficiency of the slotless PM machine with a) toroidal, b) concentrated, and c) Faulhaber windings over the PM diameter and active length of the machine. The empty area on the third figure represents infeasible designs that are due to the inability to reach the required torque value. The meshed areas represent infeasible motor designs that are due to overheating of the winding ($T_{\mathrm{w}} > 130°\mathrm{C}$) and PM ($T_{\mathrm{PM}} > 120°\mathrm{C}$). The bold points indicate the optimal design points with minimum input power.

Table 5.6: Optimal designs specifications of slotless PM machines with a) toroidal, b) concentrated, and c) Faulhaber windings for centrifugal compressor load.

Parameter, symbol [unit]	Toroidal	Concentrated	Faulhaber
Input power, P_{in} [W]	51.1	52.2	53.2
Output power, P_{out} [W]	45.5	46.0	46.1
Rated output torque, T [mNm]	5.4	5.5	5.5
Phase current, RMS, I [A_{RMS}]	2.0	2.0	1.5
Phase resistance, R [Ω]	0.22	0.33	0.37
Efficiency, η [%]	89	88	87
Current density, J [$A_{\mathrm{RMS}}/\mathrm{mm}^2$]	6	10	10
Phase turn number, N [-]	18	32	41
Number of parallel strands, a [-]	3	3	4
Conductor diameter, d_{c} [mm]	0.355	0.28	0.25
Active length, l [mm]	32	34	35
PM diameter, d_{m} [mm]	4.5	4.6	4.6
Iron inner radius, r_{si} [mm]	5.4	6.2	7.2
Iron outer radius, r_{so} [mm]	10.4	11.2	12.2
Maximum PM temperature, T_{PM} [°C]	89	88	93
Maximum winding temperature, T_{w} [°C]	89	89	99
Sleeve material	No	No	No
Maximum PM reference stress, $\sigma_{\mathrm{refm,max}}$ [MPa]	1.08	1.13	1.13

5.4 Summary

This chapter presents an approach to design high-speed slotless PM machines intended for a dynamic operation. Section 5.1 deals with evaluation of the machine output requirements depending on the speed and torque profiles. In Section 5.2, possible rotor and stator configurations of the slotless PM machines are considered, and their benefits and drawbacks for the specific application are discussed. The influence of the sleeve material on the machine performance is studied. A review of soft-magnetic materials for high-speed machines is provided. It is decided to conduct design optimization for a slotless PM machine with three types of slotless windings, namely toroidal, concentrated, and Faulhaber windings. Section 5.3 introduces the optimization routine, which is based on the parametric search

optimization. The electromagnetic, mechanical, and thermal models, built into the optimization routine, are discussed in detail. The resultant optimal designs of the three types of slotless machines are presented.

6

Experimental verification

This chapter deals with the implementation and measurement of the designed prototype of a high-speed PM machine with the Faulhaber winding.

6.1   Prototype implementation

The proposed modeling and design approach of high-speed slotless PM machines is evaluated via measurements on a prototype. Previously, in Table 5.6, the designs of three slotless PM machines with toroidal, concentrated, and Faulhaber windings intended for the respiratory application in question have been presented. Implementation of all three machines requires considerable time and financial effort. Therefore, it was decided to only manufacture the machine with the Faulhaber winding, as evaluation of this machine modeling and design approaches is more valuable from theoretical and practical points of view.

In the manufacturing process of the machine with the Faulhaber winding, the initial design was adjusted several times to meet the available manufacturing capabilities and practical restrictions, which were not considered in the design optimization. These changes are presented in Table 6.1. Among the changes is the PM material with lower magnetic characteristics, a shorter active length, a larger rotor diameter, and a different conductor diameter, which decreases the thickness of the winding. The 3D cross-section of the prototype is illustrated in Figure 6.1.

Table 6.1: Initial and final (resultant) design specifications of the slotless PM machine with the Faulhaber winding.

Parameter, symbol [unit]	Initial	Final
Output power, P_{out} [W]	46.1 (120ºC)	45.7 (20ºC)
Rated output torque, T [mNm]	5.5 (120ºC)	5.5 (20ºC)
Phase current, RMS, I [A]	1.5	2.2
Phase resistance, R [Ω]	0.37	0.28
Phase turn number, N [-]	41	35
Conductor diameter , d_{c} [mm]	0.25	0.2
Active length, l [mm]	35	28
PM diameter, d_{m} [mm]	4.6	5.5
Winding thickness, h_{w} [mm]	3.7	3
Yoke inner radius, r_{si} [mm]	7.2	7.3
Yoke outer radius, r_{so} [mm]	12.2	12
PM remanent flux density, B_{rem} [T]	1.2 (120ºC)	1.23 (20ºC)
PM relative permeability, μ_{rPM} [-]	1.035	1.088

The rotor is made of a cylindrically shaped PM and stainless steel caps at the end. The three-phase Faulhaber winding is potted with an epoxy resin into a self-supporting structure and glued to the stator iron bore. The stator iron core is made of laminations of 0.2 mm silicon (3%) iron aluminum (0.3%) alloy (Sura -
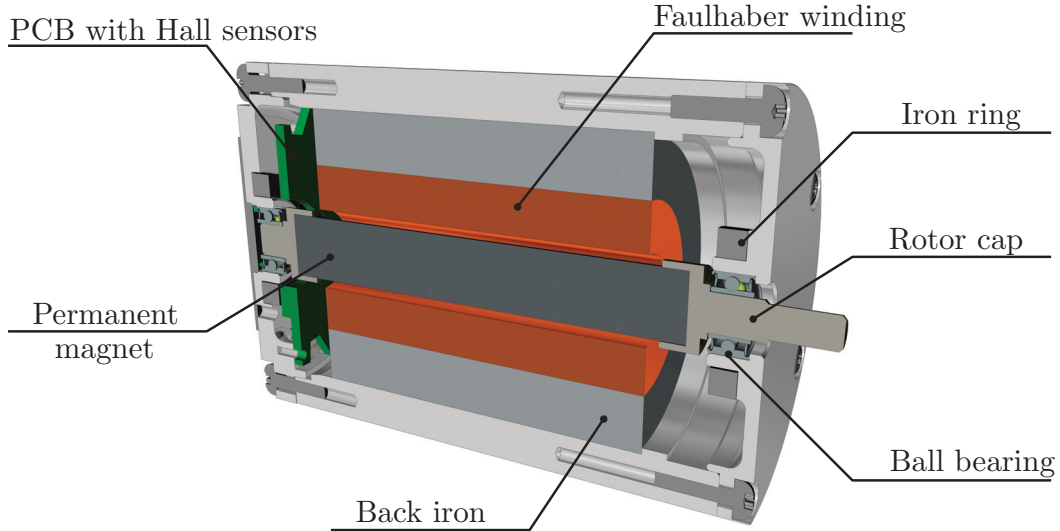
Figure 6.1: 3D cross-sectional view of the prototyped machine.
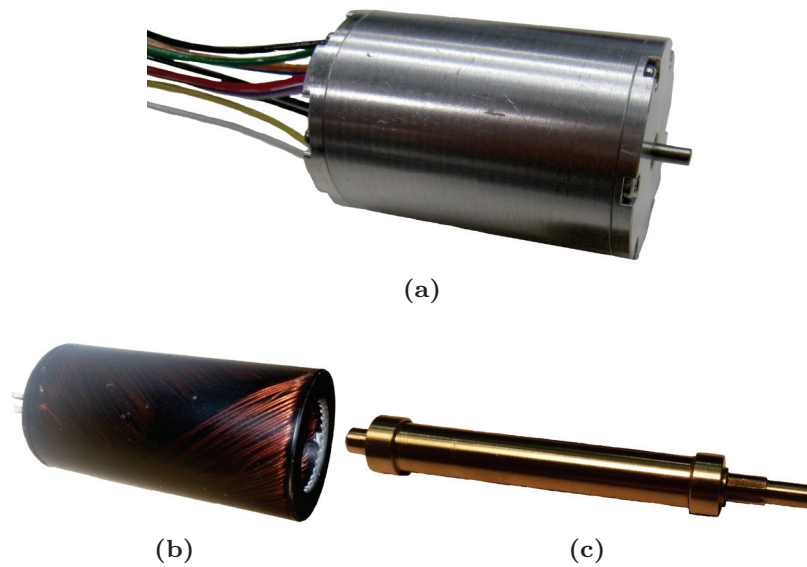

(a)

(b) **(c)**

Figure 6.2: Photos of a) assembled prototype, b) Faulhaber winding, and c) shaftless rotor.

NO20), which are directly glued to the housing. The housing of the motor is made of aluminum, and its construction allows to disassemble the motor. Additionally, the prototype contains a PCB with hall sensors to determine the rotor position and iron rings around the bearings. These iron rings protect the bearings from the leaking PM field, which in the case of the absence of these rings will pass directly through the bearings. This might cause enormous eddy-current losses in the bearings and lead to their malfunction.

A photo of the prototype machine, the encapsulated Faulhaber winding, and the rotor are illustrated in Figure 6.2. Further, in this chapter, the predicted motor characteristics are validated by measurements.

6.2   Torque and emf constants

The torque of slotless PM machines is proportional to the phase current. Therefore, the following expression can be written

$$T = k_{\mathrm{T}} I, \tag{6.1}$$

where k_{T} is the torque constant [Nm/A], and I is the RMS value of the current [A]. This torque constant is dependent on the saturation of the machine iron parts and the temperature value, which affects the magnetic properties of the materials in the machine. This statement is only valid under the assumption that the eddy currents induced by the harmonics of the magnetic field, which generates torque, have a resistance-limited nature over the range of the speeds under consideration. A similar constant dependence can be introduced between the induced emf and the mechanical speed, which can be written as

$$E_{\mathrm{PM}} = k_{\mathrm{E}} \Omega, \tag{6.2}$$

where E_{PM} is the RMS value of the phase emf induced by the PM field [V], k_{E} is the emf constant [V/s], and Ω is the mechanical angular velocity [rad/s]. These torque and emf constants are linked through the PM flux linkage value; this dependence can be obtained by the input and output power expressions of the machine and written as

$$k_{\mathrm{T}} = 3 k_{\mathrm{E}}. \tag{6.3}$$

Hence, k_{T} can be validated through k_{E} by measuring the induced PM emf. The emf measurement was performed by measuring the induced line-to-line emf at the machine terminals, while the rotor was rotated by another motor connected to the shaft. The measurement was performed at different speeds (2000 rpm, 4000 rpm, 6000 rpm) and at different motor terminals. The difference between the measured emf at the same terminals at different speeds was less than 0.1%, whereas the difference between phases, caused by the phase asymmetry, was about 1%. Table 6.2 shows the torque constant values predicted using the semianalytical model and the measured one, where the relative error between the results is less than 1%. The values of the torque constant in both cases are obtained for a temperature of 20°C.

Table 6.2: Predicted and measured torque constants.

	Predicted	Measured (mean)	Error
k_{T} (at 20°C), [mNm/A]	2.64	2.62	$< 1\%$

6.3 DC resistance and synchronous inductance

The DC resistance measurement was conducted using the LCR meter (Wayne Kerr 4270) with the four wire measurement. In total, ten samples of the Faulhaber winding, shown in Figure 6.2(b), were measured. The results of the measurements together with the predicted DC resistance value, obtained for the temperature of 20°C, are given in Table 6.3. The measured value in this table represents the mean phase DC resistance value, where the maximum deviation is less than 3% from the mean value. The predicted DC resistance value for the Faulhaber winding type can be calculated as

$$R_{\mathrm{DC}} = \frac{2\rho_{\mathrm{Cu}} N \sqrt{(\pi(r_{\mathrm{si}}/2 + r_{\mathrm{w}}/2))^2 + l^2}}{a\pi d_{\mathrm{cond}}^2/4}, \tag{6.4}$$

where ρ_{Cu} is the electric resistivity of copper [Ω·m], N is the phase turn number, a is the number of parallel strands, and d_{cond} is the conductor diameter [m]. The relative error range between the measured and predicted DC resistances is 3% - 10%. It is pointed out that the phase DC resistance is increased by 0.02 Ω at the machine terminals because of the additional resistance of the connecting wires.

Table 6.3: Predicted and measured phase DC resistance, phase synchronous inductance, and phase synchronous inductance of the winding only.

Parameter, [unit]	Predicted	Measured	Error
R_{DC} (at 20°C), [Ω]	0.3 - 0.32	0.29	3% - 10%
L_{s}, [µH]	28.9	25.3	14%
L_{s} (no iron, no rotor), [µH]	20.2	18	12%

The phase synchronous inductance can be measured indirectly using the machine voltage equation (3.21). This method requires knowledge of the phase resistance, emf constant, electrical frequency, and rotor position in order to obtain the synchronous inductance value. However, accurate determination of the mentioned parameters is often difficult. Therefore, it was decided to measure the synchronous inductance at the machine terminal at a low frequency while the rotor is locked. Measurement at a low frequency (50 Hz) guarantees that there is no influence of eddy currents induced in the rotor, stator iron, and winding conductors on the inductance measurement; in other words, the resistance-limited nature of the

induced eddy currents is ensured. The inductance value was measured at two machine terminals using the LCR meter (Wayne Kerr 4270), where the measured value was divided by two to obtain the value of the phase synchronous inductance. The measured and calculated inductance values of the prototype machine are given in Table 6.3. The relative error between the results is 14%. Additional verification of inductance calculation approach was carried out by measuring the synchronous inductance of the winding itself, without the stator iron and the rotor, and comparing it with the calculated value. The winding was supplied by a three-phase voltage of 20 kHz provided by the power supplies TOE 7621 (TOELLNER Electronic Instrumente GMBH), where the phase reactance value was measured using the power analyzer LMG 500 (ZES ZIMMER). In this case, the phase synchronous inductance was calculated by dividing the reactance value by the angular frequency of the supply voltage. The measured and calculated synchronous inductance values of the winding only are given in Table 6.3. The obtained relative error value is about 12%, which is close to the relative error obtained by the LCR meter measurement.

6.4   Loss verification

The Sankey diagram of losses in high-speed slotless PM machines (see Figure 4.1) divides them into two groups, namely losses caused by the armature current and losses caused by the rotation. The losses caused by the armature current are assumed to contain only the Joule losses on the winding DC resistance and the rotor eddy-current losses. These Joule losses are assessed by the winding DC resistance of the machine, which was verified in the previous section. In this section, the verification of the rotor eddy-current loss calculation and the losses caused by the rotor motion is demonstrated.

6.4.1   Rotor eddy-current loss measurement

The rotor eddy-current losses are mostly measured indirectly, as direct measurement of the dissipated power in the rotor represents difficulty [80]. A common way to estimate the rotor eddy-current losses in PM machines is first to validate the model available (analytical or FEM), and then based on this model and current harmonic content, to assess the rotor eddy-current losses induced in reality. Indirectly, the rotor eddy-current losses can be assessed using the loss segregation method, where these losses are subtracted from the total losses if other loss components are known. As explained in [80], the method that employs the locked-rotor and no-rotor tests is accurate and easy to implement. In this test, the input power of the machine is measured in two cases: with the locked rotor (not rotating) and without the rotor. The difference of these two input powers is the power dissipated
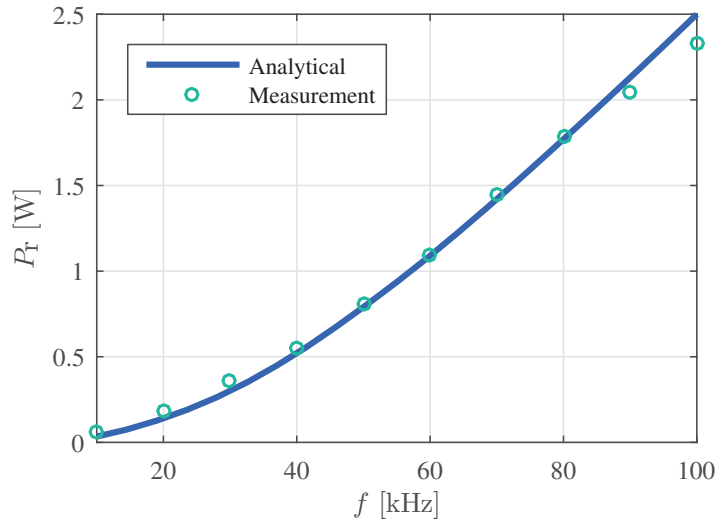
Figure 6.3: Rotor eddy-current losses versus the armature current frequency obtained during the locked-rotor test while the phase current value is kept at 1A over the whole frequency range.

by the rotor eddy currents. The phase current in both tests has to remain equal to keep the losses other than the rotor eddy-current ones constant in both tests. This method of the rotor eddy-current loss measurement is valid only for PM machines in which the equivalent permeability of the rotor is equal to one, to maintain an equal magnetic field in both cases. This is the case for the prototype machine, where the rotor consists of the PM with relative permeabilities close to one.

For the locked-rotor and no-rotor tests, the machine was supplied by a three-phase sinusoidal voltage, which is produced by two power supplies TOE 7621 (TOELL-NER Electronic Instrumente GMBH). In these tests, the three-phase input power was measured using the power analyzer LMG 500 (ZES ZIMMER). In order to eliminate the iron losses, the measurement was done using only the winding (see Figure 6.2(b)) and the rotor (see Figure 6.2(c)) without the stator iron core and other parts of the motor. The measurement was performed in the frequency range of 10–100 kHz with the phase current amplitude of 1 A. The analytical modeling of the eddy-current losses for the locked-rotor case differs from the rotating rotor case only by the modeling of the armature field in the stator reference frame, without transferring it to the rotor reference frame as shown in Section 2.6.4. The measured and modeling results of the rotor eddy-current losses for the locked-rotor test are illustrated in Figure 6.3, where a good agreement between the results is achieved. Slight deviation can be seen on the boundaries of the frequency range in question. This can be explained by the higher conductivity of the PM material than it was assumed during the simulations.
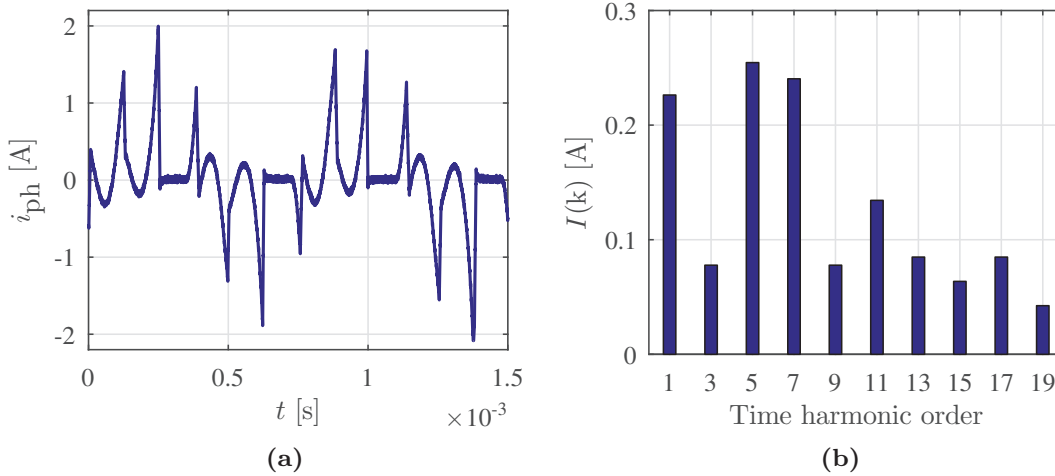
Figure 6.4: a) Phase current waveform at the no-load test and b) its harmonic content given in RMS values.

6.4.2   Measurement of losses caused by rotation

The rotation of the rotor causes mechanical losses and electromagnetic losses generated by the PM field. As explained in Section 4.1, modeling of losses caused by rotation is limited to consideration of the bearing losses, windage losses, iron losses, and proximity losses in the winding caused by the PM field. The measurement of these losses separately or using segregation methods seems infeasible without special proof-of-concept prototypes and because of the low values of these losses. Therefore, it was decided to measure them together at once by performing a no-load test of the prototype machine. In the no-load operation, the machine drains from the supply only the active power required to overcome the losses caused by rotation and the Joule losses in the winding produced by the no-load current. The input power is measured at the DC link of the converter by a power meter PW3335 (HIOKI). The converter produces square-wave three-phase voltages, the amplitude of which is not controlled by PWM but with the DC link voltage. Thus, the converter losses are significantly reduced and, therefore, neglected. The waveform of the phase current in the no-load test is illustrated in Figure 6.4(a), and the harmonic content of this current is presented in Figure 6.4(b). The Joule losses caused by the no-load current can be assessed using the DC resistance value. The rotor eddy-current losses caused by the no-load armature field are minimal, and can thus be neglected. The power is measured when the machine has reached the steady-state operation (temperature) at the speed of 80000 rpm. These measured no-load losses are given in Table 6.4.

The analytical assessment of the loss components caused by the rotation was explained in Chapters 4 and 5; however, some explanatory notes have to be given.

Table 6.4: Predicted and measured losses caused by rotation in the prototyped machine.

Parameter, [unit]	Predicted	Measured
Bearing losses, [W]	0.8	-
Windage losses, [W]	0.1	-
Strand-level proximity losses, [W]	0.4	-
Bundle-level proximity losses, [W]	0.5	-
Iron losses in stator core, [W]	0.4	-
Iron losses in rings, [W]	0.1	-
Losses caused by rotation, [W]	2.3	3.2

The Faulhaber winding used in the prototype machine has four parallel strands in the winding coils, which are not twisted. Thus, the bundle-level proximity losses have to be included in the no-load losses. These losses are calculated using the approach based on the electrical circuit, which is explained in Section 4.2. As the parallel strands are located next to each other in the circumferential direction, the phase shift between the emfs of the neighboring strands is assumed to be of one conductor angle, which is calculated as

$$\xi = \frac{d_{\text{cond}}}{\cos(\gamma)(r_{\text{si}}/2 + r_{\text{w}}/2)}, \tag{6.5}$$

where γ is defined as $\gamma = \arctan(l/(r_{\text{wc}}\pi))$. The value of the bundle-level proximity losses is accepted as the mean value of the induced losses over the one electrical period. Additionally, iron losses are generated in the iron rings (see Figure 6.1) as a result of the leakage PM field. The value of the magnetic field in the rings was preliminarily calculated using the 3D FEM, where the induced iron losses are included in the design optimization procedure using the iron loss model given in Section 4.4. The electromagnetic losses are calculated taking into account the temperature influence on the electromagnetic properties of the materials. The temperature values of the machine parts are taken from the thermal model. Because the induction temperature coefficient of the PM is unknown, it is assumed to be 0.12%/°C. The calculated losses caused by the rotation are listed in Table 6.4. The relative difference between the predicted and measured losses produced by rotation is about 30%. This considerable difference can be primarily due to the approximated model of the bearing loss calculation. Furthermore, the stray electromagnetic losses mainly caused by the eddy currents resulting from the changing PM field in the conducting machine parts can be the reason for the difference.
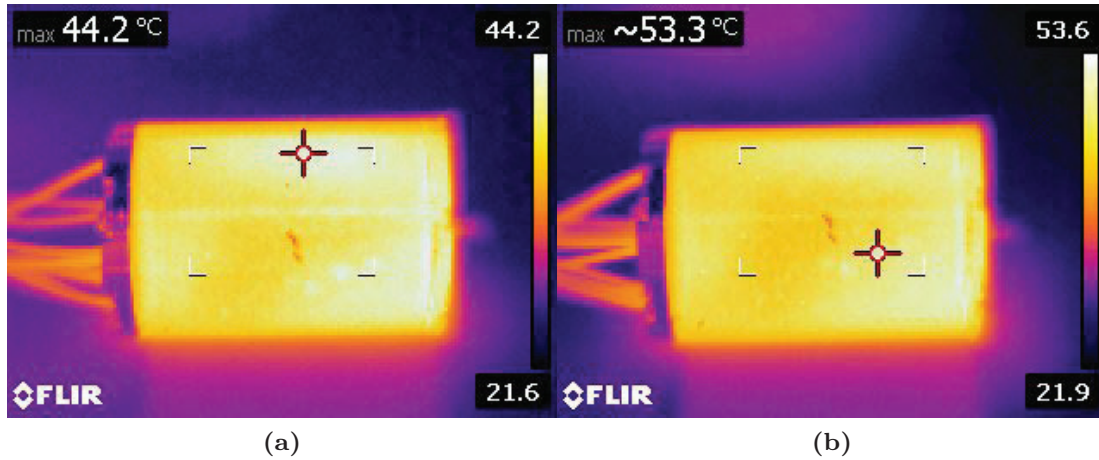
Figure 6.5: Thermal images of the prototyped machine during a) the DC current and b) no-load tests.

6.5   Thermal model verification

To verify the developed TEC model, two steady-state tests, namely the DC current and the no-load, were conducted on the prototyped machine. The DC current test was performed by conducting a DC current of 2A through two machine terminals. In this test, only Joule losses in the winding were present, which are estimated to be about 2.5 W. The no-load test is described in the previous section of this chapter. The overall losses dissipated in the machine during the no-load test were 3.4 W. The losses caused by the rotor rotation were 3.2 W as indicated in Table 6.4. It is noted that the measured value of no-load losses is used in the thermal model. The difference between the measured and predicted no-load losses is added to the bearing losses in the thermal model. In these tests, the housing and the winding temperatures were measured. The housing temperature was measured directly using a thermocouple and a thermal camera FLIR E40. The thermal images of the prototype obtained by the thermal camera during the DC current and no-load test are presented in Figure 6.5. The difference between the measured housing temperature using the thermocouple and the thermal camera was less than 1°C. The winding temperature was assessed indirectly, using the winding resistance change caused by temperature.

The thermal model circuit of the prototype is identical to the one presented in Figure 5.15, excluding the sleeve part. The ambient temperature of the thermal model is assumed to be 21°C. The predicted and measured results of the winding and housing temperatures are given in Table 6.5. The simulated results are in good agreement with those obtained by measurements. The results demonstrate a small temperature difference between the winding and the housing, which is explained

Table 6.5: Predicted and measured temperatures of the winding and housing in the prototyped machine.

Temperature	Predicted	Measured
DC current test		
Winding	48°C	45°C
Housing	45°C	44°C
No-load test		
Winding	55°C	54°C
Housing	53°C	53°C

by the low total thermal resistance from the winding to the housing. This is often the case for small-sized inner rotor slotless PM machines.

6.6   Summary

In this chapter, the implementation and measurement of the high-speed slotless PM machine prototype with the Faulhaber winding type are presented. The stator and rotor constructions of the prototype machine are discussed. Moreover, the differences between the initial and final designs, caused by the manufacturing limitations, are explained. To validate the predicted torque and emf constants, the induced emf is measured at the machine terminals while the rotor is rotated by another machine. The relative error between the results obtained by calculations and measurements does not exceed 1%. The prediction of the passive elements of the electrical circuit is also verified by measurements, where the relative error between the predicted and measured results in the case of the phase DC resistance is in the range of 3%–10%, and for the phase synchronous inductance it is 14%. The model for the rotor eddy-current loss calculation is verified by performing locked-rotor and no-rotor tests, which confirm the acceptable accuracy of the developed model. The losses caused by the rotation are validated by performing the no-load test, where the obtained relative error is about 30%. The reasons for this mismatch can be explained by the inaccurate bearing loss models and stray losses caused by the PM field. Furthermore, the thermal model is validated by measuring the housing and the winding temperatures of the prototype in DC current and no-load tests. The obtained temperature difference between the measured and predicted results is several degrees.

Part III

Closing

7

Conclusions and recommendations

7.1　Conclusions

This research has focused on development of electromagnetic modeling and design frameworks and implementation of high-speed slotless PM machines.

7.1.1　Part 1: Electromagnetic modeling framework

Electromagnetic field modeling

The slotless winding embodiments enable a wide variety of complex winding geometries with skewing, which mainly result in lower-cost manufacturing of small-sized machines. The electromagnetic field modeling of high-speed PM machines with these slotless windings lacks a unified, fast, and accurate approach. This thesis presents an extended harmonic modeling (HM) technique to model the electromagnetic field, covering the induced eddy-current phenomenon, in 3D problems in a cylindrical coordinate system. The developed models are able to evaluate PM machines with a wide range of slotless windings, including those with skewing. The extension of the HM technique incorporates the 2D HM, formulated by the vector potential, and the 3D HM, expressed by the second-order vector potential (SOVP). Such an approach has been chosen because of the space distribution of the magnetic field source given by the linear current density, which is described by a 2D Fourier series, and contains linear current density components with single and double space coordinate dependences.

The obtained electromagnetic field modeling framework has been verified by using 3D FEM models of the benchmark slotless PM machines with Faulhaber, rhombic, and diamond windings for a comparison of the magnetic and electric fields. The maximum difference obtained for the magnetic field comparison does not exceed 10% of the peak value of the magnetic field distribution. The comparison of the electric field strength on the rotor surface gives a higher maximum difference, which is about 20%.

The presented HM simulation framework has limitations concerning the actual physical properties of certain regions. The main limitation is the assumption of the nonlinear behavior of the soft-magnetic material. This assumption, however, has only a slight impact in the modeling of PM machines, especially with slotless windings. This is explained by the large effective air gap. As it has been demonstrated in the benchmark machines with the M270-35A iron material, the decrease in the relative permeability value from $\mu_{\mathrm{r}} = 10^5$ to $\mu_{\mathrm{r}} = 10^2$ causes only a 1% error in the magnetic field calculation. Besides, if a laminated iron is used, the iron magnetic properties become anisotropic, meaning that the relative permeability varies with the direction of magnetization. This influences the modeling of the

magnetic field, however the impact is minimal because of the large effective air gap in slotless PM machines.

Derivation of electromagnetic quantities

The electromagnetic field distribution modeled in Chapter 2 is further used to derive the electromagnetic quantities of slotless PM machines, namely the developed electromagnetic torque, the emf induced by the PM field, and the synchronous inductance, which is described in Chapter 3. The generalized expression to calculate the electromagnetic torque has been derived using the armature and PM field solutions in the air gap for the 2D and 3D electromagnetic problems applying Maxwell's stress tensor. The torque expression can be used to calculate the time- and position-dependent torque profiles. It has been validated for the benchmark PM machine with the Faulhaber winding by means of the 3D FEM model, where the relative error is less than 4%.

The emf induced by the PM field is calculated by integrating the magnetic field over the winding spatial distribution. The relative error of 4% is obtained in the emf calculation in comparison with the 3D FEM. The calculation of the synchronous inductance using the field predicted by the HM is able to take into account the inductance reduction produced by the rotor eddy currents. This frequency-dependent synchronous inductance value is further used to estimate the current ripple caused by the PWM voltage. The analytically evaluated synchronous inductance value demonstrates a good matching, where the maximum relative difference from the 3D FEM model does not exceed 5%.

Electromagnetic losses in high-speed slotless PM machines

Accurate modeling of losses in electrical machines is of primary importance, as it facilitates accurate prediction of the machine performance and thermal stresses on vulnerable machine parts. In order to complete the electromagnetic modeling framework, the lacking parts of the electromagnetic loss calculation in high-speed slotless PM machines have been incorporated. By using the electromagnetic field distribution in the machine, the rotor eddy-current losses have been simulated employing the Poynting vector. The rotor eddy-current losses assessed using the HM and 3D FEM demonstrate a good matching, where the maximum relative difference does not exceed 5%.

Furthermore, the strand-level proximity-effect loss calculation model for the round conductor cross-section (2D case) has been extended to the oval conductor cross-sections, which is the case for the slotless windings with skewing. The strand-level proximity-effect loss calculation model for the oval conductor cross-section has been validated by using the FEM with a relative error that does not exceed 10%.

Additionally, the approach to assess the impact of the PWM voltage on the rotor eddy-current losses in slotless PM machines has been presented. This method is based on the solution of the electrical circuit of the slotless PM machines with frequency-dependent circuit parameters, where the PWM voltage is defined as a Fourier series over the frequency. Performing the rotor eddy-current loss calculation over each time harmonic of the current ripple results in the overall impact of the PWM on the rotor eddy-current losses. This approach to obtain the current ripple content has been verified by measurements on the test machine having a toroidal winding. Two voltage-source converters, one with sinusoidal and another with space vector PWM, have been used. The comparison shows the maximum obtained relative discrepancy is 39%. The error in the measurement can be explained by the measurement error, resulting from the high frequencies and parasitic impedance present in the circuit, and error in the estimation of the electric circuit parameters of the machine and spectrum of the phase voltage.

7.1.2 Part 2: Design framework

Design of highly dynamic high-speed slotless PM machines

One of the objectives of this research has been to design a slotless PM machine for a medical ventilator system with a highly dynamic speed profile and minimum power consumption. By using the extreme cases of the motion profiles, the required rated electromagnetic torque of the machine has been defined as the maximum RMS torque value over one period. This torque value has to be updated with the change in the rotor dimensions as a function of rotor inertia.

Different slotless PM machine topologies have been analyzed with the aim to determine suitable rotor and stator combinations for the application in question. The shaftless rotor structure has been chosen because of higher magnetic loading with the identical PM outer diameter and lower mechanical stress value in the PM. Furthermore, diametrical rotor magnetization is advantageous as it produces a purely sinusoidal magnetic field. The stator configuration is mainly defined by the slotless winding topology, and complicates the selection of the possible slotless winding options. Therefore, it has been decided to design slotless PM machines with three different winding configurations, namely toroidal, concentrated, and Faulhaber ones.

The design optimization framework for high-speed slotless PM machines intended for highly dynamic operation has been developed. This framework covers the electromagnetic, thermal, and mechanical models of slotless PM machines. As the resulting multiphysical model is fast, determination of the optimal machine design by parametric search has been employed as the optimization method. In the developed design framework, iteration between the electromagnetic and thermal

models is not implemented, which requires a close guess of the material temperature of the machine parts to take into account the thermal influence. The iteration process, however, can be implemented and evaluated by the proposed approach.

Three optimal designs of the small-sized high-speed slotless PM machine with either toroidal, concentrated, or Faulhaber windings have been obtained by using the parametric search optimization framework. These identified optimal machine designs with three different windings have similar machine performance indices (input power and efficiency) and dimensions of the active part, excluding the end windings. Therefore, it is not obvious how to select the most suitable winding topology, which is, in practice, mainly defined by the manufacturing capabilities. Meanwhile, it has been observed that the common tendency is to select a decreased rotor diameter and an increased rotor length, which lead to decreased rotor inertia and, consequently, lower power consumption in this dynamic application. The decreased rotor diameter gives a lower magnetic loading. Therefore, to maintain the required torque, the electrical loading should be increased, which can be identified in the relatively large thickness of the winding. It has also been observed that with the increased winding thickness, the allowed conductor current density is decreased because of the poorer cooling capabilities. Furthermore, with the given PWM type (asymmetrical space vector), the optimal machine designs for all three winding types result in a rotor without any sleeve material, as it gives the lowest rotor eddy-current losses.

Prototype implementation and measurements

A prototype of the high-speed slotless PM machine with a Faulhaber winding has been manufactured and tested. The measurements have shown that the model gives a satisfactory agreement in the prediction of the torque constant, DC resistance, and synchronous inductance of the prototype machine with relative errors smaller than 1%, 4%, and 14%, respectively. The rotor eddy-current loss calculation model has been validated by conducting indirect measurements by no-rotor and locked-rotor tests. In order to reduce the influence of the other possible losses, a measurement was conducted with the Faulhaber winding without the back iron and a dummy cylindrical PM. The results of the measurements have proven the validity of the developed models by demonstrating a maximum relative error of about 10%.

As losses caused by the rotor motion cannot be measured separately, a no-load test of the prototype was conducted to measure them together. To separate the losses caused by the rotor motion, the losses caused by the applied current (DC Joule losses), and the rotor eddy-current losses, they are subtracted from the no-load losses. The obtained relative error between the measured and calculated losses caused by the rotation is about 30%. The significant error in the results can be explained by the poor accuracy of the predicted bearing loss modeling and stray

losses caused by the PM field.

Based on the implementation of the prototype, it can be concluded that the Faulhaber winding type is not the best candidate for a relatively large winding thickness because of the manufacturing limitations. For the prototype, a three-layer Faulhaber winding had to be manufactured to meet the thickness requirements.

7.2   Contributions

The main scientific contributions of this thesis can be summarized as:

- *Extension of the 3D harmonic modeling technique for slotless PM machines with complex winding geometries.*

- *Loss estimation mechanism in high-speed PM machines, including the rotor eddy-current phenomenon.*

- *Analysis and model implementation of the PWM influence on the rotor eddy-current losses.*

- *Design, implementation, and experimental verification of the high-speed (80 krpm) slotless PM machine with the Faulhaber winding for highly dynamic applications.*

7.3   Recommendations for future work

Drive-level modeling and design framework

High-speed electrical machines are inherently employed with power electronic converters and are driven by certain control strategies. The common practice in the drive design is to develop each of the drive components, namely the electrical machine and the converter, separately. However, such an approach easily results in an unpractical solution as the mutual influence of the drive components is not taken into account. Therefore, to make a further step in the high-speed drives design, a system-level approach has to be adopted.

Research on materials

Electromagnetic materials in highly dynamic high-speed PM machines operate within wide temperature and frequency ranges. These parameters have a strong impact on the electromagnetic material properties, and consequently, on the machine performance. Furthermore, the manufacturing processes of lamination sheets give rise to local stresses, which leads to deterioration of the material magnetic properties. Therefore, research on the accurate characterization and modeling of the material behavior is required.

More accurate prediction of the PWM current ripple

As it has been shown in Section 4.5, the discrepancy between the predicted and measured current ripple caused by the PWM can be considerable. However, this prediction accuracy can be sufficient for the preliminary estimation of the losses caused by the current ripple. To further improve the modeling of the losses in the machine, more accurate estimation of the current ripple caused by the PWM is required.

Modeling of electromagnetic losses caused by PWM current ripple

In this thesis, only the impact of the PWM current ripple on the rotor eddy-current losses has been investigated. However, the electromagnetic field generated by the current ripple is the source of the proximity effect losses in the winding (see Section 4.2) and iron losses in the stator iron (see Section 4.4). The impact of these losses can be significant, especially with an increase in the rotational speed. Therefore, it is recommended to analyze and model these losses to predict more accurately the machine behavior.

Unbalanced magnetic field modeling produced by self-supporting windings

Self-supporting windings can be considered asymmetrical ones in the radial directions as their coil sides are displaced in this direction. This displacement causes an unbalanced armature magnetic field in the air gap, which leads to undesirable forces and torque in the machine. Investigation of these forces and torque is vital for high-speed slotless PM machines with a self-magnetic bearing system as they influence the stability of the rotor levitation.

More accurate mechanical and thermal modeling

When performing thermal and mechanical modeling of high-speed electrical machines, designers usually leave a wide margin because of uncertainties in the developed thermal and mechanical models. This leads to overrated machines, which operate far from their actual physical limits. When moving towards very high speeds, these margins have to be minimized to achieve maximum material utilization and a maximum power density. Therefore, more accurate thermal and mechanical modeling of high-speed machines should facilitate an improvement in the performance of high-speed PM machines.

A

Current density distribution

A.1   Linear current density distribution

A   Linear current density of the rhombic winding

To calculate the axial component of linear current density distribution, the rhombic winding is divided into four current-carrying filaments as shown in Fig. A.1. Then, the coefficients in the distribution function (2.74) are derived using (2.75) as

$$
c_{\text{ss}} = \frac{\kappa}{4 \cdot 2l \cdot 2\pi} \cdot
$$

$$
\left(\int_{0}^{l/2} \int_{\theta_1}^{\theta_2} \sin\left(\frac{\nu 2\pi}{2\pi} \theta \right) \sin\left(\frac{m 2\pi}{2l} z \right) d\theta dz - \right.
$$

$$
\int_{0}^{l/2} \int_{\theta_3}^{\theta_4} \sin\left(\frac{\nu 2\pi}{2\pi} \theta \right) \sin\left(\frac{m 2\pi}{2l} z \right) d\theta dz +
$$

$$
\int_{-l/2}^{0} \int_{\theta_5}^{\theta_6} \sin\left(\frac{\nu 2\pi}{2\pi} \theta \right) \sin\left(\frac{m 2\pi}{2l} z \right) d\theta dz -
$$

$$\int\limits_{-l/2}^{0}\int\limits_{\theta_7}^{\theta_8}\sin\left(\frac{\nu 2\pi}{2\pi}\theta\right)\sin\left(\frac{m2\pi}{2l}z\right)d\theta dz\Bigg),\tag{A.1}$$
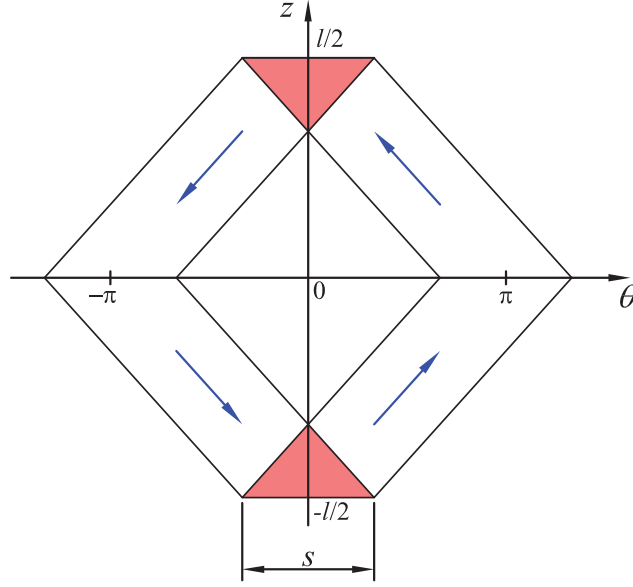

Figure A.1: Phase coil of a rhombic winding represented as four current-carrying strips. The arrows represent the direction of the current.

$$c_{\mathrm{sc}}=\frac{\kappa}{4\cdot 2l\cdot 2\pi}\cdot$$

$$\Bigg(\int\limits_{0}^{l/2}\int\limits_{\theta_1}^{\theta_2}\sin\left(\frac{\nu 2\pi}{2\pi}\theta\right)\cos\left(\frac{m2\pi}{2l}z\right)d\theta dz-$$

$$\int\limits_{0}^{l/2}\int\limits_{\theta_3}^{\theta_4}\sin\left(\frac{\nu 2\pi}{2\pi}\theta\right)\cos\left(\frac{m2\pi}{2l}z\right)d\theta dz+$$

$$+\int\limits_{-l/2}^{0}\int\limits_{\theta_5}^{\theta_6}\sin\left(\frac{\nu 2\pi}{2\pi}\theta\right)\cos\left(\frac{m2\pi}{2l}z\right)d\theta dz-$$

$$\int\limits_{-l/2}^{0}\int\limits_{\theta_7}^{\theta_8}\sin\left(\frac{\nu 2\pi}{2\pi}\theta\right)\cos\left(\frac{m2\pi}{2l}z\right)d\theta dz\Bigg),\tag{A.2}$$

$$c_{\mathrm{cs}} = \frac{\kappa}{4 \cdot 2l \cdot 2\pi} \cdot$$

$$\left(\int_0^{l/2} \int_{\theta_1}^{\theta_2} \cos\left(\frac{\nu 2\pi}{2\pi}\theta\right) \sin\left(\frac{m2\pi}{2l}z\right) d\theta dz - \right.$$

$$\int_0^{l/2} \int_{\theta_3}^{\theta_4} \cos\left(\frac{\nu 2\pi}{2\pi}\theta\right) \sin\left(\frac{m2\pi}{2l}z\right) d\theta dz +$$

$$+ \int_{-l/2}^{0} \int_{\theta_5}^{\theta_6} \cos\left(\frac{\nu 2\pi}{2\pi}\theta\right) \sin\left(\frac{m2\pi}{2l}z\right) d\theta dz -$$

$$\left. \int_{-l/2}^{0} \int_{\theta_7}^{\theta_8} \cos\left(\frac{\nu 2\pi}{2\pi}\theta\right) \sin\left(\frac{m2\pi}{2l}z\right) d\theta dz \right), \tag{A.3}$$

$$c_{\mathrm{cc}} = \frac{\kappa}{4 \cdot 2l \cdot 2\pi} \cdot$$

$$\left(\int_0^{l/2} \int_{\theta_1}^{\theta_2} \cos\left(\frac{\nu 2\pi}{2\pi}\theta\right) \cos\left(\frac{m2\pi}{2l}z\right) d\theta dz - \right.$$

$$\int_0^{l/2} \int_{\theta_3}^{\theta_4} \cos\left(\frac{\nu 2\pi}{2\pi}\theta\right) \cos\left(\frac{m2\pi}{2l}z\right) d\theta dz +$$

$$+ \int_{-l/2}^{0} \int_{\theta_5}^{\theta_6} \cos\left(\frac{\nu 2\pi}{2\pi}\theta\right) \cos\left(\frac{m2\pi}{2l}z\right) d\theta dz -$$

$$\left. \int_{-l/2}^{0} \int_{\theta_7}^{\theta_8} \cos\left(\frac{\nu 2\pi}{2\pi}\theta\right) \cos\left(\frac{m2\pi}{2l}z\right) d\theta dz \right), \tag{A.4}$$

where

$$\theta_1 = \frac{2\pi z}{l} - \frac{4\pi}{3}, \qquad\qquad \theta_2 = \frac{2\pi z}{l} - \frac{2\pi}{3},$$

$$\theta_3 = \frac{2\pi(l/2 - z)}{l} - \frac{\pi}{3}, \qquad\qquad \theta_4 = \frac{2\pi(l/2 - z)}{l} + \frac{\pi}{3},$$

$$\theta_5 = -\frac{2\pi z}{l} - \frac{4\pi}{3}, \qquad\qquad \theta_6 = -\frac{2\pi z}{l} - \frac{2\pi}{3},$$

$$\theta_7 = \frac{2\pi(l/2 + z)}{l} - \frac{\pi}{3}, \qquad\qquad \theta_8 = \frac{2\pi(l/2 + z)}{l} + \frac{\pi}{3}. \tag{A.5}$$

These coefficients contain four integrals, which correspond to the number of current-carrying filaments, and the sign preceding the integrals shows the directions of current with respect to the axial direction. The limits of the inner integrals are the equations of the filament border lines. These dependences can be derived as

$$\theta = (z - z_0)\frac{\theta_1 - \theta_0}{z_1 - z_0} + \theta_0. \tag{A.6}$$

These coefficients should be calculated for the following cases

$$1^{\text{st}} \text{ case, for } \nu > 0, \ m > 0,$$
$$2^{\text{nd}} \text{ case, for } \nu = 0, \ m > 0,$$
$$3^{\text{rd}} \text{ case, for } \nu > 0, \ m = 0,$$
$$4^{\text{th}} \text{ case, for } \nu = 0, \ m = 0, \tag{A.7}$$

which eventually results in nine coefficients. In the case of rhombic winding, only the coefficients c_{ss} and c_{sc} for $(\nu > 0, \ m > 0)$ do not result in a zero. Following some mathematical simplifications, the distribution function of three phases for the rhombic winding is

$$f(\theta, z) =$$
$$\sum_{\substack{\nu=1 \\ m=1}}^{\infty} \left(\frac{c_{\text{ss}} + c_{\text{sc}}}{2} \sin\left(\nu(\theta + x)\right) \cos\left(\frac{\left(n - \frac{m}{2}\right)\pi}{l} z \right) + \right.$$
$$\left. + \frac{c_{\text{ss}} - c_{\text{sc}}}{2} \sin\left(\nu(\theta + x)\right) \cos\left(\frac{\left(n + \frac{m}{2}\right)\pi}{l} z \right) \right), \tag{A.8}$$
$$c_{\text{ss}} = \frac{16\cos(n\pi)\sin(m\pi/4)^2\sin(n\pi/3)}{mn\pi^2},$$
$$c_{\text{sc}} = -\frac{8\sin(m\pi/2)\sin(n\pi/3)\sin(n\pi)}{mn\pi^2},$$
$$x = (0, \frac{2\pi}{3}, \frac{4\pi}{3}).$$

Substituting this distribution function into (2.73) and bearing in mind the following trigonometric identity:

$$\sin(\alpha)\cos(\beta) = \frac{\sin(\alpha + \beta) + \sin(\alpha - \beta)}{2}, \tag{A.9}$$

the axial component of the linear current density for the rhombic winding is

$$K_z(\theta, z, t) = \sum_{\substack{m=1 \\ k=1 \\ L=-\infty}}^{\infty} \left(\hat{K}_{sc1}(m, k, L) \sin\left(((3L - k)\theta + k\omega t)\right) \cos(\omega_{z1} z) + \right.$$

$$\left. + \hat{K}_{sc2}(m, k, L) \sin\left(((3L - k)\theta + k\omega t)\right) \cos(\omega_{z2} z) \right),$$ (A.10)

$$\omega_{z1} = \frac{\left(3L - k - \dfrac{m}{2}\right)\pi}{l},$$

$$\omega_{z2} = \frac{\left(3L - k + \dfrac{m}{2}\right)\pi}{l},$$

$$\hat{K}_{sc1} = \frac{3N\hat{I}}{2sr_{si}} \frac{16\cos((3L - k)\pi)\sin(m\pi/4)^2 \sin((3L - k)\pi/3)}{m(3L - k)\pi^2},$$

$$\hat{K}_{sc2} = -\frac{3N\hat{I}}{2sr_{si}} \frac{8\sin(m\pi/2)\sin((3L - k)\pi/3)\sin((3L - k)\pi)}{m(3L - k)\pi^2}.$$

B   Linear current density of the Faulhaber winding

$$K_z(\theta, z, t) = \sum_{\substack{m=1 \\ k=1 \\ L=-\infty}}^{\infty} \hat{K}_{sc} \sin\left(((3L - k)\theta + k\omega t)\right) \cdot$$

$$\cdot \left(\sin\left(\omega_{z1} z + \frac{(3L - k)\pi}{2} \right) + \sin\left(\omega_{z2} z + \frac{(3L - k)\pi}{2} \right) \right) +$$

$$+ \sum_{\substack{k=1 \\ L=-\infty}}^{\infty} \hat{K}_s \sin\left(((3L - k)\theta + k\omega t)\right) \sin\left(\omega_{z3} z + \frac{(3L - k)\pi}{2} \right),$$ (A.11)

$$\omega_{z1} = \frac{(3L - k + m)\pi}{2l},$$

$$\omega_{z2} = \frac{(3L - k - m)\pi}{2l},$$

$$\omega_{z3} = \frac{(3L - k)\pi}{2l},$$

$$\hat{K}_{sc} = \frac{3N\hat{I}}{2sr_{si}} \frac{4\sin(m\pi/2)\sin((3L - k)\pi/3)}{m(3L - k)\pi^2},$$

$$\hat{K}_s = \frac{3N\hat{I}}{2sr_{si}} \frac{2\sin((3L - k)\pi/3)}{(3L - k)\pi}.$$

C   Linear current density of the diamond winding

$$
K_z(\theta, z, t) = \sum_{\substack{m=1 \\ k=1 \\ L=-\infty}}^{\infty} \Big(\hat{K}_{ss} \sin\left(((3L - k)\theta + k\omega t)\right) \left(\cos(\omega_{z1}z) + \cos(\omega_{z2}z)\right) +
$$

$$
\hat{K}_{sc} \sin\left(((3L - k)\theta + k\omega t)\right) \cos\left(\frac{m\pi}{2l}z\right) \Big) +
$$

$$
\sum_{\substack{k=1 \\ L=-\infty}}^{\infty} \hat{K}_{s} \sin\left(((3L - k)\theta + k\omega t)\right), \tag{A.12}
$$

$$
\omega_{z1} = \frac{\left(3L - k - \dfrac{m}{2}\right)\pi}{l},
$$

$$
\omega_{z2} = \frac{\left(3L - k + \dfrac{m}{2}\right)\pi}{l},
$$

$$
\hat{K}_{ss} = \frac{3N\hat{I}}{2sr_{si}} \frac{16(1 + 2\cos(m\pi/4))\cos((3L - k)\pi)}{2m(3L - k)\pi^2}.
$$

$$
\sin(m\pi/8)^2 \sin(\pi(3L - k)/3),
$$

$$
\hat{K}_{sc} = -\frac{3N\hat{I}}{2sr_{si}} \frac{8\sin(m\pi/4)\sin((3L - k)\pi/3)\sin((3L - k)\pi/2)}{m(3L - k)\pi^2},
$$

$$
\hat{K}_{s} = -\frac{3N\hat{I}}{2sr_{si}} \frac{2(2\cos((3L - k)\pi/6) + \cos((3L - k)\pi/2))}{(3L - k)\pi}.
$$

$$
\sin((3L - k)\pi/6)^2.
$$

A.2   Fourier coefficients of winding distributions

A   Fourier coefficient for the toroidal winding distribution

$$
c_s(L, k) = -\frac{4\left(\cos\left(2(3L - k)\dfrac{\pi}{3}\right) + \cos((3L - k)\pi) + \cos\left((3L - k)\dfrac{4\pi}{3}\right)\right)}{(3L - k)\pi}.
$$

$$
\sin^2\left((3L - k)\frac{\pi}{6}\right). \tag{A.13}
$$

B   Fourier coefficient for the concentrated winding distribution

$$c_{\mathrm{s}}(L, k) = \frac{2\left(\cos\left((3L - k)\frac{\alpha}{3}\right) - \cos\left((3L - k)\frac{\pi}{3}\right)\right)}{(3L - k)\pi}. \tag{A.14}$$

B

Harmonic modeling of the permanent magnet field

The PM magnetization direction of the benchmark machine is assumed radial as shown in Figure B.1(a). It is, however, pointed out that the radial magnetization without a hole in the middle of the cylindrical PM is unrealistic. The purpose of this PM field modeling is the implementation and verification of the 2D HM.
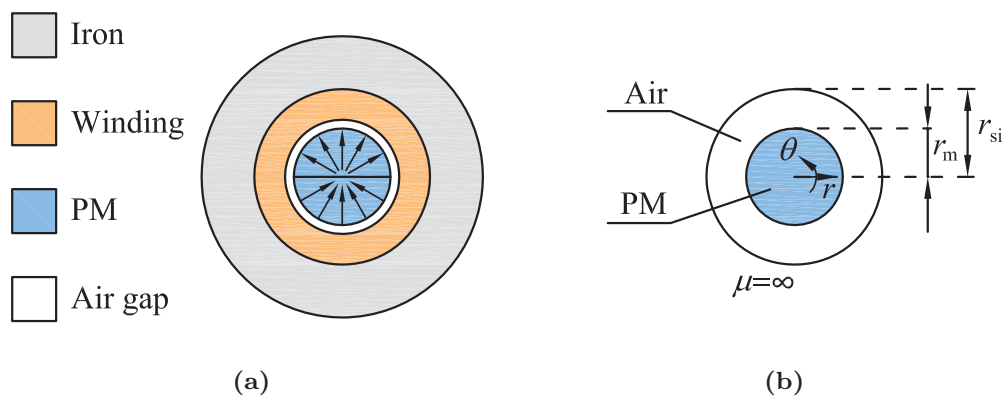

Figure B.1: a) Cross-section of a slotless PM machine. The black arrows represent the magnetization direction of the permanent magnet. b) Modeled regions in the 2D semianalytical model (winding region is substituted by air and iron is considered to be infinitely permeable).

This magnetization pattern results solely in radial magnetization components, which are converted into a Fourier series by using (2.62), (2.63) and given as

$$\bar{M}_{0r} = \sum_{\nu=-\infty}^{\infty} \frac{j\vec{B}_{\text{rem}}(\cos(\nu\pi) - 1)}{\nu\pi\mu_0} e^{j\nu\theta}, \tag{B.1}$$

$$\bar{M}_{0r} = -j\frac{B_{\text{rem}}}{\mu_0} e^{j\theta}, \tag{B.2}$$

$$\bar{M}_{0\theta} = \frac{B_{\text{rem}}}{\mu_0} e^{j\theta}.$$

To model the PM field in the benchmark machines, the back iron is assumed to be infinitely permeable. As copper permeability is close to 1, the winding region is merged with the air gap and modeled as an air region as shown in Figure B.1(b). Thus, the model contains two regions, namely the PM and air. The model is solved by means of a vector potential, where the governing equation in the air region is described by the Laplace equation (2.35), the solution is given by (2.36), and the governing equation in the PM region is the Poisson-type equation (2.42). Additionally, the inner radius of the magnet region is zero, and thus, the Dirichlet boundary condition (2.60) should be applied. This condition eliminates one unknown constant from the solution, and therefore, the solution for the two regions can be written as

$$\bar{A}_{\text{za}}(r, \theta) = \sum_{\nu=-\infty}^{\infty} (\bar{C}_{\text{a}} r^{-\nu} + \bar{D}_{\text{a}} r^{\nu}) e^{j\nu\theta}, \tag{B.3}$$

$$\bar{A}_{\text{zPM}}(r, \theta) = \sum_{\nu=-\infty}^{\infty} (\bar{D}_{\text{PM}} r^{\nu} + \hat{\bar{A}}_{\text{part}}) e^{j\nu\theta}, \tag{B.4}$$

where

$$\hat{\bar{A}}_{\text{part}} = \begin{cases} \mu_0 j\nu \hat{\bar{M}}_{0r} r \ln(r)/2, & \text{for } \nu = \pm 1, \\ \mu_0 j\nu \hat{\bar{M}}_{0r} r/(1 - \nu^2), & \text{else.} \end{cases}$$

The unknown coefficients $\bar{C}_{\text{a}}$, $\bar{D}_{\text{a}}$, and $\bar{D}_{\text{PM}}$ can be determined from the boundary conditions, which are given as

$$\begin{cases} \bar{B}_{\text{rPM}} - \bar{B}_{\text{ra}} = 0, & \text{for } r = r_{\text{m}}, \\ \bar{H}_{\theta\text{PM}} - \bar{H}_{\theta\text{a}} = 0, & \text{for } r = r_{\text{m}}, \\ \bar{H}_{\theta\text{a}} = 0, & \text{for } r = r_{\text{si}}. \end{cases}$$

Figure B.2 shows the results of the radial and circumferential flux density distributions obtained by the 2D FEM and semianalytical models. The results demonstrate good agreement, where the relative difference does not exceed 1% of the amplitude value.
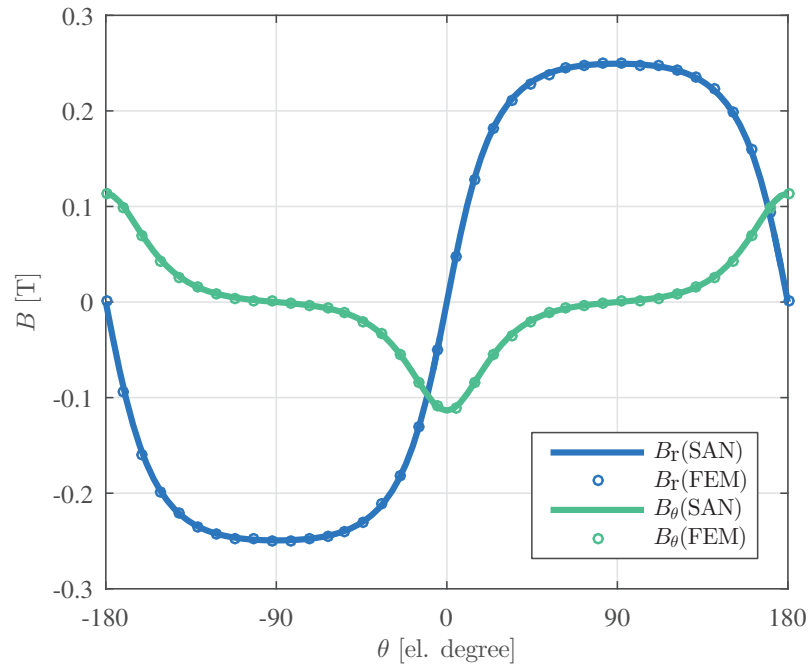
Figure B.2: Radial and tangential PM magnetic flux density distributions for the benchmark machines calculated by the 2D HM and the 2D FEM at $r = 4$ mm.

If required, the solution can be transferred to the real number domain. It is observed that if the radial magnetization pattern has only sine components, as it is the case for the example under study, then the unknown coefficient are only real numbers without an imaginary part. In the case of only the cosine radial magnetization pattern, the unknown coefficients are purely imaginary numbers. Thus, for the example, the vector potential in the air gap can be determined by taking the real part from (B.3), which results in

$$A_{\mathrm{za}} = 2 \sum_{\nu=1}^{\infty} (C_{\mathrm{a}} r^{-\nu} + D_{\mathrm{a}} r^{\nu}) \cos(\nu\theta), \tag{B.5}$$

In this expression, the coefficient 2 appears because the summation limits have been changed.

C

Torque calculation

C.1 PM field constants

$$\Lambda_{\mathrm{PM,r}} = \nu(C_{\mathrm{PM}}r^{-\nu} + D_{\mathrm{PM}}r^{\nu}),$$
$$\Lambda_{\mathrm{PM,\theta}} = \nu(C_{\mathrm{PM}}r^{-\nu-1} - D_{\mathrm{PM}}r^{\nu-1}). \tag{C.1}$$

C.2 Armature reaction field constants

A Armature reaction field constants for the 2D case

$$\bar{\Lambda}_{\mathrm{s,r}} = \mathrm{j}(3L-k)(\bar{C}_{\mathrm{s,AR}}r^{-(3L-k)} + \bar{D}_{\mathrm{s,AR}}r^{(3L-k)}),$$
$$\bar{\Lambda}_{\mathrm{c,r}} = \mathrm{j}(3L-k)(\bar{C}_{\mathrm{c,AR}}r^{-(3L-k)} + \bar{D}_{\mathrm{c,AR}}r^{(3L-k)}),$$
$$\bar{\Lambda}_{\mathrm{s,\theta}} = -(3L-k)\bar{C}_{\mathrm{s,AR}}r^{-(3L-k)-1} + (3L-k)\bar{D}_{\mathrm{s,AR}}r^{(3L-k)-1},$$
$$\bar{\Lambda}_{\mathrm{c,\theta}} = -(3L-k)\bar{C}_{\mathrm{c,AR}}r^{-(3L-k)-1} + (3L-k)\bar{D}_{\mathrm{c,AR}}r^{(3L-k)-1}. \tag{C.2}$$

B   Armature reaction field constants for the 3D case

$$
\begin{aligned}
\bar{\Lambda}_{\text{ss,r}} &= \omega_{\text{z}}(\bar{C}_{\text{ss}}I'_{3L-k}(\omega_{\text{z}}r) + \bar{D}_{\text{ss}}K'_{3L-k}(\omega_{\text{z}}r)), \\
\bar{\Lambda}_{\text{sc,r}} &= \omega_{\text{z}}(-\bar{C}_{\text{sc}}I'_{3L-k}(\omega_{\text{z}}r) - \bar{D}_{\text{sc}}K'_{3L-k}(\omega_{\text{z}}r)), \\
\bar{\Lambda}_{\text{cs,r}} &= \omega_{\text{z}}(\bar{C}_{\text{cs}}I'_{3L-k}(\omega_{\text{z}}r) + \bar{D}_{\text{cs}}K'_{3L-k}(\omega_{\text{z}}r)), \\
\bar{\Lambda}_{\text{cc,r}} &= \omega_{\text{z}}(-\bar{C}_{\text{cc}}I'_{3L-k}(\omega_{\text{z}}r) - \bar{D}_{\text{cc}}K'_{3L-k}(\omega_{\text{z}}r)), \\
\bar{\Lambda}_{\text{ss,}\theta} &= (3L-k)\omega_{\text{z}}(\bar{C}_{\text{ss}}I_{3L-k}(\omega_{\text{z}}r) + \bar{D}_{\text{ss}}K_{3L-k}(\omega_{\text{z}}r)), \\
\bar{\Lambda}_{\text{cs,}\theta} &= (3L-k)\omega_{\text{z}}(-\bar{C}_{\text{sc}}I_{3L-k}(\omega_{\text{z}}r) - \bar{D}_{\text{sc}}K_{3L-k}(\omega_{\text{z}}r)), \\
\bar{\Lambda}_{\text{sc,}\theta} &= (3L-k)\omega_{\text{z}}(-\bar{C}_{\text{cs}}I_{3L-k}(\omega_{\text{z}}r) - \bar{D}_{\text{cs}}K_{3L-k}(\omega_{\text{z}}r)), \\
\bar{\Lambda}_{\text{cc,}\theta} &= (3L-k)\omega_{\text{z}}(\bar{C}_{\text{cc}}I_{3L-k}(\omega_{\text{z}}r) + \bar{D}_{\text{cc}}K_{3L-k}(\omega_{\text{z}}r)).
\end{aligned} \tag{C.3}
$$

C   Force caused by the armature field and induced rotor eddy currents: 2D case

$$
\begin{aligned}
F_{\theta,\text{eddy2D}} = \frac{l}{\mu_0} \sum_{\substack{\nu=1 \\ k=1 \\ L=-\infty}}^{\infty} & \left[\int_{-\pi}^{\pi} \text{Im}(\bar{\Lambda}_{\text{s,r}}u)\text{Im}(\bar{\Lambda}_{\text{s,}\theta}u)\text{d}\theta + \int_{-\pi}^{\pi} \text{Im}(\bar{\Lambda}_{\text{s,r}}u)\text{Re}(\bar{\Lambda}_{\text{c,}\theta}u)\text{d}\theta + \right. \\
& \left. \int_{-\pi}^{\pi} \text{Re}(\bar{\Lambda}_{\text{c,r}}u)\text{Im}(\bar{\Lambda}_{\text{s,}\theta}u)\text{d}\theta + \int_{-\pi}^{\pi} \text{Re}(\bar{\Lambda}_{\text{c,r}}u)\text{Re}(\bar{\Lambda}_{\text{c,}\theta}u)\text{d}\theta \right],
\end{aligned} \tag{C.4}
$$

where

$$
u = \text{e}^{\text{j}((3L-k)\theta+k\omega t)} \tag{C.5}
$$

D Circumferential force caused by the armature field and induced rotor eddy currents: 3D case

$$
F_{\theta,\text{eddy3D}} = \frac{l}{\mu_0} \sum_{\substack{\nu=1 \\ k=1 \\ L=-\infty}}^{\infty} \frac{r}{\mu_0} \int_{-\pi}^{\pi} \int_{-l/2}^{l/2}
$$

$$
\begin{aligned}
&\big[\mathrm{Re}(\bar{\Lambda}_{\mathrm{ss,r}}u\cos(\omega_z z + \theta_z))\mathrm{Re}(\bar{\Lambda}_{\mathrm{ss,\theta}}u\cos(\omega_z z + \theta_z))\mathrm{d}\theta\mathrm{d}l+ \\
&+\mathrm{Re}(\bar{\Lambda}_{\mathrm{ss,r}}u\cos(\omega_z z + \theta_z))\mathrm{Re}(\bar{\Lambda}_{\mathrm{sc,\theta}}u\sin(\omega_z z + \theta_z))\mathrm{d}\theta\mathrm{d}l+ \\
&+\mathrm{Re}(\bar{\Lambda}_{\mathrm{ss,r}}u\cos(\omega_z z + \theta_z))\mathrm{Im}(\bar{\Lambda}_{\mathrm{cs,\theta}}u\cos(\omega_z z + \theta_z))\mathrm{d}\theta\mathrm{d}l+ \\
&+\mathrm{Re}(\bar{\Lambda}_{\mathrm{ss,r}}u\cos(\omega_z z + \theta_z))\mathrm{Im}(\bar{\Lambda}_{\mathrm{cc,\theta}}u\sin(\omega_z z + \theta_z))\mathrm{d}\theta\mathrm{d}l+ \\
&+\mathrm{Re}(\bar{\Lambda}_{\mathrm{sc,r}}u\sin(\omega_z z + \theta_z))\mathrm{Re}(\bar{\Lambda}_{\mathrm{ss,\theta}}u\cos(\omega_z z + \theta_z))\mathrm{d}\theta\mathrm{d}l+ \\
&+\mathrm{Re}(\bar{\Lambda}_{\mathrm{sc,r}}u\sin(\omega_z z + \theta_z))\mathrm{Re}(\bar{\Lambda}_{\mathrm{sc,\theta}}u\sin(\omega_z z + \theta_z))\mathrm{d}\theta\mathrm{d}l+ \\
&+\mathrm{Re}(\bar{\Lambda}_{\mathrm{sc,r}}u\sin(\omega_z z + \theta_z))\mathrm{Im}(\bar{\Lambda}_{\mathrm{cs,\theta}}u\cos(\omega_z z + \theta_z))\mathrm{d}\theta\mathrm{d}l+ \\
&+\mathrm{Re}(\bar{\Lambda}_{\mathrm{sc,r}}u\sin(\omega_z z + \theta_z))\mathrm{Im}(\bar{\Lambda}_{\mathrm{cc,\theta}}u\sin(\omega_z z + \theta_z))\mathrm{d}\theta\mathrm{d}l+ \\
&+\mathrm{Im}(\bar{\Lambda}_{\mathrm{cs,r}}u\cos(\omega_z z + \theta_z))\mathrm{Re}(\bar{\Lambda}_{\mathrm{ss,\theta}}u\cos(\omega_z z + \theta_z))\mathrm{d}\theta\mathrm{d}l+ \\
&+\mathrm{Im}(\bar{\Lambda}_{\mathrm{cs,r}}u\cos(\omega_z z + \theta_z))\mathrm{Re}(\bar{\Lambda}_{\mathrm{sc,\theta}}u\sin(\omega_z z + \theta_z))\mathrm{d}\theta\mathrm{d}l+ \\
&+\mathrm{Im}(\bar{\Lambda}_{\mathrm{cs,r}}u\cos(\omega_z z + \theta_z))\mathrm{Im}(\bar{\Lambda}_{\mathrm{cs,\theta}}u\cos(\omega_z z + \theta_z))\mathrm{d}\theta\mathrm{d}l+ \\
&+\mathrm{Im}(\bar{\Lambda}_{\mathrm{cs,r}}u\cos(\omega_z z + \theta_z))\mathrm{Im}(\bar{\Lambda}_{\mathrm{cc,\theta}}u\sin(\omega_z z + \theta_z))\mathrm{d}\theta\mathrm{d}l+ \\
&+\mathrm{Im}(\bar{\Lambda}_{\mathrm{cc,r}}u\sin(\omega_z z + \theta_z))\mathrm{Re}(\bar{\Lambda}_{\mathrm{ss,\theta}}u\cos(\omega_z z + \theta_z))\mathrm{d}\theta\mathrm{d}l+ \\
&+\mathrm{Im}(\bar{\Lambda}_{\mathrm{cc,r}}u\sin(\omega_z z + \theta_z))\mathrm{Re}(\bar{\Lambda}_{\mathrm{sc,\theta}}u\sin(\omega_z z + \theta_z))\mathrm{d}\theta\mathrm{d}l+ \\
&+\mathrm{Im}(\bar{\Lambda}_{\mathrm{cc,r}}u\sin(\omega_z z + \theta_z))\mathrm{Im}(\bar{\Lambda}_{\mathrm{cs,\theta}}u\cos(\omega_z z + \theta_z))\mathrm{d}\theta\mathrm{d}l+ \\
&+\mathrm{Im}(\bar{\Lambda}_{\mathrm{cc,r}}u\sin(\omega_z z + \theta_z))\mathrm{Im}(\bar{\Lambda}_{\mathrm{cc,\theta}}u\sin(\omega_z z + \theta_z))\mathrm{d}\theta\mathrm{d}l\big] ,
\end{aligned}
$$

$$(\text{C.6})$$

D

Sideband harmonics of phase PWM voltage

The phase voltage expression for sideband harmonics in the case of asymmetrical regular sampled sinusoidal PWM is given as

$$u_{\mathrm{PWM}}(t) = \frac{4U_{\mathrm{DC}}}{\sqrt{3}\pi} \sum_{m=1}^{\infty} \sum_{n=-\infty}^{\infty} \frac{m_{\mathrm{f}}}{m \cdot m_{\mathrm{f}} + n} J_n\left(\frac{(m \cdot m_{\mathrm{f}} + n)\pi M}{2m_{\mathrm{f}}}\right)$$
$$\sin\left((m+n)\frac{\pi}{2}\right) \sin\left(n\frac{\pi}{3}\right) \cos\left((m \cdot m_{\mathrm{f}} + n)\omega_1 t + n\left(x - \frac{\pi}{3}\right) + \frac{\pi}{2}\right). \qquad \text{(D.1)}$$

In the case of asymmetrical regular sampled space vector PWM, the expression is

$$u_{\mathrm{PWM}}(t) = \sum_{m=1}^{\infty} \sum_{n=-\infty}^{\infty} \frac{4U_{\mathrm{DC}}}{\sqrt{3}m\pi^2} \left[\frac{\pi}{6} \sin\left((m+n)\frac{\pi}{2}\right) \left(J_n\left(q\frac{3\pi}{4}M\right)\right.\right.$$
$$\left. +2\cos\left(n\frac{\pi}{6}\right) J_n\left(q\frac{\sqrt{3}\pi}{4}M\right)\right) + \frac{1}{n}\sin\left(m\frac{\pi}{2}\right)\cos\left(n\frac{\pi}{2}\right)\sin\left(n\frac{\pi}{6}\right) \cdot$$
$$\left. \left(J_0\left(q\frac{3\pi}{4}M\right) - J_0\left(q\frac{\sqrt{3}\pi}{4}M\right)\right)\right|_{\text{for } n\neq 0} + u_1 + u_2 \right]. \qquad \text{(D.2)}$$

where

$$u_1 = \sum_{\substack{w=1 \\ w \neq -n}}^{\infty} \frac{1}{n+w} \sin\left((m+w)\frac{\pi}{2}\right) \cos\left((n+w)\frac{\pi}{2}\right) \sin\left((n+w)\frac{\pi}{6}\right) \cdot$$
$$\left[J_w\left(q\frac{3\pi}{4}M\right) + 2\cos\left((2n+3w)\frac{\pi}{6}\right) J_w\left(q\frac{\sqrt{3}\pi}{4}M\right) \right],$$

$$u_2 = \sum_{\substack{w=1 \\ w \neq n}}^{\infty} \frac{1}{n-w} \sin\left((m-w)\frac{\pi}{2}\right) \cos\left((n-w)\frac{\pi}{2}\right) \sin\left((n+w)\frac{\pi}{6}\right) \cdot$$
$$\left[J_w\left(q\frac{3\pi}{4}M\right) + 2\cos\left((2n-3w)\frac{\pi}{6}\right) J_w\left(q\frac{\sqrt{3}\pi}{4}M\right) \right],$$

$$q = m + \frac{n}{m_{\mathrm{f}}}.$$

E

Fixed parameters for parametric search optimization

Table E.1: Fixed machine parameters.

Parameter, symbol	Value	Unit
Rated mechanical speed, Ω	80000	rpm
Air gap length, δ	0.75	mm
Retaining sleeve thickness, h_{sl}	0.25	mm
Housing thickness, h_{h}	2	mm
Additional rotor length	20	mm
End shaft radius	2.5	mm
End shaft length	3	mm
Minimum stator yoke height	5	mm
PM remanent flux density (120°C - N45HX), B_{rem}	1.2	T
PM relative permeability, μ_{rPM}	1.05	-
Sleeve relative permeability, μ_{rsl}	1	-
Continued on next page		

Table E.1 – continued from previous page

Parameter, [symbol]	Value	Unit
PM resistivity, ρ_{PM}	$1.8 \cdot 10^{-5}$	Ωm
Sleeve resistivity - stainless steel, ρ_{ss}	$6.9 \cdot 10^{-7}$	Ωm
Sleeve resistivity - titanium, ρ_{t}	$4.2 \cdot 10^{-7}$	Ωm
Sleeve resistivity - Inconel 625, ρ_{I}	$1.3 \cdot 10^{-7}$	Ωm
Frequency modulation ratio, m_{f}	60	-
Amplitude modulation ratio (space vector PWM), M	0.6	-
DC bus voltage, U_{DC}	24	V
Air kinematic viscosity, ν_{air}	$2.056 \cdot 10^{-5}$	m^2/s
Air dynamic viscosity, μ_{air}	$2.075 \cdot 10^{-5}$	Pa·s
Air mass density, ρ_{air}	1.009	kg/m^3
Soft-magnetic material - Sura NO20		
Maximum flux density value in the stator iron, $B_{\max}$	1.5	T
Hysteresis loss coefficient, C_{hyst}	$2.46 \cdot 10^{-2}$	-
Eddy current loss coefficient, C_{eddy}	$1.08 \cdot 10^{-5}$	-
Excess loss coefficient, [C_{exc}	$5.66 \cdot 10^{-4}$	-
PM mass density, $\rho_{\text{m,PM}}$	7500	kg/m^3
Sleeve mass density - stainless steel, $\rho_{\text{m,ss}}$	7900	kg/m^3
Sleeve mass density - titanium, $\rho_{\text{m,t}}$	4540	kg/m^3
Sleeve mass density - Inconel 625, $\rho_{\text{m,I}}$	8440	kg/m^3
PM ultimate tensile strength, $\sigma_{\text{u,PM}}$	83	MPa
Sleeve ultimate tensile strength - stainless steel, $\sigma_{\text{u,ss}}$	860	MPa
Sleeve ultimate tensile strength - titanium, $\sigma_{\text{u,t}}$	434	MPa
Sleeve ultimate tensile strength - Inconel 625, $\sigma_{\text{u,I}}$	900	MPa
PM Poisson's ratio, ν_{Pm}	0.24	-
Sleeve Poisson's ratio - stainless steel, ν_{Pss}	0.3	-
Sleeve Poisson's ratio - titanium, ν_{Pst}	0.3	-
Sleeve Poisson's ratio - Inconel 625, ν_{PsI}	0.31	-
Winding thermal conductivity (transverse), $k_{\text{t,w}}$	1	W/m/K
Winding thermal conductivity (longitudal), $k_{\text{t,w}}$	150	W/m/K
Iron thermal conductivity, $k_{\text{t,i}}$	28	W/m/K
Aluminum thermal conductivity, $k_{\text{t,i}}$	205	W/m/K
Sleeve thermal conductivity - stainless steel, $k_{\text{t,sss}}$	18	W/m/K
Sleeve thermal conductivity - titanium, $k_{\text{t,st}}$	20	W/m/K
Continued on next page		

Table E.1 – continued from previous page

Parameter, [symbol]	Value	Unit
Sleeve thermal conductivity - Inconel 625, $k_{\text{t,st}}$	10	W/m/K
PM thermal conductivity, $k_{\text{t,i}}$	6.4	W/m/K
Natural heat transfer coefficient housing/ambient, α_{a}	30	W/m^2/K
Maximum ambient Temperature, T_{amb}	40	^{o}C
Maximum allowed PM temperature, T_{PMmax}	120	^{o}C
Maximum allowed winding temperature, T_{wmax}	130	^{o}C
Toroidal winding space factor, k_{sCu}	0.55	-
Concentrated winding space factor, k_{sCu}	0.25	-
Faulhaber winding space factor, k_{sCu}	0.35	-
Bearing SKF 637/3-2Z		
Bearing dynamic load rating, C_{r}	216	N
Bearing inner radius, r_{b}	1.5	mm
Conductor diameter value is taken from IEC 60317-0-1 for the grade 2		

Bibliography

[1] J. Acero, J. M. Burdio, L. A. Barragan, D. Puyal, and R. Alonso, "Frequency-dependent resistance in litz-wire planar windings for all-metal domestic induction heating appliances," in *Twentieth Annual IEEE Applied Power Electronics Conference and Exposition, 2005. APEC 2005.*, vol. 2, pp. 1294–1300, March 2005.

[2] J. Acero, P. J. Hernandez, J. M. Burdio, R. Alonso, and L. A. Barragdan, "Simple resistance calculation in litz-wire planar windings for induction cooking appliances," *IEEE Transactions on Magnetics*, vol. 41, no. 4, pp. 1280–1288, April 2005.

[3] A. Anderson, J. Bumby, and B. Hassall, "Analysis of helical armature windings with particular reference to superconducting a.c. generators," *Generation, Transmission and Distribution, IEE Proceedings C*, vol. 127, no. 3, pp. 129–144, 1980.

[4] T. Baumgartner, R. M. Burkart, and J. W. Kolar, "Analysis and design of a 300-W 500 000-r/min slotless self-bearing permanent-magnet motor," *IEEE Transactions on Industrial Electronics*, vol. 61, no. 8, pp. 4326–4336, Aug 2014.

[5] T. Baumgartner and J. W. Kolar, "Multivariable state feedback control of a 500 000-r/min self-bearing permanent-magnet motor," *IEEE/ASME Transactions on Mechatronics*, vol. 20, no. 3, pp. 1149–1159, June 2015.

[6] G. Bertotti, "Physical interpretation of eddy current losses in ferromagnetic materials. i. theoretical considerations," *J. Appl. Phys. 57, 2110*, 1985.

[7] G. Bertotti, "Physical interpretation of eddy current losses in ferromagnetic materials. ii. analysis of experimental results," *J. Appl. Phys. 57, 2118*, 1985.

[8] X. Bian and Y. Liang, "Circuit network model of stator transposition bar in large generators and calculation of circulating current," *IEEE Transactions on Industrial Electronics*, vol. 62, no. 3, pp. 1392–1399, March 2015.

[9] N. Bianchi, S. Bolognani, and F. Luise, "Potentials and limits of high speed PM motors," in *38th IAS Annual Meeting on Conference Record of the Industry Applications Conference, 2003.*, vol. 3, pp. 1918–1925 vol.3, Oct 2003.

[10] E. Bilgen and R. Boulos, "Functional dependence of torque coefficient of coaxial cylinders on gap width and Reynolds numbers," *Journal of Fluids Engineering*, vol. 95(1), pp. 122–126, 1973.

[11] A. Binder and T. Schneider, "High-speed inverter-fed AC drives," in *International Aegean Conference on Electrical Machines and Power Electronics, 2007*, pp. 9–16, Sept 2007.

[12] A. Boglietti, A. Cavagnino, T. L. Mthombeni, and P. Pillay, "Comparison of lamination iron losses supplied by PWM voltages: US and European experiences," in *IEEE International Conference on Electric Machines and Drives, 2005.*, pp. 1431–1436, May 2005.

[13] A. Borisavljevic, S. Jumayev, and E. Lomonova, "Toroidally-wound permanent magnet machines in high-speed applications," in *2014 International Conference on Electrical Machines (ICEM)*, pp. 2588–2593, Sept 2014.

[14] A. Borisavljevic, "Limits, modeling and design of high-speed permanent magnet machines," Ph.D. dissertation, Technische Universiteit Delft, 2011.

[15] A. Borisavljevic, *Limits, Modeling and Design of High-Speed Permanent Magnet Machines.* Springer-Verlag Berlin Heidelberg, 2013.

[16] B. Bossmanns and J. F. Tu, "A power flow model for high speed motorized spindlesheat generation characterization," *Journal of Manufacturing Science and Engineering*, vol. 123, pp. 494–505, 2000.

[17] R. G. Budynas and J. K. Nisbett, *Shigley's Mechanical Engineering Design.* McGraw-Hill Education, 2015.

[18] C. J. Carpenter, "Surface-integral methods of calculating forces on magnetized iron parts," *Proceedings of the IEE - Part C: Monographs*, vol. 107, no. 11, pp. 19–28, March 1960.

[19] A. Cavagnino and A. Boglietti, "Iron loss prediction with PWM supply: An overview of proposed methods from an engineering application point of view," in *IEEE Industry Applications Annual Meeting*, pp. 81–88, Sept 2007.

[20] A. Chebak, P. Viarouge, and J. Cros, "Optimal design of a high-speed slotless permanent magnet synchronous generator with soft magnetic composite stator yoke and rectifier load," *Mathematics and Computers in Simulation*, vol. 81, no. 2, pp. 239 – 251, 2010, modelling and Simulation of Electrical Machines, Converters and Power Systems.

[21] J. Coulomb and G. Meunier, "Finite element implementation of virtual work principle for magnetic or electric force and torque computation," *IEEE Transactions on Magnetics*, vol. 20, no. 5, pp. 1894–1896, Sep 1984.

[22] B. Dehez, F. Baudart, M. Markovic, and Y. Perriard, "Theoretical and experimental investigation of flex-PCB air-gap windings in slotless BLDC machines," *IEEE Transactions on Industry Applications*, vol. 50, no. 5, pp. 3153–3160, Sept 2014.

[23] B. Dehez, F. Baudart, and Y. Perriard, "Analysis of a new topology of flexible PCB winding for slotless BLDC machines," in *International Conference on Electrical Machines (ICEM), 2014*, pp. 1963–1969, Sept 2014.

[24] B. Dehez, F. Baudart, and Y. Perriard, "Comparison of FPCB windings of BLDC machines with paralelly and radially magnetized rotor poles," in *2014 17th International Conference on Electrical Machines and Systems (ICEMS)*, pp. 3331–3337, Oct 2014.

[25] B. Dehez, M. Markovic, and Y. Perriard, "Analysis of BLDC motor with zigzag and rhombic winding," in *XIX International Conference on Electrical Machines (ICEM), 2010*, pp. 1–5, Sept 2010.

[26] F. Dubas, C. Espanet, and A. Miraoui, "Design of a high-speed permanent magnet motor for the drive of a fuel cell air-compressor," in *2005 IEEE Vehicle Power and Propulsion Conference*, pp. 8 pp.–, Sept 2005.

[27] J. A. Ferreira, "Improved analytical modeling of conductive losses in magnetic components," *IEEE Transactions on Power Electronics*, vol. 9, no. 1, pp. 127–131, Jan 1994.

[28] F. Fiorillo and A. Novikov, "An improved approach to power losses in magnetic laminations under nonsinusoidal induction waveform," *IEEE Transactions on Magnetics*, vol. 26, no. 5, pp. 2904–2910, Sep 1990.

[29] J. B. J. Fourier, *Thorie analytique de la chaleur.* Chez Firmin Didot, pre et fils, 1822.

[30] E. P. Furlani, *Permanent Magnet and Electromechanical Devices*, I. Meyergoyz, Ed. Academic Press, 2001.

[31] M. van der Geest, H. Polinder, and J. A. Ferreira, "Influence of pwm switching frequency on the losses in pm machines," in *International Conference on Electrical Machines (ICEM)*, pp. 1243–1247, Sept 2014.

[32] M. van der Geest, H. Polinder, J. A. Ferreira, and D. Zeilstra, "Current sharing analysis of parallel strands in low-voltage high-speed machines," *IEEE Transactions on Industrial Electronics*, vol. 61, no. 6, pp. 3064–3070, June 2014.

[33] D. Gerada, A. Mebarki, N. Brown, C. Gerada, A. Cavagnino, and A. Boglietti, "High-speed electrical machines: Technologies, trends, and developments," *IEEE Transactions on Industrial Electronics*, vol. 61, no. 6, pp. 2946–2959, June 2014.

[34] J. W. Gibbs, "Fourier series," *Nature 59: 200 and 606*, 1899.

[35] Z. Gmyrek, A. Boglietti, and A. Cavagnino, "Iron loss prediction with pwm supply using low- and high-frequency measurements: Analysis and results comparison," *IEEE Transactions on Industrial Electronics*, vol. 55, no. 4, pp. 1722–1728, April 2008.

[36] A. J. Grobler, "Thermal modelling of a high-speed permanent magnet sychronous machines," Ph.D. dissertation, Potchefstroom campus of the North-West University, 2011.

[37] Y. G. Guo and J. G. Zhu, "Applications of soft magnetic composite materials in electrical machines," *Australian Journal of Electrical and Electronics Engineering*, vol. 3, pp. 37–46, 2006.

[38] B. L. J. Gysen, K. J. Meessen, J. J. H. Paulides, and E. A. Lomonova, "General formulation of the electromagnetic field distribution in machines and devices using fourier analysis," *IEEE Transactions on Magnetics*, vol. 46, no. 1, pp. 39–52, Jan 2010.

[39] B. Hague, *Electromagnetic problems in electrical engineering.* Oxford University Press, London, UK, 1929.

[40] H. Hämäläinen, J. Pyrhönen, and J. Nerg, "AC resistance factor in one-layer form-wound winding used in rotating electrical machines," *IEEE Transactions on Magnetics*, vol. 49, no. 6, pp. 2967–2973, June 2013.

[41] P. Hammond, "The calculation of the magnetic field of rotating machines. part 3: Eddy currents induced in a solid slab by a circular current loop," *Proceedings of the IEE - Part C: Monographs*, vol. 109, no. 16, pp. 508–515, Sep. 1962.

[42] P. Hammond, "Use of potentials in calculation of electromagnetic fields," *Physical Science, Measurement and Instrumentation, Management and Education - Reviews, IEE Proceedings A*, vol. 129, no. 2, pp. 106–112, March 1982.

[43] T. A. Harris, *Rolling bearing analysis.* Wiley, 2001.

[44] J. R. Hendershot and T. J. E. Miller, *Design of Brushless Permanent-Magnet Machines.* Motor Design Books LLC, 2010.

[45] T. Hillen, I. Leonard, and H. van Roessel, *Partial Differential Equations for Engineering and Scientists.* University of Alberta, 2010.

[46] S. Holm, "Modeling and optimization of a permanent magnet machine in a flywheel," Ph.D. dissertation, Delft University of Technology, 2003.

[47] D. G. Holmes and T. A. Lipo, *Pulse Width Modulation For Power Converters*, I. P. E. Board, Ed. IEEE Press, 2003.

[48] D. A. Howey, P. R. N. Childs, and A. S. Holmes, "Air-gap convection in rotating electrical machines," *IEEE Transactions on Industrial Electronics*, vol. 59, no. 3, pp. 1367–1375, March 2012.

[49] S. Isert, "Heat transfer thought a rotating ball bearing at low angular velocities," Master's thesis, Utah State University, 2011.

[50] S. Iwasaki, R. P. Deodhar, Y. Liu, A. Pride, Z. Q. Zhu, and J. J. Bremner, "Influence of PWM on the proximity loss in permanent-magnet brushless ac machines," *IEEE Transactions on Industry Applications*, vol. 45, no. 4, pp. 1359–1367, July 2009.

[51] H. Jordan, "Die ferromagnetischen konstanten für schwache wechselfelder," *Elektrische Nachrichtentechnik, vol.1, p. 8*, 1924.

[52] S. Jumayev, A. Borisavljevic, K. Boynov, E. A. Lomonova, and J. Pyrhnen, "Force and torque calculation methods for airgap windings in permanent magnet machines," in *Eighth International Conference and Exhibition on Ecological Vehicles and Renewable Energies (EVER)*, March 2013.

[53] S. Jumayev, A. Borisavljevic, K. Boynov, E. A. Lomonova, and J. Pyrhönen, "Comparative analysis of inductances of air-gap windings," in *XVI International Symposium on Electromagnetic Fields in Mechatronics (ISEF)*, September 2013.

[54] S. Jumayev, A. Borisavljevic, K. Boynov, E. A. Lomonova, and J. Pyrhönen, "Analysis of rotor eddy current losses in slotless high-speed permanent magnet machines," in *16th European Conference on Power Electronics and Applications*, pp. 1–10, Aug 2014.

[55] S. Jumayev, K. O. Boynov, J. J. H. Paulides, E. A. Lomonova, and J. Pyrhönen, "Slotless pm machines with skewed winding shapes: 3-D electromagnetic semianalytical model," *IEEE Transactions on Magnetics*, vol. 52, no. 11, pp. 1–12, Nov 2016.

[56] S. Jumayev, M. Merdzan, K. O. Boynov, J. J. Paulides, J. Pyrhnen, and E. Lomonova, "The effect of pwm on rotor eddy-current losses in high-speed permanent magnet machines," in *IEEE Magnetics Conference (INTERMAG)*, May 2015.

[57] S. Jumayev, M. Merdzan, K. O. Boynov, J. J. H. Paulides, J. Pyrhnen, and E. A. Lomonova, "The effect of PWM on rotor eddy-current losses in high-speed permanent magnet machines," *IEEE Transactions on Magnetics*, vol. 51, no. 11, pp. 1–4, Nov 2015.

[58] S. Jumayev, J. J. H. Paulides, K. O. Boynov, J. Pyrhönen, and E. A. Lomonova, "Three-dimensional analytical model of helical winding PM machines including rotor eddy-currents," *IEEE Transactions on Magnetics*, vol. 52, pp. 1–8, 2016.

[59] S. Jumayev, A. Borisavljevic, K. Boynov, J. Pyrhönen, and E. A. Lomonova, "Inductance calculation of high-speed slotless permanent magnet machines," *COMPEL - The international journal for computation and mathematics in electrical and electronic engineering*, vol. 34, no. 2, pp. 413–427, 2015.

[60] R. Keller, "High performance-motor with bell-shaped air gap winding," in *Innovative Small Drives and Micro-Motor Systems*, 2013.

[61] H. V. Khang and A. Arkkio, "Eddy-current loss modeling for a form-wound induction motor using circuit model," *IEEE Transactions on Magnetics*, vol. 48, no. 2, pp. 1059–1062, Feb 2012.

[62] D.-H. Kim, D. A. Lowther, and J. K. Sykulski, "Efficient force calculations based on continuum sensitivity analysis," *IEEE Transactions on Magnetics*, vol. 41, no. 5, pp. 1404–1407, May 2005.

[63] T. H. Kim, S. H. Lee, and W. M. Kim, "Design and characteristic analysis of high speed slotless permanent magnet sychoronous motor for surgical hand-piece," in *2014 IEEE International Conference on Industrial Technology (ICIT)*, pp. 219–222, Feb 2014.

[64] D. Krahenbuhl, C. Zwyssig, H. Horler, and J. W. Kolar, "Design considerations and experimental results of a 60 W compressed-air-to-electric-power system," in *2008 IEEE/ASME International Conference on Mechatronic and Embedded Systems and Applications*, pp. 375–380, Oct 2008.

[65] A. Krings, "Iron losses in electrical machines: Influence of material properties, manufacturing processes, and inverter operation," Ph.D. dissertation, KTH Royal Institute of Technology, 2014.

[66] D. C. J. Krop, "Integration of dual electromagnetic energy conversions: linear actuation with integrated contactless energy transfer," Ph.D. dissertation, Eindhoven University of Technology, 2013.

[67] J. Lammeraner and M. Štafl, *Eddy Currents*. Iliffe Books Ltd., London, 1966.

[68] R. Larsonneur, "Design and control of active magnetic bearing ssystem for high speed rotation," Ph.D. dissertation, Swiss Federal Institute of Technology, 1990.

[69] D. P. Lathrop, J. Fineberg, and H. L. Swinney, "Turbulent flow between concentric rotating cylinders at large reynolds number," *Phys. Rev. Lett.*, vol. 68, pp. 1515–1518, Mar 1992.

[70] A. Lehikoinen, N. Chiodetto, E. Lantto, A. Arkkio, and A. Belahcen, "Monte carlo analysis of circulating currents in random-wound electrical machines," *IEEE Transactions on Magnetics*, vol. 52, no. 8, pp. 1–12, Aug 2016.

[71] R. Liu, C. C. Mi, and D. W. Gao, "Modeling of eddy-current loss of electrical machines and transformers operated by pulsewidth-modulated inverters," *IEEE Transactions on Magnetics*, vol. 44, no. 8, pp. 2021–2028, Aug 2008.

[72] A. Looser, T. Baumgartner, C. Zwyssig, and J. Kolar, "Analysis and measurement of 3D torque and forces for permanent magnet motors with slotless windings," in *Energy Conversion Congress and Exposition (ECCE), IEEE*, pp. 3792–3797, Sept 2010.

[73] H. von Markus, "Uber die dreidimensionale analytische berechnung der elektrischen wirbelstrome in kreiszylinderschalen," Ph.D. dissertation, Technischen Universitat Munchen, 1977.

[74] E. Matagne, B. Dehez, and K. Ben-Naoum, "Exact special 2D spectral expression of the magnetic field in air gap with skewed source," in *XXth International Conference on Electrical Machines (ICEM), 2012*, pp. 2825–2831, Sept 2012.

[75] *Maxon DC motor: Permanent magnet DC motor with coreless winding*, Maxon Academy, www.maxonmotor.com/maxon/view/content/service-academy-motor.

[76] K. J. Meessen, J. J. H. Paulides, and E. A. Lomonova, "Force calculations in 3-D cylindrical structures using fourier analysis and the Maxwell stress tensor," *IEEE Transactions on Magnetics*, vol. 49, no. 1, pp. 536–545, Jan 2013.

[77] P. H. Mellor, D. Roberts, and D. R. Turner, "Lumped parameter thermal model for electrical machines of TEFC design," *IEE Proceedings B - Electric Power Applications*, vol. 138, no. 5, pp. 205–218, Sept 1991.

[78] M. Merdzan, A. Borisavljevic, and E. A. Lomonova, "Modeling the influence of commutation in voltage source inverters on rotor losses of permanent magnet machines," in *16th European Conference on Power Electronics and Applications*, pp. 1–10, Aug 2014.

[79] M. Merdzan, S. Jumayev, A. Borisavljevic, K. O. Boynov, J. J. Paulides, and E. Lomonova, "Electrical and magnetic model coupling of permanent magnet machines based on harmonic analysis," in *IEEE Magnetics Conference (INTERMAG)*, May 2015.

[80] M. Merdzan, J. J. H. Paulides, A. Borisavljevic, and E. A. Lomonova, "The influence of the inverter switching frequency on rotor losses in high-speed permanent magnet machines: An experimental study," in *IEEE International Electric Machines Drives Conference (IEMDC)*, pp. 1628–1633, May 2015.

[81] M. Merdzan, J. J. H. Paulides, and E. A. Lomonova, "Comparative analysis of rotor losses in high-speed permanent magnet machines with different winding configurations considering the influence of the inverter pwm," in *Tenth International Conference on Ecological Vehicles and Renewable Energies (EVER)*, pp. 1–8, March 2015.

[82] W. Muller, "Comparison of different methods of force calculation," *IEEE Transactions on Magnetics*, vol. 26, no. 2, pp. 1058–1061, Mar 1990.

[83] X. Nan and C. R. Sullivan, "Simplified high-accuracy calculation of eddy-current loss in round-wire windings," in *IEEE 35th Annual Power Electronics Specialists Conference, 2004*, vol. 2, pp. 873–879, June 2004.

[84] J. Nerg, M. Rilla, and J. Pyrhönen, "Thermal analysis of radial-flux electrical machines with a high power density," *IEEE Transactions on Industrial Electronics*, vol. 55, no. 10, pp. 3543–3554, Oct 2008.

[85] P. Pfister, "Very high-speed slotless permanent-magnet motors: theory, design and validation," Ph.D. dissertation, cole polytechnique fdrale de Lausanne, 2010.

[86] P.-D. Pfister and Y. Perriard, "Slotless permanent-magnet machines: General analytical magnetic field calculation," *IEEE Transactions on Magnetics*, vol. 47, no. 6, pp. 1739–1752, June 2011.

[87] K. Pipis, "Eddy-current testing modeling of axisymmetric pieces with discontinuities along the axis by means of an integral equation approach," Ph.D. dissertation, Universite Paris-Saclay, 2015.

[88] K. J. W. Pluk, J. W. Jansen, and E. A. Lomonova, "Modeling of noncuboidal magnetic sources in 3-D Fourier modeling," *IEEE Transactions on Magnetics*, vol. 51, no. 11, pp. 1–4, Nov 2015.

[89] M. Popescu and D. G. Dorrell, "Proximity losses in the windings of high speed brushless permanent magnet AC motors with single tooth windings and parallel paths," *IEEE Transactions on Magnetics*, vol. 49, no. 7, pp. 3913–3916, July 2013.

[90] J. H. Poynting, "On the transfer of energy in the electromagnetic field," *Philosophical Transactions of the Royal Society of London, 175: 343-361*, 1884.

[91] J. Pyrhönen, T. Jokinen, and V. Hrabovcova, *Design of Rotating Electrical Machines*. John Wiley & Sons, Ltd, 2009.

[92] P. Ragot, M. Markovic, and Y. Perriard, "Analytical determination of the phase inductances for a brushless DC motor with faulhaber windings," *IEEE Transactions on Industry Applications*, vol. 45, pp. 1360–1366, 2010.

[93] P. B. Reddy and T. M. Jahns, "Analysis of bundle losses in high speed machines," in *International Power Electronics Conference (IPEC)*, pp. 2181–2188, June 2010.

[94] P. B. Reddy, T. M. Jahns, and T. P. Bohn, "Transposition effects on bundle proximity losses in high-speed pm machines," in *IEEE Energy Conversion Congress and Exposition*, pp. 1919–1926, Sept 2009.

[95] J. Reinert, A. Brockmeyer, and R. W. A. A. D. Doncker, "Calculation of losses in ferro- and ferrimagnetic materials based on the modified steinmetz equation," *IEEE Transactions on Industry Applications*, vol. 37, no. 4, pp. 1055–1061, Jul 2001.

[96] Z. Ren, "Comparison of different force calculation methods in 3D finite element modelling," *IEEE Transactions on Magnetics*, vol. 30, no. 5, pp. 3471–3474, Sep 1994.

[97] J. Saari, "Thermal analysis of high-speed induction machine," Ph.D. dissertation, Helsinki university of technology, 1998.

[98] L. Schwager, A. Tysz, C. Zwyssig, and J. W. Kolar, "Modeling and comparison of machine and converter losses for PWM and PAM in high-speed drives," in *XXth International Conference on Electrical Machines*, pp. 2441–2447, Sept 2012.

[99] S. Sgobba, "Physics and measurements of magnetic materials," *CERN*, 2010.

[100] *Rolling bearings*, SKF, 2016.

[101] J. P. C. Smeets, T. T. Overboom, J. W. Jansen, and E. A. Lomonova, "Three-dimensional analytical modeling technique of electromagnetic fields of air-cored coils surrounded by different ferromagnetic boundaries," *IEEE Transactions on Magnetics*, vol. 49, pp. 5698–5708, 2013.

[102] W. R. Smythe, *Static and dynamic electricity*, 3rd ed. New York : McGraw-Hill, 1967.

[103] C. P. Steinmetz, "On the law of hysteresis," *Transactions of the American Institute of Electrical Engineers*, vol. IX, no. 1, pp. 1–64, Jan 1892.

[104] R. L. Stoll and P. Hammond, "Calculation of the magnetic field of rotating machines. part 4: Approximate determination of the field and the losses associated with eddy currents in conducting surfaces," *Proceedings of the Institution of Electrical Engineers*, vol. 112, no. 11, pp. 2083–2094, November 1965.

[105] C. R. Sullivan, "Optimal choice for number of strands in a litz-wire transformer winding," *IEEE Transactions on Power Electronics*, vol. 14, no. 2, pp. 283–291, Mar 1999.

[106] C. R. Sullivan, "Computationally efficient winding loss calculation with multiple windings, arbitrary waveforms, and two-dimensional or three-dimensional field geometry," *IEEE Transactions on Power Electronics*, vol. 16, no. 1, pp. 142–150, Jan 2001.

[107] T. Theodoulidis, C. S. Antonopoulos, and E. E. Kriezis, "Analytical solution for the eddy current problem inside a conducting cylinder using the second order magnetic vector potential," *COMPEL - The International Journal for Computation and Mathematics in Electrical and Electronic Engineering*, vol. Vol. 14, No. 4, pp. 45–48, 1995.

[108] G. Venter, *Review of Optimization Techniques.* John Wiley & Sons, Ltd, 2010.

[109] D. Voltmer, *Fundamentals of Electromagnetic Volume 2: Quasistatistics and Waves.* Morgan & Claypool, 2007.

[110] K. Weigelt, "Uber die dreidimensionale analytische berechnung von wirbel-stromen in gekoppelten kreiszylinderschalen," Ph.D. dissertation, Technischen Universitat Munchen, 1986.

[111] Y. Yamada, "Torque resistance of a flow between rotating co-axial cylinders having axial flow," *Bulletin of JSME*, vol. 5, no. 20, pp. 634–642, 1962.

[112] J. Yoshida, N. Hino, K. Takahashi, A. Nakahara, A. Komura, and K. Hattori, "Calculation method of circulating current in parallel armature windings in consideration of magnetic circuit," in *IEEE Power Energy Society General Meeting*, pp. 1–5, July 2013.

[113] Z. Q. Zhu, K. Ng, N. Schofield, and D. Howe, "Improved analytical modelling of rotor eddy current loss in brushless machines equipped with surface-mounted permanent magnets," *IEE Proceedings - Electric Power Applications*, vol. 151, no. 6, pp. 641–650, Nov 2004.

[114] Z. Zhu and D. Howe, "Instantaneous magnetic field distribution in brushless permanent magnet DC motors. ii. armature-reaction field," *IEEE Transactions on Magnetics*, vol. 29, no. 1, pp. 136–142, Jan 1993.

[115] C. Zwyssig, M. Duerr, D. Hassler, and J. W. Kolar, "An ultra-high-speed, 500000 rpm, 1 kW electrical drive system," in *Power Conversion Conference - Nagoya*, pp. 1577–1583, April 2007.

[116] C. Zwyssig, S. D. Round, and J. W. Kolar, "Power electronics interface for a 100 W, 500000 rpm gas turbine portable power unit," in *Twenty-First Annual IEEE Applied Power Electronics Conference and Exposition, 2006. APEC '06.*, March 2006.

[117] C. Zwyssig, S. D. Round, and J. W. Kolar, "An ultrahigh-speed, low power electrical drive system," *IEEE Transactions on Industrial Electronics*, vol. 55, no. 2, pp. 577–585, Feb 2008.

Acknowledgments

The results of this PhD span are not only the current thesis, but also the professional and life experience that I have gained during this time. This is a merit of many people and would have been impossible without them. Therefore, I would like to use this chance to thank all these people.

First of all, I would like to express my deepest gratitude to my first promoter (supervisor) Prof. Elena Lomonova for the opportunity she gave to me to get through this interesting journey, for the long, fruitful, and inspiring discussions we had, and for her immeasurable contribution to the professional and social aspects of my knowledge and life.

Further, I am particularly grateful to my second promoter (supervisor) Prof. Juha Pyrhönen for his technical guidance and discussions, patience, for being an example of a responsible and practical person, and especially for his openness, which was important for me.

I would also like to thank my co-promoter Dr. Konstantin Boynov for his always positive and constructive attitude and inestimable support with practical issues.

Further, I would like to express my appreciation to Dr. Helm Jansen for selflessly sharing his knowledge in the analytical and FEM modeling of electrical machines with me and giving useful comments on my thesis.

My special thanks go to Dr. Hanna Niemelä for correcting my English and making the thesis readable and clear not only for me but also for a wider audience. I enjoyed the editing process because of her very professional attitude.

Especially, I wish to thank the members of my PhD committee: Prof. Christopher Gerada, Prof. Luc Dupré, Dr. Roland Keller, and Dr. Timo Overboom for their time reading my thesis and providing me with valuable feedback.

I am very grateful to Dr. Aleksandar Borisavljević and Dr. Johan Paulides for their valuable input during different periods of my PhD research.

My special thanks go to Dr. Fritz Faulhaber GmbH & Co. KG, and personally,

Curriculum Vitae

Sultan Jumayev was born on the 13th of April, 1988 in Seydi, Turkmenistan. He received his Specialist degree in Electrical Engineering from Saint-Petersburg Technological University of Plant Polymers, Russian Federation in 2010. In 2011, he received his M.Sc. (Tech.) degree in Electrical Engineering from Lappeenranta University of Technology, Finland.

In November 2011, he started a double-degree PhD program within the Electromechanics and Power Electronics group (Eindhoven University of Technology, the Netherlands) and the Laboratory of Electrical Drives Technology (Lappeenranta University of Technology, Finland). His main research interest is the electromagnetic modeling of high-speed rotating electrical machines.